

FEBRUARY 2023

AJNR

VOLUME 44 • PP 117-234

AJNR

AMERICAN JOURNAL OF NEURORADIOLOGY

FEBRUARY 2023
VOLUME 44
NUMBER 2
WWW.AJNR.ORG

THE JOURNAL OF DIAGNOSTIC AND
INTERVENTIONAL NEURORADIOLOGY

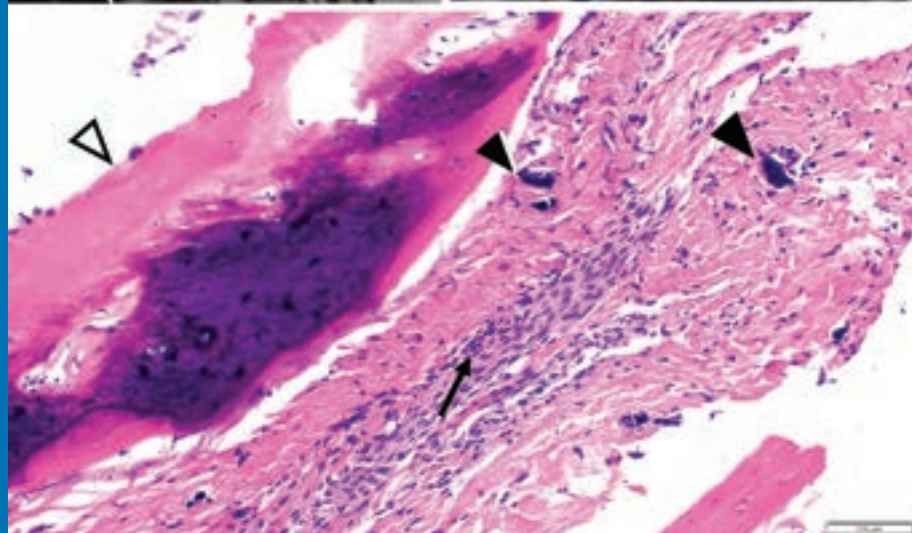
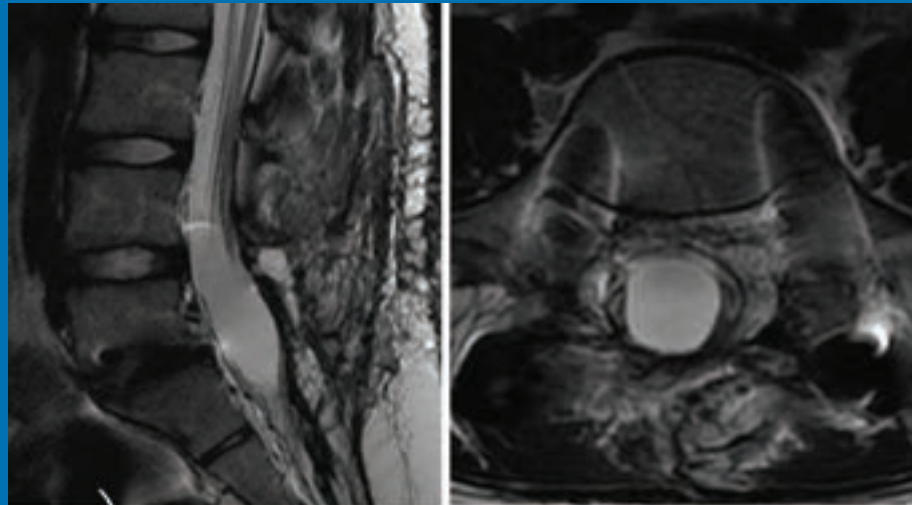
ASL, DCE, DSE perfusion in recurrent glioma

Radiation-induced changes associated with obliteration of brain AVMs

7T MR imaging of the trochlear nerve

Intrathecal ossification in arachnoiditis ossificans

Official Journal ASNR • ASFNR • ASHNR • ASPNR • ASSR



FRED™ X™

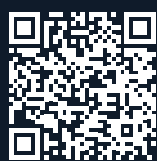
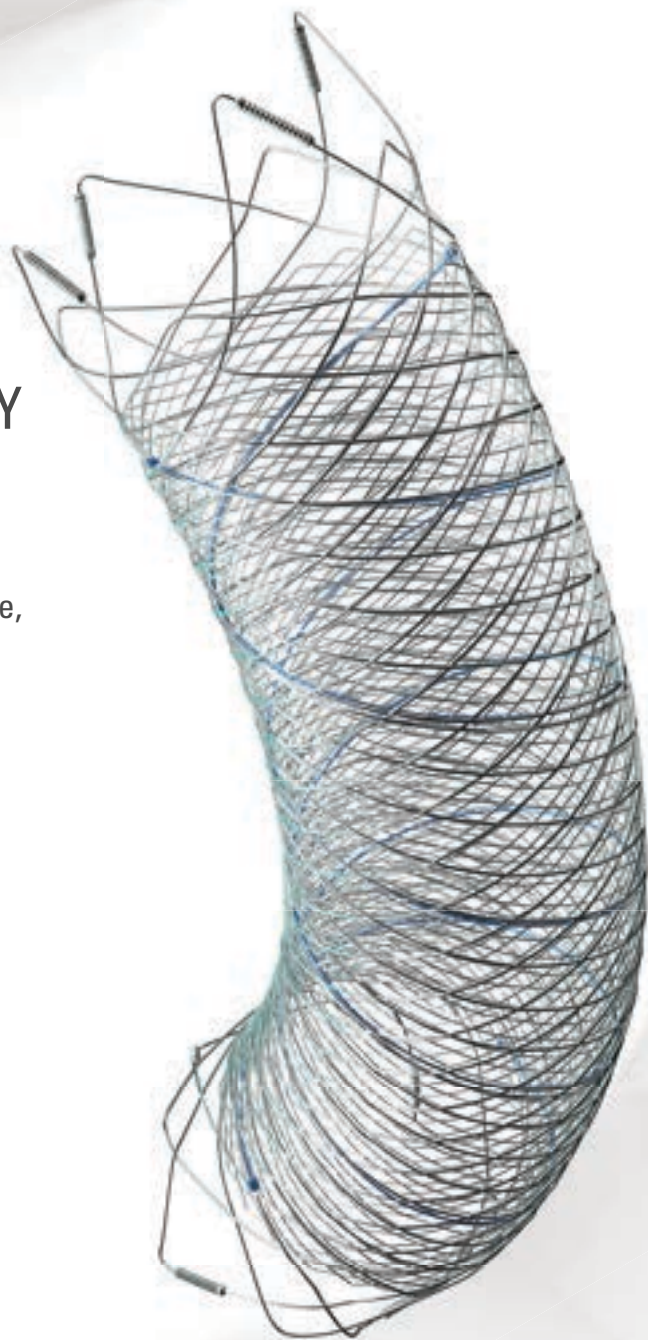
Flow Diverter Stent

THE NEXT ADVANCEMENT IN FLOW DIVERSION TECHNOLOGY

The FRED™ X Flow Diverter features the same precise placement and immediate opening of the FRED™ Device, now with X Technology. X Technology is a covalently bonded, nanoscale surface treatment, designed to:

- **REDUCE MATERIAL THROMBOGENICITY¹**
- **MAINTAIN NATURAL VESSEL HEALING RESPONSE^{2,3,4}**
- **IMPROVE DEVICE DELIVERABILITY AND RESHEATHING¹**

The only FDA PMA approved portfolio with a 0.021" delivery system for smaller device sizes, and no distal lead wire.



For more information, contact your local MicroVention sales representative or visit our website. www.microvention.com



^{*} Data is derived from in vivo and ex vitro testing and may not be representative of clinical performance.

¹ Data on file

² Tanaka M et al. Design of biocompatible and biodegradable polymers based on intermediate water concept. Polymer Journal. 2015;47:114-121.

³ Tanaka M et al. Blood compatible aspects of poly(2-methoxyethylacrylate) (PMEA) – relationship between protein adsorption and platelet adhesion on PMEAs surface. Biomaterials. 2000;21:1471-1481.

⁴ Schiel L et al. X Coating™: A new biopassive polymer coating. Canadian Perfusion Canadienne. June 2001;11(2):9.

Indications for Use: The FRED X System is indicated for use in the internal carotid artery from the petrous segment to the terminus for the endovascular treatment of adult patients (22 years of age or older) with wide-necked (neck width 4 mm or dome-to-neck ratio < 2) saccular or fusiform intracranial aneurysms arising from a parent vessel with a diameter 2.0 mm and 5.0 mm.

Rx Only: Federal (United States) law restricts this device to sale by or on the order of a physician. For Healthcare professionals intended use only.

MICROVENTION, FRED and HEADWAY are registered trademarks of MicroVention, Inc. in the United States and other jurisdictions. Stylized X is a trademark of MicroVention, Inc. © 2022 MicroVention, Inc. MM1222 US 03/22

WEB™ 17

Aneurysm Embolization System

LOWER PROFILE



NEW SIZES



MORE ACCESS OPTIONS



INDICATIONS FOR USE:

The WEB Aneurysm Embolization System is intended for the endovascular embolization of ruptured and unruptured intracranial aneurysms and other neurovascular abnormalities such as arteriovenous fistulae (AVF). The WEB Aneurysm Embolization System is also intended for vascular occlusion of blood vessels within the neurovascular system to permanently obstruct blood flow to an aneurysm or other vascular malformation.

POTENTIAL COMPLICATIONS:

Potential complications include but are not limited to the following: hematoma at the site of entry, aneurysm rupture, emboli, vessel perforation, parent artery occlusion, hemorrhage, ischemia, vasospasm, clot formation, device migration or misplacement, premature or difficult device detachment, non-detachment, incomplete aneurysm filling, revascularization, post-embolization syndrome, and neurological deficits including stroke and death. For complete indications, potential complications, warnings, precautions, and instructions, see instructions for use (IFU provided with the device).

VIA 21, 27, 33 - The VIA Microcatheter is intended for the introduction of interventional devices (such as the WEB device/stents/flow diverters) and infusion of diagnostic agents (such as contrast media) into the neuro, peripheral, and coronary vasculature.

VIA 17,17 Preshaped - The VIA Microcatheter is intended for the introduction of interventional devices (such as the WEB device/stents/flow diverters) and infusion of diagnostic agents (such as contrast media) into the neuro, peripheral, and coronary vasculature.

The VIA Microcatheter is contraindicated for use with liquid embolic materials, such as n-butyl 2-cyanoacrylate or ethylene vinyl alcohol & DMSO (dimethyl sulfoxide).

The device should only be used by physicians who have undergone training in all aspects of the WEB Aneurysm Embolization System procedure as prescribed by the manufacturer.

RX Only: Federal law restricts this device to sale by or on the order of a physician.

For healthcare professional intended use only.



MicroVention Worldwide
Innovation Center PH +1.714.247.8000

35 Enterprise
Aliso Viejo, CA 92656 USA
MicroVention UK Limited PH +44 (0) 191 258 6777
MicroVention Europe, S.A.R.L. PH +33 (1) 39 21 77 46
MicroVention Deutschland GmbH PH +49 211 210 798-0
Website microvention.com



WEB™ and VIA™ are registered trademarks
of Sequent Medical, Inc. in the United States.

©2021 MicroVention, Inc. MM1184 WW 11/2021

LIFE IS FULL OF COMPROMISES.
IT'S TIME TO TAKE A STAND.

NO COMPROMISE

HIGH RELAXIVITY, HIGH STABILITY:^{1,2}
I CHOOSE BOTH.

The individual who appears is for illustrative purposes. The person depicted is a model and not a real healthcare professional. Please see Brief Summary of Prescribing Information including Boxed Warning on adjacent page.

VUEWAY™ (gadopiclenol) solution for injection

Indications

VUEWAY injection is indicated in adults and children aged 2 years and older for use with magnetic resonance imaging (MRI) to detect and visualize lesions with abnormal vascularity in:

- the central nervous system (brain, spine and surrounding tissues),
- the body (head and neck, thorax, abdomen, pelvis, and musculoskeletal system).

IMPORTANT SAFETY INFORMATION

WARNING: NEPHROGENIC SYSTEMIC FIBROSIS (NSF)

Gadolinium-based contrast agents (GBCAs) increase the risk for NSF among patients with impaired elimination of the drugs. Avoid use of GBCAs in these patients unless the diagnostic information is essential and not available with non-contrast MRI or other modalities. NSF may result in fatal or debilitating fibrosis affecting the skin, muscle and internal organs.

- **The risk for NSF appears highest among patients with:**
 - **Chronic, severe kidney disease (GFR < 30 mL/min/1.73 m²), or**
 - **Acute kidney injury.**
- **Screen patients for acute kidney injury and other conditions that may reduce renal function. For patients at risk for chronically reduced renal function (e.g. age > 60 years,**

hypertension, diabetes), estimate the glomerular filtration rate (GFR) through laboratory testing.

- **For patients at highest risk for NSF, do not exceed the recommended VUEWAY dose and allow a sufficient period of time for elimination of the drug from the body prior to any re-administration.**

Contraindications

VUEWAY injection is contraindicated in patients with history of hypersensitivity reactions to VUEWAY.

Warnings

Risk of **nephrogenic systemic fibrosis** is increased in patients using GBCA agents that have impaired elimination of the drugs, with the highest risk in patients chronic, severe kidney disease as well as patients with acute kidney injury. Avoid use of GBCAs among these patients unless the diagnostic information is essential and not available with non-contrast MRI or other modalities.

Hypersensitivity reactions, including serious hypersensitivity reactions, could occur during use or shortly following VUEWAY administration. Assess all patients for any history of a reaction to contrast media, bronchial asthma and/or allergic disorders, administer VUEWAY only in situations where trained personnel and therapies are promptly available for the treatment of hypersensitivity reactions, and observe patients for signs and symptoms of hypersensitivity reactions after administration.



MR Suite

IN MRI

INTRODUCING


Vueway™
(gadopiclenol) injection
485.1 mg/mL

HALF THE GADOLINIUM DOSE COMPARED TO OTHER
MACROCYCLIC GBCAs IN APPROVED INDICATIONS.^{1,3-6}
FROM BRACCO, YOUR TRUSTED PARTNER IN MRI.



LIFE FROM INSIDE

Gadolinium retention can be for months or years in several organs after administration. The highest concentrations (nanomoles per gram of tissue) have been identified in the bone, followed by other organs (brain, skin, kidney, liver and spleen). Minimize repetitive GBCA imaging studies, particularly closely spaced studies, when possible.

Acute kidney injury requiring dialysis has occurred with the use of GBCAs in patients with chronically reduced renal function. The risk of acute kidney injury may increase with increasing dose of the contrast agent.

Ensure catheter and venous patency before injecting as **extravasation** may occur, and cause tissue irritation.

VUEWAY may **impair the visualization of lesions** seen on non-contrast MRI. Therefore, caution should be exercised when Vueway MRI scans are interpreted without a companion non-contrast MRI scan.

The most common adverse reactions (incidence \geq 0.5%) are injection site pain (0.7%), and headache (0.7%).

You are encouraged to report negative side effects of prescription drugs to the FDA. Visit www.fda.gov/medwatch or call 1-800-FDA-1088.

Please see BRIEF SUMMARY of Prescribing Information for VUEWAY, including BOXED WARNING on Nephrogenic Systemic Fibrosis.

Manufactured for Bracco Diagnostics Inc. by Liebel-Flarsheim Company LLC - Raleigh, NC, USA 27616.

VUEWAY is a trademark of Bracco Imaging S.p.A.

References: **1.** Vueway™ (gadopiclenol) Injection Full Prescribing Information. Monroe Twp., NJ: Bracco Diagnostics Inc.; September 2022. **2.** Robic C, Port M, Rousseaux O, et al. Physicochemical and Pharmacokinetic Profiles of Gadopiclenol: A New Macrocylic Gadolinium Chelate With High T1 Relaxivity. *Invest Radiol.* 2019 Aug;54: 475–484. **3.** GADAVIST® (gadobutrol) Injection. Full Prescribing Information. Bayer HealthCare Pharmaceuticals Inc. Whippany, NJ; April 2022. **4.** DOTAREM® (gadoterate meglumine) Injection. Full Prescribing Information. Guerbet LLC. Princeton, NJ; April 2022. **5.** CLARISCAN™ (gadoterate meglumine) injection for intravenous use. Full Prescribing Information. GE Healthcare. Marlborough, MA; February 2020. **6.** ProHance® (Gadoteridol) Injection. Full Prescribing Information and Patient Medication Guide. Monroe Twp., NJ: Bracco Diagnostics Inc.; December 2020.

Bracco Diagnostics Inc.
259 Prospect Plains Road, Building H
Monroe Township, NJ 08831 USA
Phone: 609-514-2200
Toll Free: 1-877-272-2269 (U.S. only)
Fax: 609-514-2446
© 2022 Bracco Diagnostics Inc.
All Rights Reserved. US-VW-2200012 10/22

VISIT
VUEWAY.COM
FOR MORE
INFORMATION



Vueway™

(gadopiclenol) injection, for intravenous use

BRIEF SUMMARY: Please see package insert of full prescribing information.

WARNING: NEPHROGENIC SYSTEMIC FIBROSIS (NSF)
Gadolinium-based contrast agents (GBCAs) increase the risk for NSF among patients with impaired elimination of the drugs. Avoid use of GBCAs in these patients unless the diagnostic information is essential and not available with non-contrast MRI or other modalities. NSF may result in fatal or debilitating fibrosis affecting the skin, muscle and internal organs.

- The risk for NSF appears highest among patients with:
 - Chronic, severe kidney disease (GFR <30 mL/min/1.73 m²), or
 - Acute kidney injury.
- Screen patients for acute kidney injury and other conditions that may reduce renal function. For patients at risk for chronically reduced renal function (e.g. age >60 years, hypertension, diabetes), estimate the glomerular filtration rate (GFR) through laboratory testing.
- For patients at highest risk for NSF, do not exceed the recommended Vueway dose and allow a sufficient period of time for elimination of the drug from the body prior to any re-administration [see Warnings and Precautions (5.1) in the full Prescribing Information].

INDICATIONS AND USAGE

Vueway™ (gadopiclenol) is a gadolinium-based contrast agent indicated in adult and pediatric patients aged 2 years and older for use with magnetic resonance imaging (MRI) to detect and visualize lesions with abnormal vascularity in:

- the central nervous system (brain, spine, and associated tissues),
- the body (head and neck, thorax, abdomen, pelvis, and musculoskeletal system).

CONTRAINDICATIONS

Vueway is contraindicated in patients with history of hypersensitivity reactions to gadopiclenol.

WARNINGS AND PRECAUTIONS

Nephrogenic Systemic Fibrosis Gadolinium-based contrast agents (GBCAs) increase the risk for nephrogenic systemic fibrosis (NSF) among patients with impaired elimination of the drugs. Avoid use of GBCAs among these patients unless the diagnostic information is essential and not available with non-contrast MRI or other modalities. The GBCA-associated NSF risk appears highest for patients with chronic, severe kidney disease (GFR <30 mL/min/1.73 m²) as well as patients with acute kidney injury. The risk appears lower for patients with chronic, moderate kidney disease (GFR 30-59 mL/min/1.73 m²) and little, if any, for patients with chronic, mild kidney disease (GFR 60-89 mL/min/1.73 m²). NSF may result in fatal or debilitating fibrosis affecting the skin, muscle, and internal organs. Report any diagnosis of NSF following Vueway administration to Bracco Diagnostics Inc. (1-800-257-5181) or FDA (1-800-FDA-1088 or www.fda.gov/medwatch).

Screen patients for acute kidney injury and other conditions that may reduce renal function. Features of acute kidney injury consist of rapid (over hours to days) and usually reversible decrease in kidney function, commonly in the setting of surgery, severe infection, injury or drug-induced kidney toxicity. Serum creatinine levels and estimated GFR may not reliably assess renal function in the setting of acute kidney injury. For patients at risk for chronically reduced renal function (e.g., age >60 years, diabetes mellitus or chronic hypertension), estimate the GFR through laboratory testing.

Among the factors that may increase the risk for NSF are repeated or higher than recommended doses of a GBCA and the degree of renal impairment at the time of exposure. Record the specific GBCA and the dose administered to a patient. For patients at highest risk for NSF, do not exceed the recommended Vueway dose and allow a sufficient period of time for elimination of the drug prior to re-administration. For patients receiving hemodialysis, physicians may consider the prompt initiation of hemodialysis following the administration of a GBCA in order to enhance the contrast agent's elimination [see Use in Specific Populations (8.6) and Clinical Pharmacology (12.3) in the full Prescribing Information]. The usefulness of hemodialysis in the prevention of NSF is unknown.

Hypersensitivity Reactions With GBCAs, serious hypersensitivity reactions have occurred. In most cases, initial symptoms occurred within minutes of GBCA administration and resolved with prompt emergency treatment.

- Before Vueway administration, assess all patients for any history of a reaction to contrast media, bronchial asthma and/or allergic disorders. These patients may have an increased risk for a hypersensitivity reaction to Vueway.
- Vueway is contraindicated in patients with history of hypersensitivity reactions to Vueway [see Contraindications (4) in the full Prescribing Information].
- Administer Vueway only in situations where trained personnel and therapies are promptly available for the treatment of hypersensitivity reactions, including personnel trained in resuscitation.
- During and following Vueway administration, observe patients for signs and symptoms of hypersensitivity reactions.

Gadolinium Retention Gadolinium is retained for months or years in several organs. The highest concentrations (nanomoles per gram of tissue) have been identified in the bone, followed by other organs (e.g. brain, skin, kidney, liver, and spleen). The duration of retention also varies by tissue and is longest in bone. Linear GBCAs cause more retention than macrocyclic GBCAs. At equivalent doses, gadolinium retention varies among the linear agents with gadodiamide causing greater retention than other linear agents such as gadoxetate disodium, and gadobenate dimeglumine. Retention is lowest and similar

among the macrocyclic GBCAs such as gadoterate meglumine, gadobutrol, gadoteridol, and gadopiclenol.

Consequences of gadolinium retention in the brain have not been established. Pathologic and clinical consequences of GBCA administration and retention in skin and other organs have been established in patients with impaired renal function [see Warnings and Precautions (5.1) in the full Prescribing Information]. There are rare reports of pathologic skin changes in patients with normal renal function. Adverse events involving multiple organ systems have been reported in patients with normal renal function without an established causal link to gadolinium.

While clinical consequences of gadolinium retention have not been established in patients with normal renal function, certain patients might be at higher risk. These include patients requiring multiple lifetime doses, pregnant and pediatric patients, and patients with inflammatory conditions. Consider the retention characteristics of the agent when choosing a GBCA for these patients. Minimize repetitive GBCA imaging studies, particularly closely spaced studies, when possible.

Acute Kidney Injury in patients with chronically reduced renal function, acute kidney injury requiring dialysis has occurred with the use of GBCAs. The risk of acute kidney injury may increase with increasing dose of the contrast agent. Do not exceed the recommended dose.

Extravasation and Injection Site Reactions Injection site reactions such as injection site pain have been reported in the clinical studies with Vueway [see Adverse Reactions (6.1) in the full Prescribing Information]. Extravasation during Vueway administration may result in tissue irritation [see Nonclinical Toxicology (13.2) in the full Prescribing Information]. Ensure catheter and venous patency before the injection of Vueway.

Interference with Visualization of Lesions Visible with Non-Contrast MRI As with any GBCA, Vueway may impair the visualization of lesions seen on non-contrast MRI. Therefore, caution should be exercised when Vueway MRI scans are interpreted without a companion non-contrast MRI scan.

ADVERSE REACTIONS

The following serious adverse reactions are discussed elsewhere in labeling:

- Nephrogenic Systemic Fibrosis [see Warnings and Precautions (5.1) in the full Prescribing Information]
- Hypersensitivity Reactions [see Contraindications (4) and Warnings and Precautions (5.2) in the full Prescribing Information]

Clinical Trials Experience Because clinical trials are conducted under widely varying conditions, adverse reaction rates observed in the clinical trials of a drug cannot be directly compared to rates in the clinical trials of another drug and may not reflect the rates observed in clinical practice.

The safety of Vueway was evaluated in 1,047 patients who received Vueway at doses ranging from 0.025 mmol/kg (one half the recommended dose) to 0.3 mmol/kg (six times the recommended dose). A total of 708 patients received the recommended dose of 0.05 mmol/kg. Among patients who received the recommended dose, the average age was 51 years (range 2 years to 88 years) and 56% were female. The ethnic distribution was 79% White, 10% Asian, 7% American Indian or Alaska native, 2% Black, and 2% patients of other or unspecified ethnic groups.

Overall, approximately 4.7% of subjects receiving the labeled dose reported one or more adverse reactions.

Table 1 lists adverse reactions that occurred in >0.2% of patients who received 0.05 mmol/kg Vueway.

TABLE 1. ADVERSE REACTIONS REPORTED IN >0.2% OF PATIENTS RECEIVING VUEWAY IN CLINICAL TRIALS	
Adverse Reaction	Vueway 0.05 mmol/kg (n=708) (%)
Injection site pain	0.7
Headache	0.7
Nausea	0.4
Injection site warmth	0.4
Injection site coldness	0.3
Dizziness	0.3
Local swelling	0.3

Adverse reactions that occurred with a frequency < 0.2% in patients who received 0.05 mmol/kg Vueway included: maculopapular rash, vomiting, worsened renal impairment, feeling hot, pyrexia, oral paresthesia, dysgeusia, diarrhea, pruritus, allergic dermatitis, erythema, injection site paresthesia, Cystatin C increase, and blood creatinine increase.

Adverse Reactions in Pediatric Patients

One study with a single dose of Vueway (0.05 mmol/kg) was conducted in 80 pediatric patients aged 2 years to 17 years, including 60 patients who underwent a central nervous system (CNS) MRI and 20 patients who underwent a body MRI. One adverse reaction (maculopapular rash of moderate severity) in one patient (1.3%) was reported in the CNS cohort.

USE IN SPECIFIC POPULATIONS

Pregnancy Risk Summary There are no available data on Vueway use in pregnant women to evaluate for a drug-associated risk of major birth defects, miscarriage or other adverse maternal or fetal outcomes. GBCAs cross the human placenta and result in fetal exposure and gadolinium retention. The available human data on GBCA exposure during pregnancy and adverse fetal outcomes are limited and inconclusive (see Data). In animal reproduction studies, there were no adverse developmental effects observed in rats or rabbits with intravenous administration of Vueway during organogenesis (see Data). Because of the potential risks of gadolinium to the fetus, use Vueway only if imaging is essential during pregnancy and cannot be delayed. The estimated background risk of major birth defects and miscarriage for the indicated population(s) are unknown. All pregnancies have a background risk of birth defect, loss, or other adverse outcomes. In the U.S. general population, the estimated background risk of major birth defects and miscarriage in clinically recognized pregnancies is 2% to 4% and 15% to 20% respectively. Data Human Data Contrast enhancement is visualized in the placenta and fetal tissues after maternal GBCA administration. Cohort studies and case reports on exposure to GBCAs during pregnancy have not reported a clear association between GBCAs and adverse effects in the exposed neonates. However, a retrospective cohort study comparing pregnant women who had a GBCA MRI to pregnant women who did not have an MRI reported a higher occurrence of stillbirths and neonatal deaths in the group receiving GBCA MRI. Limitations of this study include a lack of comparison with non-contrast MRI and lack of information about the maternal indication for MRI. Overall, these data preclude

a reliable evaluation of the potential risk of adverse fetal outcomes with the use of GBCAs in pregnancy.

Animal Data Gadolinium Retention: GBCAs administered to pregnant non-human primates (0.1 mmol/kg on gestational days 85 and 135) result in measurable gadolinium concentration in the offspring in bone, brain, skin, liver, kidney, and spleen for at least 7 months. GBCAs administered to pregnant mice (2 mmol/kg daily on gestational days 16 through 19) result in measurable gadolinium concentrations in the pups in bone, brain, kidney, liver, blood, muscle, and spleen at one-month postnatal age.

Reproductive Toxicology: Animal reproduction studies conducted with gadopiclenol showed some signs of maternal toxicity in rats at 10 mmol/kg and rabbits at 5 mmol/kg (corresponding to 52 times and 57 times the recommended human dose, respectively). This maternal toxicity was characterized in both species by swelling, decreased activity, and lower gestation weight gain and food consumption.

No effect on embryo-fetal development was observed in rats at 10 mmol/kg (corresponding to 52 times the recommended human dose). In rabbits, a lower mean fetal body weight was observed at 5 mmol/kg (corresponding to 57 times the recommended human dose) and this was attributed as a consequence of the lower gestation weight gain.

Lactation Risk Summary There are no data on the presence of gadopiclenol in human milk, the effects on the breastfed infant, or the effects on milk production. However, published lactation data on other GBCAs indicate that 0.01% to 0.04% of the maternal gadolinium dose is excreted in breast milk. Additionally, there is limited GBCA gastrointestinal absorption in the breast-fed infant. Gadopiclenol is present in rat milk. When a drug is present in animal milk, it is likely that the drug will be present in human milk (see Data). The developmental and health benefits of breastfeeding should be considered along with the mother's clinical need for Vueway and any potential adverse effects on the breastfed infant from Vueway or from the underlying maternal condition. Data In lactating rats receiving single intravenous injection of [¹⁵²Gd]-gadopiclenol, 0.3% and 0.2% of the total administered radioactivity was transferred to the pups via maternal milk at 6 hours and 24 hours after administration, respectively. Furthermore, in nursing rat pups, oral absorption of gadopiclenol was 3.6%.

Pediatric Use The safety and effectiveness of Vueway for use with MRI to detect and visualize lesions with abnormal vascularity in the CNS (brain, spine, and associated tissues), and the body (head and neck, thorax, abdomen, pelvis, and musculoskeletal system) have been established in pediatric patients aged 2 years and older.

Use of Vueway in this age group is supported by evidence from adequate and well-controlled studies in adults with additional pharmacokinetic and safety data from an open-label, uncontrolled, multicenter, single dose study of Vueway (0.05 mmol/kg) in 80 pediatric patients aged 2 to 17 years. The 80 patients consisted of 60 patients who underwent a CNS MRI and 20 patients who underwent a body MRI [see Adverse Reactions (6.1) and Clinical Pharmacology (12.3) in the full Prescribing Information].

The safety and effectiveness of Vueway have not been established in pediatric patients younger than 2 years of age.

Geriatric Use Of the total number of Vueway-treated patients in clinical studies, 270 (26%) patients were 65 years of age and over, while 62 (6%) patients were 75 years of age and over. No overall differences in safety or efficacy were observed between these subjects and younger subjects.

This drug is known to be substantially excreted by the kidney, and the risk of adverse reactions to this drug may be greater in patients with impaired renal function. Because elderly patients are more likely to have decreased renal function, it may be useful to monitor renal function.

Renal Impairment in patients with renal impairment, the exposure of gadopiclenol is increased compared to patients with normal renal function. This may increase the risk of adverse reactions such as nephrogenic systemic fibrosis (NSF). Avoid use of GBCAs among these patients unless the diagnostic information is essential and not available with non-contrast MRI or other modalities. No dose adjustment of Vueway is recommended for patients with renal impairment. Vueway can be removed from the body by hemodialysis [see Warnings and Precautions (5.1, 5.3, 5.4) and Clinical Pharmacology (12.3) in the full Prescribing Information].

OVERDOSAGE

Among subjects who received a single 0.3 mmol/kg intravenous dose of gadopiclenol (6 times the recommended dose of Vueway), headache and nausea were the most frequently reported adverse reactions. Gadopiclenol can be removed from the body by hemodialysis [see Clinical Pharmacology (12.3) in the full Prescribing Information].

PATIENT COUNSELING INFORMATION Advise the patient to read the FDA-approved patient labeling (Medication Guide).

Nephrogenic Systemic Fibrosis Inform the patient that Vueway may increase the risk for NSF among patients with impaired elimination of the drugs and that NSF may result in fatal or debilitating fibrosis affecting the skin, muscle and internal organs.

Instruct the patients to contact their physician if they develop signs or symptoms of NSF following Vueway administration, such as burning, itching, swelling, scaling, hardening and tightening of the skin; red or dark patches on the skin; stiffness in joints with trouble moving, bending or straightening the arms, hands, legs or feet; pain in the hip bones or ribs; or muscle weakness [see Warnings and Precautions (5.1) in the full Prescribing Information].

Gadolinium Retention Advise patients that gadolinium is retained for months or years in brain, bone, skin, and other organs following Vueway administration even in patients with normal renal function. The clinical consequences of retention are unknown. Retention depends on multiple factors and is greater following administration of linear GBCAs than following administration of macrocyclic GBCAs [see Warnings and Precautions (5.3) in the full Prescribing Information].

Injection Site Reactions Inform the patient that Vueway may cause reactions along the venous injection site, such as mild and transient burning or pain or feeling of warmth or coldness at the injection site [see Warnings and Precautions (5.5) in the full Prescribing Information].

Pregnancy Advise pregnant women of the potential risk of fetal exposure to Vueway [see Use in Specific Populations (8.1) in the full Prescribing Information].

Rx only

US Patent No. 10,973,934
Manufactured for Bracco Diagnostics Inc. by Liebel-Flarsheim Company LLC - Raleigh, NC, USA 27616.
Toll Free: 1-877-272-2269 (U.S. only)
Revised November 2022

CALL FOR AJNR EDITORIAL FELLOWSHIP CANDIDATES

ASNR and AJNR are pleased once again to join efforts with other imaging-related journals that have training programs on editorial aspects of publishing for trainees or junior staff (<5 years on staff), including Radiology (Olmsted fellowship), AJR (Figley and Rogers fellowships), JACR (Bruce J. Hillman fellowship), and Radiologia.

2023 Candidate Information and Requirements

GOALS

- Increase interest in editorial and publication-related activities in younger individuals.
- Increase understanding and participation in the AJNR review process.
- Incorporate into AJNR's Editorial Board younger individuals who have previous experience in the review and publication process.
- Fill a specific need in neuroradiology not offered by other similar fellowships.
- Increase the relationship between "new" generation of neuroradiologists and more established individuals.
- Increase visibility of AJNR among younger neuroradiologists.

ACTIVITIES OF THE FELLOWSHIP

- Serve as Editorial Fellow for one year. This individual will be listed on the masthead as such.
- Review at least one manuscript per month for 12 months. Evaluate all review articles submitted to AJNR.
- Learn how electronic manuscript review systems work.
- Be involved in the final decision of selected manuscripts together with the Editor-in-Chief.
- Participate in all monthly Senior Editor telephone conference calls.
- Participate in 2 virtual meetings of the Editorial Board.
- Evaluate progress and adjust program to specific needs in annual meeting or telephone conference with the Editor-in-Chief.
- Embark on an editorial scientific or bibliometric project that will lead to the submission of an article to AJNR or another appropriate journal as determined by the Editor-in-Chief. This project will be presented by the Editorial Fellow at the ASNR annual meeting. The Foundation of the ASNR will provide \$2000 funding for this activity.
- Recruit trainees as reviewers as determined by the Editor-in-Chief.
- Serve as Guest Editor for an issue of AJNR's News Digest with a timely topic.

QUALIFICATIONS

- Be a fellow in neuroradiology from North America, including Canada (this may be extended to include other countries).
- Be a junior faculty neuroradiology member (< 5 years) in either an academic or private environment.
- Be an "in-training" or member of ASNR in any other category.

APPLICATION

- Include a short letter of intent with statement of goals and desired research project. CV must be included.
- Include a letter of recommendation from the Division Chief or fellowship program director. A statement of protected time to perform the functions outlined is desirable.
- Applications will be evaluated by AJNR's Senior Editors prior to the ASNR annual meeting. The name of the selected individual will be announced at the meeting.
- Applications should be received by March 1, 2023 and sent to Ms. Karen Halm, AJNR Managing Editor, electronically at khalm@asnr.org.

In Planning for Brain Metastases Treatment, Imaging may be the Missing Link in Cost Containment¹

When faced with a patient presenting with metastatic brain cancer, determining whether to use up-front stereotactic radiosurgery (SRS) vs. first treating with whole brain radiotherapy (WBRT) is a significant clinical decision.

WBRT: The whole story on cognitive impairment

While whole brain radiotherapy (WBRT) has been the main treatment option for many years, experts agree that it often results in cognitive deterioration and a negative impact on quality of life. This mental decline has a devastating impact on patients and their families and adds ongoing costs for the healthcare systems managing these symptoms.

Using WBRT instead of SRS in some patients is estimated to decrease the total costs of brain metastasis management, though with increased toxicity.

SRS: Fewer side effects but greater risk of missed tumors

The cost of upfront SRS is the greatest contributor to cost of brain metastasis management.¹ SRS is often more expensive than WBRT. What's more, multiple applications of SRS can increase the cost of treatment greatly.

Stereotactic radiosurgery (SRS) has far fewer side effects, but upfront use of SRS is expensive and can carry the risk of missed tumors, requiring repeat procedures such as salvage SRS.¹

Number of lesions and lesion size are key factors to be considered when determining the treatment plan for these patients. It follows that increased diagnostic information and accuracy could be beneficial in directing the proper therapy and improving overall long-term patient outcomes and containing costs. Getting the diagnosis right the first time is crucial to ensure proper treatment begins quickly, and high cost/high stakes procedures such as SRS need precise surgical planning.

What does optimal visualization mean for outcomes and cost?

For surgical planning with SRS, radiologists need the best visualization achievable to accurately count the number and size of the lesions. These metrics are the key predictors of the need for SRS,¹ WBRT, or a combination of both.

By selecting the ideal contrast agent and equipment protocols, neuroradiologists can identify the proximate numbers of metastases for upfront treatment and reduced salvage treatment occurrences.

The role of radiology

As medical care for oncology patients continues to evolve, it will be increasingly important to assess the cost of various interventions given the often-limited life expectancy of cancer patients, the rising costs of cancer therapy, and the increasing prevalence of cancer in an aging population.

Through seeing all the tumors and tumor borders as clearly as technology allows, radiology can play a part in ensuring that proper treatment can begin quickly,

while containing costs through optimized patient care. Efforts to carefully manage treatment approaches require improvements in protocol design, contrast administration in imaging, and utilizing multimodal imaging approaches.

In this era of precision medicine, radiology departments' contribution to this improved standard of care will have significant short and long-term implications by reducing cost of care, providing a more proximate diagnosis, and ensuring optimal patient outcomes. ■



Getting the diagnosis right the first time is crucial to ensure proper treatment begins quickly.

Reference: 1. Shenker, R. F., McTyre, E. R., Taksler, D et al. Analysis of the drivers of cost of management when patients with brain metastases are treated with upfront radiosurgery. *Clin Neurol Neurosurg.* 2019 Jan;176:10-14.



The ASNR Career Center

The Go-To Job Site for Neuroradiology Employers and Job Seekers

For Job Seekers

- Access to an expanded network of jobs via the National Healthcare Career Network
- Confidential resume posting
- Professional online profile

For Employers

- Employer resources to help you recruit top talent
- Multiple pricing options, including free Fellowship listings
- Resume search

Start here: careers.asnr.org

AJNR

AMERICAN JOURNAL OF NEURORADIOLOGY

FEBRUARY 2023
VOLUME 44
NUMBER 2
WWW.AJNR.ORG

Publication Preview at www.ajnr.org features articles released in advance of print. Visit www.ajnrblog.org to comment on AJNR content and chat with colleagues and AJNR's News Digest at <http://ajnrdigest.org> to read the stories behind the latest research in neuroimaging.

117 **PERSPECTIVES** *T. Kalelioğlu*

REVIEW ARTICLE

-   118 **Nonstenotic Carotid Plaques and Embolic Stroke of Undetermined Source: A Multimodality Review** *A.S. Larson, et al.*

**EXTRACRANIAL
VASCULAR**

GENERAL CONTENTS

-   125 **Clinical Evaluation of Scout Accelerated Motion Estimation and Reduction Technique for 3D MR Imaging in the Inpatient and Emergency Department Settings** *M. Lang, et al.*
-  134 **Diagnostic Accuracy of Arterial Spin-Labeling, Dynamic Contrast-Enhanced, and DSC Perfusion Imaging in the Diagnosis of Recurrent High-Grade Gliomas: A Prospective Study** *T.B. Nguyen, et al.*
-  143 **Radiation-Induced Changes Associated with Obliteration of Brain AVMs after Repeat Radiosurgery** *T. Sasagasako, et al.*
-  150 **Reliability of Functional and Diffusion MR Imaging Near Cerebral Cavernous Malformations** *M. Colasurdo, et al.*
-   157 **Connectomic Basis for Tremor Control in Stereotactic Radiosurgical Thalamotomy** *E.H. Middlebrooks, et al.*
-  165 **Use of the Woven EndoBridge Device for Sidewall Aneurysms: Systematic Review and Meta-analysis** *A. Rodriguez-Calienes, et al.*
-  171 **Evolution of Radiographic Changes of a Vascularized Pedicled Nasoseptal Flap after Endonasal Endoscopic Skull Base Surgery** *J.L. Birkenbeuel, et al.*
- 176 **Enhancement in the Round Window Niche: A Potential Pitfall in High-Resolution MR Imaging of the Internal Auditory Canal** *T. Brinjikji, et al.*
-     180 **Ultrasound Fusion-Guided Core Needle Biopsy for Deep Head and Neck Space Lesions: Technical Feasibility, Histopathologic Yield, and Safety** *X. Li, et al.*
-  186 **High-Resolution 7T MR Imaging of the Trochlear Nerve** *T. Kumar, et al.*
-    192 **The Impact of Interactive MRI-Based Radiologist Review on Radiotherapy Target Volume Delineation in Head and Neck Cancer** *D. Adjogatse, et al.*

AJNR (Am J Neuroradiol ISSN 0195-6108) is a journal published monthly, owned and published by the American Society of Neuroradiology (ASNR), 820 Jorie Boulevard, Oak Brook, IL 60523. Annual dues for the ASNR include approximately 19% for a journal subscription. The journal is printed by Intellicor Communications, 330 Eden Road, Lancaster, PA 17601; Periodicals postage paid at Oak Brook, IL and additional mailing offices. Printed in the U.S.A. POSTMASTER: Please send address changes to American Journal of Neuroradiology, P.O. Box 3000, Denville, NJ 07834, U.S.A. Subscription rates: nonmember \$452 (\$530 foreign) print and online, \$320 online only; institutions \$520 (\$594 foreign) print and basic online, \$1029 (\$1103 foreign) print and extended online, \$380 online only (basic), \$825 online only (extended); single copies are \$35 each (\$40 foreign). Indexed by PubMed/MEDLINE, BIOSIS Previews, Current Contents (Clinical Medicine and Life Sciences), EMBASE, Google Scholar, HighWire Press, Q-Sensei, RefSeek, Science Citation Index, SCI Expanded, ReadCube, and Semantic Scholar. Copyright © American Society of Neuroradiology.

-

PEDIATRICS

PEDIATRICS

PEDIATRICS

SPINE
FUNCTIONAL

SPINE

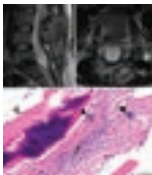
ONLINE FEATURES

LETTERS

- E11 **Regarding “Rates of Epidural Blood Patch following Lumbar Puncture Comparing Atraumatic versus Bevel-Tip Needles Stratified for Body Mass Index”** *B. Branstetter, et al.*
- E12 **Reply** *J.T. Philip, et al.*
- E13 **CAA-ri and ARIA: Two Faces of the Same Coin?** *M. Zedde, et al.*

BOOK REVIEWS *R.M. Quencer, Section Editor*

Please visit www.ajnrblog.org to read and comment on Book Reviews.



Lumbar arachnoiditis from Thejeel, et al, in this issue.

-  Indicates Editor's Choices selection
-  Indicates Fellows' Journal Club selection
-  Indicates open access to non-subscribers at www.ajnr.org
-  Indicates article with supplemental online data
-  Indicates article with supplemental online video
-  Evidence-Based Medicine Level 1
-  Evidence-Based Medicine Level 2

EDITOR-IN-CHIEF

Jeffrey S. Ross, MD

Professor of Radiology, Department of Radiology,
Mayo Clinic College of Medicine, Phoenix, AZ

SENIOR EDITORS

Harry J. Cloft, MD, PhD

Professor of Radiology and Neurosurgery,
Department of Radiology, Mayo Clinic College of
Medicine, Rochester, MN

Christopher G. Filippi, MD

Professor and Alice Ettinger-Jack R. Dreyfuss
Chair of Radiology,
Tufts University School of Medicine,
Radiologist-in-Chief
Tufts University Medical Center, Boston, MA

Thierry A.G.M. Huisman, MD, PD, FICIS, FACR

Radiologist-in-Chief and Chair of Radiology, Texas
Children's Hospital,
Professor of Radiology, Pediatrics, Neurosurgery,
and OBGYN, Baylor College of Medicine,
Houston, TX

Yvonne W. Lui, MD

Associate Professor of Radiology,
Chief of Neuroradiology,
New York University School of Medicine,
New York, NY

C.D. Phillips, MD, FACR

Professor of Radiology, Weill Cornell Medical
College, Director of Head and Neck Imaging,
New York-Presbyterian Hospital, New York, NY

Lubdha M. Shah, MD, MS

Professor of Radiology and Director of Spine
Imaging, University of Utah Department of
Radiology and Imaging Sciences, Salt Lake City, UT

STATISTICAL SENIOR EDITOR

Bryan A. Comstock, MS

Senior Biostatistician,
Department of Biostatistics,
University of Washington, Seattle, WA

ARTIFICIAL INTELLIGENCE DEPUTY EDITOR

Peter D. Chang, MD

Assistant Professor-in-Residence,
Departments of Radiological Sciences,
Computer Sciences, and Pathology,
Director, Center for Artificial Intelligence in
Diagnostic Medicine (CAIDM),
University of California, Irvine, Irvine, CA

EDITORIAL BOARD

Ashley H. Aiken, Atlanta, GA

Matthew D. Alexander, Salt Lake City, UT

Lea M. Alhilali, Phoenix, AZ

Jason W. Allen, Atlanta, GA

Mohammed A. Almekhlafi, Calgary, Alberta,
Canada

Niranjan Balu, Seattle, WA

Matthew J. Barkovich, San Francisco, CA

Joachim Berkefeld, Frankfurt, Germany

Karen Buch, Boston, MA

Judah Burns, New York, NY

Danielle Byrne, Dublin, Ireland

Federico Cagnazzo, Montpellier, France

Gloria C. Chiang, New York, NY

Daniel Chow, Irvine, CA

Kars C.J. Compagne, Rotterdam, The Netherlands

Yonghong Ding, Rochester, MN

Birgit Ertl-Wagner, Toronto, Ontario, Canada

Aaron Field, Madison, WI

Nils D. Forkert, Calgary, Alberta, Canada

Frank Gaillard, Melbourne, Australia

Joseph J. Gemmete, Ann Arbor, Michigan

Brent Griffith, Detroit, MI

Michael J. Hoch, Philadelphia, PA

Joseph M. Hoxworth, Phoenix, AZ

Raymond Y. Huang, Boston, MA

Susie Y. Huang, Boston, MA

Ferdinand K. Hui, Honolulu, HI

Christof Karmonik, Houston, TX

Gregor Kasprian, Vienna, Austria

Timothy J. Kaufmann, Rochester, MN

Hillary R. Kelly, Boston, MA

Toshibumi Kinoshita, Akita, Japan

Ioannis Koktzoglou, Evanston, IL

Stephen F. Kralik, Houston, TX

Luke Ledbetter, Los Angeles, CA

Franklin A. Marden, Chicago, IL

Markus A. Möhlenbruch, Heidelberg, Germany

Mahmud Mossa-Basha, Morrisville, NC

Renato Hoffmann Nunes, Sao Paulo, Brazil

Sam Payabvash, New Haven, CT

Johannes A.R. Pfaff, Salzburg, Austria

Eike I. Piechowiak, Bern, Switzerland

Laurent Pierot, Reims, France

Alexander R. Podgorsak, Chicago, IL

Eytan Raz, New York, NY

Jeff Rudie, San Diego, CA

Paul M. Ruggieri, Cleveland, OH

Fatih Seker, Heidelberg, Germany

Maksim Shapiro, New York, NY

Timothy Shepherd, New York, NY

Mark S. Shiroishi, Los Angeles, CA

Neetu Soni, Rochester, NY

Ashok Srinivasan, Ann Arbor, MI

Jason F. Talbott, San Francisco, CA

Anderanik Tomasian, Los Angeles, CA

Fabio Triulzi, Milan, Italy

Arastoo Vossough, Philadelphia, PA

Richard Watts, New Haven, CT

Elysa Widjaja, Toronto, Ontario, Canada

Ronald Wolf, Philadelphia, Pennsylvania

Shuang Xia, Tianjin, China

Leonard Yeo, Singapore

Woong Yoon, Gwangju, South Korea

David M. Yousem, Evergreen, CO

Carlos Zamora, Chapel Hill, NC

Chengcheng Zhu, Seattle, WA

EDITORIAL FELLOW

Alexandre Boutet, Toronto, Ontario, Canada

SPECIAL CONSULTANTS TO THE EDITOR

AJNR Blog Editor

Neil Lall, Denver, CO

Case of the Month Editor

Nicholas Stence, Aurora, CO

Case of the Week Editors

Matylda Machnowska, Toronto, Ontario, Canada

Anvita Pauranik, Calgary, Alberta, Canada

Classic Case Editor

Sandy Cheng-Yu Chen, Taipei, Taiwan

Health Care and Socioeconomics Editor

Pina C. Sanelli, New York, NY

Physics Editor

Greg Zaharchuk, Stanford, CA

Podcast Editor

Kevin Hiatt, Winston-Salem, NC

Twitter Editor

Jacob Ormsby, Albuquerque, NM

Official Journal:

American Society of Neuroradiology

American Society of Functional Neuroradiology

American Society of Head and Neck Radiology

American Society of Pediatric Neuroradiology

American Society of Spine Radiology

Founding Editor

Juan M. Taveras

Editors Emeriti

Mauricio Castillo, Robert I. Grossman,

Michael S. Huckman, Robert M. Quencer

Managing Editor

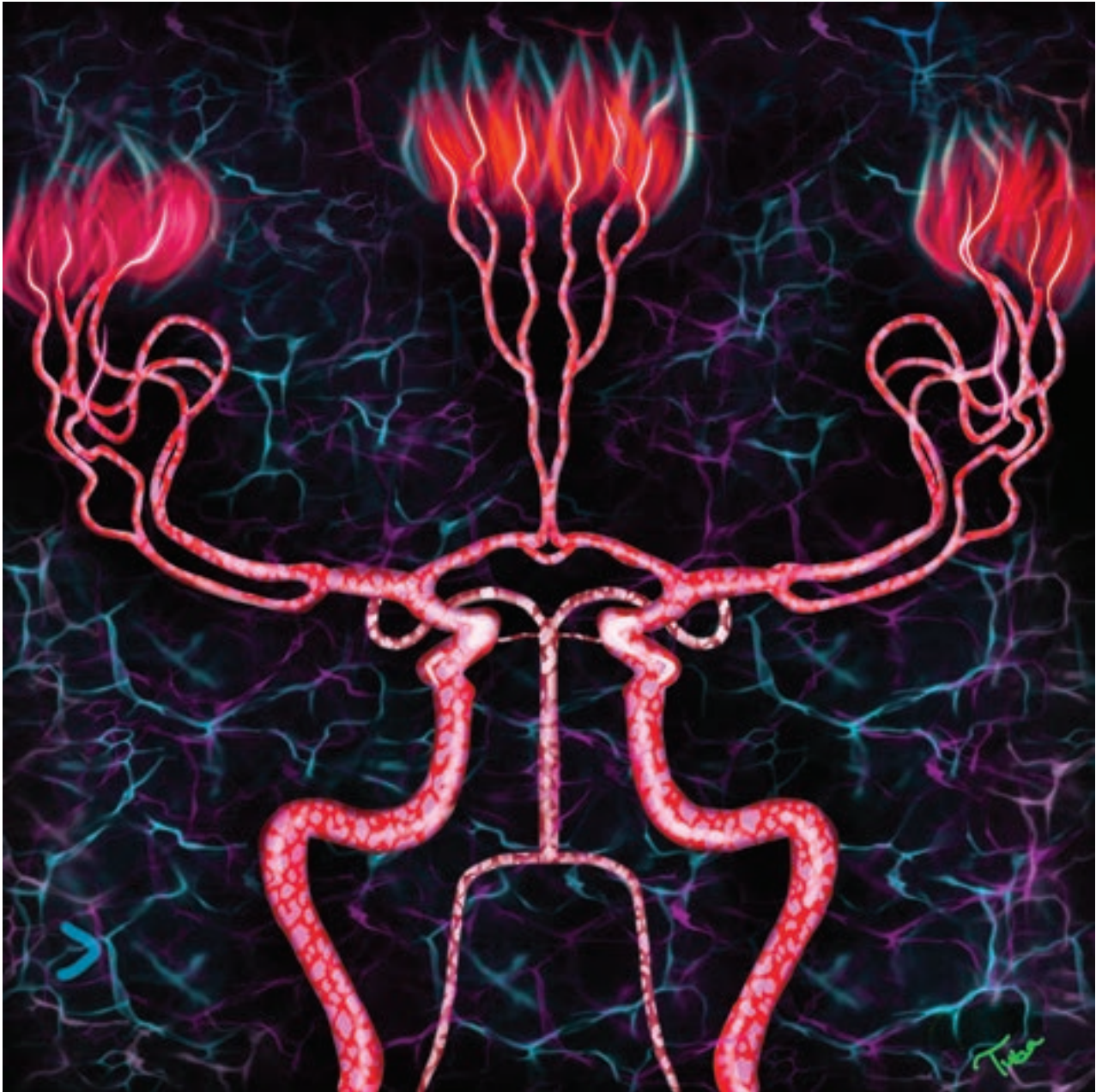
Karen Halm

Assistant Managing Editor

Laura Wilhelm

Executive Director, ASNR

Mary Beth Hepp



Title: Power of Cerebral Blood Supply. A significant amount of cardiac output supplies brain parenchyma and the entire blood supply of the brain depends only on 2 paired arteries. However, the intracranial arterial collateral system is not that simple. I wanted to emphasize the power of collateral circulation as flames by using the Procreate digital art app.

Tuba Kalelioğlu, *Neuroradiology Fellow, University of Virginia*

Nonstenotic Carotid Plaques and Embolic Stroke of Undetermined Source: A Multimodality Review

A.S. Larson, W. Brinjikji, A. Lekah, J.P. Klaas, G. Lanzino, J. Huston, L. Saba, and J.C. Benson



ABSTRACT

Symptomatic nonstenotic carotid artery disease has been increasingly recognized as a thromboembolic source in patients who would otherwise be classified as having embolic stroke of undetermined source. Evidence suggests that certain plaque features seen on sonography, CT, and MR imaging in nonstenotic carotid artery disease may predispose to recurrent stroke in patients with embolic stroke of undetermined source. We performed a focused literature review to further study plaque features in the context of embolic stroke of undetermined source and to determine which plaque features may be associated with ipsilateral ischemic events in such patients. Plaque thickness as seen on both ultrasound and CT appears to have a consistent association with ipsilateral stroke in patients with embolic stroke of undetermined source across multiple studies. Intraplaque hemorrhage as seen on MR imaging is now understood to have a strong association with ipsilateral stroke in patients with embolic stroke of undetermined source. Continued study of various plaque features as seen on different modalities is warranted to uncover other potential associations.

ABBREVIATIONS: ESUS = embolic stroke of undetermined source; IPH = intraplaque hemorrhage; LRNC = lipid-rich necrotic core; SyNC = symptomatic nonstenotic carotid artery disease; US = ultrasound

Up to one-third of strokes have no established mechanism and are considered to be cryptogenic.¹ In 2014, the term “embolic stroke of undetermined source” (ESUS) was established as a clinical entity in patients with nonlacunar cryptogenic stroke in which an embolic source was thought to be most likely, despite an appropriate diagnostic evaluation with negative findings (Fig 1).² This term (along with “cryptogenic stroke”) has also been used to define patients who may have multiple, competing stroke etiologies in which a definitive source cannot be determined. Patients with ESUS have been estimated to have a >4% risk of recurrent stroke per annum despite being on antiplatelet medication.¹ Subsequent thought was directed to the idea that anticoagulation may be beneficial in such patients, given the likelihood that emboli originated from various nonevident atheroembolic sources.³ This premise provided the impetus for 2 large clinical trials that compared anticoagulation with aspirin alone in patients with ESUS.^{4,5} Despite this plausible theory, no benefit of anticoagulation was observed. These results spurred continued interest in additional

diagnostics in order to identify potential embolic sources in patients with ESUS.

One such avenue has been the use of adjunctive and advanced imaging techniques, as well as alternative imaging features on traditional studies to identify potential embolic sources. Of particular interest has been a deeper interrogation of carotid artery plaque features beyond the degree of luminal stenosis. Current guidelines suggest that large-artery atherosclerosis may be the cause of an ischemic stroke in cases in which the degree of ipsilateral stenosis is >50% as calculated by the NASCET criteria.^{6,7} This rule is based on data from trials performed in the 1970s and 80s that could assess only the degree of stenosis and luminal morphology. Therefore, a biomarker was produced according to the only threshold that could be assessed at that time. Currently, however, advanced imaging modalities have enabled the assessment of the plaque itself and not only its effects, such as the stenosis, along with the detection of various carotid plaque features that have been highly associated with the presence of ipsilateral ischemic stroke, even in cases of <50% ipsilateral stenosis.⁸⁻¹⁰

Even in the case of traditional imaging modalities such as ultrasound (US) and CTA, several studies have indicated that the presence of certain carotid features may be associated with ipsilateral ischemic stroke in patients who would otherwise have been classified as having ESUS. Given the multitude of such studies showing an increased risk of recurrent stroke in patients with ESUS with nonstenotic carotid artery disease with certain

Received August 26, 2022; accepted after revision October 10.

From the Departments of Radiology (A.S.L., W.B., A.L., G.L., J.H., J.C.B.), Neurosurgery (W.B., G.L.), and Neurology (J.P.K.), Mayo Clinic, Rochester, Minnesota; and Department of Medical Sciences (L.S.), University of Cagliari, Cagliari, Italy.

Please address correspondence to Anthony Larson, MD, Department of Radiology, Mayo Clinic, 200 First St SW, Rochester, MN, 55905; e-mail: lars4689@umn.edu

Indicates open access to non-subscribers at www.ajnr.org

Indicates article with online supplemental data.

<http://dx.doi.org/10.3174/ajnr.A7750>

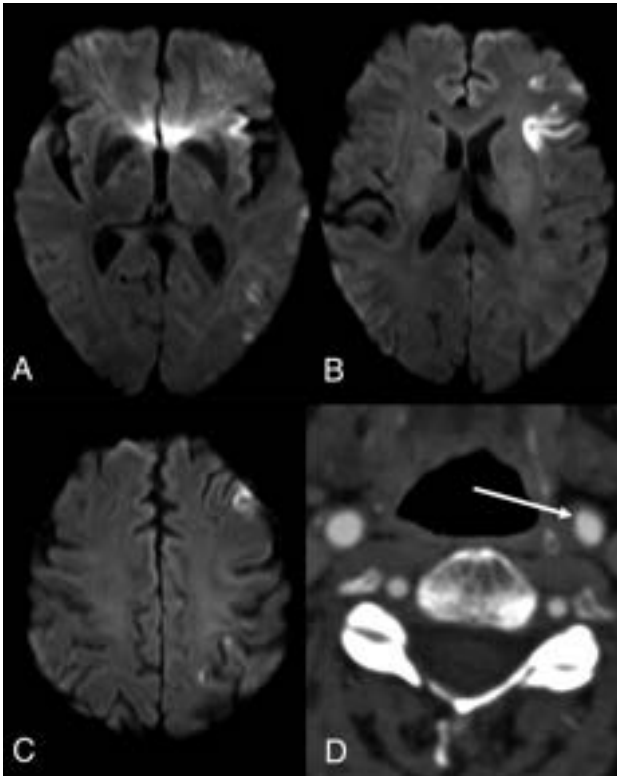


FIG 1. Sample case of ESUS. A–C, Axial diffusion-weighted MR images demonstrate multiple foci of restricted diffusion throughout the left MCA territory, consistent with an embolic stroke. Subsequent work-up for a cardioembolic source was negative. In addition, axial CTA of the cervical carotid artery demonstrates likely atherosclerotic disease resulting in <50% luminal stenosis (D, arrow). Given the diagnostic evaluation with negative findings and a likely embolic source, this patient meets the criteria for ESUS, despite a minimal degree of luminal carotid stenosis.

radiographic features, Goyal et al⁸ have proposed that symptomatic nonstenotic carotid artery disease (SyNC) is a plausible stroke etiology in patients with ESUS. These patients may, therefore, benefit from a targeted therapeutic approach.^{11,12}

Although the SyNC criteria remain in their infancy and will likely evolve, an important feature of the SyNC criteria is the presence of carotid plaque with high-risk features. An understanding of which radiographic features have been associated with ipsilateral ischemic stroke in patients with ESUS is crucial to determine whether a patient likely meets the criteria for SyNC and may, therefore, benefit from targeted therapy. To date however, a review of such features that may be associated with ipsilateral ischemic events in patients with ESUS specifically is absent from the literature. We therefore aimed to provide such a review of carotid artery features as seen on US, CT, and MR imaging in the context of ESUS.

MATERIALS AND METHODS

We performed a focused literature search related to radiographic carotid plaque features specifically in patients with ESUS. This was not a systematic review or meta-analysis and did not, therefore, use rigorous search criteria or inclusion/exclusion criteria. PubMed was queried using words such as “carotid,” “plaque,”

“nonstenotic,” “ESUS,” “stroke,” “ischemia,” and “cryptogenic.” Titles and abstracts were reviewed for relevance. Full articles were accessed when titles/abstracts suggested that a study consisted of evaluation of carotid plaque features in patients with ESUS or in patients with cryptogenic stroke. Articles were fully reviewed, and the references of each article were scrutinized for additional studies of interest.

The strength of associations between plaque features and ipsilateral stroke in patients with ESUS was graded in a subjective fashion as follows: If all or nearly all studies of a particular feature demonstrated such an association, the evidence for that feature being associated with ipsilateral stroke in ESUS was considered “strong.” If most studies demonstrated an association, that feature was considered as having “moderate” evidence. If roughly half of studies demonstrated a relationship while roughly the other half demonstrated no such relationship, the evidence for that feature was graded as “conflicting.” If a feature did not demonstrate a relationship across all or nearly all studies or had only been minimally studied, the evidence was graded as “weak.”

Ultrasound

Ultrasound has historically been the most-commonly used imaging technique to evaluate carotid artery disease because of its ease of use and lack of radiation exposure. The results of NASCET provided further impetus for the use of US for assessment of suspected carotid artery disease.⁶ However, the use of US has limited consideration for operative interventions to the degree of stenosis alone without consideration of other US features that may have been associated with ischemic events. In fact, some studies performed in the 1980s before the completion of NASCET suggested that specific plaque features on US were likely associated with ipsilateral ischemic stroke.^{13,14} While the degree of luminal stenosis remains a critical feature, advances in US technology have likely led to identification of other US plaque features that require consideration as a culprit lesion in patients with stroke.^{15,16} Unfortunately, a paucity of data specific to patients with ESUS exists.

Several studies (some of which were performed pre-NASCET) have indicated that US features such as fibrous cap ulceration, the presence of thrombus, plaque length, plaque volume, and hypochoic/heterogeneous plaque likely indicate vulnerable plaques that may be culprit lesions in patients with stroke.¹⁷ Recently, Buon et al¹⁸ evaluated 22 patients with carotid atherosclerosis with <50% stenosis. Despite a relatively small sample size, the presence of plaque echolucency was more prevalent in carotid arteries ipsilateral to the presenting ischemic symptoms versus contralateral carotid arteries (100% versus 63%, respectively), though statistical significance was not reached. Most intriguing, the difference in plaque ulceration and thrombus did not reach statistical significance. However, carotid arteries on the symptomatic side had a higher median plaque thickness, length, and volume index.

In a similar study, Komatsu et al¹⁹ found that carotid plaques with >1.5 mm intimal medial thickness were present in the carotid artery ipsilateral to symptoms in 59% of patients with ESUS compared with 42% on the contralateral asymptomatic side, a finding that was statistically significant. Hypochoic plaques were present on the ipsilateral side in 9% of patients versus

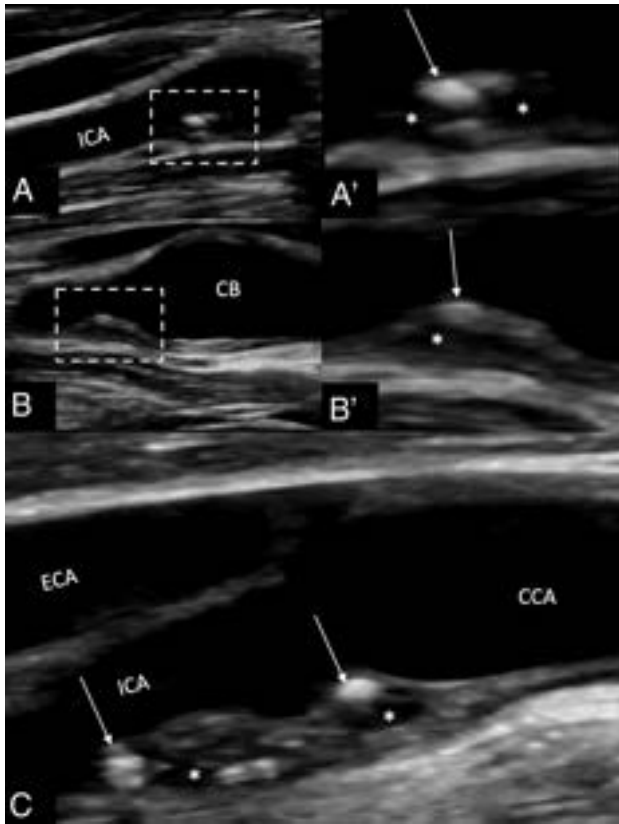


FIG 2. Carotid sonography demonstrating large (≥ 3 mm), heterogeneous, nonstenotic carotid plaque in a 66-year-old man who presented with acute-onset vision loss in his right eye, suspicious for retinal ischemia. The patient underwent bilateral carotid US. A, B-mode long axis view of the right carotid vasculature demonstrates the presence of a moderately-sized (~ 3 mm) complicated plaque in the proximal ICA. A', Close-up of the plaque demonstrates heterogeneous plaque with areas both hyperechoic (*arrow*) and echolucent (*asterisk*). B and B', Long view of the proximal ICA and carotid bulb (CB) demonstrates heterogeneous plaque as seen in A and A'. C, The left proximal ICA also demonstrates the presence of large (> 3 mm) heterogeneous plaque with hyperechoic (*arrow*) and echolucent (*asterisk*) areas. The right-sided plaque may be smaller than the left secondary to recent dislodgment and embolization of plaque material. The patient underwent appropriate work-up to identify a potential embolic source, which was negative. This patient was diagnosed with ESUS despite the presence of moderately-sized, heterogeneous plaque on the right resulting in $< 50\%$ luminal stenosis. Although more data are needed relating to plaque US in the context of ESUS, plaque thickness appears to have a consistent association with ipsilateral stroke across the existing literature. To date, plaque echolucency has not been found to have such an association, which is significant. ECA indicates external carotid artery; CCA, common carotid artery.

4% on the contralateral side, though this difference did not reach statistical significance. Together, data from these 2 studies suggest that features related to plaque size and thickness may be more important US markers of culprit lesions in patients with ESUS compared with other features. Patients with these lesions may, therefore, be more strongly considered for intervention to reduce the risk of recurrent stroke. However, these studies assess an association between features and the presence of ipsilateral ESUS in a cross-sectional manner. It is therefore uncertain whether these

features place patients at risk for additional, recurrent ischemic events. An example case of a patient with ESUS and US findings suggestive of carotid plaque as a culprit lesion is demonstrated in Fig 2.

To our knowledge, these are the only studies in the literature evaluating plaque features on US in the context of ESUS. Given the ease, availability, low cost, and lack of radiation in using US, additional studies evaluating potential US biomarkers of ipsilateral stroke in patients with ESUS are warranted.

CTA

Like US, CTA represents a quick and easily accessible method of assessing carotid artery disease in patients with stroke. Technical advances in CT technology (ie, such as high-speed multidetector hardware and 3D reformatting software) have enabled detection of carotid artery disease on the scale of millimeters.¹⁶ Because CTA is performed as a part of most institutional acute stroke algorithms, any features of nonstenotic plaques associated with ipsilateral stroke would be easily assessed in the clinical setting. Thus, CTA may, therefore, be the most practical technique to assess nonstenotic plaque features.¹⁶ Unlike US however, more data exist regarding which plaque features on CTA are associated with ipsilateral ischemic events in nonstenotic carotid arteries in patients with ESUS specifically. Unfortunately, conflicting evidence has been reported for multiple plaque features up to this point.

Coutinho et al²⁰ were the first to hypothesize that large, nonstenotic plaques were more prevalent in carotid arteries ipsilateral to cryptogenic stroke. In this original study that included a cohort of 85 patients with ESUS, 2 primary findings were evident. First, large-but-nonstenotic plaques > 3 mm in thickness were found to be associated with ipsilateral cryptogenic strokes. Second, there was no difference in the percentage of stenosis in ipsilateral-versus-contralateral carotid arteries.

Following this original study by Coutinho et al,²⁰ Ospel et al²¹ analyzed patients with ESUS from the Identifying New Approaches to Optimize Thrombus Characterization for Predicting Early Recanalization and Reperfusion with IV Alteplase and Other Treatments Using Serial CT Angiography (INTERRSeCT) study²² to determine the prevalence of nonstenotic carotid plaques ipsilateral to the side of the stroke. The authors found that in patients with $< 50\%$ stenosis, plaques were more prevalent within the carotid artery ipsilateral to the side of the stroke, suggesting that nonstenotic plaques may be culprit lesions in patients with ESUS. Most interesting, several plaque features (irregularity, ulceration, hypoattenuation, and so forth) had no significant association with ipsilateral stroke, though plaque thickness (> 3 mm) was more prevalent on the ipsilateral side but did not reach statistical significance.

More recently, Singh et al²³ analyzed the Systematic Evaluation of Patients Treated with Neurothrombectomy Devices for Acute Ischemic Stroke (STRATIS) registry to retrospectively evaluate plaque features on CTA in 141 patients diagnosed with cryptogenic stroke. In essence, plaque surface irregularity, plaque hypodensity, and increasing plaque thickness were all associated with ipsilateral stroke in patients diagnosed as having cryptogenic stroke. Notably, predominately calcified and ulcerated plaques had no association with ipsilateral cryptogenic stroke.

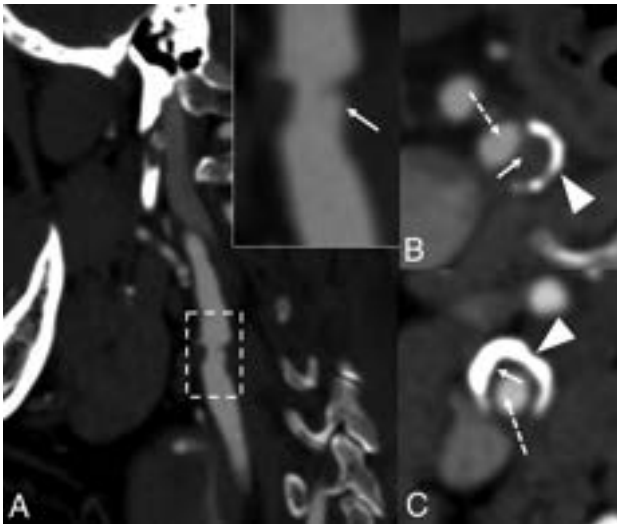


FIG 3. Example of “vulnerable” plaque features as seen on CTA in 3 different patients. *A*, Ulcerated plaque within the proximal ICA (*dashed box*) seen on CTA. Inset in *A* demonstrates an area of slight luminal stenosis with plaque surface irregularity suspicious for ulceration (*arrow*). *B*, CTA from a different patient demonstrates hypodense (“soft”) plaque (*solid arrow*) with a thin band of peripheral calcifications (*arrowhead*), resulting in luminal narrowing (*dashed arrow*). Similar findings are seen in *C* apart from a much thicker peripheral band of calcification. Hypodense plaques may represent the presence of LRNC or IPH, though it can be difficult to distinguish between the 2 on CTA. Plaque hypodensity has been reported to be associated with ipsilateral ischemia in patients with ESUS in most studies. Conflicting evidence exists regarding the relationship between surface irregularity, ulceration, and ipsilateral stroke. In contrast, calcification appears to be unrelated to ipsilateral stroke in patients with ESUS.

The Plaque at Risk (PARISK) study was a recently published multicenter, prospective analysis of carotid plaque CT and MR imaging biomarkers and recurrent stroke risk in patients with carotid stenosis of <70% by the NASCET criteria.²⁴ Most interesting, plaque calcifications and ulcerations were not found to be statistically significant risk factors for recurrent ipsilateral stroke at a mean follow-up of 5 years. In terms of CT plaque features, these findings suggest that ulceration and proportional calcification are not likely to be risk factors for recurrent ischemic events. Whether a longer follow-up interval changes these findings remains unclear.

In contrast, a recent retrospective study of 152 patients with ESUS by Jumah et al²⁵ found that plaque ulceration as seen on CTA was more prevalent in ipsilateral carotid arteries versus contralateral ones. In addition, plaque thickness (>3mm), plaque length (>1 cm), and hypodense plaque were significantly associated with ipsilateral stroke, whereas calcification was not.

Certainly, these studies further support the theory that the presence of carotid plaque (regardless of the degree of stenosis) may be a culprit lesion in patients with ESUS without another identifiable source. Furthermore, it also appears that plaque thickness of >3 mm has been most consistently reported across studies associated with ipsilateral ischemic events in patients with ESUS (Fig 3). Although certain CT features of carotid plaques such as surface irregularity, ulceration, hypodensity, and calcification are thought to represent features of vulnerable plaque, their

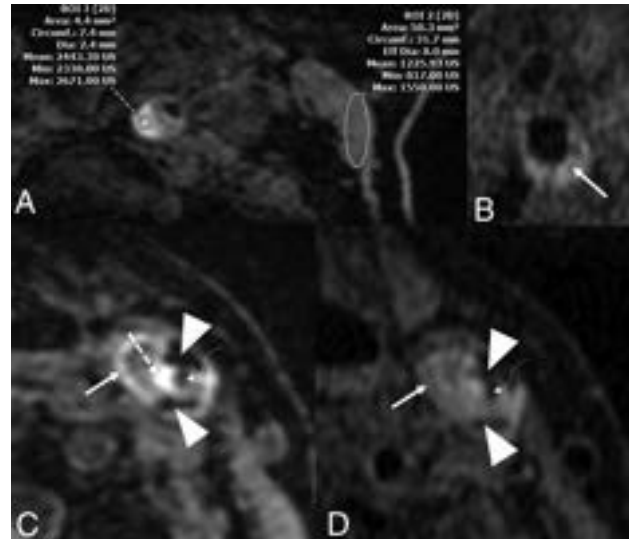


FIG 4. Representative MR imaging plaque features that may have an association with ipsilateral stroke in patients with ESUS. *A*, MPRAGE of a patient showing an area of hyperintensity within the proximal ICA (*left circle*), which has a mean intensity value of 200× that of the adjacent sternocleidomastoid muscle (*right circle*). These findings suggest the presence of IPH. This patient had >50% luminal stenosis. *B*, TI Cube (GE Healthcare) imaging of a different patient shows a LRNC. *C*, MPRAGE in another patient demonstrates multiple features including hypointense areas suggestive of peripheral calcifications (*arrowheads*), a hyperintense area (*dashed arrow*) adjacent to the narrowed carotid lumen (*curved arrow*) and a peripheral area of LRNC (*solid arrow*). *D*, The same patient/artery as in *C* with TI Cube imaging demonstrating the narrowed lumen (*curved arrow*) along with peripheral calcifications (*arrowheads*) and a LRNC (*solid arrow*). IPH is not as apparent on TI Cube imaging as on MPRAGE sequences. This patient also had >50% luminal stenosis. Strong evidence exists suggesting that IPH is associated with ipsilateral stroke in ESUS. A LRNC as seen on MR imaging has also been consistently reported to have such an association, albeit not to the same degree as IPH.

association with ipsilateral stroke in patients with ESUS remains unclear in the context of conflicting reports (Fig 3).^{10,23,25,26} Given the high clinical utility of CT and CTA in the acute stroke setting, continued exploration of the potential association between these features and ischemic events in patients with ESUS is likely worthwhile to clarify these discrepancies.

MR Imaging

Without doubt, advances in MR imaging technology have enhanced detection and interrogation of carotid plaque features.^{16,27} Not the least of these is carotid vessel wall imaging, which uses flow-suppression techniques to null signal from adjacent flowing blood. This enables enhanced detection of carotid plaque features beyond the degree of luminal stenosis or plaque size. MR imaging of plaque is, therefore, considered as the criterion standard for carotid wall analysis, particularly in patients with ESUS.¹⁶

Several MR imaging plaque biomarkers have been proposed to be associated with ipsilateral ischemic events, specifically in patients with ESUS.¹⁰ Of these, intraplaque hemorrhage (IPH) has been established as being associated with cerebral ischemia (Fig 4). Pathologically, IPH involves extravasation of hematogenous constituents from fragile neocapillaries within an atheromatous

plaque.^{28,29} The presence of this inflammatory milieu within the plaque can result in thrombus formation, plaque growth, plaque rupture, and distal embolization of thrombotic material.²⁹ Most commonly, IPH can be visualized on heavily T1-weighted sequences such as MPRAGE. On such sequences, IPH appears as a region of hyperintensity in a carotid plaque that carries a signal intensity of 50% of the adjacent sternocleidomastoid muscle.³⁰

Despite a suspicion that IPH is associated with distal events, the association of IPH in ESUS has been uncertain until recently.³¹ Of all MR imaging biomarkers of plaque vulnerability, IPH has been most strongly associated with ipsilateral ischemia in patients with ESUS, even in cases of minimal luminal stenosis.^{9,21,32-36} In fact, our group has demonstrated that patients with ESUS with ipsilateral IPH had an annual recurrence rate of 9.5% compared with 2.5% in patients without IPH.⁹ Perhaps the most convincing evidence to date comes from the aforementioned PARISK study, in which patients with MR imaging evidence of IPH were at higher risk of developing recurrent ischemic events at 5-year follow-up.²⁴

With these multiple sources of evidence suggesting an independent association between IPH and ipsilateral stroke, the presence of IPH on vessel wall MR imaging in patients without an otherwise-defined thromboembolic source should be strongly considered as a culprit lesion. Some studies have even suggested that patients with ischemic stroke and ipsilateral IPH in minimal carotid stenosis may benefit from carotid endarterectomy.^{11,12}

Nevertheless, several questions remain regarding IPH. For example, IPH may persist within a plaque for years without any obvious progression or distal ischemic events.³⁷ This finding has led some to postulate that the mere presence of IPH may not be adequate in determining whether a patient is at risk. In turn, more specific features of the IPH have been assessed, including the signal intensity within the hemorrhage and the size of the IPH.^{30,38}

Beyond IPH, the presence of a lipid-rich necrotic core (LRNC) within a carotid plaque has also been suggested as a potential culprit in patients with ESUS.^{16,36,39,40} For example, the Carotid Plaque Imaging in Acute Stroke (CAPIAS) study demonstrated that patients with cryptogenic strokes had larger-volume LRNC ipsilateral to the stroke compared with patients with known cardioembolic or small-vessel stroke. Other MR imaging features such as ulceration and thinning/rupture of the fibrous cap have been identified as vulnerable features but have not been studied in patients with ESUS specifically.^{41,42}

Summary and Future Directions

Our understanding of symptomatic, nonstenotic carotid disease as a cause of ESUS continues to evolve. Several plaque features are important to consider in this context (Online Supplemental Data). On US and CT, volumetric features including plaque volume and plaque thickness have been demonstrated to have an association with ipsilateral stroke in nonstenotic carotid disease. Regarding CT specifically, hypodense plaque has also had such an association, albeit in a smaller number of studies. Additional investigation is required to identify other potential US and CT plaque features as markers of culprit lesions in nonstenotic disease. Intraplaque hemorrhage, as identified on vessel wall MR imaging, has been most strongly associated with ipsilateral stroke

in patients with ESUS. Therefore, the presence of IPH in patients without an otherwise identifiable source should raise strong suspicion for a culprit lesion. However, additional work is required to identify more specific features of IPH that indicate an active lesion. Other MR imaging features of plaque vulnerability have been suggested as being associated with ipsilateral stroke (ie, LRNC, thinning/rupture of the fibrous cap, and ulceration). Besides LRNC, these features have yet to be studied in patients with ESUS. Further work is, therefore, necessary to examine the role of these features in the context of ESUS.

Although these radiographic features are important to evaluate in patients with ESUS, their presence should not preclude evaluation of other potential causes of embolic stroke. Grosse et al⁴³ demonstrated that the presence of nonstenosing carotid artery plaques was associated with markers of left atrial disease and atrial fibrillation. Although the reasoning for this association is unclear, the importance of a thorough evaluation for potential cardiac causes of stroke in patients with ESUS is emphasized. Moreover, recent evidence has also suggested that a high proportion of patients with ESUS have multiple, potential embolic sources, further stressing the importance of thorough evaluation beyond plaque features.⁴⁴

Of course, many patients with suspected ESUS will have carotid imaging performed by >1 technique. This may be particularly true with a more widespread understanding of SyNC. For example, a patient with US findings suggestive of thick plaque may undergo an MR imaging or CT study of the plaque to further characterize additional features such as hypodensity or IPH, which may, in turn, guide further management. To our knowledge, the combinatorial benefit of imaging modalities for assessment of plaque in patients with ESUS has not been directly addressed. Such information would be beneficial in improving the detection of plaque features and determining which patients would benefit from advanced imaging. Further study in this regard is therefore warranted.

The use of molecular-based imaging modalities has been of recent interest to detect inflammatory activity in carotid plaques. In the clinical realm, plaque uptake on FDG-PET studies is used as a surrogate marker for plaque inflammation and has, indeed, been correlated with inflammatory markers.^{45,10} Most intriguing, a systematic review and meta-analysis performed by Chaker et al⁴⁶ demonstrated that recent ipsilateral cerebral ischemic events may be associated with an increased plaque uptake of [¹⁸F] FDG on PET imaging, independent of the degree of luminal stenosis. While detection of more specific molecular markers of inflammation and plaque vulnerability remains largely within the research realm, the potential role of molecular plaque imaging in the context of ESUS is an exciting avenue of discovery.

Certainly, the primary objective in detecting carotid plaque as a potential source of embolism in patients with ESUS is to ultimately provide a targeted form of therapy to reduce the risk of future ischemic events. This objective contrasts with general stroke prevention, without an identifiable source. In theory, patients meeting the criteria for SyNC may benefit from carotid endarterectomy. Early data have suggested that endarterectomy for patients with SyNC is safe and may have a benefit in preventing recurrent ischemia.^{11,12} However, well-designed clinical

studies are needed to draw more robust conclusions regarding the efficacy of endarterectomy in preventing future ischemic events in patients meeting criteria for SyNC.

Disclosure forms provided by the authors are available with the full text and PDF of this article at www.ajnr.org.

REFERENCES

- Hart RG, Catanese L, Perera KS, et al. **Embolic stroke of undetermined source: a systematic review and clinical update.** *Stroke* 2017;48:867–72 CrossRef Medline
- Hart RG, Diener HC, Coutts SB, et al; Cryptogenic Stroke/ESUS International Working Group. **Embolic strokes of undetermined source: the case for a new clinical construct.** *Lancet Neurol* 2014;13:429–38 CrossRef Medline
- Navi BB, Kasner SE, Elkind MS, et al. **Cancer and embolic stroke of undetermined source.** *Stroke* 2021;52:1121–30 CrossRef Medline
- Hart RG, Connolly SJ, Mundl H; NAVIGATE ESUS Investigators. **Rivaroxaban for stroke prevention after embolic stroke of undetermined source.** *N Engl J Med* 2018;379:987–2201 CrossRef
- Diener HC, Sacco RL, Easton JD, et al; RE-SPECT ESUS Steering Committee and Investigators. **Dabigatran for prevention of stroke after embolic stroke of undetermined source.** *N Engl J Med* 2019;380:1906–17 CrossRef Medline
- North American Symptomatic Carotid Endarterectomy Trial Collaborators. **Beneficial effect of carotid endarterectomy in symptomatic patients with high-grade carotid stenosis.** *N Engl J Med* 1991;325:445–53 CrossRef Medline
- Adams HP Jr, Bendixen BH, Kappelle LJ, et al. **Classification of subtype of acute ischemic stroke: definitions for use in a multicenter clinical trial.** TOAST—Trial of Org 10172 in Acute Stroke Treatment. *Stroke* 1993;24:35–41 CrossRef Medline
- Goyal M, Singh N, Marko M, et al. **Embolic stroke of undetermined source and symptomatic nonstenotic carotid disease.** *Stroke* 2020;51:1321–25 CrossRef Medline
- Larson AS, Nasr DM, Rizvi A, et al. **Embolic stroke of undetermined source: the association with carotid intraplaque hemorrhage.** *JACC Cardiovasc Imaging* 2021;14:506–08 CrossRef Medline
- Saba L, Agarwal N, Cau R, et al. **Review of imaging biomarkers for the vulnerable carotid plaque.** *JVS Vasc Sci* 2021;2:149–58 CrossRef Medline
- Larson A, Nardi V, Brinjikji W, et al. **Endarterectomy for symptomatic non-stenotic carotids: a systematic review and descriptive analysis.** *Stroke Vasc Neurol* 2022;7:6–12 CrossRef Medline
- Nardi V, Benson JC, Larson AS, et al. **Carotid artery endarterectomy in patients with symptomatic non-stenotic carotid artery disease.** *Stroke Vasc Neurol* 2022;7:251–57 CrossRef Medline
- Gray-Weale AC, Graham JC, Burnett JR, et al. **Carotid artery atheroma: comparison of preoperative B-mode ultrasound appearance with carotid endarterectomy specimen pathology.** *J Cardiovasc Surg (Torino)* 1988;29:676–81 Medline
- Steffen C, Gray-Weale A, Byrne K, et al. **Carotid artery atheroma: ultrasound appearance in symptomatic and asymptomatic vessels.** *Aust N Z J Surg* 1989;59:529534 CrossRef Medline
- Scoutt LM, Gunabushanam G. **Carotid ultrasound.** *Radiol Clin North Am* 2019;57:501–18 CrossRef Medline
- Saba L, Antignani PL, Gupta A, et al. **International Union of Angiology (IUA) consensus paper on imaging strategies in atherosclerotic carotid artery imaging: from basic strategies to advanced approaches.** *Atherosclerosis* 2022;354:23–40 CrossRef Medline
- Bluth E, Kay D, Merritt C, et al. **Sonographic characterization of carotid plaque: detection of hemorrhage.** *AJNR Am J Neuroradiol* 1986;146:1061–65 CrossRef Medline
- Buon R, Guidolin B, Jaffre A, et al. **Carotid ultrasound for assessment of nonobstructive carotid atherosclerosis in young adults with cryptogenic stroke.** *J Stroke Cerebrovasc Dis* 2018;27:1212–16 CrossRef Medline
- Komatsu T, Iguchi Y, Arai A, et al. **Large but nonstenotic carotid artery plaque in patients with a history of embolic stroke of undetermined source.** *Stroke* 2018;49:3054–56 CrossRef Medline
- Coutinho JM, Derkatch S, Potvin AR, et al. **Nonstenotic carotid plaque on CT angiography in patients with cryptogenic stroke.** *Neurology* 2016;87:665–72 CrossRef Medline
- Ospe JM, Singh N, Marko M, et al. **Prevalence of ipsilateral nonstenotic carotid plaques on computed tomography angiography in embolic stroke of undetermined source.** *Stroke* 2020;51:1743–49 CrossRef Medline
- Lau HL, Gardener H, Coutts SB, et al. **Radiographic characteristics of mild ischemic stroke patients with visible intracranial occlusion: the INTERSeCT study.** *Stroke* 2022;53:913–20 CrossRef Medline
- Singh N, Ospe J, Mayank A, et al; STRATIS Investigators. **Nonstenotic carotid plaques in ischemic stroke: analysis of the STRATIS Registry.** *AJNR Am J Neuroradiol* 2021;42:1645–52 CrossRef Medline
- van Dam-Nolen DH, Truijman MT, van der Kolk AG, et al. **Carotid plaque characteristics predict recurrent ischemic stroke and TIA: the PARISK (Plaque At Risk) study.** *JACC: Cardiovasc Imaging* 2022;15:1715–26 CrossRef Medline
- Jumah A, Aboul Nour H, Intikhab O, et al. **Non-stenosing carotid artery plaques in embolic stroke of undetermined source: a retrospective analysis.** *Neurol Sci* 2022 Sept 27. [Epub ahead of print] CrossRef Medline
- Baradaran H, Al-Dasuqi K, Knight-Greenfield A, et al. **Association between carotid plaque features on CTA and cerebrovascular ischemia: a systematic review and meta-analysis.** *AJNR Am J Neuroradiol* 2017;38:2321–26 CrossRef Medline
- Saba L, Yuan C, Hatsukami T, et al; Vessel Wall Imaging Study Group of the American Society of Neuroradiology. **Carotid artery wall imaging: perspective and guidelines from the ASNR vessel wall imaging study group and expert consensus recommendations of the American Society of Neuroradiology.** *AJNR Am J Neuroradiol* 2018;39:E9–31 CrossRef Medline
- Mura M, Della Schiava N, Long A, et al. **Carotid intraplaque haemorrhage: pathogenesis, histological classification, imaging methods and clinical value.** *Ann Transl Med* 2020;8:1273–73 CrossRef Medline
- Holmes DR Jr, Alkhouli MA, Klaas JP, et al. **Change of heart: the underexplored role of plaque hemorrhage in the evaluation of stroke of undetermined etiology.** *J Am Heart Assoc* 2022;11:e025323 CrossRef Medline
- Larson AS, Brinjikji W, Kroll NJ, et al. **Normalized intraplaque hemorrhage signal on MP-RAGE as a marker for acute ischemic neurological events.** *Neuroradiol J* 2022;35:112–18 CrossRef Medline
- Takaya N, Yuan C, Chu B, et al. **Presence of intraplaque hemorrhage stimulates progression of carotid atherosclerotic plaques: a high-resolution magnetic resonance imaging study.** *Circulation* 2005;111:2768–75 CrossRef Medline
- Larson A, Brinjikji W, Savastano L, et al. **Carotid intraplaque hemorrhage and stenosis: at what stage of plaque progression does intraplaque hemorrhage occur, and when is it most likely to be associated with symptoms?** *AJNR Am J Neuroradiol* 2021;42:1285–90 CrossRef Medline
- Nardi V, Benson J, Bois MC, et al. **Carotid plaques from symptomatic patients with mild stenosis is associated with intraplaque hemorrhage.** *Hypertension* 2022;79:271–82 CrossRef Medline
- Singh N, Moody AR, Panzov V, et al. **Carotid intraplaque hemorrhage in patients with embolic stroke of undetermined source.** *J Stroke Cerebrovasc Dis* 2018;27:1956–59 CrossRef Medline
- Tao L, Li XQ, Hou XW, et al. **Intracranial atherosclerotic plaque as a potential cause of embolic stroke of undetermined source.** *J Am Coll Cardiol* 2021;77:680–91 CrossRef Medline
- Kopczak A, Schindler A, Bayer-Karpinska A, et al. **Complicated carotid artery plaques as a cause of cryptogenic stroke.** *J Am Coll Cardiol* 2020;76:2212–22 CrossRef Medline
- Sun J, Underhill HR, Hippe DS, et al. **Sustained acceleration in carotid atherosclerotic plaque progression with intraplaque hemorrhage: a**

- long-term time course study.** *JACC Cardiovasc Imaging* 2012;5:798–804 CrossRef Medline
38. Liu Y, Wang M, Zhang B, et al. **Size of carotid artery intraplaque hemorrhage and acute ischemic stroke: a cardiovascular magnetic resonance Chinese atherosclerosis risk evaluation study.** *J Cardiovasc Magn Reson* 2019;21:9 CrossRef Medline
39. Kashiwazaki D, Shiraishi K, Yamamoto S, et al. **Efficacy of carotid endarterectomy for mild (<50%) symptomatic carotid stenosis with unstable plaque.** *World Neurosurg* 2019;121:e60–69 CrossRef Medline
40. Gupta A, Baradaran H, Schweitzer AD, et al. **Carotid plaque MRI and stroke risk: a systematic review and meta-analysis.** *Stroke* 2013;44:3071–77 CrossRef Medline
41. Rafailidis V, Chrysosgonidis I, Tegos T, et al. **Imaging of the ulcerated carotid atherosclerotic plaque: a review of the literature.** *Insights Imaging* 2017;8:213–25 CrossRef Medline
42. Benson JC, Cheek H, Aubry MC, et al. **Cervical carotid plaque MRI.** *Clin Neuroradiol* 2021;31:295–306 CrossRef Medline
43. Grosse GM, Sieweke JT, Biber S, et al. **Nonstenotic carotid plaque in embolic stroke of undetermined source: interplay of arterial and atrial disease.** *Stroke* 2020;51:3737–41 CrossRef Medline
44. Ntaios G, Pearce LA, Veltkamp R, et al; NAVIGATE ESUS Investigators. **Potential embolic sources and outcomes in embolic stroke of undetermined source in the NAVIGATE-ESUS trial.** *Stroke* 2020;51:1797–1804 CrossRef Medline
45. Kerwin W, Alessio A, Ferguson M, et al. **High-resolution [18] fluoro-deoxyglucose-positron emission tomography and coregistered magnetic resonance imaging of atherosclerotic plaque from a patient undergoing carotid endarterectomy.** *Circ Cardiovasc Imaging* 2012;5:683–84 CrossRef Medline
46. Chaker S, Al-Dasuqi K, Baradaran H, et al. **Carotid plaque positron emission tomography imaging and cerebral ischemic disease: a systematic review and meta-analysis.** *Stroke* 2019;50:2072–79 CrossRef Medline

Clinical Evaluation of Scout Accelerated Motion Estimation and Reduction Technique for 3D MR Imaging in the Inpatient and Emergency Department Settings

M. Lang, A. Tabari, D. Polak, J. Ford, B. Clifford, W.-C. Lo, K. Manzoor, D.N. Splitthoff, L.L. Wald, O. Rapalino, P. Schaefer, J. Conklin, S. Cauley, and S.Y. Huang



ABSTRACT

BACKGROUND AND PURPOSE: A scout accelerated motion estimation and reduction (SAMER) framework has been developed for efficient retrospective motion correction. The goal of this study was to perform an initial evaluation of SAMER in a series of clinical brain MR imaging examinations.

MATERIALS AND METHODS: Ninety-seven patients who underwent MR imaging in the inpatient and emergency department settings were included in the study. SAMER motion correction was retrospectively applied to an accelerated T1-weighted MPRAGE sequence that was included in brain MR imaging examinations performed with and without contrast. Two blinded neuroradiologists graded images with and without SAMER motion correction on a 5-tier motion severity scale (none = 1, minimal = 2, mild = 3, moderate = 4, severe = 5).

RESULTS: The median SAMER reconstruction time was 1 minute 47 seconds. SAMER motion correction significantly improved overall motion grades across all examinations ($P < .005$). Motion artifacts were reduced in 28% of cases, unchanged in 64% of cases, and increased in 8% of cases. SAMER improved motion grades in 100% of moderate motion cases and 75% of severe motion cases. Sixty-nine percent of nondiagnostic motion cases (grades 4 and 5) were considered diagnostic after SAMER motion correction. For cases with minimal or no motion, SAMER had negligible impact on the overall motion grade. For cases with mild, moderate, and severe motion, SAMER improved the motion grade by an average of 0.3 (SD, 0.5), 1.1 (SD, 0.3), and 1.1 (SD, 0.8) grades, respectively.

CONCLUSIONS: SAMER improved the diagnostic image quality of clinical brain MR imaging examinations with motion artifacts. The improvement was most pronounced for cases with moderate or severe motion.

ABBREVIATIONS: CNR = contrast-to-noise ratio; SAMER = scout accelerated motion estimation and reduction; SENSE = sensitivity encoding

Patient motion is a frequent cause of image quality degradation in MR imaging examinations and has been reported to be present in approximately 29% of inpatient and emergency department

examinations.¹ Associated motion artifacts such as ring artifacts, image blurring, and signal drop-out may result in suboptimal image quality that negatively affects interpretation and diagnosis. Advanced MR imaging techniques and 3D volumetric sequences rely on higher spatial resolution and have greater sequence complexity and longer acquisition times, making them more prone to motion artifacts.^{2,3}

Rapid imaging techniques such as parallel imaging and advanced encoding methods can reduce motion artifacts and provide high clinical value in time-critical emergency situations. While these techniques are valuable, there are often compromises and trade-offs in terms of image quality and contrast compared with standard brain sequences.^{4,5} Moreover, fast imaging techniques still do not fully solve the motion problem because patient motion can occur on a time scale on the order of seconds.^{6,7}

Navigator-free retrospective motion-correction approaches estimate patient motion in a purely data-driven manner using only the raw k -space data from the standard data acquisition. Scout accelerated motion estimation and reduction (SAMER) further exploits a

Received September 6, 2022; accepted after revision December 11.

From the Department of Radiology (M.L., A.T., D.P., J.F., K.M., L.L.W., O.R., P.S., J.C., S.C., S.Y.H.), Athinoula A. Martinos Center for Biomedical Imaging, Massachusetts General Hospital, Charlestown, Massachusetts; Harvard Medical School (M.L., A.T., J.F., K.M., L.L.W., O.R., P.S., J.C., S.C., S.Y.H.), Boston, Massachusetts; Siemens Healthcare (D.P., D.N.S.), Erlangen, Germany; Siemens Medical Solutions (B.C., W.-C.L.), Boston, Massachusetts; and Harvard-MIT Health Sciences and Technology (L.L.W.), Massachusetts Institute of Technology, Cambridge, Massachusetts.

M. Lang and A. Tabari contributed equally to this work.

This work was supported by the National Institutes of Health under award number P41EB030006 and a research grant from Siemens Healthineers.

Please address correspondence to Susie Y. Huang, MD, PhD, Athinoula A. Martinos Center for Biomedical Imaging, Department of Radiology, Massachusetts General Hospital, 149 13th St, Room 2301, Charlestown, MA, 02129; e-mail: susie.huang@mgh.harvard.edu; @SusieHuangMDPhD; @Azitabari

Indicates open access to non-subscribers at www.ajnr.org

Indicates article with online supplemental data.

<http://dx.doi.org/10.3174/ajnr.A7777>

single 3- to 5-second scout image and an optimized sequence ordering.⁸ The highly accelerated scout provides sufficient motion artifact-free *k*-space data to determine the motion trajectory of subsequent image acquisitions without needing to repeat full or partial image updates. When one knows the motion trajectory, the motion artifacts are mitigated by including the motion information in the generalized inverse problem used for image reconstruction. In addition, SAMER allows each motion state to be independently determined by using fully separable motion optimizations across all shots.⁸⁻¹⁰ The ability to independently estimate motion for all shots allows the optimization to be accelerated, which reduces the reconstruction time to clinically acceptable levels (~4 seconds per shot). The ability to perform motion correction retrospectively makes clinical deployment easier because the reconstruction can be performed after the scan.

The goal of this study was to perform a retrospective clinical evaluation of the SAMER framework on 3D T1-weighted MPRAGE examinations acquired in inpatient and emergency department settings. We hypothesized that the SAMER framework would improve motion artifacts in examinations characterized by moderate-to-severe motion and would not adversely affect the image quality of examinations characterized by minimal or no motion.

MATERIALS AND METHODS

This retrospective study was approved by the institutional review board of Mass General Brigham and was compliant with the Health Insurance Portability and Accountability Act. Given that the SAMER *k*-space sampling strategy was embedded in the T1-weighted MPRAGE sequence included as part of the clinical protocol, the institutional review board waived the need for signed informed consent. Instead, an information sheet describing the research study was provided to all study participants, who could decline participation in the study before undergoing their scan.

SAMER Framework

The SAMER framework and mathematic model were previously described in detail by Polak et al.⁸ Briefly, the SAMER framework is based on a sensitivity encoding (SENSE) parallel imaging reconstruction using a generalized forward model inversion; the SENSE model is extended to account for the effect of motion.¹¹ The technique acquires an ultra-fast, low-resolution 3- to 5-second scout image at the beginning of the examination that is presumed to be motion artifact-free. SAMER uses the scout image to directly provide estimates of the motion trajectory across all subsequent acquisitions. By means of 6 rigid-body parameters, the individual motion states of each shot are used in the generalized forward model inversion to reconstruct motion-mitigated images. A T1-weighted MPRAGE research package using the SAMER framework was used to acquire and retrospectively reconstruct the data in this study.

Brain MR Imaging Protocol

Four brain MR imaging protocols included the SAMER embedded T1-weighted MPRAGE sequences: routine brain without

contrast (Routine w/o), routine brain without and with contrast (Routine w/o & w), memory loss without contrast (ML w/o), and memory loss without and with contrast (ML w/o & w). The non-contrast MPRAGE images from the Routine w/o and the ML w/o protocols and the postcontrast MPRAGE images from the Routine w/o & w and ML w/o & w protocols were used for retrospective SAMER motion correction. The parameters for the MPRAGE sequence used for SAMER motion correction were the following: resolution = $1 \times 1 \times 1$ mm, acceleration factor = 2×2 , turbo factor = 192, TE = 3.5 ms, TI = 1100 ms, TR = 2500 ms, FOV = $256 \times 256 \times 192$ mm, bandwidth = 200 Hz/pixel. The acquisition time was 2 minutes 40 seconds.

Data Acquisition

Ninety-seven patients who underwent routine brain MR imaging examination between August 2021 and January 2022 in the inpatient and emergency department settings were included in this study. The examinations were performed on a 3T MR imaging system (Magnetom Skyra; Siemens) by using either a 20-channel head-neck coil or a 32-channel head-only coil. Imaging protocols of all cases included an R = 4-fold accelerated T1-weighted MPRAGE sequence that was acquired using a custom linear + checkered sequence reordering.⁸ The linear + checkered reordering involved uniformly distributed sampling across the low-frequency elements of *k*-space and linear traversal across the remainder of the *k*-space to preserve the contrast and minimize blurring of the reconstructed images.⁸

The raw *k*-space data from the MPRAGE images were extracted from the scanners within 48 hours of acquisition. SAMER framework was then retrospectively applied to the extracted MPRAGE raw data for motion correction. For examinations performed using the Routine w/o protocol, MPRAGE without contrast images was used for SAMER motion correction. Given that the motion grade was the primary outcome of interest and is relatively independent of image contrast, the motion grades for the MPRAGE without contrast images and MPRAGE with contrast images were aggregated for analysis.

Motion Grading

Two neuroradiologists (M.L. and J.F. with 3 and 5 years of experience, respectively) performed independent blinded reviews of unlabeled MPRAGE images without and with SAMER motion correction. The order of the study and the type of study (baseline-versus-SAMER motion-corrected images) were randomized by A.T. for the reviewing neuroradiologists. Cases with any discrepant grades were adjudicated independently by a third blinded senior neuroradiologist (J.C.) with >10 years of experience. A previously established 5-point motion scale was used for grading (Fig 1).¹ Grade 1 indicates the absence of detectable motion artifacts; grade 2 indicates minimal motion with barely detectable motion artifacts and a negligible effect on image quality and diagnosis; grade 3 indicates mild motion with noticeable motion artifacts that likely do not have diagnostic consequences; grade 4 indicates moderate motion artifacts that degrade and possibly obscure underlying pathology; and grade 5 indicates severe motion artifacts that distort anatomy and obscure underlying pathology. Grades 1, 2, and 3 were

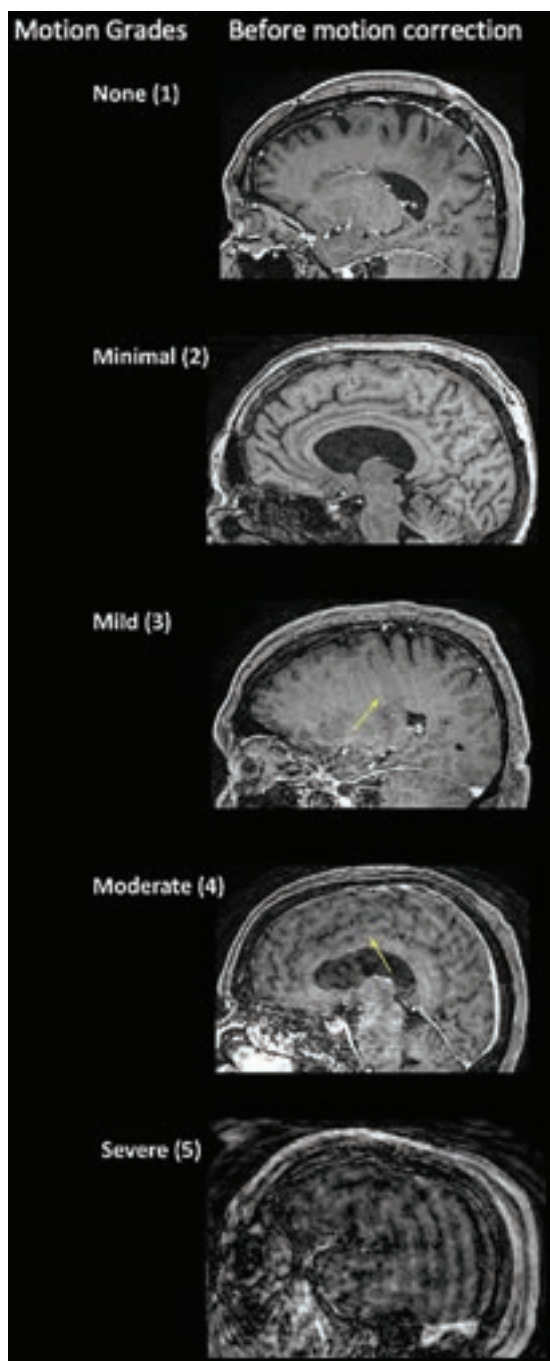


FIG 1. Motion scale used for the clinical quantification of motion artifacts along with representative cases before motion correction. The arrows point to areas of image blurring due to motion artifacts.

considered diagnostic quality with regard to motion artifacts, whereas grades 4 and 5 were considered nondiagnostic, as defined in the original article by Andre et al.¹ The motion grade improvement was defined as the precorrection motion grade minus the postcorrection grade.

Head-to-Head Image Evaluation

The same 2 neuroradiologists (M.L. and J.F.) independently reviewed 79 of 97 cases with pathology in a blinded fashion; 18 cases did not have visible pathology on MPRAGE images. The

screen position (left versus right) of non-motion-corrected and SAMER motion-corrected MPRAGE images and the order of the cases were all randomized. All cases were graded on a 5-point Likert scale, in which positive numbers favored the images on the right side of the screen and negative numbers favored the images on the left side of the screen. Head-to-head comparison was made of pathology conspicuity, pathology sharpness, and the evaluation of surrounding anatomy. Disagreements between readers were adjudicated by a third neuroradiologist (J.C.).

Quantitative Assessment

Contrast-to-noise ratio (CNR) and SNR measurements were performed for T1 MPRAGE images without and with SAMER motion correction. To measure signal intensity, we placed ROIs on the left basal ganglia (gray matter) and on the left inferior frontal subcortical white matter. For each subject, we sampled noise using 25-voxel ROIs in air-containing regions above the left aspect of the head. The SD of the background noise was calculated for the same ROIs on the non-motion-corrected and SAMER motion-corrected MPRAGE images. The SNR in gray and white matter was calculated by dividing the mean signal intensity by the SD of the background noise. The CNR was calculated by dividing the difference in gray and white matter intensities by the SD of the background noise.

Statistical Analysis

The motion grades of examinations with and without SAMER motion correction were compared using the nonparametric Wilcoxon rank-sum test. A Welch *t* test was used for the comparison of mean SNR and CNR. Statistical analysis was performed by using R Studio (<http://rstudio.org/download/desktop>). Statistical significance was set at $P < .05$.

RESULTS

Demographics, clinical indications for the MR imaging examinations, and MR imaging protocol breakdown are provided in Table 1. Among the 97 patients studied, brain mass or lesion was the most common indication for the MR imaging examinations ($n = 32$), followed by stroke ($n = 17$) and mental status change ($n = 15$). Thirty-four examinations were performed without contrast, and 63 were performed with contrast. Eighty-four examinations were performed using the 20-channel head-neck coil, and 13 examinations, using the 32-channel head-only coil. The median SAMER reconstruction time was 1 minute 47 seconds.

Of the 97 cases, 5 cases showed no motion (motion grade 1), 46 cases showed minimal motion (motion grade 2), 30 cases showed mild motion (motion grade 3), 8 cases showed moderate motion (motion grade 4), and 8 cases showed severe motion (motion grade 5). Mean motion grades of the motion-corrected examinations using SAMER were significantly lower compared with the uncorrected examinations (2.4 [SD, 0.8] for motion-corrected images and 2.7 [SD, 1.0] for uncorrected images ($P < .001$; Table 2). SAMER motion correction led to decreased motion artifacts in a total of 27 cases (28%), of which 23 cases exhibited motion improvement of 1 grade and 4 cases exhibited motion improvement of 2 grades.

Among the 5 cases with baseline no motion (motion grade 1), there was no change in the motion grade after SAMER motion correction. Of the 46 cases with minimal motion (motion grade 2), most cases (78%) showed no change in motion grade, while motion artifacts worsened by 1 grade in 8 cases (17%) and improved in 2 cases (4%). The Online Supplemental Data show an example of a case with minimal motion (grade 2) at baseline that worsened to mild motion (grade 3) on SAMER motion correction. Note that the degree of motion in the SAMER motion-corrected images is still quite small and did not compromise the diagnostic quality of the image. In 30 cases with baseline mild motion (motion grade 3), there was no change in the motion grade for 19 cases (63%) and improvement in 11 cases (37%). Representative side-by-side comparison of baseline and SAMER motion-corrected images are provided in Fig 2.

In baseline nondiagnostic cases of moderate or severe motion (motion grades 4 or 5, respectively), SAMER motion correction reduced motion artifacts in 87.5% (14/16) of cases (Fig 3), which included 100% of moderate motion cases (grade 4) and 75% of

severe motion cases (grade 5). In fact, 11 of the 16 nondiagnostic grade cases (69%) were considered diagnostic in quality after SAMER motion correction, ie, they were reduced from a score of 4 or 5 to a score of ≤ 3 . Representative images comparing cases with severe motion before and after SAMER motion correction are provided in Fig 4. For cases with minimal, mild, moderate, and severe motion, SAMER improved the motion grade by an average 0.13 (SD, 0.7), 0.3 (SD, 0.5), 1.1 (SD, 0.25), and 1.1 (SD, 0.83) grades, respectively (Table 2).

In a head-to-head comparison, SAMER motion-corrected images were preferred over baseline images for pathology conspicuity in 19% of cases, pathology sharpness in 29% of cases, and evaluation of surrounding anatomy in 20% of cases (Fig 5). While evaluation of pathology was considered similar between baseline and SAMER motion-corrected images in most cases (>70%), no baseline image was preferred over SAMER motion-corrected images for pathology evaluation. Quantitative assessment of SNR and CNR showed that MPRAGE images with SAMER motion correction had significantly higher mean CNR ($P < .001$) and mean SNR in the gray and white matter ($P < .001$) compared with matched MPRAGE images without SAMER motion correction (Fig 6).

Motion grades improved following SAMER motion correction for both noncontrast and contrast-enhanced images. For the noncontrast-enhanced images, mean motion grades improved from 2.6 (SD, 1.1) at baseline to 2.2 (SD, 0.6) following SAMER motion correction ($P = .01$; Table 3). For the contrast-enhanced images, mean motion grades improved from 2.7 (SD, 0.9) to 2.6 (SD, 0.8) following SAMER motion correction ($P = .03$; Table 4). The extent of motion grade improvement was most prominent for baseline, moderate, and severe motion examinations (grades 4 and 5, respectively), regardless of whether the images were acquired without or with contrast (Tables 3 and 4).

DISCUSSION

In this work, we have shown that motion correction using SAMER significantly reduced motion artifacts in volumetric T1-weighted MPRAGE images obtained in a clinical setting within clinically feasible reconstruction times. In most cases with moderate and severe motion artifacts, SAMER reconstruction was able to mitigate motion artifacts sufficiently to improve the quality of the examination from nondiagnostic to diagnostic. In cases with

Table 1: Clinical characteristics of the patients

	Value
No. of subjects	97
Mean age (yr)	60.2 (SD, 16)
Sex (F/M)	48:49
Clinical indication for MR imaging (No.) (%)	
Tumor	32 (33%)
Stroke	17 (17.5%)
AMS	15 (15.4%)
Neurologic deficit	11 (11.3%)
Abscess	3 (3%)
Dementia	2 (2%)
Headache	2 (2%)
Seizure	2 (2%)
TBI	2 (2%)
TIA	2 (2%)
Other	9 (9.2%)
MR imaging protocol (No.) (%)	
SAMER MPRAGE without contrast	34 (35%)
Routine brain without contrast	33 (34%)
Memory loss without contrast	1 (1%)
SAMER MPRAGE with contrast	63 (65%)
Routine brain without and with contrast	61 (63%)
Memory loss without and with contrast	2 (2%)

Note:—AMS indicates altered mental status; TBI, traumatic brain injury.

Table 2: Overall change in motion grade after SAMER implementation

Before Motion Correction, Motion Grade (No. of cases)	After Motion, Correction Motion Grade (No. of cases)	Change in Motion Grade (mean)
Grade 1 (5)	Grade 1 (5)	0
Grade 2 (46)	Grade 1 (2)	0.1 (SD, 0.7)
	Grade 2 (36)	
Grade 3 (30)	Grade 3 (8)	−0.3 (SD, 0.5)
	Grade 2 (11)	
	Grade 3 (19)	
Grade 4 (8)	Grade 2 (1)	−1.1 (SD, 0.3)
	Grade 3 (7)	
Grade 5 (8)	Grade 3 (3)	−1.1 (SD, 0.8)
	Grade 4 (3)	
	Grade 5 (2)	
Mean motion grade (2.7 [SD, 1.0])	Mean motion grade (2.4 [SD, .08])	Change in motion grade (−0.2 [SD, 0.7])

Note:—Grade 1 indicates no motion; grade 2, minimal motion; grade 3, mild motion; grade 4, moderate motion; grade 5, severe motion.

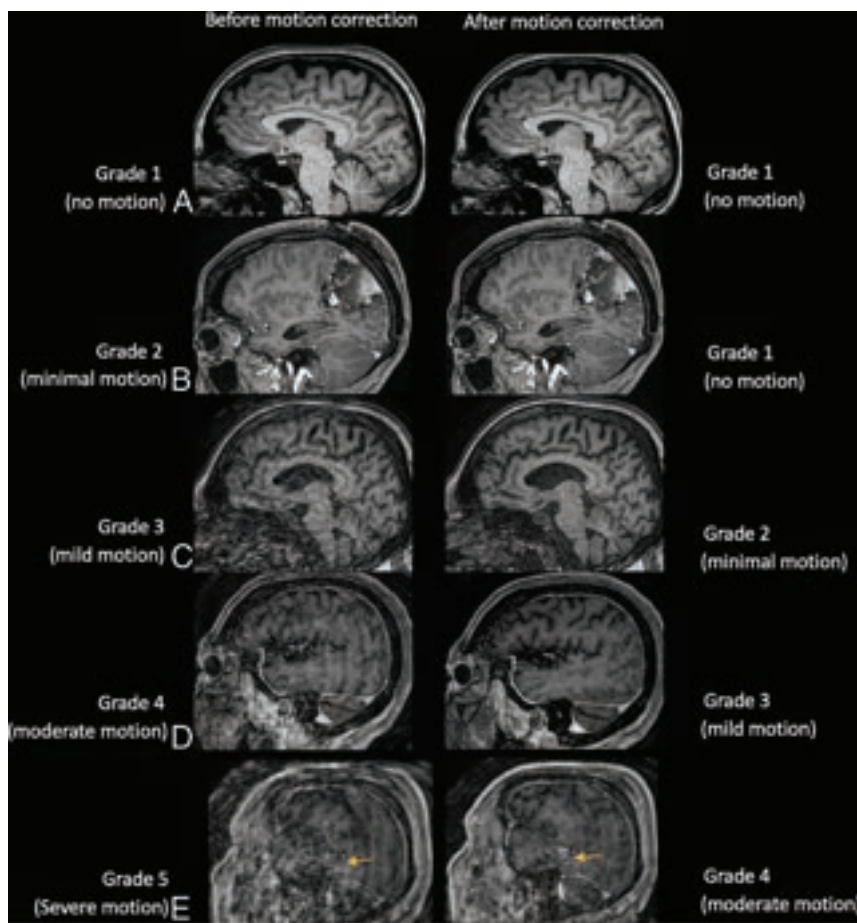


FIG 2. Sagittal T1 MPRAGE images illustrating examples of cases with motion artifacts (grades 1–5) for which SAMER reconstruction improved motion by 1 grade. *A*, A 23-year-old woman with a normal brain. *B*, Postoperative findings from resection of a left parietal lobe tumor in a 59-year-old woman with a history of anaplastic oligodendroglioma. *C*, Diffuse parenchymal volume loss with disproportionate involvement of the frontal and parietal lobes and, to a lesser extent, the left temporal lobe in a 59-year-old man with history of cognitive impairment. *D*, An 83-year-old woman with history of chronic cerebral small-vessel disease. *E*, Expected postoperative changes and enhancement from left temporal parietal craniotomy (arrows) are demonstrated in a 63-year-old man with history of glioblastoma.

absent, minimal, or mild motion, application of SAMER provided comparable image quality without significantly impacting the overall motion grades. CNR and SNR were overall significantly higher in SAMER motion-corrected studies than baseline studies. Our findings suggest that motion-prone patients such as those scanned in the emergency and/or inpatient settings may greatly benefit from SAMER to reduce motion artifacts and prevent time-consuming repeat acquisitions and/or callback examinations, without sacrificing overall image quality.

Techniques for motion mitigation include alternative *k*-space sampling trajectories that are more robust to motion such as radial or spiral acquisitions, ultra-fast imaging techniques (eg, controlled aliasing in parallel imaging [CAIPI], wave-CAIPI, compressed sensing),^{7,11–21} and retrospective or prospective motion-correction techniques.^{3,22} Accelerated MR imaging techniques can reduce motion artifacts by reducing acquisition times. Very rapid brain MR imaging protocols have been developed with 1–2 minutes of the total scan time.^{4,23} The highly accelerated MR imaging

techniques rely on high-end multi-channel receiver arrays that may not always be clinically available or feasible to implement, eg, in large patients. Accelerated imaging techniques and SAMER motion correction are not mutually exclusive, and a combination of these methods may provide additional benefits. Future work is needed to evaluate the potential synergistic benefits of applying SAMER motion correction to accelerated MR imaging techniques.

Prospective motion-correction methods include MR imaging–based motion navigator and optical-based motion tracking systems.^{18,24} MR imaging–based navigator systems are motion-robust because they provide extra motion information from the oversampled central *k*-space.¹⁸ These techniques provide real-time positional information, allowing mitigation of motion through real-time updates of the imaging FOV. These techniques, however, require MR imaging systems that are capable of dynamic updates during image acquisition, installation of additional hardware, and extending the acquisition time to collect additional data used for motion estimation. Furthermore, prospective techniques can have measurement and estimation errors that can degrade image quality. In these quality-degraded cases in which the original uncorrected images are not available, re-acquisition may be required. These factors limit the implementation of prospective motion-correction techniques into existing radiology

workflow without dramatic changes in operation, cost, software, and hardware.^{25,26}

In contrast, retrospective motion-correction techniques use motion information that is encoded from multichannel receiver arrays and is extracted for postacquisition correction through nonlinear inversion of a physics model.^{8,27} Retrospective motion-correction techniques require an iterative approach and are often limited by high computational requirements and reconstruction times.¹⁸ The SAMER framework overcomes these limitations by exploiting a single 3- to 5-second scout image used to jump-start and stabilize the motion-trajectory estimations and an optimized linear + checkered sequence ordering in addition to the scout image to facilitate the separation of the image and motion parameter unknowns.⁸ The low-spatial-resolution and highly accelerated ($R = 6$) initial scout sequence used for motion correction has an echo-train length of ~ 1 second, which essentially eliminates patient motion on the scout image and makes it a good motion-free baseline. SAMER further reduces the computational footprint

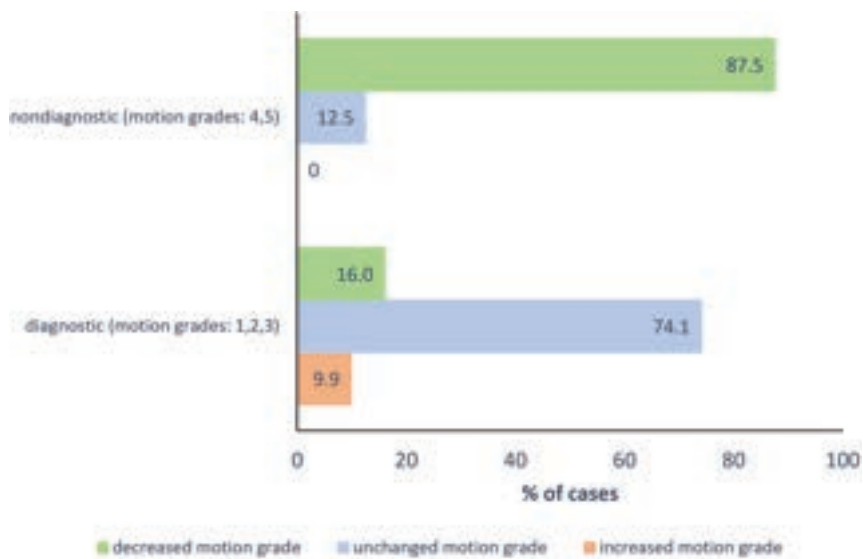


FIG 3. Proportion of nondiagnostic and diagnostic examinations that demonstrated worsening, no change, and improvement of motion grade after SAMER correction. Motion grades 1 (no motion), 2 (minimal), and 3 (mild) are considered diagnostic in terms of motion artifacts, whereas motion grades 4 (moderate) and 5 (severe) are considered nondiagnostic in terms of motion artifacts.

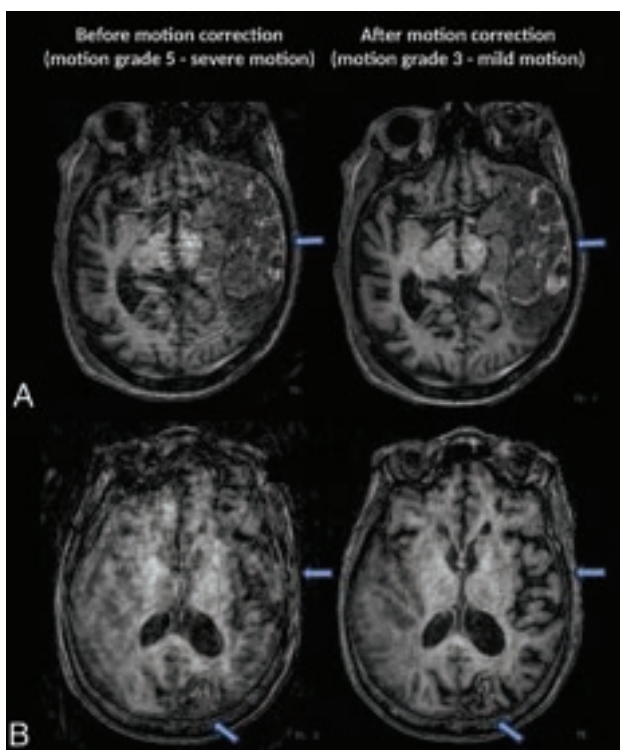


FIG 4. Axial MR images of 2 cases with severe motion artifacts (grade 5) in which SAMER motion correction restored diagnostic value (by reducing motion grade to 3). *A*, The extent of cortical/gyral enhancement (arrows) and edematous expansion of the left temporoparietal region with a mild rightward mass effect is better visualized on the motion-corrected image of a 67-year-old man with traumatic brain injury. *B*, Motion-corrected image shows better visualization of cortical laminar necrosis in the left occipital lobe (arrows) and better evaluation of left temporal lobe volume loss (arrows) in an 86-year-old woman with history of stroke.

by restricting readout voxels, using coil compression, and having only a single iteration step, reaching a median reconstruction time of 107 seconds in this study compared with several minutes with other retrospective motion correction techniques.^{8,28} A further added advantage of all the retrospective motion-correction techniques is that they can be applied to existing clinical protocols, equipment, and workflow through modifications to the sequence and reconstruction software, without incurring additional burden to the patients or operators by obviating the need for external markers or cameras.²⁹⁻³¹

SAMER motion correction disproportionately benefited studies that had moderate and severe motion artifacts, with most nondiagnostic motion cases exhibiting an improvement in the motion grade. In fact, 69% of nondiagnostic cases were considered diagnostic with regard to motion artifacts

following SAMER motion correction. In contrast, most examinations with mild-to-no motion, in which motion correction would offer little benefit in a clinical setting, were not significantly impacted by SAMER motion correction. These findings suggest that SAMER motion correction may provide the most benefit to examinations with moderate-to-severe motion, in which the image quality would otherwise be considered nondiagnostic and the underlying pathology might be obscured. In cases of extreme motion, it can be very difficult to perform retrospective correction accurately, seen in 2 cases in this study. The main reason is that extreme head rotation during image-acquisition causes large gaps in *k*-space that parallel imaging is unable to fill,³² ie, the gaps in *k*-space data were too large to allow retrospective motion correction with the existing data. This feature is a limitation of SAMER and other retrospective methods, and in these instances, either a full or partial repeat image acquisition was required.

Application of motion-correction techniques could potentially introduce unwanted reconstruction artifacts through imperfections in the motion estimation. SAMER uses a data-driven approach for motion correction, in which we optimize over a SENSE + motion model to estimate the patient's motion trajectory.⁸ Small instabilities in this nonconvex optimization can lead to small inaccuracies in the motion parameters. This outcome was seen in 8 cases with uncorrected mild motion (grade 2), in which SAMER introduced a small number of unintended artifacts and worsened the motion grade by 1 point (Online Supplemental Data). However, even if SAMER causes slightly increased artifacts in a small number of cases, this result should not negatively impact the diagnostic quality of the examination because the original (non-motion-corrected) images are still available to the radiologist for reference and interpretation, safeguarding against potential worsening of motion due to the alternative *k*-space

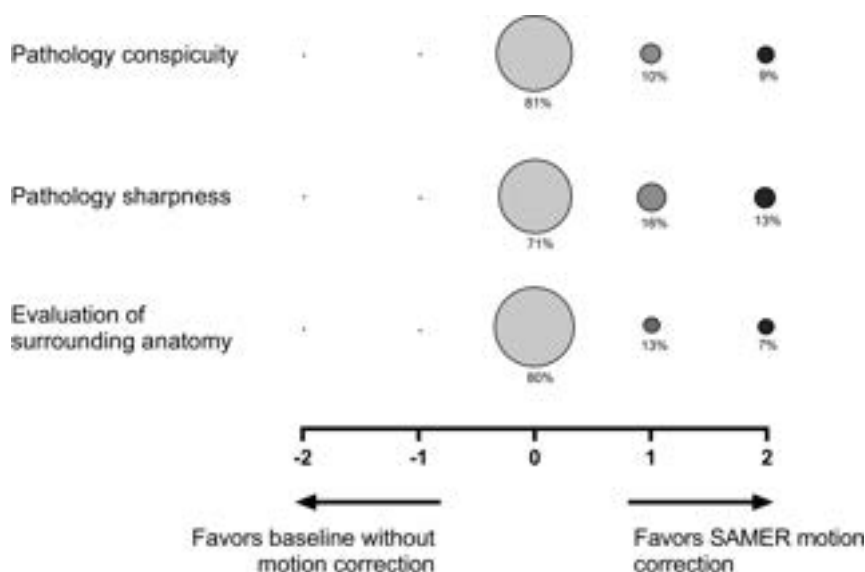


FIG 5. Balloon plot showing the results of the head-to-head comparison of baseline MPRAGE and SAMER motion-corrected MPRAGE studies for pathology conspicuity, pathology sharpness, and evaluation of surrounding anatomy. A total 79 of 97 cases had pathology on imaging and were included in this assessment. The size of the circle correlates to the percentage of cases assigned a given score, and the percentage of cases receiving a given score is indicated below each circle. A zero score indicates equivalency, negative scores (*left*) favor baseline MPRAGE images, and positive scores (*right*) favor SAMER motion-corrected MPRAGE images.

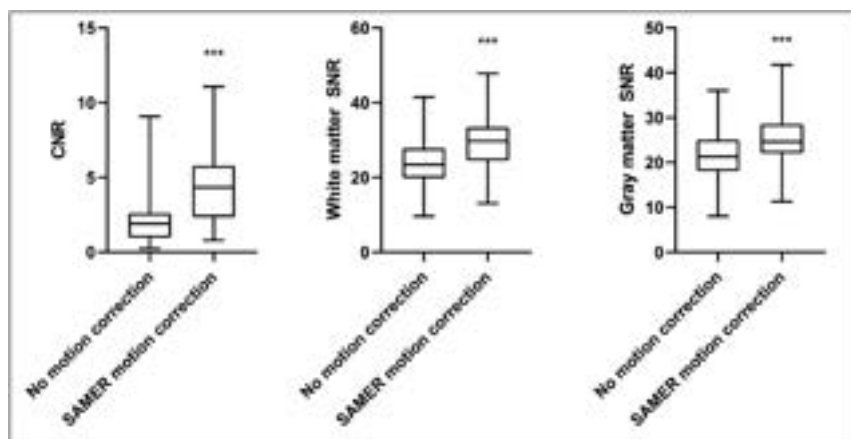


FIG 6. Boxplot charts demonstrating the distribution of CNR and SNR in the gray matter and white matter in MPRAGE without and with SAMER motion correction. CNRs and SNRs are significantly greater ($P < .001$) in the MPRAGE SAMER motion-corrected images compared with baseline MPRAGE images. Triple asterisks indicate $P < .001$.

sampling strategy adopted to mitigate motion artifacts. As the technique is further refined and the negative impact on artifacts is diminished, only SAMER motion-corrected images may be needed for interpretation to minimize image bloat for the radiologist.

The SAMER framework also offers the ability to track the motion trajectory through use of motion-guidance lines at fixed k -space locations.⁸ In addition, SAMER allows motion states to be determined during acquisition from each single shot. This feature allows motion data to be made immediately available at the end of the acquisition rather than having to wait for data

reconstruction. Although it was not explored here, the motion trajectories provided by SAMER and other approaches can be used to design and train classification systems for automated prediction of motion severity as well as the level of artifact reduction that SAMER and other motion correction techniques might provide. These types of systems could enhance the technologist and radiologist workflow by automatically identifying motion-degradation and correction viability, possibly even before scan completion. This enhancement may potentially allow the technologist to terminate an incomplete-but-nondiagnostic acquisition and troubleshoot to obtain a better repeat acquisition. While SAMER motion correction was only applied to the 3D T1-weighted MPRAGE sequence in this study, it can, in principle, also be extended to other sequences including 2D spin-echo and gradient-echo sequences.⁸ Motion correction in 2D sequences is limited by the greater section thickness and missing information from section gaps compared with 3D sequences. Deep learning models can improve image interpolation errors for 2D sequence motion-correction techniques^{10,32} and could play a role in the extension of SAMER to 2D motion correction in the future.

Limitations of the current study include its retrospective nature and inclusion of only one 3D volumetric MR sequence. This was intended as a feasibility study to demonstrate the efficacy of SAMER on a single pulse sequence (3D T1-weighted MPRAGE) in a clinical setting. Testing of SAMER on additional MR images, 2D and volumetric sequences, is needed. In addition, the included MR imaging examinations were heterogeneous in that some

examinations were performed without contrast and others were performed with contrast. While the results demonstrated that SAMER was able to improve motion artifacts in both noncontrast and contrast-enhanced MPRAGE images, the small sample size limited further evaluation of whether SAMER could mitigate motion to the same degree if contrast was present or absent. The focus of this study was to evaluate the ability of SAMER to mitigate motion and not on the conspicuity of findings. Nonetheless, future studies with larger numbers of patients are needed to explore how the presence of contrast may potentially affect the degree of motion correction achieved by SAMER.

Table 3: Change in motion grade after SAMER implementation for noncontrast examinations

Before Motion Correction, Motion Grade (No. of Cases)	After Motion Correction, Motion Grade (No. of Cases)	Change in Motion Grade (mean)
Grade 1 (3)	Grade 1 (3)	0
Grade 2 (18)	Grade 2 (16)	0.1 (SD, 0.3)
	Grade 3 (2)	
Grade 3 (7)	Grade 2 (5)	-0.7 (SD, 0.4)
	Grade 3 (2)	
Grade 4 (2)	Grade 2 (1)	-1.5 (SD, 0.7)
	Grade 3 (1)	
Grade 5 (4)	Grade 3 (3)	-1.7 (SD, 0.5)
	Grade 4 (1)	
Mean motion grade (2.6 [SD, 1.1])	Mean motion grade (2.2 [SD, 0.6])	Change in motion grade (-0.4 [SD, 0.8])

Table 4: Change in motion grade after SAMER implementation for contrast-enhanced examinations

Before Motion Correction, Motion Grade (No. of Cases)	After Motion Correction, Motion Grade (No. of Cases)	Change in Motion Grade (mean)
Grade 1 (2)	Grade 1 (2)	0
Grade 2 (28)	Grade 1 (2)	0.1 (SD, 0.5)
	Grade 2 (20)	
	Grade 3 (6)	
Grade 3 (23)	Grade 2 (6)	-0.2 (SD, 0.4)
	Grade 3 (17)	
Grade 4 (6)	Grade 3 (6)	-1 (SD, 0)
Grade 5 (4)	Grade 4 (2)	-0.5 (SD, 0.5)
	Grade 5 (2)	
Mean motion grade (2.7 [SD, 0.9])	Mean motion grade (2.6 [SD, 0.8])	Change in motion grade (-0.2 [SD, 0.6])
Mean motion grade (2.6 [SD, 1.1])	Mean motion grade (2.2 [SD, 0.6])	Change in motion grade (-0.4 [SD, 0.8])

CONCLUSIONS

SAMER significantly reduced motion artifacts in clinical brain MR imaging examinations. The image-quality improvement was most pronounced for cases with moderate or severe motion. SAMER transformed 69% of nondiagnostic cases to the diagnostic category. The effective motion correction offered by SAMER may facilitate timely diagnosis and reduce repeat imaging and callbacks in acute clinical settings.

Disclosure forms provided by the authors are available with the full text and PDF of this article at www.ajnr.org.

REFERENCES

- Andre JB, Bresnahan BW, Mossa-Basha M, et al. **Toward quantifying the prevalence, severity, and cost associated with patient motion during clinical MR examinations.** *J Am Coll Radiology* 2015;12:689–95 CrossRef Medline
- Havsteen I, Ohlhues A, Madsen KH, et al. **Are movement artifacts in magnetic resonance imaging a real problem? A narrative review.** *Front Neurol* 2017;8:232 CrossRef Medline
- Ali SH, Modic ME, Mahmoud SY, et al. **Reducing clinical MRI motion degradation using a prescan patient information pamphlet.** *AJR Am J Roentgenol* 2013;200:630–34 CrossRef Medline
- Clifford B, Conklin J, Huang SY, et al. **An artificial intelligence-accelerated 2-minute multi-shot echo planar imaging protocol for comprehensive high-quality clinical brain imaging.** *Magn Reson Med* 2022;87:2453–63 CrossRef Medline
- Yanasak NE, Kelly MJ. **MR imaging artifacts and parallel imaging techniques with calibration scanning: a new twist on old problems.** *Radiographics* 2014;34:532–48 CrossRef Medline
- Shenton ME, Hamoda HM, Schneiderman JS, et al. **A review of magnetic resonance imaging and diffusion tensor imaging findings in mild traumatic brain injury.** *Brain Imaging Behav* 2012;6:137–92 CrossRef Medline
- Breuer FA, Blaimer M, Heidemann RM, et al. **Controlled aliasing in parallel imaging results in higher acceleration (CAIPIRINHA) for multi-slice imaging.** *Magn Reson Med* 2005;53:684–91 CrossRef Medline
- Polak D, Splitthoff DN, Clifford B, et al. **Scout accelerated motion estimation and reduction (SAMER).** *Magn Reson Med* 2022;87:163–78 CrossRef Medline
- Haskell MW, Cauley SF, Wald LL. **Targeted Motion Estimation and Reduction (TAMER): data consistency based motion mitigation for MRI using a reduced model joint optimization.** *IEEE Trans Med Imaging* 2018;37:1253–65 CrossRef Medline
- Haskell MW, Cauley SF, Bilgic B, et al. **Network Accelerated Motion Estimation and Reduction (NAMER): convolutional neural network guided retrospective motion correction using a separable motion model.** *Magn Reson Med* 2019;82:1452–61 CrossRef Medline
- Pipe JG. **Motion correction with PROPELLER MRI: application to head motion and free-breathing cardiac imaging.** *Magn Reson Med* 1999;42:963–69 CrossRef Medline
- Breuer FA, Blaimer M, Mueller MF, et al. **Controlled aliasing in volumetric parallel imaging (2D CAIPIRINHA).** *Magn Reson Med* 2006;55:549–56 CrossRef Medline
- Lustig M, Donoho D, Pauly JM. **Sparse MRI: The application of compressed sensing for rapid MR imaging.** *Magn Reson Med* 2007;58:1182–95 CrossRef Medline
- Bilgic B, Gagoski BA, Cauley SF, et al. **Wave-CAIPI for highly accelerated 3D imaging.** *Magn Reson Med* 2015;73:2152–62 CrossRef Medline
- Polak D, Setsompop K, Cauley SF, et al. **Wave-CAIPI for highly accelerated MP-RAGE imaging.** *Magn Reson Med* 2018;79:401–06 CrossRef Medline
- Polak D, Cauley S, Huang SY, et al. **Highly-accelerated volumetric brain examination using optimized wave-CAIPI encoding.** *J Magn Reson Imaging* 2019;50:961–74 CrossRef Medline

17. Gagoski BA, Bilgic B, Eichner C, et al. **RARE/turbo spin echo imaging with simultaneous multislice wave-CAIPI.** *Magn Reson Med* 2015;73:929–38 CrossRef Medline
18. Godenschweger F, Kägebein U, Stucht D, et al. **Motion correction in MRI of the brain.** *Phys Med Biol* 2016;61:R32–56 CrossRef Medline
19. Longo MGF, Conklin J, Cauley SF, et al. **Evaluation of ultrafast Wave-CAIPI MPRAGE for visual grading and automated measurement of brain tissue volume.** *AJNR Am J Neuroradiol* 2020;41:1388–96 CrossRef Medline
20. Ngamsombat C, Gonçalves Filho ALM, Longo MGF, et al. **Evaluation of ultrafast Wave-controlled aliasing in parallel imaging 3D-FLAIR in the visualization and volumetric estimation of cerebral white matter lesions.** *AJNR Am J Neuroradiol* 2021;42:1584–90 CrossRef Medline
21. Gonçalves Filho ALM, Awan KM, Conklin J, et al. **Validation of a highly accelerated post-contrast wave-controlled aliasing in parallel imaging (CAIPI) 3D-T1 MPRAGE compared to standard 3D-T1 MPRAGE for detection of intracranial enhancing lesions on 3-T MRI.** *Eur Radiol* 2022;2:1–11 CrossRef Medline
22. Blumenthal JD, Zijdenbos A, Molloy E, et al. **Motion artifact in magnetic resonance imaging: implications for automated analysis.** *Neuroimage* 2002;16:89–92 CrossRef Medline
23. Skare S, Sprenger T, Norbeck O, et al. **A 1-minute full brain MR exam using a multicontrast EPI sequence.** *Magn Reson Med* 2018;79:3045–54 CrossRef Medline
24. Gumus K, Keating B, White N, et al. **Comparison of optical and MR-based tracking.** *Magn Reson Med* 2015;74:894–902 CrossRef Medline
25. Zaitsev M, Akin B, LeVan P, et al. **Prospective motion correction in functional MRI.** *Neuroimage* 2017;154:33–42 CrossRef Medline
26. Maclaren J, Herbst M, Speck O, et al. **Prospective motion correction in brain imaging: a review.** *Magn Reson Med* 2013;69:621–36 CrossRef Medline
27. Usman M, Latif S, Asim M, et al. **Retrospective motion correction in multishot MRI using generative adversarial network.** *Sci Rep* 2020;10:4786 CrossRef Medline
28. Vecchiato K, Egloff A, Carney O, et al. **Evaluation of DISORDER: retrospective image motion correction for volumetric brain MRI in a pediatric setting.** *AJNR Am J Neuroradiol* 2021;42:774–81 CrossRef Medline
29. Zaitsev M, Dold C, Sakas G, et al. **Magnetic resonance imaging of freely moving objects: prospective real-time motion correction using an external optical motion tracking system.** *Neuroimage* 2006;31:1038–50 CrossRef Medline
30. Aksoy M, Forman C, Straka M, et al. **Real-time optical motion correction for diffusion tensor imaging.** *Magn Reson Med* 2011;66:366–78 CrossRef Medline
31. Ooi MB, Krueger S, Thomas WJ, et al. **Prospective real-time correction for arbitrary head motion using active markers.** *Magn Reson Med* 2009;62:943–54 CrossRef Medline
32. Holdsworth SJ, Skare S, Bammer R. **On the application of phase correction and use of k-space entropy in partial Fourier diffusion-weighted EPI.** In: *Proceedings of the International Society for Magnetic Resonance in Medicine*, Honolulu, Hawaii. April, 18–24, 2009
33. Pirkel CM, Cencini M, Kurzawski JW, et al. **Learning residual motion correction for fast and robust 3D multiparametric MRI.** *Med Image Anal* 2022;77:102387 CrossRef Medline

Diagnostic Accuracy of Arterial Spin-Labeling, Dynamic Contrast-Enhanced, and DSC Perfusion Imaging in the Diagnosis of Recurrent High-Grade Gliomas: A Prospective Study

T.B. Nguyen, N. Zakhari, S. Velasco Sandoval, A. Guarnizo-Capera, M. Alexios Gulak, J. Woulfe, G. Jansen, R. Thornhill, N. Majtenyi, and G.O. Cron



ABSTRACT

BACKGROUND AND PURPOSE: For patients with high-grade gliomas, the appearance of a new, enhancing lesion after surgery and chemoradiation represents a diagnostic dilemma. We hypothesized that MR perfusion without and with contrast can differentiate tumor recurrence from radiation necrosis.

MATERIALS AND METHODS: In this prospective study, we performed 3 MR perfusion methods: arterial spin-labeling, DSC, and dynamic contrast enhancement. For each lesion, we measured CBF from arterial spin-labeling, uncorrected relative CBV, and leakage-corrected relative CBV from DSC imaging. The volume transfer constant and plasma volume were obtained from dynamic contrast-enhanced imaging without and with T1 mapping using modified Look-Locker inversion recovery (MOLLI). The diagnosis of tumor recurrence or radiation necrosis was determined by either histopathology for patients who underwent re-resection or radiologic follow-up for patients who did not have re-resection.

RESULTS: There were 26 patients with 32 lesions, 19 lesions with tumor recurrence and 13 lesions with radiation necrosis. Compared with radiation necrosis, lesions with tumor recurrence had higher CBF ($P = .033$), leakage-corrected relative CBV ($P = .048$), and plasma volume using MOLLI T1 mapping ($P = .012$). For differentiating tumor recurrence from radiation necrosis, the areas under the curve were 0.81 for CBF, 0.80 for plasma volume using MOLLI T1 mapping, and 0.71 for leakage-corrected relative CBV. A correlation was found between CBF and leakage-corrected relative CBV ($r_s = 0.54$), volume transfer constant, and plasma volume ($0.50 < r_s < 0.77$) but not with uncorrected relative CBV ($r_s = 0.20$, $P = .29$).

CONCLUSIONS: In the differentiation of tumor recurrence from radiation necrosis in a newly enhancing lesion, the diagnostic value of arterial spin-labeling–derived CBF is similar to that of DSC and dynamic contrast-enhancement–derived blood volume.

ABBREVIATIONS: ASL = arterial spin-labeling; AUC = area under the curve; DCE = dynamic contrast-enhanced; k^{trans} = volume transfer constant; MOLLI = modified Look-Locker inversion recovery; pCASL = pseudocontinuous pulse ASL; rCBV = relative CBV (CBV lesion/CBV normal contralateral white matter); ROC = receiver operating characteristic; SI = signal intensity; SMART₁Map = saturation method using adaptive recovery times for cardiac T1 mapping; Vp = plasma volume

In the monitoring of patients with high-grade gliomas treated with standard chemoradiation, the presence of a newly enhancing lesion seen on MR imaging often represents a diagnostic

dilemma. While subjective radiologic assessment of MR imaging contrast-enhancement patterns can be useful for differentiating recurrence from treatment-related effects,¹ there is evidence that quantitative perfusion can improve diagnostic accuracy.^{2,3}

DSC MR imaging is the most widely used perfusion technique in clinical practice. There have been fewer reports on the diagnostic accuracy of other perfusion techniques such as dynamic contrast-enhanced (DCE) MR imaging and arterial spin-labeling (ASL) in differentiating tumor recurrence and treatment-related effects.⁴⁻⁶ Unlike DSC and DCE techniques, ASL does not require any contrast injection and can provide simple quantification of CBF.⁷ While earlier applications of ASL on 1.5T clinical systems had inadequate signal-to-noise, the increased availability of 3T scanners has made the technique suitable for broader clinical translation. Our hypothesis is that ASL can provide diagnostic value similar to that of DSC MR imaging and DCE MR imaging

Received July 28, 2022; accepted after revision December 30.

From the Department of Radiology (T.B.N., N.Z., R.T.), Radiation Oncology and Medical Physics, and Department of Pathology and Laboratory Medicine (J.W., G.J.), The Ottawa Hospital, Ottawa, Ontario, Canada; University of Ottawa (T.B.N., N.Z., J.W., G.J., R.T.), Ottawa, Ontario, Canada; The Ottawa Hospital Research Institute (T.B.N., J.W., G.J., R.T.), Ottawa, Ontario, Canada; Division of Neuroradiology (S.V.S., A.G.-C.), Department of Radiology, Hospital Universitario Fundación Santa Fe de Bogotá, Bogotá, D.C., Colombia; Department of Anesthesiology and Pain Medicine (M.A.G.), University of Toronto, Toronto, Ontario, Canada; Department of Medical Physics (N.M.), Grand River Regional Cancer Centre, Kitchener, Ontario, Canada; and Stanford University (G.O.C.), Stanford, California.

Grant support was provided by GE Healthcare for this researcher-initiated study.

Please address correspondence to Thanh B. Nguyen, MD, Department of Radiology, The Ottawa Hospital, Civic Campus, 1053 Carling Ave, Room J1115, Ottawa, ON, K1Y 4E9, Canada; e-mail: thnguyen@toh.ca

<http://dx.doi.org/10.3174/ajnr.A7771>

in the characterization of a newly enhancing lesion seen in patients with treated high-grade gliomas. Our primary objective was to evaluate the diagnostic accuracy of ASL, DCE MR imaging, and DSC MR imaging in the differentiation of recurrent tumor from treatment-related changes in patients with treated high-grade gliomas. A secondary objective was to compare different methods of T1 mapping for DCE MR imaging.

MATERIALS AND METHODS

Study Population

This study was approved by the local ethics board (REB#20160425-01H, The Ottawa Hospital). Written informed consent was obtained from each patient enrolled in this study. Patients who presented with a newly enhancing lesion suspicious for a recurrent glioma between December 2017 and November 2021 at our hospital were prospectively enrolled. We included adult patients (18 years of age or older) who developed a new parenchymal enhancing lesion on follow-up MR imaging after receiving standard treatment. Treatment was based on the Stupp Protocol and consisted of surgical resection followed by standard radiation treatment with concomitant temozolomide. Patients were excluded for the following reasons: 1) a small enhancing lesion (measuring <1 cm in maximal length); 2) patients who did not have a re-resection and had incomplete radiologic or clinical follow-up following the research MR imaging; 3) delay between MR imaging and the operation (>65 days); and 4) no perfusion imaging or the lesion not covered on perfusion imaging.

Imaging Acquisition

Each patient was scanned on a 3T MR imaging scanner (Discovery MR750W; GE Healthcare). The conventional MR imaging protocol used axial T1 precontrast (TR = 8.1 ms, TE = 3 ms, TI = 450 ms, flip angle = 90°, voxel size = 0.44 × 0.44 × 1 mm); axial T2 FLAIR (TR = 1000 ms, TE = 92 ms, TI = 2651 ms, flip angle = 160°, voxel size = 0.86 × 0.86 × 3 mm); and axial T1 postcontrast (TR = 13 ms, TE = 2.9 ms, flip angle = 12°, voxel size = 1 × 1 × 1 mm). Axial DWI was acquired (multiple b-values from 10 to 1000 s/mm², TR = 5000 ms, TE = 98.9 ms, voxel size = 0.94 × 0.94 × 4.5 mm). ADC maps were generated in-line (on the scanner). Before gadolinium injection, ASL was performed using pseudocontinuous pulse ASL (pCASL) with a 3D stack of fast spin-echo readout (TR = 4588 ms, TE = 10.3 ms, flip angle = 111°, postlabeling delay = 2025 ms, voxel size = 1.8 × 1.8 × 5 mm, number of slices = 16, number of excitations = 3, duration = 4 minutes 13 seconds). Five background suppression (inversion) pulses were used.

For both DCE MR imaging and DSC MR imaging, we used intravenous injections of Gadovist 1.0 (Bayer Schering Pharma). For DCE MR imaging, a fixed dose of 0.05 mmol/kg of Gadovist was injected at 2 mL/s. For DSC MR imaging, a second dose of gadolinium (0.05 mmol/kg) was injected 10 minutes after the first injection at a rate of 4 mL/s. DCE MR imaging was performed using a 3D spoiled gradient-recalled sequence (TR = 5.3 ms, TE = 1.1 ms, flip angle = 25°, voxel size = 1.9 × 2.5 × 5 mm, 80 phases, duration = 4 minutes 35 seconds). For DSC MR imaging, we used a T2*-weighted EPI gradient recalled-echo sequence (TR = 1275 ms, TE = 45 ms, flip angle = 90°, voxel size = 1.8 ×

1.8 × 5 mm, 50 phases, duration = 2 minutes 8 seconds). Two T1-mapping sequences were performed before and after contrast injection for all patients except for the last 10: saturation method by using adaptive recovery times for cardiac T1 mapping (SMART₁Map) (TR = 4.1 ms, TE = 1.6 ms, flip angle = 20°, voxel size = 1.9 × 2.5 × 5 mm, duration = 2 minutes 53 seconds) and modified Look-Locker inversion recovery (MOLLI) (TR = 4.5 ms, TE = 1.6 ms, flip angle = 20°, voxel size = 1.9 × 2.5 × 5 mm, duration = 2 minutes 53 seconds).⁸

Postprocessing of ASL Images

The perfusion-weighted images were produced in-line and were quantified into CBF values via a single compartment model by using the following equation:

$$CBF_{ASL} = 6000 \times \lambda \frac{\left[1 - \exp\left(-\frac{ST(s)}{T1b(s)}\right)\right] \exp\left(\frac{PLD(s)}{T1b(s)}\right)}{2T1b(s) \left[1 - \exp\left(-\frac{LT(s)}{T1b(s)}\right)\right]} \varepsilon \times NEX \left(\frac{PW}{SF \times PD}\right).$$

For this equation, *T1b* is the T1 of blood and is assumed to be 1.6 seconds. The partial saturation of the reference image (*PD*) is corrected for using a *T1t* of 1.2 seconds (typical of gray matter). *ST* is saturation time and is set to 2 seconds. The partition coefficient λ is set to the whole-brain average, 0.9. The efficiency, ε , is a combination of both inversion efficiency (0.8) and background suppression efficiency (0.75), resulting in an overall efficiency of 0.6. *PLD* is the postlabeling delay. *LT* is the labeling duration set to 1.5 seconds. *PW* is the perfusion-weighted or the raw difference image. *SF* is the scaling factor of the *PW* sequence. The CBF is reported in milliliters/100 g/minute. *NEX* is the number of excitations for *PW* images.

Postprocessing of DSC Images

DSC images were processed using singular value decomposition and deconvolution as implemented in a commercially available software package (Olea Sphere 3.0; Olea Medical). MR signal intensity was converted to a T2* relaxation rate. An automated algorithm selected the most suitable pixels for the vascular input function. The signal intensity (SI) was converted to relative change in R2* using the standard expression: $\Delta R2^*(t) = -\ln[S(t) / S_0] / TE$, where *S* is the SI at time *t*; *S*₀, the baseline SI; and *TE*, the echo time. Correction for leakage in CBV calculations was done using a pre-injection of contrast agent from the DCE acquisition and linear fitting to estimate the T1 contamination caused by extravasation of contrast agent. Both uncorrected and corrected CBV maps were generated.

Postprocessing of DCE Images

Three methods were used to process the DCE images: 1) without T1 correction, 2) T1 correction with a SMART₁Map acquisition, and 3) T1 correction with MOLLI acquisitions. The extended Tofts model was used in all cases. For all patients, DCE images were processed directly in the software (Olea Sphere 3.0) to generate maps of plasma volume (*Vp*) and volume transfer constant (*K*^{trans}). The SI was converted to percentage change in signal intensity (relSI) using the expression: $\text{relSI}(t) = 100 \times [S(t) - S_0] / S_0$,

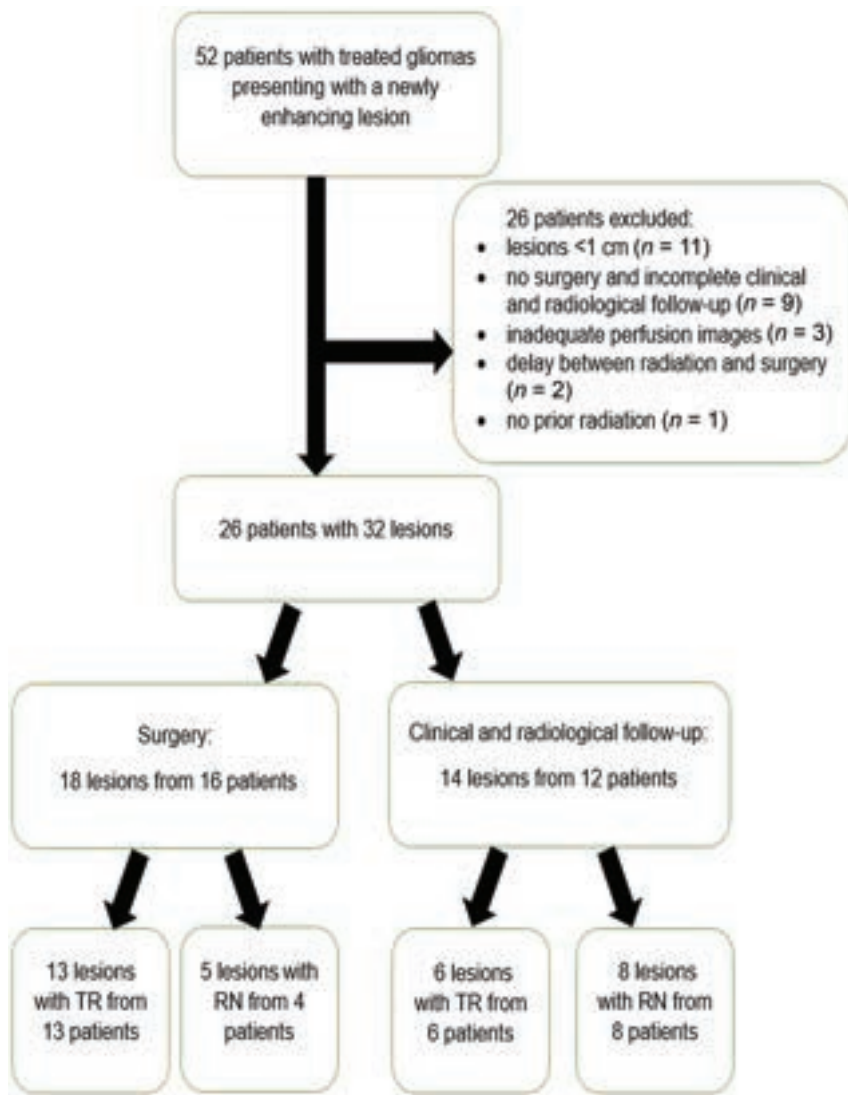


FIG 1. Flow chart of patients included and excluded in the study. Among the 26 patients included in the study, 6 patients had 2 lesions, 2 patients had 1 lesion with tumor recurrence (TR) and 1 lesion with radiation necrosis (RN), both confirmed with clinical/radiologic follow-up; 1 patient with 2 lesions with RN confirmed with surgery; 1 patient had 1 lesion with TR and 1 lesion with RN confirmed with surgery; 1 patient with 1 lesion with TR confirmed by surgery and 1 lesion with RN confirmed with clinical/radiology follow-up; 1 patient had 1 lesion with TR confirmed with surgery and 1 lesion with TR confirmed with clinical/radiologic follow-up.

where S is the SI at time t and S_0 is the baseline SI. The vascular input function was selected from a small ROI placed in the superior sagittal sinus directly from the DCE images. Signal conversion was set as SI to $\text{relSI}(\%)$. For patients who also had T1 mapping, the SI-versus-time curve was converted to gadolinium-versus-time using the T1 maps obtained before and after contrast from either the SMART₁Map or MOLLI acquisitions. This bookend T1 mapping has been described elsewhere.⁹ V_p and K^{trans} were then calculated for both T1-mapping techniques using the same Olea Sphere software.

Image Interpretation

A senior neuroradiologist trained a senior neuroradiology fellow on ROI placement and verified the technique. For each patient,

the fellow, who was blinded to the outcome, drew an ROI over the largest solid component of the newly enhancing lesion using axial T1-weighted postcontrast images avoiding adjacent vessels and cystic, necrotic, or hemorrhagic areas. This ROI was coregistered on all the other parametric maps. For the uncorrected CBV and corrected CBV maps, an additional ROI was placed in the contralateral unaffected white matter to obtain a ratio (normalized value). The mean value for each ROI on each parametric map was recorded.

Reference Standard

For patients who underwent resection of the newly enhancing lesions, a neuropathologist blinded to the imaging results assessed the presence and percentage of viable tumor and/or radiation necrosis in the surgical specimens. Visual assessment was performed under $\times 4$ high-power-field microscopy to determine the approximate percentage area of radiation necrosis or tumor recurrence relative to the whole-tissue area on all available slides. The following criteria were used for the diagnosis of radiation necrosis: the presence of coagulative necrosis and hyalinized vessels. For the diagnosis of recurrent tumor, we used the following criteria: the presence of increased cellularity and nuclear pleomorphism. In lesions in which there was a mixture of viable tumor and radiation necrosis, a lesion was categorized as tumor recurrence if the percentage of viable tumor was higher than the percentage of radiation necrosis.

For patients who did not undergo an operation, clinical and radiologic follow-up following the research MR imaging was used to classify the lesion as radiation necrosis or tumor recurrence. Two neuroradiologists, blinded to the perfusion analysis, assessed the change in the morphology and size of the enhancing lesion on the follow-up MR imaging using conventional and diffusion-weighted sequences. The presence of a centrally restricted diffusion pattern in an enhancing lesion was found to be associated with a treatment-related effect.¹⁰ Thus, our criteria for tumor recurrence were the following: 1) presence of a nodular or solid component that progressively increases in size with time; and 2) absence of restricted diffusion in the central area of necrosis on visual assessment of the $b = 1000$ images and the ADC map. Criteria for radiation necrosis were the following: 1) a peripheral rim of enhancement that remains stable or

Table 1: Clinical and characteristics of patient population^a

	Radiation Necrosis	Tumor Recurrence	P Value
Median age (yr) (95% CI)	54 (44–63.2)	59 (50.9–65.3)	.34
Female/male	13% (1/12)	21% (4/15)	.35
Initial tumor grade: grade 3, grade 4	0, 13	4, 15	.098
Median duration from radiation treatment to study MR imaging (days), (95% CI)	179 (142–462)	275 (191–915)	.066
% Lesions with resection	30% (5/13)	68% (13/19)	.27
Median duration from imaging to resection (days) (95% CI)	20	15 (13.5–26)	.96
Median Karnofsky score (range)	80 (75.3–90)	80 (70–90)	.43

^aPatients with 2 lesions are entered as 2 separate entries for the purpose of this table.

Table 2: Comparison of perfusion parameters for lesions diagnosed as tumor recurrence versus radiation necrosis

	Radiation Necrosis			Tumor Recurrence			P Value
	No.	Median	95% CI	No.	Median	95% CI	
CBF_AS_L (mL/100 g/min)	13	24.1	17.8–38.3	19	36.0	33.9–62.2	.003 ^a
rCBV	13	1.81	1.55–3.18	19	3.69	2.02–5.03	.058
Corrected rCBV	13	1.24	0.83–2.89	19	2.50	1.60–3.15	.048
k^{trans}_{SI} (min ⁻¹)	13	0.013	0.0062–0.039	19	0.019	0.011–0.048	.28
Vp_SI	13	0.16	0.12–0.29	19	0.27	0.21–0.39	.063
k^{trans}_{MOLLI} (min ⁻¹)	11	0.052	0.024–0.094	14	0.055	0.047–0.11	.44
Vp_MOLLI	11	0.17	0.13–0.28	14	0.28	0.20–0.41	.012
k^{trans}_{SMART} (min ⁻¹)	11	0.042	0.020–0.075	14	0.046	0.037–0.071	.48
Vp_SMART	11	0.12	0.082–0.23	14	0.21	0.15–0.33	.080

^aSignificance following Holm Bonferroni correction.

decreases in size, or 2) the presence of a central area of restricted diffusion on visual assessment of the $b = 1000$ images and the ADC map. The 2 neuroradiologists agreed on the classification of 12 of 14 lesions. Consensus reading was obtained for the remaining 2 lesions.

Statistical Analysis

For each lesion, the spatial coefficient of variation for each perfusion parameter was calculated as the SD of the parameter divided by the mean value of the parameter within the tumor ROI.¹¹

For certain continuous clinical variables (such as age and duration between MR imaging and the operation) and for each perfusion parameter, differences between the 2 patient groups were assessed via Mann-Whitney *U* tests. While *P* values < $\alpha = .05$ were considered statistically significant, a stepwise Holm Bonferroni procedure was applied to minimize the potential for type I errors due to multiple comparisons.¹² Associations between variables were investigated using the Spearman coefficients of rank correlation. Associations with coefficients of >0.8 were considered very strong; between 0.60 and 0.79, strong; between 0.40 and 0.59, moderate; and <0.39, weak. Receiver operator characteristic (ROC) curves were constructed for each variable and the area under each ROC was evaluated. Both the standard error of the area under each ROC curve and comparisons between areas under each ROC curve were evaluated using the method of DeLong et al.¹³ All data were analyzed using MedCalc (Version 12; MedCalc Software).

RESULTS

There were 52 patients who were prospectively enrolled in this study. We excluded the following patients: one patient had a recurrence but did not have prior radiation ($n = 1$); 2 patients had resection >3 months after the MR imaging ($n = 2$); 11 patients

had a newly enhancing lesion measuring <1 cm in maximal length ($n = 11$); 9 patients did not have resection and had short clinical and radiologic follow-up of <3 months duration ($n = 9$); and 3 patients were missing one of the perfusion imaging sequences ($n = 1$) or had perfusion imaging that did not cover the lesion ($n = 2$) (Fig 1). The clinical and demographic information for these 26 patients is listed in Table 1. In the final analysis, there were 32 lesions, with 6 patients having 2 lesions. Histopathology was obtained for 18 lesions with 13 lesions categorized as tumor recurrence (7 lesions with mixed pathology but a higher proportion of tumor and 6 lesions with only tumor) and 5 lesions categorized as radiation necrosis (3 lesions with mixed pathology but a higher proportion of radiation necrosis and 2 lesions with pure radiation necrosis). Clinical and radiologic follow-up was used to assess the outcome of 14 lesions (6 tumor recurrence, 8 radiation necrosis).

The mean area for the lesion ROI was 350.1 (SD, 263.6) mm². The mean area for the contralateral normal white matter was 34 (SD, 6.7) mm². For the 32 lesions, the mean spatial coefficient of variation for the ASL_perfusion-weighted values was 27.4%, which was lower than those derived from Vp_MOLLI (57.6%), Vp_SMART (60%), Vp_SI (53.8%), CBV (90.2%), and corrected CBV (70%).

For ASL perfusion imaging, the median CBF value was lower for patients with radiation necrosis (24.1 mL/100 g/min; 95% CI, 17.8–38.3 mL/100 g/min) compared with those with tumor recurrence (36.0 mL/100 g/min; 95% CI, 33.9–62.2 mL/100 g/min) (Table 2). For DSC perfusion imaging, the median corrected relative CBV (rCBV) was also lower for patients with radiation necrosis (1.24; 95% CI, 0.83–2.89) compared with patients with tumor recurrence (2.50; 95% CI, 1.60–3.15). There was a trend toward lower median uncorrected rCBV for patients with radiation necrosis (1.81; 95% CI, 1.55–3.18) compared with patients with

Table 3: Correlogram between different perfusion parameters using the Spearman rank correlation coefficient^a

	CBF_ASL (ml/100g/min)	rCBV	Corrected rCBV	Ktrans_SI (min ⁻¹)	Vp_SI	Ktrans_MOLLI (min ⁻¹)	Vp_MOLLI	Ktrans_SMART (min ⁻¹)	Vp_SMART
CBF_ASL (ml/100g/min)		0.195	0.542	0.503	0.581	0.633	0.769	0.655	0.593
rCBV	0.195		0.478	0.061	0.225	0.088	0.078	0.128	0.081
Corrected rCBV	0.542	0.478		0.286	0.552	0.441	0.642	0.476	0.549
Ktrans_SI (min ⁻¹)	0.503	0.061	0.286		0.784	0.829	0.594	0.788	0.394
Vp_SI	0.581	0.225	0.552	0.784		0.523	0.728	0.531	0.618
Ktrans_MOLLI (min ⁻¹)	0.633	0.088	0.441	0.829	0.523		0.636	0.981	0.506
Vp_MOLLI	0.769	0.078	0.642	0.594	0.728	0.636		0.653	0.766
Ktrans_SMART (min ⁻¹)	0.655	0.128	0.476	0.788	0.531	0.981	0.653		0.595
Vp_SMART	0.593	0.476	0.549	0.394	0.618	0.506	0.766	0.595	

^a Color coding is red for a very strong correlation ($r_s > 0.8$); orange for a strong correlation ($0.6 \leq r_s \leq 0.79$), yellow for a moderate correlation ($0.4 \leq r_s \leq 0.59$), and green for a weak correlation ($r_s < 0.4$).

tumor recurrence (3.69; 95% CI, 2.02–5.03) ($P = .058$). For DCE imaging, Vp_SI and K^{trans}_{SI} (derived from percentage change in signal intensity without T1 mapping) were not statistically significantly different between the 2 groups ($P = .063$ and $P = .28$, respectively, Table 2). For the subgroup of patients who underwent T1 mapping with either MOLLI or SMART₁Map sequences, exploratory analysis of 25 lesions (11 radiation necrosis and 14 tumor recurrence) revealed that Vp_MOLLI (derived from MOLLI T1 mapping) was lower for radiation necrosis than for tumor recurrence (0.17; 95% CI, 0.13–0.28 versus 0.28; 95% CI, 0.20–0.41). Vp_SMART (derived from SMART₁Map mapping), K^{trans}_{SMART} , and K^{trans}_{MOLLI} were not statistically significant between the 2 groups ($P = .08$, $P = .48$, and $P = .44$, respectively). Following the Holm Bonferroni stepwise correction for multiple comparisons ($n = 9$), CBF_ASL was the only perfusion parameter that remained statistically significantly different between the 2 groups ($P < .0055$).

The correlation between CBF_ASL and Vp_MOLLI was very strong ($r_s = 0.77$, $P < .001$, Table 3). Correlations between CBF_ASL and other DCE parameters (K^{trans}_{MOLLI} , K^{trans}_{SI} ,

K^{trans}_{SMART} , Vp_SI, and Vp_SMART) were moderate-to-strong (r_s between 0.50 and 0.66, $P \leq .004$). There was a moderate correlation between CBF_ASL and the corrected CBV ratio ($r_s = 0.54$, $P = .001$). Only a weak and insignificant correlation was found between CBF_ASL and the uncorrected CBV ratio ($r_s = 0.20$, $P = .29$).

In the differentiation between radiation necrosis and tumor recurrence, the diagnostic accuracy for CBF_ASL was good (AUC = 0.81; 95% CI, 0.64–0.98, Table 4). By means of the criterion of CBF > 30 mL/100 g/min, sensitivity was 0.84 (95% CI, 0.62–0.97) and specificity was 0.77 (95% CI, 0.46–0.95). Among the three lesions which were misclassified as false negatives with ASL, one case was likely due to ineffective labeling, because the CBF was lower in the entire right cerebral hemisphere compared with the left (Fig 2).

Compared with ASL-derived CBF, the diagnostic accuracies for uncorrected rCBV (AUC = 0.70; 95% CI, 0.52–0.89) and corrected rCBV (AUC = 0.71; 95% CI, 0.51–0.90, Table 4) were slightly lower, though these differences did not reach statistical significance ($P = .4$ and $P = .30$, respectively). By means of the

Table 4: Diagnostic accuracy of various parameters in the differentiation between tumor recurrence and radiation necrosis for all lesions (n=32 lesions) and for subgroup analysis of patients with DCE T1 mapping (n=25 lesions)^a

Parameters	No.	AUC (95% CI)	P Value	Optimal Threshold	Sensitivity (%)	Specificity (%)
ASL_CBF	32	0.81 (0.63–0.93)	<.001	>30 mL/100 g/min	84 (60–97)	77 (46–95)
rCBV	32	0.70 (0.52–0.89)	.033	>2.43	69 (43–87)	77 (46–95)
Corrected rCBV	32	0.71 (0.51–0.90)	.037	>1.54	79 (54–94)	69 (39–91)
K^{trans}_{SI}	32	0.61 (0.41–0.82)	.27	>0.0093 (min ⁻¹)	84 (60–97)	46 (19–75)
Vp_SI	32	0.69 (0.51–0.88)	.038	>0.18	79 (54–94)	62 (32–86)
K^{trans}_{SI}	25	0.66 (0.43–0.88)	.17	>0.0092 (min ⁻¹)	86 (57–98)	55 (23–83)
Vp_SI	25	0.68 (0.46–0.90)	.10	>0.18	79 (49–95)	64 (31–89)
K^{trans}_{MOLLI}	25	0.59 (0.36–0.82)	.44	>0.045 (min ⁻¹)	78 (49–95)	45 (17–77)
Vp_MOLLI	25	0.80 (0.62–0.98)	<.001	>0.19	86 (57–98)	63 (31–89)
K^{trans}_{SMART}	25	0.58 (0.34–0.83)	.49	>0.024 (min ⁻¹)	92 (66–1)	27 (6–61)
Vp_SMART	25	0.71 (0.49–0.88)	.057	>0.12	93 (66–1)	54 (23–83)

^aStatistics are listed with their 95% CI.

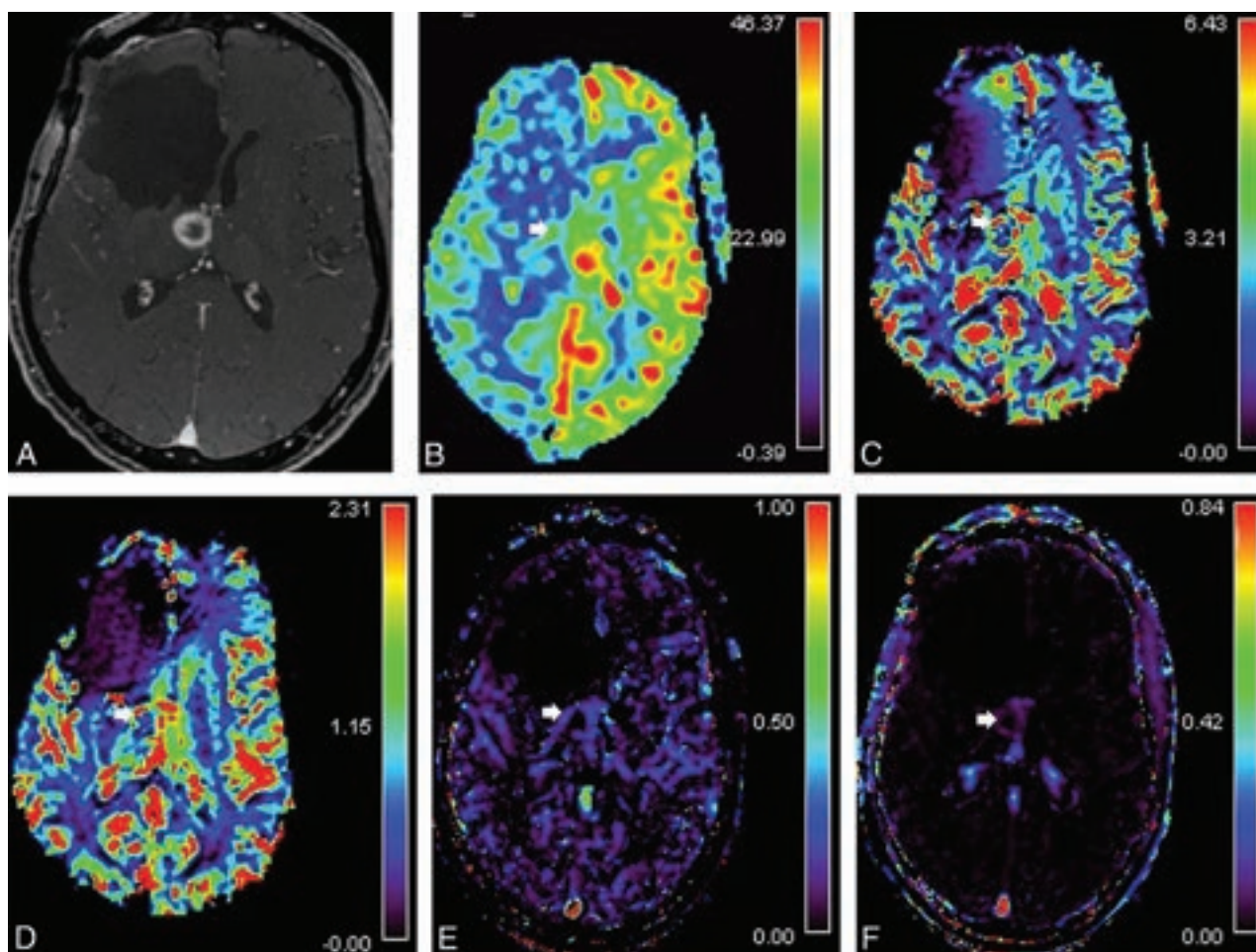


FIG 2. Sample of a case of recurrent glioblastoma multiforme with a false-negative ASL study due to probable ineffective labeling. Patient had a history of a right frontal grade IV glioma and had undergone resection and chemoradiation 3 years earlier. A, Axial T1-weighted image shows a newly enhancing lesion in the right anterior thalamus. B, ASL-derived CBF reveals a low CBF value in the enhancing lesion (arrow). The CBF in the right hemispheric cortex is lower than on the left side, presumably due to ineffective labeling from dental hardware. DSC MR imaging demonstrates a high, uncorrected rCBV value (C) and leakage-corrected rCBV value (D) at the rim of the enhancing lesion (arrow). DCE MR imaging using MOLLI T1 mapping shows high Vp (E) and K^{trans} (F) values in the lesion (arrows). Pathology confirmed glioblastoma recurrence.

criterion of rCBV > 2.43, sensitivity was 0.69 (95% CI, 0.43–0.87) and specificity was 0.77 (95% CI, 0.46–0.95). By means of the criterion of corrected rCBV > 1.54, sensitivity was 0.79 (95% CI, 0.54–0.94) and specificity was 0.69 (95% CI, 0.39–0.91). Among the 4 patients with false-negative findings, 1 patient had a right temporal lesion that was obscured by susceptibility artifacts on

the CBV map from DSC but was correctly identified on the CBF map from ASL and DCE MR imaging (Fig 3).

For patients who underwent DCE imaging with T1 mapping, Vp derived from MOLLI had the best diagnostic accuracy (AUC = 0.80; 95% CI, 0.62–0.98), which was statistically higher than that of K^{trans}_{MOLLI} (AUC = 0.59; 95% CI, 0.36–0.82)

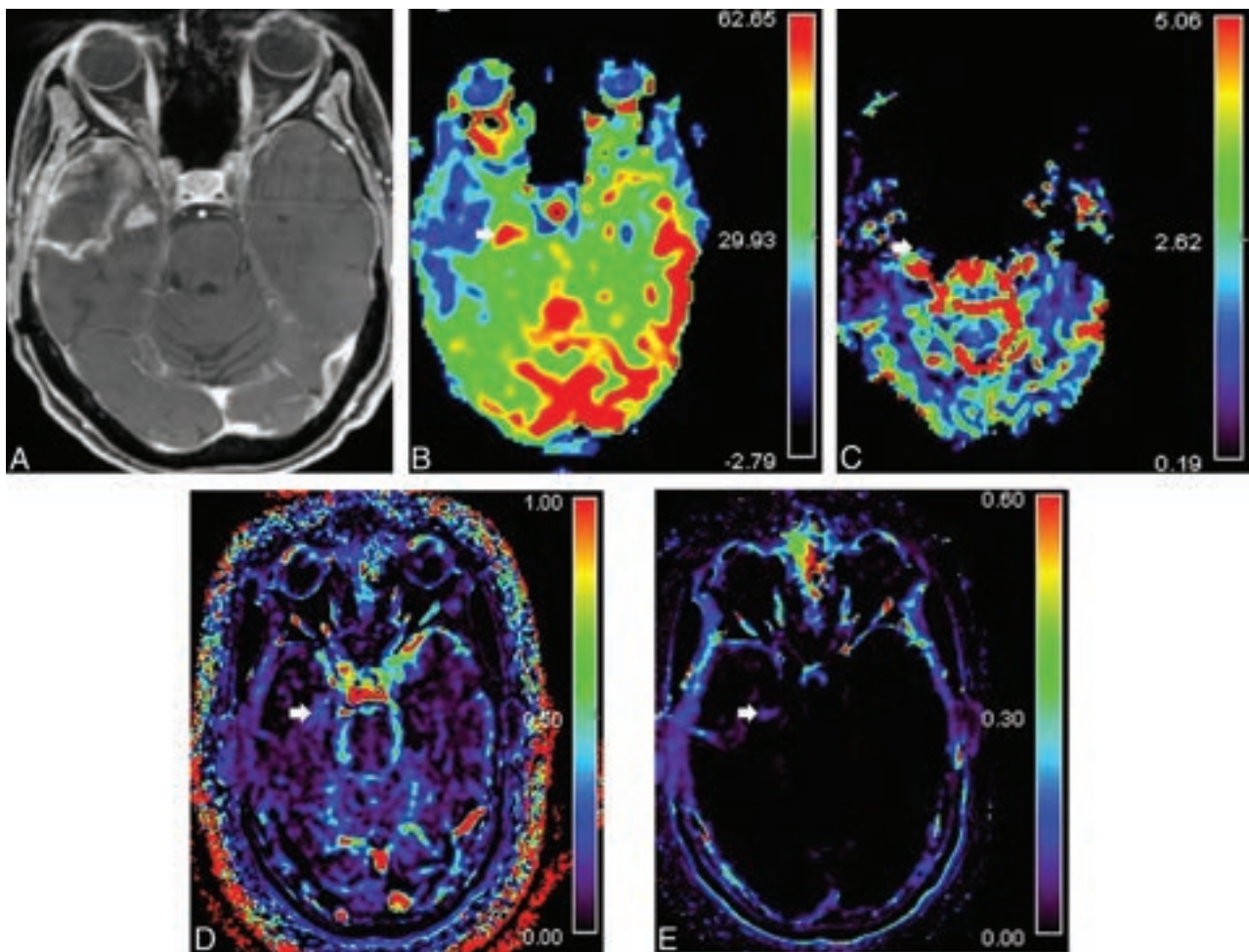


FIG 3. Example of a case of recurrent glioblastoma multiforme with a false-negative DSC study due to susceptibility artifacts. *A*, Axial T1-weighted image shows a newly enhancing lesion in the right mesial temporal lobe. *B*, ASL-derived CBF map demonstrates a marked increase in CBF in the lesion (*arrow*). *C*, Corrected CBV map is unreliable in the tumoral region due to susceptibility artifacts (*arrow*). DCE MR imaging performed without T1 mapping reveals high Vp (*D*) and K^{trans} (*E*) values in the lesion (*arrow*), which correlate with the high CBF value.

and $K^{\text{trans}}_{\text{SMART}}$ (AUC = 0.58; 95% CI, 0.34–0.83) ($P = .04$ and $P = .035$, respectively). The diagnostic accuracy of Vp_SI (AUC = 0.68; 95% CI, 0.46–0.90), Vp_SMART (AUC = 0.71; 95% CI, 0.49–0.88), and $K^{\text{trans}}_{\text{SI}}$ (AUC = 0.66; 95% CI, 0.43–0.88) was lower than that for Vp_MOLLI, though this did not reach statistical significance ($P > .05$). Using a criterion of Vp_MOLLI > 0.19 , sensitivity was 0.86 (95% CI, 0.57–0.98) and specificity was 0.63 (95% CI, 0.31–0.89).

DISCUSSION

The results of this prospective study suggest that ASL-derived CBF measurements offer a degree of accuracy similar to that of DSC-derived CBV measurements in differentiating tumor recurrence and radiation necrosis. Our results are in line with those of prior studies published in the literature. A meta-analysis by Wang et al³ revealed a pooled sensitivity of 79% and specificity of 78% for ASL. Two other studies not included in that meta-analysis reported sensitivities of 92% and 100% and specificities of 93% and 88%.^{14,15} Manning et al¹⁴ reported that 6 lesions located near the skull base were correctly identified by ASL but were misclassified by DSC MR imaging because of susceptibility artifacts. We

had 1 such patient in our study in whom the tumor was misclassified by DSC because of susceptibility artifacts due to the temporal bone but was correctly identified by ASL. However, ASL perfusion might also be affected by susceptibility artifacts at the skull base or in the neck, which can cause poor labeling. There was 1 patient with a thalamic lesion that was misclassified on ASL due to probable poor labeling but correctly identified on CBV derived from DSC. Thus, differences in the reported diagnostic accuracy of ASL and DSC imaging in the literature might be influenced by the inclusion or exclusion of cases with susceptibility artifacts in the study. Use of ASL perfusion has many advantages in the clinical workflow: absence of gadolinium injection, reasonable acquisition time (< 5 minutes), relative standardization of the acquisition methods, and minimal postprocessing time. A consensus article by the International Society of Magnetic Resonance in Medicine perfusion study group and the European Consortium for ASL in Dementia recommended the use of a 3D multiecho segmented readout scheme with the pCASL labeling method on a 3T MR imaging scanner. CBF maps are usually calculated directly from the MR imaging console without the need for additional off-line postprocessing and are immediately sent to the PACS for clinical review.

In the differentiation between tumor recurrence and radiation necrosis using DCE imaging, we have found that plasma volume was more accurate than K^{trans} . A systematic review and meta-analysis found that K^{trans} had a pooled sensitivity of 0.75 and specificity of 0.79 in the diagnosis of tumor recurrence versus treatment-related changes.¹⁶ However, some authors have reported lower sensitivities for K^{trans} (0.62 and 0.51, respectively), which are in agreement with our study.^{17,18} Bolcaen et al¹⁹ found higher wash-in and washout rates on the dynamic contrast-enhancement curves in rats with glioblastoma versus those with radiation necrosis, but no difference in K^{trans} was found between the 2 groups. They believed that K^{trans} measurements in their study could have been biased because the commercial software performed a voxel-by-voxel analysis for each parameter, which can introduce more noise than performing the calculation on a number of pixels inside a specific ROI.

Our study suggests that the diagnostic accuracy of Vp in the differentiation of glioma recurrence from radiation necrosis can be improved with the use of a T1-mapping technique, such as the Look Locker method, compared with a method that does not use any T1 mapping. Current recommendations by Quantitative Imaging Biomarkers MRI Biomarker Committee suggest the use of a variable flip angle technique for T1 mapping, which is more readily available than the MOLLI sequence. However, the MOLLI technique might offer higher reproducibility than the variable flip angle technique.²⁰ Alternatively, a model-independent analysis based on the integration of the signal intensity curve across time as proposed by Hamilton et al²¹ could provide diagnostic accuracy similar to that of more complex model-dependent analysis, which requires T1 mapping.

A major limitation of our study is the small sample size, which might not have allowed us to detect a statistical difference in the diagnostic accuracy between ASL and DSC/DCE imaging. A second limitation is the lack of direct spatial correlation between the ROI measurements on perfusion maps with histopathologic findings. There is a risk of misclassification because the ROI might not match the resected area. In our study, we tried to mitigate this risk by obtaining an ROI over the entire enhancing lesion rather than a small hot-spot ROI within the enhancing lesion because most of the enhancing lesion was usually resected at surgery and sent to pathology at our institution.

CONCLUSIONS

In patients with high-grade gliomas who developed a newly enhancing lesion following standard chemoradiation treatment, the accuracy of ASL-derived CBF is similar to that of DSC and DCE-derived blood volume for the differentiation of tumor recurrence from radiation necrosis.

Disclosure forms provided by the authors are available with the full text and PDF of this article at www.ajnr.org.

REFERENCES

- Mullins ME, Barest GD, Schaefer PW, et al. **Radiation necrosis versus glioma recurrence: conventional MR imaging clues to diagnosis.** *AJNR Am J Neuroradiol* 2005;26:1967–72 Medline
- van Dijken BR, van Laar PJ, Holtman GA, et al. **Diagnostic accuracy of magnetic resonance imaging techniques for treatment response evaluation in patients with high-grade glioma: a systematic review and meta-analysis.** *Eur Radiol* 2017;27:4129–44 CrossRef Medline
- Wang L, Wei L, Wang J, et al. **Evaluation of perfusion MRI value for tumor progression assessment after glioma radiotherapy: a systematic review and meta-analysis.** *Medicine (Baltimore)* 2020;99:e23766 CrossRef Medline
- Wang YL, Chen S, Xiao HF, et al. **Differentiation between radiation-induced brain injury and glioma recurrence using 3D pCASL and dynamic susceptibility contrast-enhanced perfusion-weighted imaging.** *Radiother Oncol* 2018;129:68–74 CrossRef Medline
- Choi YJ, Kim HS, Jahng GH, et al. **Pseudoprogression in patients with glioblastoma: added value of arterial spin labeling to dynamic susceptibility contrast perfusion MR imaging.** *Acta Radiol* 2013;54:448–54 CrossRef Medline
- Ozsunar Y, Mullins ME, Kwong K, et al. **Glioma recurrence versus radiation necrosis? A pilot comparison of arterial spin-labeled, dynamic susceptibility contrast enhanced MRI, and FDG-PET imaging.** *Acad Radiol* 2010;17:282–90 CrossRef Medline
- Alsop DC, Detre JA, Golay X, et al. **Recommended implementation of arterial spin-labeled perfusion MRI for clinical applications: a consensus of the ISMRM perfusion study group and the European consortium for ASL in dementia.** *Magn Reson Med* 2015;73:102–16 CrossRef Medline
- Cron G, Gulak MA, Majtenyi N, et al. **MOLLI versus SMART1 mapping for quantitative brain tumor DCE MRI on a 3T GE 750w: initial experience.** In: *Proceedings of the Annual Meeting and Exhibition of the International Society of Magnetic Resonance in Medicine*, Montreal, Quebec, Canada. May 16, 2019 (abstract 2903)
- Footitt C, Cron GO, Hogan MJ, et al. **Determination of the venous output function from MR signal phase: feasibility for quantitative DCE-MRI in human brain.** *Magn Reson Med* 2010;63:772–81 CrossRef Medline
- Zakhari N, Taccone MS, Torres C, et al. **Diagnostic accuracy of centrally restricted diffusion in the differentiation of treatment-related necrosis from tumor recurrence in high-grade gliomas.** *AJNR Am J Neuroradiol* 2018;39:260–64 CrossRef Medline
- Mutsaerts HJ, Petr J, Václavů L, et al. **The spatial coefficient of variation in arterial spin labeling cerebral blood flow images.** *J Cereb Blood Flow Metab* 2017;37:3184–92 CrossRef Medline
- Holm S. **A simple sequentially rejective multiple test procedure.** *Scandinavian Journal of Statistics* 1979;6:65–70
- DeLong ER, DeLong DM, Clarke-Pearson DL. **Comparing the areas under two or more correlated receiver operating characteristic curves: a nonparametric approach.** *Biometrics* 1988;44:837–45 CrossRef Medline
- Manning P, Daghighi S, Rajaratnam MK, et al. **Differentiation of progressive disease from pseudoprogression using 3D PCASL and DSC perfusion MRI in patients with glioblastoma.** *J Neurooncol* 2020;147:681–90 CrossRef Medline
- Jovanovic M, Radenkovic S, Stosic-Opincal T, et al. **Differentiation between progression and pseudoprogression by arterial spin labeling MRI in patients with glioblastoma multiforme.** *J BUON* 2017;22:1061–67 Medline
- Okuchi S, Rojas-Garcia A, Ulyte A, et al. **Diagnostic accuracy of dynamic contrast-enhanced perfusion MRI in stratifying gliomas: a systematic review and meta-analysis.** *Cancer Med* 2019;8:5564–73 CrossRef Medline
- Seeger A, Braun C, Skardelly M, et al. **Comparison of three different MR perfusion techniques and MR spectroscopy for multiparametric assessment in distinguishing recurrent high-grade gliomas from stable disease.** *Acad Radiol* 2013;20:1557–65 CrossRef Medline
- Zakhari N, Taccone MS, Torres CH, et al. **Prospective comparative diagnostic accuracy evaluation of dynamic contrast-enhanced (DCE) vs. dynamic susceptibility contrast (DSC) MR perfusion in differentiating**

- tumor recurrence from radiation necrosis in treated high-grade gliomas. *J Magn Reson Imaging* 2019;50:573–82 CrossRef Medline
19. Bolcaen J, Descamps B, Acou M, et al. **In vivo DCE-MRI for the discrimination between glioblastoma and radiation necrosis in rats.** *Mol Imaging Biol* 2017;19:857–66 CrossRef Medline
20. Bane O, Hectors SJ, Wagner M, et al. **Accuracy, repeatability, and interplatform reproducibility of T₁ quantification methods used for DCE-MRI: results from a multicenter phantom study.** *Magn Reson Med* 2018;79:2564–75 CrossRef Medline
21. Hamilton JD, Lin J, Ison C, et al. **Dynamic contrast-enhanced perfusion processing for neuroradiologists: model-dependent analysis may not be necessary for determining recurrent high-grade glioma versus treatment effect.** *AJNR Am J Neuroradiol* 2015;36:686–93 CrossRef Medline

Radiation-Induced Changes Associated with Obliteration of Brain AVMs after Repeat Radiosurgery

T. Sasagasako, H. Mori, E.Y.Hattori, T. Ikedo, E. Hamano, K. Shimonaga, Y. Kushi, K. Iihara, and H. Kataoka



ABSTRACT

BACKGROUND AND PURPOSE: Radiation-induced changes can occur after stereotactic radiosurgery for brain AVMs, potentially causing symptomatic complications. We evaluated the incidence of such changes and the efficacy of repeat gamma knife radiosurgery for incompletely obliterated AVMs.

MATERIALS AND METHODS: We retrospectively evaluated 150 patients who underwent gamma knife radiosurgery for AVMs between 2002 and 2020; twenty-five underwent further radiosurgical procedures for incompletely obliterated AVMs. We recorded the median margin doses at the first (median, 20 Gy; range, 12–23 Gy; AVM volume, 0.026–31.3 mL) and subsequent procedures (median, 18 Gy; range, 12–23 Gy; AVM volume, 0.048–9.2 mL).

RESULTS: After the first treatment, radiologic radiation-induced changes developed in 48 (32%) patients, eight of whom had symptomatic changes. After repeat gamma knife radiosurgery, 16 of 25 patients achieved complete AVM obliteration (64%). The development of radiation-induced changes after the first treatment was significantly associated with successful obliteration by subsequent radiosurgery (OR = 24.0, 95% CI 1.20–483, $P = .007$). Radiation-induced changes occurred in only 5 (20%) patients who underwent a second gamma knife radiosurgery, one of whom experienced transient neurologic deficits. Between the first and repeat gamma knife radiosurgery procedures, there was no significant difference in radiologic and symptomatic radiation-induced changes ($P = .35$ and $P = 1.0$, respectively).

CONCLUSIONS: Radiation-induced changes after the first gamma knife radiosurgery were associated with AVM obliteration after a repeat procedure. The risk of symptomatic radiation-induced changes did not increase with retreatment. When the first procedure fails to achieve complete AVM obliteration, a favorable outcome can be achieved by a repeat gamma knife radiosurgery, even if radiation-induced changes occur after the first treatment.

ABBREVIATIONS: GKRS = gamma knife radiosurgery; RICs = radiation-induced changes

Gamma knife radiosurgery (GKRS) is a standard treatment for patients with intracranial AVMs. Total obliteration rates vary from 60% to 80% during the 3- to 5-year period after the first GKRS procedure.^{1,2} If the first procedure fails to achieve complete obliteration, the hemorrhage risk will persist.³ Additional treatments may include repeat GKRS, resection, endovascular embolization, or any combination thereof.

The most frequent complications after GKRS for AVMs are radiation-induced changes (RICs), which typically occur 6–18 months after treatment and before AVM occlusion.⁴ These

manifest on follow-up MR imaging as perinidal T2WI radiographic changes.⁵ Although most RICs are asymptomatic, some are accompanied by focal neurologic deficits.^{4,6} We do not know if the risk of symptomatic RICs is greater after repeat GKRS than after the first treatment.⁷ The relationship between RICs and AVM obliteration is also unclear. We addressed these questions through a retrospective review of repeat GKRS outcomes in patients with AVM and histories of RICs after the first treatment. We evaluated RIC incidence, factors associated with total obliteration, and hemorrhage risk.

MATERIALS AND METHODS

Patient Population

The National Cerebral and Cardiovascular Center's ethics committee approved this study (M30-013). We retrospectively reviewed consecutive patients with AVMs treated with GKRS at our institution between January 2002 and December 2020. This study

Received August 26, 2022; accepted after revision December 30.

From the National Cerebral and Cardiovascular Center, Suita, Osaka, Japan.

Please address correspondence to Hisae Mori, MD, Department of Neurosurgery, National Cerebral and Cardiovascular Center, 6-1 Kishibe Shimmachi, Suita, Osaka 564-8565, Japan; e-mail: himori@ncvc.go.jp

 Indicates article with online supplemental data.

<http://dx.doi.org/10.3174/ajnr.A7772>

excluded patients who had been treated by volume-staged GKRS or who had <1 year of follow-up.

We additionally included patients who died of cerebral hemorrhage during follow-up without an MRA because they presumably had patent AVMs.

Radiosurgical Technique

All GKRS procedures were performed using a Leksell Gamma Knife model B (2002–2009), model 4C (2009–2019), or Icon (2020) (Elekta). Patients underwent biplane stereotactic angiography, 1.5T MR T2WI, TOF, and CT for dose planning. This plan was designed to minimize the risk of radiation-induced complications as predicted by the nidus volume and the radiosensitivity of the brain location.

The marginal dose was planned as 50% of the maximum prescription dose and included the entire AVM nidus volume. The median prescription dose delivered to the nidus margin was 20 Gy (range, 12–23 Gy); the median AVM volume was 3.51 mL (range, 0.026–31.3 mL) for the first GKRS. For repeat procedures, the median prescription dose was 18 Gy (range, 12–23 Gy) and the median AVM volume was 0.77 mL (range, 0.048–9.2 mL).

When the AVM volume exceeded 10 mL, planned volume-staged GKRS was considered. The total AVM nidus volume was outlined on MR imaging and divided into approximately equal volumes based on anatomic landmarks such as major feeding arteries. The second procedure was scheduled 3–6 months after the first treatment.

In principle, repeat GKRS was considered if the AVM was patent 3–4 years after the first procedure and if there were no AVM composition changes evident on MR imaging. If the MR imaging follow-up showed an ongoing obliteration process, there should be a 5-year waiting period for additional treatment after the initial GKRS. In the present study, there were no AVM shrinkage cases >5 years after the initial GKRS. Direct surgery, with or without embolization, was considered in cases with persistent dural feeders or bleeding after the first GKRS.

Patient Outcomes and Data Collection

We recorded each patient's age, sex, follow-up period, rupture history, Spetzler-Martin grade, previous embolization, AVM score, venous drainage, AVM location, AVM volume, and radiation dose.⁸ The modified Pollock-Flickinger AVM grading score was calculated as follows: Score = (0.1) (Volume in mL) + (0.02) (Age in Years) + (0.5) (Location: Basal Ganglia, Thalamus, or Brainstem = 1, Others = 0).⁹ The statistical end points were complete AVM nidus obliteration, RIC development, delayed cyst formation, and hemorrhage. The volume change ratio was calculated as follows: Target Volume at the First GKRS/Target Volume at Repeat GKRS.¹⁰

After GKRS, MRAs and MRIs were reviewed every 3–4 months. T2WI and FLAIR hyperintensity images were assessed on brain MR imaging. RICs were defined as new lesions with increased T2WI or as FLAIR imaging changes surrounding the treated nidus. Radiologic RICs included any MR imaging evidence of perinidal T2-weighted hyperintensities post-GKRS. Symptomatic RICs were considered radiologic RICs associated

with new or worsening neurologic symptoms. In this study, unless otherwise specified, RICs refers to radiologic RICs.

If MR imaging/MRA findings in patients with at least a 1-year follow-up were consistent with obliteration, then cerebral angiography was requested to confirm the obliteration. A few study patients refused to undergo follow-up conventional angiography. For those patients, obliteration was evaluated on the basis of the most recent MR imaging results. On the MR imaging/MRA study, total AVM obliteration after radiosurgery was defined as the complete absence of the former nidus based on T2-weighted imaging and 3D-TOF MRA.

Statistical Analysis

All statistical analyses were performed using EZR software (<https://www.jichi.ac.jp/saitama-sct/SaitamaHP.files/windowsEN.html>).¹¹ Kaplan-Meier survival analysis was performed to calculate obliteration and hemorrhage rates. The log-rank test was used to assess survival curve differences. Univariate analysis was used to evaluate patient characteristics at the first and repeat GKRS and relevant factors affecting total AVM obliteration. In detail, the Fisher exact test was performed to assess the following: 1) the male/female ratio, 2) the relationship between obliteration and AVM characteristics (rupture, deep drainage, location, eloquent cortex within adjacent brain tissue, prior embolization, >50% reduction in volume after the first GKRS, and RICs), and 3) incidences of RIC or cyst formation after the first and repeat GKRS. The Mann-Whitney *U* test was used to evaluate the relationship between obliteration and continuous data describing AVM characteristics (AVM score, AVM volume, and margin dose) and the AVM volume change ratio after the first and repeat GKRS. Continuous data are expressed as the mean (SD). *P* values < .05 were considered statistically significant. We performed the calculations for diagnosis-to-first GKRS, first GKRS-to-obliteration or repeat treatment, and post-repeat-GKRS periods. The annual hemorrhage rate was calculated as the hemorrhagic events number during the predefined period divided by the sum of the duration of individual observation periods.

RESULTS

Patient Demographics

During the study period, 175 patients with 178 AVMs underwent GKRS in our department. Of these, 4 patients had been treated by volume-staged GKRS and were excluded from this study. Moreover, 21 patients with 24 AVMs were excluded due to follow-up durations of <1 year (*n* = 9) and incomplete clinical data (*n* = 12). This exclusion left 150 patients with 150 AVMs in the first GKRS group. Complete obliteration following the first GKRS was achieved in 104 (67.5%) patients. Of the 46 patients with incomplete obliteration, 25 underwent repeat GKRS (repeat GKRS group). Four patients underwent surgery after the first GKRS, 3 for nidus removal due to rupture of the residual nidus and 1 for an AVF. Eight patients refused additional treatment, and 7 patients were lost to follow-up (Online Supplemental Data). Two patients died due to hemorrhage.

The median ages of the first and repeat GKRS groups were 37 (range, 9–79) and 39 (range, 14–69) years, respectively (Table 1).

The median follow-up durations after the first and repeat GKRS were 102 (range, 15–221 months) and 79 months (range, 22–209 months), respectively. On average, repeat GKRS was performed 58 months (range, 36–94 months) after the first procedure.

AVM Characteristics

Before diagnosis, 53 AVMs (35.3%) presented with hemorrhage (Table 2). The Spetzler-Martin grades were grade I/II in 80 (53.3%) and grades III/IV/V in 70 (46.7%). The median AVM score was 1.19 (range, 0.289–3.92). The AVMs were located in cerebral lobar ($n = 112$; 74.7%), thalamus/basal ganglia/brainstem ($n = 22$; 14.7%), and cerebellar ($n = 16$; 10.7%) regions; notably,

82 (54.6%) were present in eloquent areas.⁸ The median AVM volume was 3.51 mL (range, 0.026–31.3 mL).

At the time of repeat GKRS, 18 AVMs (72%) had hemorrhage histories (Table 3). Among these patients, one had a hemorrhage before and after the first treatment and one had a hemorrhage after the first procedure with no previous bleeding history. The Spetzler-Martin grades were grade I/II in 5 (20%) and grade III/IV/V in 20 (80%). The median AVM score was 1.17 (range, 0.320–2.20). The AVMs requiring repeat GKRS were located in cerebral lobar ($n = 13$; 52%), thalamus/basal ganglia/brainstem ($n = 10$; 40%), and cerebellar regions ($n = 2$; 8%); 17 (68%) were present in eloquent areas. The median AVM volume was 0.77 mL (range, 0.048–9.2).

Table 1: The demographics of patients with AVMs of the brain at initial and repeat GKRS

	Initial GKRS	Repeat GKRS	P Value
No.	150	25	
Male (No.) (%)	85 (56.7)	10 (40)	.12
Median age (range) (yr)	37 (9–79)	39 (14–69)	.55
Median follow-up after each GKRS (range) (mo)	102 (15–221)	79 (22–209)	.01
Median interval between the initial and repeat GKRS (range) (mo)	–	58 (36–94)	–

Note:—The dash (–) indicates not applicable.

Outcomes of the First GKRS

Of the 150 patients, 104 achieved complete obliteration (69.3%) after the first GKRS. Of these, 64 were confirmed by catheter DSA. The overall obliteration rates 4, 5, 7, and 10 years after the first GKRS were 49.7%, 65.8%, 80.1%, and 97.0% (Online Supplemental Data). Univariate analysis demonstrated that

Table 2: AVM characteristics and factors associated with obliteration at initial GKRS

	Total No. ($n = 150$)	Obliteration ($n = 104$) (69.3%)	Incomplete Obliteration ($n = 46$) (30.7%)	P Value
Rupture (No.) (%)	53 (35.3)	33 (31.7)	20 (43.5)	.13
Spetzler-Martin grade (No.) (%)				<.001
I/II	80 (53.3)	68 (65.4)	12 (26.1)	
III/IV/V	70 (46.7)	36 (34.6)	34 (73.9)	
Median AVM score (range)	1.19 (0.289–3.92)	1.16 (0.289–2.23)	1.28 (0.302–3.92)	.05
Deep drainage (No.) (%)	86 (57.3)	54 (52.0)	32 (69.6)	.04
Location (No.) (%)				.016
Lobar	112 (74.7)	80 (76.9)	32 (69.6)	
Thalamus/basal ganglia/brainstem	22 (14.7)	10 (9.6)	12 (26.1)	
Cerebellum	16 (10.7)	14 (13.5)	2 (4.3)	
Eloquent cortex of adjacent brain (No.) (%)	82 (54.6)	50 (48.1)	32 (69.6)	.02
Prior embolization (No.) (%)	15 (10.0)	10 (9.6)	5 (10.9)	.77
Median AVM volume (range) (mL)	3.51 (0.026–31.3)	1.51 (0.026–13.6)	3.6 (0.027–31.3)	.007
Median margin dose (range) (Gy)	20 (12–23)	20 (12–23)	18 (12–23)	<.001

Table 3: AVM characteristics and factors associated with obliteration after repeat GKRS

	Total No. ($n = 25$)	Obliteration ($n = 16$) (64%)	Incomplete Obliteration ($n = 9$) (36%)	P Value
Rupture (No.) (%)	18 (72)	11 (69)	7 (78)	1.0
Spetzler-Martin grade (No.) (%)				.62
I/II	5 (20)	4 (25)	1 (11)	
III/IV/V	20 (80)	12 (75)	8 (89)	
Median AVM score (range)	1.17 (0.320–2.20)	1.25 (0.675–2.20)	0.86 (0.320–1.95)	.12
Deep drainage (No.) (%)	17 (72)	10 (63)	7 (78)	.66
Location (No.) (%)				.85
Lobar	13 (52)	9 (57)	4 (44)	
Thalamus/basal ganglia/brainstem	10 (40)	6 (38)	4 (33)	
Cerebellum	2 (12)	1 (6.3)	1 (11)	
Eloquent cortex of adjacent brain (No.) (%)	17 (68)	11 (69)	6 (67)	1.0
Prior embolization (No.) (%)	6 (25)	4 (25)	2 (22)	1.0
Median AVM volume at initial GKRS (range) (mL)	3.70 (0.03–31.3)	4.90 (0.06–31.3)	3.5 (0.42–12.3)	.80
Median AVM volume at repeat GKRS (range) (mL)	0.77 (0.048–9.2)	0.59 (0.054–9.2)	0.77 (0.048–4.1)	.93
Median margin dose (range) (Gy)	18 (14–20)	20 (14–20)	18 (16–20)	.36
>50% Reduction in volume after initial GKRS (No.) (%)	19 (76)	12 (75)	7 (77.8)	1.0

Table 4: The relationship between the development of RICs and AVM obliteration after each GKRS

	Obliteration	Incomplete Obliteration	P Value
Initial GKRS (No.)	104	46	
RICs (No.) (%)	34 (32.7)	16 (34.8)	.85
Repeat GKRS (No.)	16	9	
Radiologic RICs after initial GKRS (No.) (%)	9 (56.3)	0 (0)	.007
Radiologic RICs after repeat GKRS(No.) (%)	3 (18.8)	2 (22.2)	1.0

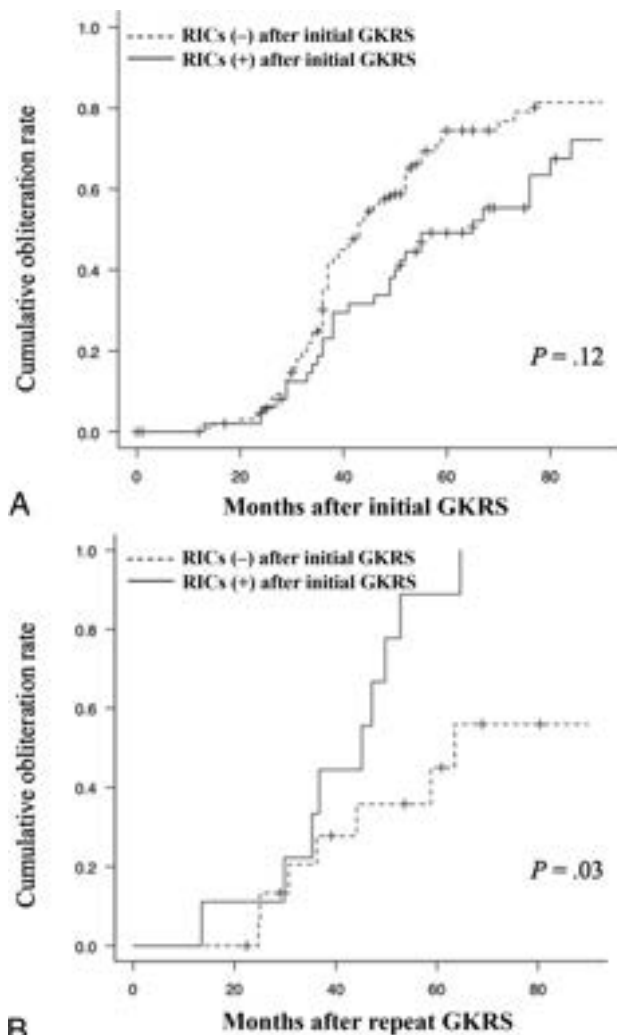


FIG 1. A, Kaplan-Meier curve for the obliteration of AVMs after the first GKRS. Cumulative complete obliteration of AVMs after the first GKRS with or without the development of RICs. RIC development was not significantly associated with AVM obliteration ($P = .12$). The dotted line represents AVMs without RICs (-), and the solid line, those with RICs (+). B, Cumulative obliteration of AVMs after repeat GKRS with or without the development of RICs after the first GKRS. The development of RICs was significantly associated with AVM obliteration ($P = .03$).

complete obliteration was associated with Spetzler-Martin grade ($P < .001$), deep drainage ($P = .04$), lesions within eloquent areas of adjacent brain cortex ($P = .02$), AVM volume ($P = .007$), and prescribed margin dose ($P < .001$) (Table 2). Location was also

significantly related to AVM obliteration ($P = .016$) because a Bonferroni correction found $P < .017$ to be statistically significant.

After the first GKRS, RICs occurred in 50 patients (33.3%). Table 4 shows the relationship between RIC and AVM obliteration. Of the 104 patients who achieved AVM obliteration after the first GKRS, 34 (32.7%) developed RICs. Of the 46 with incomplete obliteration, 16 (34.8%) developed RICs. Thus, RIC development after the first GKRS appeared not to be related to AVM obliteration (OR = 0.91; 95% CI, 0.44–1.89; $P = .85$). Kaplan-Meier analysis also revealed that RICs were not significantly related to obliteration after the first GKRS ($P = .12$) (Fig 1A). In 50 patients with incomplete obliteration after the first treatment, 25 patients with 25 AVMs underwent repeat GKRS.

Outcome and Obliteration Predictors of Repeat GKRS

After repeat GKRS, 16 (64%) of the 25 patients with 25 AVMs achieved complete obliteration. Among these 16 patients, 3 were confirmed by DSA and 13 were diagnosed on the basis of MR imaging/MRA. The median interval between the first and repeat GKRS was 58 months (range, 36–94 months), and the median follow-up after repeat radiosurgery was 79 months (range, 22–209 months) (Table 1). Of the 18 (72%) patients with ruptured AVMs at the repeat GKRS, 1 had hemorrhaged after the first GKRS with no bleeding history before the first procedure. Overall obliteration 4, 5, and 7 years after repeat GKRS was achieved in 50.5%, 65.4%, and 76.9% (Online Supplemental Data). There was no significant difference in the latency period before obliteration between the first and repeat GKRS procedures ($P = .77$).

Among 16 patients without RIC histories after the first GKRS, 7 (43.8%) achieved complete obliteration after the repeat procedure. On the other hand, 9 patients who underwent repeat GKRS had histories of RIC after the first treatment; all these patients achieved complete obliteration (OR = 24.0; 95% CI, 1.2–489; $P = .007$) (Table 4). Five patients showed RICs after repeat GKRS. Three of these 5 patients achieved complete obliteration. RIC development after repeat GKRS had no significant relationship with obliteration ($P = 1.0$).

Kaplan-Meier analysis found that patients with AVMs who developed RICs after the first GKRS had a significantly higher obliteration rate after a repeat procedure ($P = .03$) (Fig 1B). After repeat GKRS, the complete obliteration rates at 4, 5, and 7 years were 36.8%, 45.8%, and 56.7% for patients without RICs after the first GKRS and 66.7%, 88.9%, and 100% for those with RICs after the first GKRS. Factors associated with AVM obliteration after the first treatment (ie, Spetzler-Martin grade, deep drainage, location, eloquent cortex of the adjacent brain, AVM volume, and margin dose) were not significantly related to obliteration after repeat GKRS (Table 3). Among patients with repeat GKRS, the median AVM volume change rate after the first treatment was 21.1% (range, 3.18%–231%) (Fig 2). The median AVM volume change rates were 32.2% (range, 6.9%–205%) for patients without RICs ($n = 16$) and 10.2% (range, 3.18%–231%) for those with RICs ($n = 9$) ($P = .01$) (Fig 2).

Postradiosurgery Complications

After the first GKRS, 48 RICs (32%) were noted (Table 5). Among these, 8 patients presented with neurologic deficits

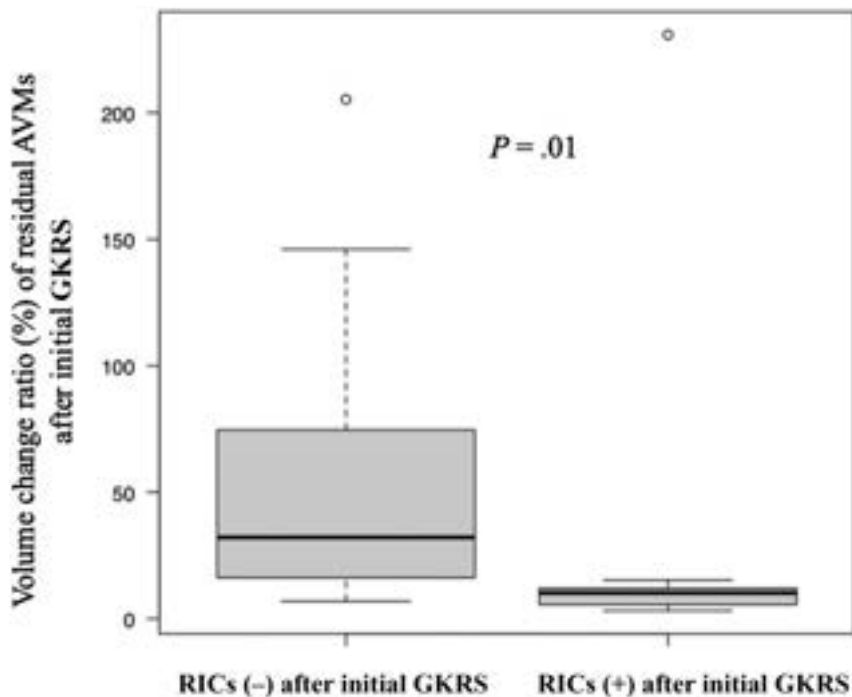


FIG 2. Radiation-induced changes and the volume change ratio of residual AVMs after the first GKRS. The association between RIC development and AVM volume reduction after the first GKRS. Among patients who underwent repeat GKRS, the median rate of AVM volume change after the first treatment was 32.2% (range, 6.9%–205%) for patients without RICs (–) and 10.2% (range, 3.18%–231%) for those with RICs (+), respectively ($P = .01$).

Table 5: The development of RICs and cyst formation after each GKRS in patients with AVMs of the brain

	Initial GKRS ($n = 150$)	Repeat GKRS ($n = 25$)	P Value
Radiologic RICs (No.) (%)	48 (32)	5 (20)	.35
Symptomatic RICs (No.) (% of radiologic RICs)	8 (17)	1 (20)	1.0
Cyst formation (No.) (%)	2 (1.3)	0 (0.0)	.56

(including 6 with transient and 2 with permanent symptoms). The transient neurologic deficits after the first GKRS included seizures ($n = 2$), upper-extremity weakness ($n = 2$), sensory dysfunction ($n = 1$), scintillating scotoma ($n = 1$), and visual field deficits ($n = 2$). Permanent symptoms after the first GKRS included impaired consciousness due to deep drainage congestion ($n = 1$) and visual field deficits ($n = 1$).

After repeat GKRS, 5 (20%) patients developed RICs, including one (4%) with symptomatic RICs, which led to transient scintillating scotoma. Most important, no patients developed permanent symptoms after repeat GKRS. One patient developed RICs after both the first and repeat GKRS procedures; however, both were asymptomatic. Delayed cyst formation occurred in 2 patients (1.3%) after the first GKRS; both were symptomatic. No cysts were observed after repeat GKRS. The incidences of radiologic RIC, symptomatic RIC, and cysts did not significantly differ between the first and repeat GKRS procedures ($P = .35$, 1.0, and 0.56, respectively).

RICs and Postradiosurgery Hemorrhages

Among patients with initial GKRS ($n = 150$), 1 hemorrhage event was documented between AVM diagnosis and initial GKRS (median follow-up, 1.5 months; range, 0.03–261 months); thus, the annual hemorrhage risk before initial GKRS was 0.71%/year.

During the latency interval after the first GKRS and before obliteration or additional treatment, 19 hemorrhages occurred in 15 (10%) patients (median follow-up, 43 months; range, 1–114 months). Only 2 patients died due to hemorrhage. The overall annual preobliteration hemorrhage risk was 2.5%/year for all AVMs after the initial GKRS. Among the 15 patients who experienced hemorrhage after the initial treatment, RICs developed in 6 patients (20%). In patients with RICs, Kaplan-Meier analysis identified the cumulative hemorrhage rates as 4.1% at 1 year, 10.2% at 4 years, and 12.7% at 10 years after the first GKRS, compared with 4.0%, 7.0%, and 8.3%, respectively, in patients without RIC (Online Supplemental Data). The RIC incidence after the first GKRS was not related to the postradiosurgery cumulative hemorrhage rate ($P = .44$).

Among the 25 patients with repeat radiosurgery, 2 events in 2 patients (8.0%) were documented after repeat GKRS. They also experienced hemorrhage during the latency period between the initial and repeat treatment (median follow-up, 45 months; range, 14–165

months). After the repeat GKRS, the annual hemorrhage risk before obliteration was 1.8%/year. The median follow-up duration after AVM obliteration diagnosis was 61.7 months (range, 0.0–178 months) for the patients with initial GKRS and 41.5 months (range, 0.0–159 months) for those with repeat treatment. After initial or repeat GKRS, no hemorrhage occurred after AVM obliteration diagnosis.

DISCUSSION

Radiation-Induced Changes and AVM Obliteration

RIC development after the first GKRS was significantly correlated with complete obliteration after repeat radiosurgery. Of the 9 patients with RICs after the first GKRS who underwent repeat GKRS, all achieved complete obliteration; in contrast, 43.8% (7/16 patients) of those without RICs after the first GKRS achieved complete obliteration ($P = .007$). Kaplan-Meier analysis also revealed that RIC development after the first GKRS was associated with a

significantly higher rate of obliteration after repeat GKRS ($P = .03$).

Kano et al¹⁰ retrospectively reviewed 105 patients who underwent repeat GKRS for incompletely obliterated AVMs and found that greater volume reduction after the first procedure was significantly associated with complete obliteration after the repeat procedure ($P = .035$). We also found that RIC development was significantly associated with a higher volume reduction of the AVM nidus after the first GKRS. This led to complete obliteration after repeating the procedure. We speculate that RICs might represent radiologic reactivity in AVMs.

RICs could be epiphenomena of ongoing AVM obliteration.^{12,13} Yen et al¹² reported that 62.8% of AVM cases that developed RICs achieved total obliteration versus 52.1% of those without RICs ($P < .001$). They also found that AVMs with extensive RICs were more likely to achieve total obliteration than those with mild RICs. We found RICs to be associated with a higher volume reduction of the AVM nidus after failed obliteration after the first radiosurgery ($P = .01$) (Fig 2). RICs appear to indicate AVM obliteration progress after GKRS.

The mechanisms underlying post-GKRS RICs are incompletely understood but could be related to perinidal edema resulting from tissue injury or venous congestion.^{4,14} Direct tissue damage, especially to endothelial or glial cells, may damage the blood-brain barrier, cause excessive production of free radicals, and induce inflammation.^{4,14} Venous congestion-induced imaging changes result from obstruction of venous outflow due to AVM obliteration.¹⁵

Complications of Repeat GKRS

Our results indicated that repeat GKRS did not increase the risk of symptomatic complications compared with the first procedure. The development of RICs was 32% after the first GKRS and 20% after repeat GKRS ($P = .35$). After repeat GKRS, 1/25 (4%) patients demonstrated symptomatic RICs with transient neurologic deficits. In contrast, 8/150 patients (5.3%) demonstrated symptomatic RICs after the first procedure. The incidence of symptomatic RICs was not higher after repeat GKRS ($P = 1.0$). One patient (4%) developed RICs after both the first and repeat GKRS procedures; however, in both instances the changes were asymptomatic. Delayed cyst formation occurred in 2 patients (1.3%) after the first GKRS and was not observed after the repeat procedure. Hence, repeat GKRS did not increase the risk of delayed cyst formation ($P = .56$) (Table 5).

In previous research, 30%–40% of AVMs developed RICs after the first GKRS; however, only 2.5%–10.8% developed symptomatic RICs, with a minimal number having permanent deficits.^{12,14,16} After repeat treatment for residual AVMs, Karlsson et al¹⁷ reported an overall complication rate of up to 14%, higher than that observed after the first treatment. However, many patients in their study underwent treatment in the 1970s and early 1980s, when technologies such as stereotactic 3D imaging for brain AVMs and refined dosimetric protocols were not yet available.^{15,18} Studies that reviewed patients who underwent repeat radiosurgery procedures during the late 1980s to 2000s found rates of symptomatic RICs ranging from 3.6% to 9.5% after repeat treatment.^{7,19} Therefore, we do not

expect repeat GKRS to increase the risk of complications compared with the first GKRS.

Repeat Radiosurgery for Residual AVMs

The high obliteration rate on retreatment and the relatively low risk of complications indicated that repeat GKRS for residual AVMs is a safe and beneficial treatment option. Several studies have found no difference in the AVM hemorrhage risk pre- to post-GKRS (incompletely obliterated).²⁰ Additional treatments are recommended to eliminate residual AVMs after the first procedure.^{7,20}

Large-scale studies have demonstrated the effectiveness of repeat GKRS for residual AVMs, with total obliteration rates ranging from 55% to 62%,^{7,18,19} concordant with our finding of 64%. These authors concluded that patients who had a residual nidus after the first treatment nonetheless demonstrated a substantial therapeutic effect (volume reduction) and were encouraged to undergo repeat GKRS.

Limitations

This study was limited by our relatively small patient cohort; subsequent, well-powered studies are needed. Additionally, this study was retrospective, and the external validity may be limited by patient selection bias in our treatment algorithms. Throughout our 15-year experience, our understanding of dose-volume relationships, conformality, treatment plan selectivity, and reliance on both angiographic and 3D MR imaging data have gradually changed. Patients treated in the latter years of this study likely benefited from our greater knowledge and improved technique. The incidence of GKRS-related complications and hemorrhage may be slightly inaccurate because we excluded patients who had volume-staged GKRS ($n = 4$) and those with a follow-up period of <1 year ($n = 9$) and incomplete clinical data ($n = 7$). Furthermore, careful longitudinal clinical follow-up studies are needed to continue monitoring long-term complications after GKRS.

CONCLUSIONS

RICs after the first GKRS are a favorable indicator of AVM obliteration after repeat GKRS. Although RICs occurred in 25%–33% of patients, most did not result in neurologic deficits and permanent sequelae were uncommon. Moreover, the risk of symptomatic RICs after repeat GKRS is comparable with that following the first procedure. When the first GKRS fails to achieve complete obliteration and results in RICs, a favorable outcome can occur by repeating the procedure.

Disclosure forms provided by the authors are available with the full text and PDF of this article at www.ajnr.org.

REFERENCES

1. Shin M, Maruyama K, Kurita H, et al. Analysis of nidus obliteration rates after gamma knife surgery for arteriovenous malformations based on long-term follow-up data: The University of Tokyo experience. *J Neurosurg* 2004;101:18–24 CrossRef Medline
2. Douglas JG, Goodkin R. Treatment of arteriovenous malformations using gamma knife surgery: the experience at the University of

- Washington from 2000 to 2005. *J Neurosurg* 2008;109(Suppl):51–56 CrossRef Medline
3. Maruyama K, Kawahara N, Shin M, et al. **The risk of hemorrhage after radiosurgery for cerebral arteriovenous malformations.** *N Engl J Med* 2005;352:146–53 CrossRef Medline
 4. Daou BJ, Palmateer G, Wilkinson DA, et al. **Radiation-induced imaging changes and cerebral edema following stereotactic radiosurgery for brain AVMs.** *AJNR Am J Neuroradiol* 2021;42:82–87 CrossRef Medline
 5. Ding D, Yen CP, Xu Z, et al. **Radiosurgery for patients with unruptured intracranial arteriovenous malformations: clinical article.** *J Neurosurg* 2013;118:958–66 CrossRef Medline
 6. Daou BJ, Palmateer G, Thompson BG, et al. **Stereotactic radiosurgery for brain arteriovenous malformations.** *J Stroke Cerebrovasc Dis* 2020;29:104863–69 CrossRef Medline
 7. Yen CP, Jain S, Haq IU, et al. **Repeat gamma knife surgery for incompletely obliterated cerebral arteriovenous malformations.** *Neurosurgery* 2010;67:55–64; discussion 64 CrossRef Medline
 8. Spetzler RF, Martin NA. **A proposed grading system for arteriovenous malformations.** *J Neurosurg* 1986;65:476–83 CrossRef Medline
 9. Wegner RE, Oysul K, Pollock BE, et al. **A modified radiosurgery-based arteriovenous malformation grading scale and its correlation with outcomes.** *Int J Radiat Oncol Biol Phys* 2011;79:1147–50 CrossRef Medline
 10. Kano H, Kondziolka D, Flickinger JC, et al. **Stereotactic radiosurgery for arteriovenous malformations, Part 3: outcome predictors and risks after repeat radiosurgery: clinical article.** *J Neurosurg* 2012;116:21–32 CrossRef Medline
 11. Kanda Y. **Investigation of the freely available easy-to-use software “EZR” for medical statistics.** *Bone Marrow Transplant* 2013;48:452–58 CrossRef Medline
 12. Yen CP, Matsumoto JA, Wintermark M, et al. **Radiation-induced imaging changes following gamma knife surgery for cerebral arteriovenous malformations: clinical article.** *J Neurosurg* 2013;118:63–73 CrossRef Medline
 13. Yen CP, Khaled MA, Schwyzer L, et al. **Early draining vein occlusion after gamma knife surgery for arteriovenous malformations.** *Neurosurgery* 2010;67:1293–302; discussion 1302 CrossRef Medline
 14. Kano H, Flickinger JC, Tonetti D, et al. **Estimating the risks of adverse radiation effects after gamma knife radiosurgery for arteriovenous malformations.** *Stroke* 2017;48:84–90 CrossRef Medline
 15. Spiegelmann R, Friedman WA, Bova FJ. **Limitations of angiographic target localization in planning radiosurgical treatment.** *Neurosurgery* 1992;30:619–23 CrossRef Medline
 16. Ganz JC, Reda WA, Abdelkarim K, et al. **A simple method for predicting imaging-based complications following gamma knife surgery for cerebral arteriovenous malformations.** *J Neurosurg* 2005;102 (Suppl):4–7 CrossRef Medline
 17. Karlsson B, Kihlström L, Lindquist C, et al. **Gamma knife surgery for previously irradiated arteriovenous malformations.** *Neurosurgery* 1998; 42:1–5 CrossRef Medline
 18. Foote KD, Friedman WA, Ellis TL, et al. **Salvage retreatment after failure of radiosurgery in patients with arteriovenous malformations.** *J Neurosurg* 2003;98:337–41 CrossRef Medline
 19. Stahl JM, Chi YY, Friedman WA. **Repeat radiosurgery for intracranial arteriovenous malformations.** *Neurosurgery* 2012;70:150–54; discussion 154 CrossRef Medline
 20. Karlsson B, Jokura H, Yamamoto M, et al. **Is repeated radiosurgery an alternative to staged radiosurgery for very large brain arteriovenous malformations?** *J Neurosurg* 2007;107:740–44 CrossRef Medline

Reliability of Functional and Diffusion MR Imaging Near Cerebral Cavernous Malformations

M. Colasurdo, H. Chen, R. Navarra, E. Piccirilli, A. Delli Pizzi, V. Panara, and M. Caulo



ABSTRACT

BACKGROUND AND PURPOSE: Surgical resection of cerebral cavernous malformations close to eloquent regions frequently uses fMRI and DTI for surgical planning to best preserve neurologic function. This study investigates the reliability of fMRI and DTI near cerebral cavernous malformations.

MATERIALS AND METHODS: Consecutive patients with cerebral cavernous malformations undergoing presurgical fMRI and DTI mapping were identified. Each cerebral cavernous malformation was hand-contoured; 2 sequential 4-mm expansion shells (S1 and S2) were created, generating 2 ROIs and 2 contralateral controls. Fractional anisotropy and regional homogeneity measurements were then extracted from each ROI and compared with the contralateral controls. Reliability, accuracy, and precision were compared as appropriate.

RESULTS: Fifty-four patients were identified and included. Errors of fractional anisotropy were significantly lower than those of regional homogeneity in S1 and S2 ($P < .001$), suggesting that fractional anisotropy is more reliable than regional homogeneity near cerebral cavernous malformations. Proximity to cerebral cavernous malformations worsened the reliability of regional homogeneity (S1 versus S2, $P < .001$), but not fractional anisotropy ($P = .24$). While fractional anisotropy was not significantly biased in any ROI ($P > .05$), regional homogeneity was biased toward lower signals in S1 and S2 ($P < .05$), an effect that was attenuated with distance from cerebral cavernous malformations ($P < .05$). Fractional anisotropy measurements were also more precise than regional homogeneity in S1 and S2 ($P < .001$ for both).

CONCLUSIONS: Our findings suggest that hemosiderin-rich lesions such as cerebral cavernous malformations may lead to artifactual depression of fMRI signals and that clinicians and surgeons should interpret fMRI studies near cerebral cavernous malformations with caution. While fMRI is considerably affected by cerebral cavernous malformation-related artifacts, DTI appears to be relatively unaffected and remains a reliable imaging technique near cerebral cavernous malformations.

ABBREVIATIONS: APE = absolute percentage error; BOLD = blood oxygen level-dependent; CCM = cerebral cavernous malformations; DVA = developmental venous anomalies; FA = fractional anisotropy; PE = percentage error; ReHo = regional homogeneity; S1 = Shell1; S2 = Shell2

Cerebral cavernous malformations (CCMs) are well-circumscribed and multilobulated vascular lesions lacking intervening brain parenchyma¹ that are often in close proximity to developmental venous anomalies (DVA).² Although many CCMs are clinically silent and can be managed conservatively,³ some lesions present with hemorrhage or refractory epilepsy,⁴ which may necessitate neurosurgical or neuroradiological intervention.

Optimal neurosurgical or neuroradiological approaches require a balance between gross total resection and preservation of neurologic function, especially in eloquent brain regions. Historically, fMRI and DTI have been used for surgical planning in eloquent regions.⁵⁻⁸ However, the reliability of these techniques near CCMs depends heavily on the assumption that signals are not influenced by proximity to artifacts caused by vascular lesions. CCMs often have intralésional hemosiderin deposits with higher concentrations on their outer borders, and because fMRI relies on capturing subtle changes in paramagnetism seen with shifting concentrations of oxygenated and deoxygenated hemoglobin, the nearby presence of superparamagnetic substances such as hemosiderin can potentially compromise the reliability of fMRI signals near CCMs. Furthermore, both fMRI and DTI sequences are echo-planar-based techniques, which could also make them both susceptible to paramagnetism-related

Received August 8, 2022; accepted after revision December 19.

From the Departments of Neuroscience, Imaging and Clinical Sciences (M.C., R.N., E.P., V.P., M.C.) and Innovative Technologies in Medicine & Dentistry (A.D.P.), G. D'Annunzio University of Chieti, Pescara, Chieti, Italy; and National Institutes of Health (H.C.), Bethesda, Maryland.

Please address correspondence to Marco Colasurdo, MD, Università degli Studi Gabriele d'Annunzio Chieti e Pescara, Neuroscienze ed Imaging, ITAB via Luigi Polacchi 11, 66100, Chieti Scalo, CH, Italy; e-mail: Italmcolasurdo@gmail.com



Indicates article with online supplemental data.

<http://dx.doi.org/10.3174/ajnr.A7765>

artifacts near vascular anomalies.⁹ To date, the overall reliability of fMRI and DTI techniques for surgical planning near CCMs is unclear.

This study investigates the reliability of fMRI and DTI near CCMs. We hypothesize that proximity to CCMs may impair the accuracy and precision of fMRI and DTI and that fMRI may be more prone to artifacts than DTI.

MATERIALS AND METHODS

Consecutive patients who underwent presurgical mapping with fMRI and DTI were retrospectively identified from June 2008 to June 2019 at a single institution performed at Università degli Studi Gabriele d'Annunzio, Chieti e Pescara, at the Department of Imaging and Neuroscience. Written informed consent was obtained from all patients before undergoing MR imaging, and this study was approved by the local Ethics Committee.

Patients with a diagnosis of CCM were then selected, and all subjects without a diagnosis of CCM were excluded.

Additional exclusion criteria were the following: 1) the presence of multiple brain CCMs; 2) the presence of prior brain surgery leading to significant distortion of images; 3) a CCM located within the infratentorial compartment; or 4) a study performed on magnets with field strengths lower than 3T (Fig 1).

Data Acquisition and Study Design

All patients underwent a standardized multimodal imaging protocol that included conventional and advanced MR images obtained during a single imaging session (Table 1).

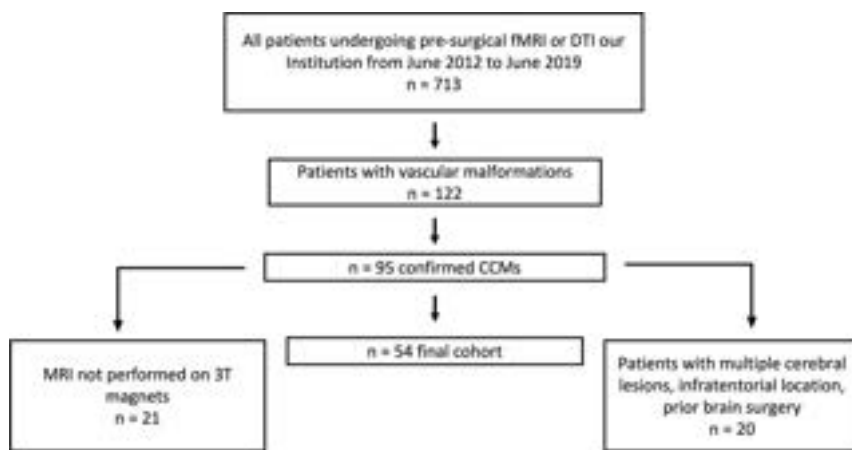


FIG 1. Flow chart of study selection.

Table 1: MR imaging parameters for conventional and advanced sequences

Sequences	Parameters
3D turbo field-echo T1-weighted	Sagittal acquisition; TR/TE = 8.1, 3.7 ms; section thickness = 1-mm isovoxel; matrix = 256 × 256
Turbo spin-echo T2-weighted	Axial acquisition; TR/TE = 3000/80 ms; section thickness = 3 mm; matrix = 420 × 272
FLAIR	Axial acquisition; TR/TE = 11,000/125 ms; matrix = 320 × 200 ms; T1 = 2800 ms
T2*-weighted fast-field echo	Axial acquisition; TR/TE = 1061/16 ms; matrix = 232 × 141
SWI	Axial acquisition; TR/TE = 31/7.2 ms; Δ TE = 6.2 ms; matrix = 288 × 235
DTI	Single-shot spin-echo echo-planar imaging; TR/TE = 6502/70 ms; matrix = 112 × 110; b-values = 0–800 mm ² /s; 32 diffusion-sensitive directions
BOLD functional imaging	T2*-weighted echo-planar; TR/TE = 2000/35 ms; matrix = 96 × 96; flip angle = 90°; section thickness = 3 mm

Images were acquired with a 3T MR imaging system (Achieva X-Series; Philips Healthcare) using a sensitivity encoding 8-channel head coil.

DTI, fMRI, and conventional MR imaging sequence images from the scanner were converted to a Neuroimaging Informatics Technology Initiative (Nifti) compressed format using the dcm2nii tool from MRICron (<https://www.nitrc.org/projects/mricron>).

Each CCM was hand-contoured on T2 sequences using the open-source software ITK-SNAP (<http://www.itksnap.org/pmwiki/pmwiki.php>),¹⁰ and on the basis of the T2 segmentation, 2 sequential expansion shells (S1 and S2) were created with a thickness measuring 4 mm, generating 3 different ROIs surrounding the lesions. Subsequently every ROI was flipped in the normal contralateral hemisphere with the following originally created algorithm, obtaining a total of 6 ROIs per subject. Shells were computed by 2 sequential dilations and subtraction of the main ROI. Flipped control ROIs were obtained by registration to Montreal Neurological Institute space (which assures symmetric space) and then flipped back to the original space. Registration among spaces was performed using Advanced Normalization Tools (ANTs, <http://stnava.github.io/ANTs/>) (Fig 2).¹¹

Volumetric segmentation of 3D fast-field echo sequences was performed with the FreeSurfer image analysis suite (<http://surfer.nmr.mgh.harvard.edu/>) using procedures described in prior publications.^{12–15} Voxels corresponding to gray matter within the ROIs were automatically segmented to calculate regional homogeneity (ReHo).

Denosing steps were applied to DTI acquisitions then a low b-value volume was extracted and skull-stripped. DTI indexes were computed using FSL Toolbox dti-fit (<https://fsl.fmrib.ox.ac.uk/fsl/fslwiki/FDT/UserGuide#DTIFIT>) with tensor fitting with weighted least squares after eddy current correction and gradient direction rotation. Voxels with fractional anisotropy (FA) values outside the range (0,1) or negative diffusion were marked and excluded from the ROIs.

ReHo. Whole-brain time courses from residuals of the general linear model on task-based fMRI acquisitions were extracted using the FSL Toolbox FEAT pipeline (<https://fsl.fmrib.ox.ac.uk/fsl/fslwiki/FEAT>)^{16,17} after section time

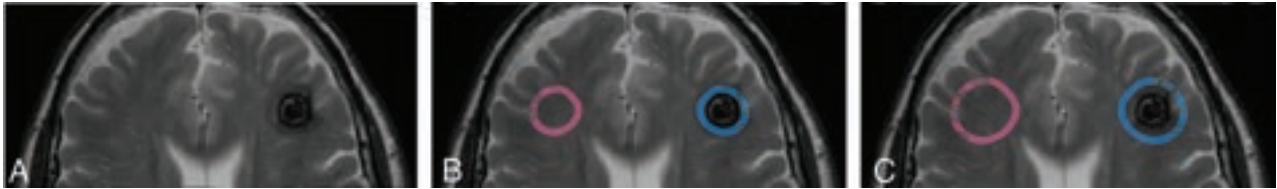


FIG 2. Conventional T2 TSE showing a left frontal subcortical cavernous hemangioma. White and gray matter segmentations of ROIs of the first and second expansion shells (4 mm each) are seen in light blue. On the contralateral hemisphere, computation of control ROIs is shown in light red.

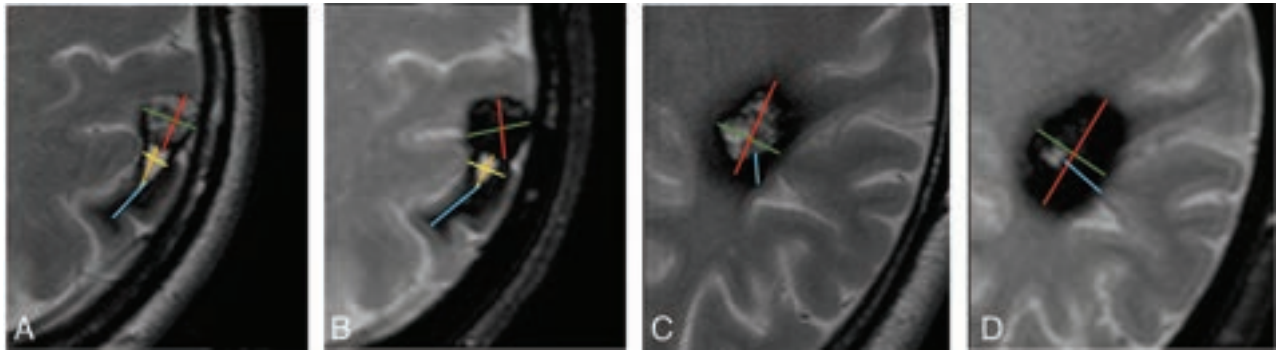


FIG 3. Images exemplifying qualitative data analysis in 2 different patients (A and C) with T2 TSE and T2 gradient sequences (B and D). A 43-year-old woman with a superficial, previously ruptured left parietal CCM with a collection of qualitative characteristics. CCM maximum diameters (red and green, A and B), hematoma maximum diameters (yellow and orange, A and B), and maximum thickness of hemosiderin rim thickness (light blue, A and B). A 52-year-old man with a left subcortical CCM with measurement of maximum diameters (green and red, C and D) and maximum hemosiderin rim thickness (light blue, C and D).

and motion correction. Affine registration from EPI space to structural space was performed using white-matter boundary methods (BBR; https://fsl.fmrib.ox.ac.uk/fsl/fslwiki/FLIRT_BBR#:~:text=The%20white-matter%20boundary%20is%20mapped%20to%20the%20EPI,paired%20is%20used%20to%20calculate%20the%20cost%20function) implemented on FSL Toolbox FLIRT.¹⁶⁻²²

Analysis of Functional NeuroImages (AFNI; <https://afni.nimh.nih.gov/>),²³ the Functional and Tractographic Connectivity Analysis Toolbox (FATCAT),²⁴ and 3dReHo (https://afni.nimh.nih.gov/pub/dist/doc/program_help/3dReHo.html)²⁵ were used to extract regional homogeneity from ROIs.

Qualitative Data Acquisition

Using conventional MR imaging sequences, 2 neuroradiologists with 5 and 9 years of experience performed a qualitative evaluation of each CCM in a consensus reading assessing the following characteristics (Fig 3): 1) signs of rupture; 2) the presence of a nearby developmental venous anomaly; 3) the presence of edema; 4) baseline T1 signal hyperintensity; 5) T2 signal hyperintensity; 6) T2 hemosiderin ring features (categorized as regular, irregular, continuous, discontinuous); 7) the thickness of the hemosiderin ring (measured on T1, T2, T2*, and SWI); 8) maximum axial diameters of the lesion (measured on T1, T2, T2*, and SWI); and 9) the presence of intra- or extralesional hematoma. If a hematoma was present, then they also collected the following additional variables: 10) the maximum thickness of the wall of the hematoma (measured on T1, T2, T2*, and SWI); and 11) the maximum axial diameters of the hematoma (measured on T1, T2, T2*, and SWI).

Statistical Analysis. To assess the reliability of ReHo and FA in each ROI, we calculated the absolute percentage error (APE) by

dividing measurements in CCMs, S1, and S2 by measurements in their respective contralateral (control) ROIs. APEs were compared within and between imaging modalities using the Wilcoxon matched-pairs signed-rank test. Adjusted *P* values were calculated using the Bonferroni method; values < .05 were statistically significant. To assess bias, percentage error (PE) was log-transformed and outliers were removed using the ROUT method with a *Q* of 1%; normal distribution was confirmed by visual inspection as well as the Anderson-Darling test. One-sample *t* tests were performed to identify significant bias in each ROI from contralateral controls; *P* values < .05 were statistically significant. Welch *t* tests were performed to identify significant differences within and between modalities; adjusted *P* values (calculated using the Bonferroni method) < .05 were statistically significant. Finally, to assess variance, we performed *F*-tests of equal variances on normalized PEs, and comparisons were made within and between modalities. The Bonferroni method raw *P* values were multiplied by the number of comparisons to keep the same .05 significance threshold. Adjusted *P* values (calculated using the Bonferroni method) < .05 were statistically significant.

RESULTS

Patient Characteristics

Fifty-four patients were identified and included in our study (Online Supplemental Data). Forty-one percent were men, the median age was 42 years, and 85% of patients were right-handed. Thirty-seven percent of lesions were on the left side, 65% were in the frontal lobe, and 85% were superficial. Lesions had a median maximum diameter of 16 mm, and the median border thickness

Table 2: Errors, bias, and variance of ReHo and FA measurements near CCMs^a

fMRI (ReHo)		
Variable	Shell 1: 0–4 mm	Shell 2: 4–8 mm
Error, median APE (IQR)	25.1% (13.5–43.6)	15.0% (6.9–26.4)
Bias, mean PE (95% CI)	–27.2% (–33.8 to –19.8) ^b	–8.3% (–14.9 to –1.1) ^c
Variance, % deviation from mean	28.3%–39.5%	22.6%–29.2%
DTI (FA)		
Variable	Shell 1: 0–4 mm	Shell 2: 4–8 mm
Error, median APE (IQR)	9.2% (4.4–17.6)	6.5% (2.1–11.7)
Bias, mean PE (95% CI)	–0.3% (–4.1–4.8) ^d	–0.1% (–3.1–2.9) ^e
Variance, % deviation from mean	14.6%–17.1%	10.4%–11.6%
ReHo vs FA: <i>P</i> value		
Variable	Shell 1: 0–4 mm	Shell 2: 4–8 mm
Error	<.001	<.001
Bias	<.001	.16
Variance	<.001	<.001

Note:—IQR indicates interquartile range.

^a *P* values of the 1-sample *t* test to identify statistically significant bias.

^b <.001.

^c .023.

^d .90.

^e .93.

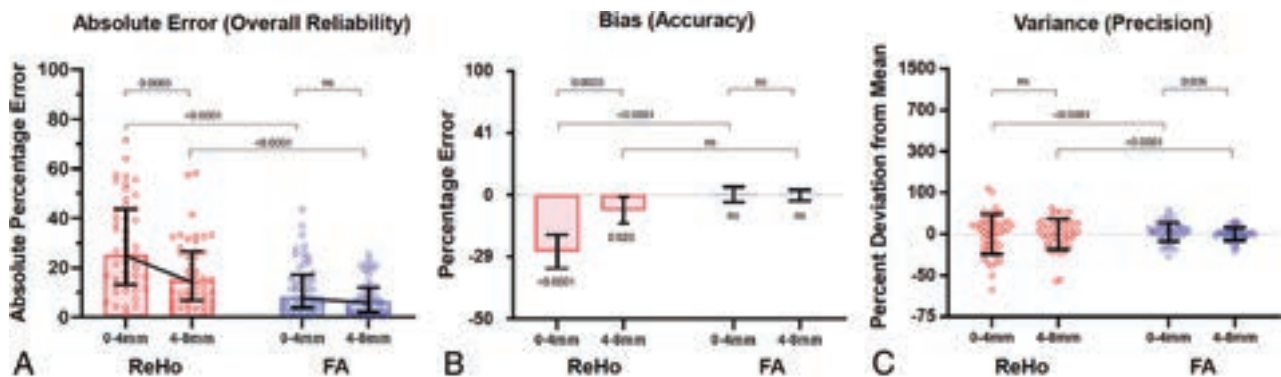


FIG 4. Error, bias, and variance of ReHo and FA measurements near CCMs. *A*, Absolute errors of each ROI compared with their contralateral controls (median with interquartile range and adjusted *P* values from the Wilcoxon matched-pairs signed-rank test). *B*, Biases of each ROI compared with their contralateral controls. Mean with standard error of mean is shown. *P* values from 1-sample *t* tests are shown below the bars, and adjusted *P* values from Welch *t* tests are shown above the bars (*C*). Variances of each ROI compared with their contralateral controls and SDs are shown. Adjusted *P* values from *F*-tests for equality of variance are shown. *P* values or adjusted *P* values > .05 were deemed nonsignificant and marked as ns.

was 3.2 mm. Forty-three percent of lesions had a nearby DVA, and 56% of CCMs were ruptured.

Absolute Error (Overall Reliability)

To assess the overall reliability of fMRI and DTI, we compared ReHo and FA measurements in CCMs, S1 (0–4 mm from the CCM borders), and S2 (4–8 mm from CCM borders) with measurements in their respective contralateral control ROIs. APRs were calculated, and these errors were compared between groups (Table 2 and Fig 4A). Here, we found that ReHo had significantly higher absolute errors than FA in S2 (15.0% versus 6.5%, adjusted *P* < .001) and S1 (25.1% versus 9.2%, adjusted *P* < .001). Proximity to CCMs significantly worsened the reliability of ReHo, with significantly higher errors in S1 than S2 (adjusted *P* < .001). On the other hand, proximity to CCMs did not seem to significantly impact the reliability of FA (adjusted *P* = .12) (Table 2).

Bias (Accuracy)

To identify sources of error for ReHo and FA measurements, we assessed both modalities for possible measurement biases in CCMs, S1, and S2 (Table 2 and Fig 4B). Statistically, bias represents a deviation of the average of measurements from a theoretic mean, suggesting systemic over- or underestimation of true signals. Here, we found that ReHo measurements were significantly biased toward lower signals in S1 and S2 (*P* < .001 and *P* = .02, respectively). Furthermore, this effect was increased with proximity to CCMs, as seen by a significantly larger bias in S1 than in S2 (–27.2 versus –8.3%, adjusted *P* < .001). On the other hand, FA measurements were not significantly biased toward higher or lower signals in CCMs, S1, or S2, and there were no differences in bias of FA measurements among ROIs (*P* > .99). Finally, ReHo was significantly more biased than FA in S1 (–27.2% versus –0.3%, respectively; adjusted *P* < .001), but not in S2 (adjusted *P* = .16) (Table 2).

Variance (Precision)

We also assessed the variance of measurements to investigate whether differences in precision may have contributed to the differences in overall reliability between ReHo and FA measurements (Table 2 and Fig 4C). Statistically, variance represents the spread of measurements around the measurement mean, providing a quantification of noise or inherent imprecisions within measurement techniques. Here, we found that FA was significantly more precise than ReHo in S1 and S2 (adjusted $P < .001$ for both). We also found that for ReHo, there were no significant differences in precision between S1 and S2 ($P = .31$), whereas for FA, S2 had lower variance than S1 ($P = .03$) (Table 2).

Qualitative Associations

Finally, we investigated whether qualitative characteristics of CCMs (eg, CCM location, size, border thickness, border morphology, T2-signal intensity within CCMs, nearby DVA, CCM rupture, and so forth) may have impacted the reliability of either imaging technique. We did not identify any characteristics of CCMs that significantly impacted the overall reliability of ReHo or FA measurements.

DISCUSSION

fMRI and DTI are cornerstones of optimal presurgical planning for CCMs near eloquent brain areas;^{5-8,26-33} however, the reliability of these techniques near vascular lesions such as CCMs is not well-understood. In this study, we show the following: 1) fMRI is prone to significant error near CCMs, likely due to hemosiderin-induced artifactual depression of blood oxygen level-dependent (BOLD) signals; and 2) DTI is largely accurate near CCMs and does not appear to be significantly compromised by CCM-related artifacts. These findings are original, and they provide valuable insight into how to optimize preoperative planning for CCMs. DTI and fMRI are often considered unreliable near vascular malformations and are frequently overlooked by both neuroradiologists and neurosurgeons when considering preoperative planning protocols. Although relatively surprising given the relative paucity of studies³⁴⁻³⁶ that have tried to address this matter, our findings, especially the consistent, quantifiable reliability of DTI, should encourage its frequent use in clinical practice.

ReHo, a mathematic technique to assess whether the BOLD signal of a given voxel is similar to that of its neighbors, was chosen as our primary measurement.²⁵ Neuronal firing often occurs in regional clusters, which can present as concordant BOLD signals across multiple neighboring voxels. Thus, higher ReHo values indicate higher concordance signals of a given voxel with its neighbors, which can be a marker of resting-state functional connectivity.³⁷ Our results demonstrate that ReHo values are prone to large errors near CCMs, likely driven by CCM-related artifacts. Hemosiderin, a superparamagnetic blood-degradation product rich in Fe^{3+} can cause substantial signal distortions near CCMs and alter BOLD signals. Given that BOLD signals rely on measuring subtle changes in paramagnetism, the overwhelming superparamagnetism of hemosiderin near CCMs can significantly compromise the sensitivity of fMRI to detect subtle paramagnetic shifts. Substantial BOLD signal distortions near CCMs can result in low values of ReHo due to increased heterogeneity; thus, it is not surprising that our findings

show high measurement errors of ReHo near CCMs and that these errors attenuate with distance from CCMs.

In stark contrast, FA measurements near CCMs are largely accurate. Unlike BOLD signals, DTI signals do not directly assess changes in paramagnetism; thus, hemosiderin deposits near CCMs would be expected to have little impact on DTI measurements. Of note, because fMRI and DTI both use echo-planar sequences, they may have gross geometric image distortions from susceptibility artifacts due to relatively long gradient-echo trains.⁹ However, we did not observe significant measurement errors near CCMs for DTI, suggesting that this phenomenon likely plays a minimal role and that the errors seen with fMRI are likely unrelated to this general limitation of echo-planar-based imaging.

Most interesting, qualitative characteristics postulated to contribute to signal artifacts near CCMs were not significantly associated with differences in errors for either fMRI or DTI. While the lack of statistical significance is likely due to the nature of the sample size and the lack of statistical power, it is also possible that there may be some degree of underlying change in the brain parenchyma near CCMs that gives rise to changes in MR imaging signals. For example, hemosiderin rims can cause neuronal hyperexcitability and have been proposed as a possible etiology of epilepsy. Thus, functional derangements and astrogliosis³⁸ near CCMs may ensue, causing changes in fMRI and DTI signals. While this hypothesis might be plausible, our study is not conceived or powered to assess the degree of astrogliosis adjacent to CCMs and its potential interactions with fMRI. Furthermore, fMRI and DTI both had some imprecision near CCMs, also contributing to overall errors. Unlike the artifactual signal depression seen with ReHo, these imprecisions were not strongly associated with proximity to CCMs; thus, they may be intrinsic to their specific signal resolutions. Low precision can potentially be overcome with the use of multishot sequences or parallel imaging. Despite reduction of the echo-train length and the use of stronger magnets that could improve precision, these strategies may exponentiate susceptibility-related artifacts.

Our study has limitations. First, while resting-state fMRI allows us to reliably compare signals to contralateral control ROIs, task-based fMRI may provide more valuable and direct information on the functional relevance of areas near CCMs. Nonetheless, our observation that BOLD signals may be depressed near CCMs would also be expected to affect task-based fMRI. Second, we used resting periods during task-based fMRI studies for our analysis. This methodology exposes our data to potential inaccuracies as changes in cerebral blood flow, thus, BOLD signals, may persist after tasks and create signal biases during resting states. Next, our use of contralateral ROIs as controls relies on the assumption that the human brain is symmetrically organized. While past studies provide evidence for organizational symmetry,³⁹⁻⁴¹ there are inevitably differences between hemispheres within each subject. Finally, our study population included MR imaging examinations obtained during 11 years, and changes in study protocols with time may introduce heterogeneity.

CONCLUSIONS

Our results are consistent with the hypothesis that hemosiderin-rich lesions such as CCMs may lead to artifactual depression of

fMRI signals and that clinicians and surgeons should interpret fMRI studies near CCMs with caution. While fMRI is significantly affected by CCM-related artifacts, DTI appears to be relatively unaffected and remains a reliable imaging technique near CCMs. Future studies should further elucidate the mechanisms underlying these findings and develop mitigating strategies to improve the accuracy and precision of these imaging modalities.

Disclosure forms provided by the authors are available with the full text and PDF of this article at www.ajnr.org.

REFERENCES

- Ellis JA, Barrow DL. **Supratentorial cavernous malformations.** *Handb Clin Neurol* 2017;143:283–89 CrossRef Medline
- Robinson JR, Awad IA, Masaryk TJ, et al. **Pathological heterogeneity of angiographically occult vascular malformations of the brain.** *Neurosurgery* 1993;33:547–54, discussion 554–55 CrossRef Medline
- Akers A, Al-Shahi Salman R, Awad IA, et al. **Synopsis of Guidelines for the Clinical Management of Cerebral Cavernous Malformations: Consensus Recommendations Based on Systematic Literature Review by the Angioma Alliance Scientific Advisory Board Clinical Experts Panel.** *Neurosurgery* 2017;80:665–80 CrossRef Medline
- Stapleton CJ, Barker FG. **Cranial cavernous malformations: natural history and treatment.** *Stroke* 2018;49:1029–35 CrossRef Medline
- Winkler D, Lindner D, Strauss G, et al. **Surgery of cavernous malformations with and without navigational support—a comparative study.** *Minim Invasive Neurosurg* 2006;49:15–19 CrossRef Medline
- Flores BC, Whittemore AR, Samson DS, et al. **The utility of preoperative diffusion tensor imaging in the surgical management of brainstem cavernous malformations.** *J Neurosurg* 2015;122:653–62 CrossRef Medline
- Januszewski J, Albert L, Black K, et al. **The usefulness of diffusion tensor imaging and tractography in surgery of brainstem cavernous malformations.** *World Neurosurg* 2016;93:377–88 CrossRef Medline
- Li D, Jiao YM, Wang L, et al. **Surgical outcome of motor deficits and neurological status in brainstem cavernous malformations based on preoperative diffusion tensor imaging: a prospective randomized clinical trial.** *J Neurosurg* 2018;130:286–301 CrossRef Medline
- Dietrich O, Biffar A, Baur-Melnyk A, et al. **Technical aspects of MR diffusion imaging of the body.** *Eur J Radiol* 2010;76:314–22 CrossRef Medline
- Yushkevich PA, Gerig G. **ITK-SNAP: an intractive medical image segmentation tool to meet the need for expert-guided segmentation of complex medical images.** *IEEE Pulse* 2017;8:54–57 CrossRef Medline
- Avants BB, Tustison NJ, Song G, et al. **A reproducible evaluation of ANTs similarity metric performance in brain image registration.** *Neuroimage* 2011;54:2033–44 CrossRef Medline
- Desikan RS, Ségonne F, Fischl B, et al. **An automated labeling system for subdividing the human cerebral cortex on MRI scans into gyral based regions of interest.** *Neuroimage* 2006;31:968–80 CrossRef Medline
- Fischl B, van der Kouwe A, Destrieux C, et al. **Automatically parcellating the human cerebral cortex.** *Cereb Cortex* 2004;14:11–22 CrossRef Medline
- Reuter M, Schmansky NJ, Rosas HD, et al. **Within-subject template estimation for unbiased longitudinal image analysis.** *Neuroimage* 2012;61:1402–18 CrossRef Medline
- Reuter M, Rosas HD, Fischl B. **Highly accurate inverse consistent registration: a robust approach.** *Neuroimage* 2010;53:1181–96 CrossRef Medline
- Woolrich MW, Jbabdi S, Patenaude B, et al. **Bayesian analysis of neuroimaging data in FSL.** *Neuroimage* 2009;45:S173–86 CrossRef Medline
- Jenkinson M, Beckmann CF, Behrens TEJ, et al. **FSL.** *Neuroimage* 2012;62:782–90 CrossRef Medline
- Jenkinson M, Bannister P, Brady M, et al. **Improved optimization for the robust and accurate linear registration and motion correction of brain images.** *Neuroimage* 2002;17:825–41 CrossRef Medline
- Leemans A, Jones DK. **The B-matrix must be rotated when correcting for subject motion in DTI data.** *Magn Reson Med* 2009;61:1336–49 CrossRef Medline
- Woolrich MW, Ripley BD, Brady M, et al. **Temporal autocorrelation in univariate linear modeling of FMRI data.** *Neuroimage* 2001;14:1370–86 CrossRef Medline
- Smith SM, Jenkinson M, Woolrich MW, et al. **Advances in functional and structural MR image analysis and implementation as FSL.** *Neuroimage* 2004;23(Suppl 1):S208–19 CrossRef Medline
- Sladky R, Friston KJ, Tröstl J, et al. **Slice-timing effects and their correction in functional MRI.** *Neuroimage* 2011;58:588–94 CrossRef Medline
- Cox RW. **AFNI: software for analysis and visualization of functional magnetic resonance neuroimages.** *Comput Biomed Res* 1996;29:162–73 CrossRef Medline
- Taylor PA, Saad ZS. **FATCAT: (an efficient) functional and tractographic connectivity analysis toolbox.** *Brain Connect* 2013;3:523–35 CrossRef Medline
- Zang Y, Jiang T, Lu Y, et al. **Regional homogeneity approach to fMRI data analysis.** *Neuroimage* 2004;22:394–400 CrossRef Medline
- Thickbroom GW, Byrnes ML, Morris IT, et al. **Functional MRI near vascular anomalies: comparison of cavernoma and arteriovenous malformation.** *J Clin Neurosci* 2004;11:845–48 CrossRef Medline
- Zotta D, Di Rienzo A, Scogna A, et al. **Supratentorial cavernomas in eloquent brain areas: application of neuronavigation and functional MRI in operative planning.** *J Neurosurg Sci* 2005;49:13–19 Medline
- Campbell PG, Jabbour P, Yadla S, et al. **Emerging clinical imaging techniques for cerebral cavernous malformations: a systematic review.** *Neurology Focus* 2010;29:E6 CrossRef Medline
- Caulo M, Esposito R, Mantini D, et al. **Comparison of hypothesis- and a novel hybrid data/hypothesis-driven method of functional MR imaging analysis in patients with brain gliomas.** *AJNR Am J Neuroradiol* 2011;32:1056–64 CrossRef Medline
- Chen CM, Hou BL, Holodny AI. **Effect of age and tumor grade on BOLD functional MR imaging in preoperative assessment of patients with glioma.** *Radiology* 2008;248:971–78 CrossRef Medline
- Jack CR, Thompson RM, Butts RK, et al. **Sensory motor cortex: correlation of presurgical mapping with functional MR imaging and invasive cortical mapping.** *Radiology* 1994;190:85–92 CrossRef Medline
- Cauley KA, Andrews T, Gonyea JV, et al. **Magnetic resonance diffusion tensor imaging and tractography of intracranial cavernous malformations: preliminary observations and characterization of the hemosiderin rim.** *J Neurosurg* 2010;112:814–23 CrossRef Medline
- Faraji AH, Abhinav K, Jarbo K, et al. **Longitudinal evaluation of corticospinal tract in patients with resected brainstem cavernous malformations using high-definition fiber tractography and diffusion connectometry analysis: preliminary experience.** *J Neurosurg* 2015;123:1133–44 CrossRef Medline
- Abhinav K, Nielsen TH, Singh R, et al. **Utility of a quantitative approach using diffusion tensor imaging for prognostication regarding motor and functional outcomes in patients with surgically resected deep intracranial cavernous malformations.** *Neurosurgery* 2020; 86:665–75 CrossRef Medline
- Rogalska M, Antkowiak L, Mandra M. **Clinical application of diffusion tensor imaging and fiber tractography in the management of brainstem cavernous malformations: a systematic review.** *Neurosurg Rev* 2022;45:2027–40 CrossRef Medline
- Lin Y, Lin F, Kang D, et al. **Supratentorial cavernous malformations adjacent to the corticospinal tract: surgical outcomes and predictive value of diffusion tensor imaging findings.** *J Neurosurg* 2018;128:541–52 CrossRef Medline

37. Yuan R, Di X, Kim EH, et al. **Regional homogeneity of resting-state fMRI contributes to both neurovascular and task activation variations.** *Magn Reson Imaging* 2013;31:1492–500 CrossRef Medline
38. Rosenow F, Alonso-Vanegas MA, Baumgartner C, et al; Surgical Task Force, Commission on Therapeutic Strategies of the ILAE. **Cavernoma-related epilepsy: review and recommendations for management—report of the Surgical Task Force of the ILAE Commission on Therapeutic Strategies.** *Epilepsia* 2013;54:2025–35 CrossRef Medline
39. Wahl M, Li YO, Ng J, et al. **Microstructural correlations of white matter tracts in the human brain.** *Neuroimage* 2010;51:531–41 CrossRef Medline
40. Fox MD, Snyder AZ, Vincent JL, et al. **The human brain is intrinsically organized into dynamic, anticorrelated functional networks.** *Proc Natl Acad Sci U S A* 2005;102:9673–78 CrossRef Medline
41. Oouchi H, Yamada K, Sakai K, et al. **Diffusion anisotropy measurement of brain white matter is affected by voxel size: underestimation occurs in areas with crossing fibers.** *AJNR Am J Neuroradiol* 2007;28:1102–06 CrossRef Medline

Connectomic Basis for Tremor Control in Stereotactic Radiosurgical Thalamotomy

E.H. Middlebrooks, R.A. Popple, E. Greco, L. Okromelidze, H.C. Walker, D.A. Lakhani, A.R. Anderson, E.M. Thomas, H.D. Deshpande, B.A. McCullough, N.P. Stover, V.W. Sung, A.P. Nicholas, D.G. Standaert, T. Yacoubian, M.N. Dean, J.A. Roper, S.S. Grewal, M.T. Holland, J.N. Bentley, B.L. Guthrie, and M. Bredel



ABSTRACT

BACKGROUND AND PURPOSE: Given the increased use of stereotactic radiosurgical thalamotomy and other ablative therapies for tremor, new biomarkers are needed to improve outcomes. Using resting-state fMRI and MR tractography, we hypothesized that a “connectome fingerprint” can predict tremor outcomes and potentially serve as a targeting biomarker for stereotactic radiosurgical thalamotomy.

MATERIALS AND METHODS: We evaluated 27 patients who underwent unilateral stereotactic radiosurgical thalamotomy for essential tremor or tremor-predominant Parkinson disease. Percentage postoperative improvement in the contralateral limb Fahn-Tolosa-Marin Clinical Tremor Rating Scale (TRS) was the primary end point. Connectome-style resting-state fMRI and MR tractography were performed before stereotactic radiosurgery. Using the final lesion volume as a seed, “connectivity fingerprints” representing ideal connectivity maps were generated as whole-brain R-maps using a voxelwise nonparametric Spearman correlation. A leave-one-out cross-validation was performed using the generated R-maps.

RESULTS: The mean improvement in the contralateral tremor score was 55.1% (SD, 38.9%) at a mean follow-up of 10.0 (SD, 5.0) months. Structural connectivity correlated with contralateral TRS improvement ($r = 0.52$; $P = .006$) and explained 27.0% of the variance in outcome. Functional connectivity correlated with contralateral TRS improvement ($r = 0.50$; $P = .008$) and explained 25.0% of the variance in outcome. Nodes most correlated with tremor improvement corresponded to areas of known network dysfunction in tremor, including the cerebello-thalamo-cortical pathway and the primary and extrastriate visual cortices.

CONCLUSIONS: Stereotactic radiosurgical targets with a distinct connectivity profile predict improvement in tremor after treatment. Such connectomic fingerprints show promise for developing patient-specific biomarkers to guide therapy with stereotactic radiosurgical thalamotomy.

ABBREVIATIONS: BOLD = blood oxygen level–dependent MRI; DBS = deep brain stimulation; DRTT = dentato-rubro-thalamic tract; SMS = simultaneous multislice; SRS = stereotactic radiosurgery; TRS = Fahn-Tolosa-Marin Clinical Tremor Rating Scale; VIM = ventral intermediate nucleus

Tremor is a debilitating neurologic condition that is seen with multiple disorders, most commonly in essential tremor and Parkinson’s disease.¹ Patients who are refractory to pharmacologic

therapies are potentially candidates for surgical intervention. Deep brain stimulation (DBS) is the current criterion standard surgical treatment; however, not all patients are candidates or wish to undergo DBS. Recently, there has been a resurgence in ablative therapies using incisionless ablative techniques such as stereotactic radiosurgery (SRS) and MR imaging–guided focused ultrasound. While ablative treatment mechanisms might overlap with DBS, little is known on the connectomics of SRS and tremor improvement.

In contrast to traditional “localizationist” models of the brain, a more recent shift to a network, or “connectomic,” model has greatly enhanced our understanding of brain function and pathology.² Such a shift has also occurred in the realm of neuromodulation with recognition of many disorders as “circuitopathies”³ and the need for targeted network surgery, or “connectomic surgery.”⁴ The connectomic model, using MR tractography as a measure of structural connectivity and resting-state fMRI as a measure of

Received September 8, 2022; accepted after revision December 30.

From the Departments of Radiology (E.H.M., E.G., L.O., D.A.L.) and Neurosurgery (E.H.M., S.S.G.), Mayo Clinic, Jacksonville, Florida; Departments of Radiation Oncology (R.A.P., A.R.A., E.M.T., M.B.), Neurology (H.C.W., B.A.M., N.P.S., V.W.S., A.P.N., D.G.S., T.Y., M.N.D.), Radiology (H.D.D.), and Neurosurgery (M.T.H., J.N.B., B.L.G.), University of Alabama at Birmingham, Birmingham, Alabama; Department of Radiology (D.A.L.), West Virginia University, Morgantown, West Virginia; Department of Radiation Oncology (E.M.T.), Ohio State University, Columbus, Ohio; and School of Kinesiology (J.A.R.), Auburn University, Auburn, Alabama.

This prospective clinical trial was funded by Varian Medical Systems Inc under the study protocol RAD 1601: EDGE Radiosurgery for Intractable Essential Tremor and Tremor-Dominant Parkinson’s Disease (NCT03305588).

Please address correspondence to Erik H. Middlebrooks, MD, Department of Radiology, Mayo Clinic Florida, 4500 San Pablo Rd, Jacksonville, FL 32224; e-mail: Middlebrooks.Erik@mayo.edu; @EMiddlebrooksMD

Indicates article with online supplemental data.

<http://dx.doi.org/10.3174/ajnr.A7778>

functional connectivity, has been previously applied to better understand treatment effects in DBS surgery.⁵⁻²² In treatment of tremor, this has led to the consolidation of the role of the cerebello-thalamo-cortical sensorimotor network in explaining many previously reported “sweet spots” in the DBS literature.⁵⁻¹⁴

To date, there has been limited application of the connectomic model to SRS in tremor. Using a combination of resting-state functional MR imaging and MR tractography, we explored whether the therapeutic network for SRS in treatment of tremor displays a “connectome fingerprint” that correlates with tremor improvement. Identification of such a network may provide further insight into the mechanism of tremor improvement and guide targeting in SRS. We also hypothesized that the similarity of any patient’s individual connectivity map to the connectome fingerprint of tremor improvement will predict his or her measured tremor improvement, which may establish feasibility for the potential of connectivity fingerprints to guide SRS targeting.

MATERIALS AND METHODS

This prospective clinical trial was approved by the University of Alabama at Birmingham institutional review board. All patients gave verbal and written consent. The trial was registered at <https://www.clinicaltrials.gov/> under trial NCT03305588. Subjects were recruited in collaboration with the University of Alabama at Birmingham Neurology, Neurosurgery, Movement Disorders, and Radiation Oncology Departments. Patients with medically refractory essential tremor or tremor-dominant Parkinson disease older than 18 years of age with Eastern Cooperative Oncology Group Performance Status of ≤ 2 were included. Patients were not candidates for DBS on the basis of either medical/surgical comorbidities or by their own choice. Patients were ineligible if they had prior brain radiosurgery or therapeutic brain radiation therapy or if there was a contraindication to MR imaging.

Imaging Protocol

Before thalamotomy, patients were scanned on a 3T Magnetom Prisma (Siemens) scanner with a high-performance, 80 mT/m gradient system and a 64-channel head/neck coil. Patients’ heads were tightly packed in the head coil to minimize motion.

Diffusion imaging was obtained with a spin-echo EPI sequence using simultaneous multislice (SMS) excitation. A total of 64 diffusion directions were obtained with a b-value = 1500 s/mm² plus 6 B₀ volumes without diffusion-weighting. The diffusion scan was repeated with an opposing phase-encoding direction for distortion correction. Additional relevant parameters include TR = 3.3 seconds, TE = 90 ms, SMS factor = 4, in-plane acceleration = 2, phase partial Fourier = 6/8, receiver bandwidth = 1232 Hz/px, echo spacing = 0.94 ms, EPI factor = 140, in-plane resolution = 1.5 × 1.5 mm, section thickness = 1.5 mm, with scan time = 4 minutes and 21 seconds per acquisition.

A connectome-style resting-state fMRI was acquired with a multiecho blood oxygen level-dependent (BOLD) gradient-echo EPI sequence using SMS excitation. The temporal SNR of BOLD imaging is generally lower in subcortical regions due to many factors, including the distance from the receive coil and increased physiologic noise. To address this issue, we used a multiecho BOLD approach that significantly improves subcortical

connectivity measures.²³ Additionally, the use of a reduced TR with high spatial resolution and a long, connectome-style BOLD acquisition has all been shown to improve the statistical analysis of resting-state fMRI data. Relevant parameters include the following: TR = 1.5 seconds, echo times = 12.4, 34.3, and 56.2 ms, flip angle = 65°, SMS factor = 4, in-plane acceleration = 2, phase partial Fourier = 6/8, receiver bandwidth = 1850 Hz/px, echo spacing = 0.66 ms, EPI factor = 81, in-plane resolution = 2.0 × 2.0 mm, section thickness = 2.0 mm. The scan was repeated with opposing phase-encoding directions to account for directional bias. A total of 1180 measurements were obtained with a total scan time of 31 minutes and 28 seconds.

A T1-weighted MPRAGE sequence was used for structural registration and performed before SRS. At 3 months after SRS, 3D T1-weighted images were repeated with intravenous contrast. See the Online Supplemental Data for sequence details.

SRS Procedure

Frameless SRS was performed using a thermoplastic mask with an open face molded to the patient’s head. Plans were created using the Eclipse treatment planning system (Varian Medical Systems), and the dose was calculated using either the Analytical Anisotropic Algorithm or AcurosXB algorithm (Varian Eclipse Treatment Planning System) with grid spacing of 1 mm. Patients were treated using an Edge (Varian) linear accelerator equipped with a high-definition multileaf collimator and a 10 MV flattening-filter-free beam by using the virtual cone technique.²⁴ Optical surface guidance was used to monitor the patient position during treatment.²⁵ For full details of the procedure, see the Online Supplemental Data .

Clinical Testing

Before SRS, a baseline Fahn-Tolosa-Marin Clinical Tremor Rating Scale (TRS) was assessed. The TRS was repeated at each follow-up assessment after SRS, and the last documented TRS score was used for analysis. TRS was assessed by a single examiner who was blinded to the imaging results at the time of assessment. The primary outcome measure for the study was a percentage decrease in contralateral upper and lower body tremors, measured as the sum of the lateralized TRS scores from Part I on the body side opposite of the treatment hemisphere. Any disease-related medications were maintained at preoperative doses for follow-up.

Image Preprocessing

The postoperative postcontrast T1-weighted images were coregistered to the preoperative T1-weighted images using Advanced Normalization Tools (<http://stnava.github.io/ANTs/>). The final lesion location was manually segmented as the enhancing region on the 3-month postoperative postcontrast T1-weighted images.

The diffusion data underwent eddy current correction, section-to-volume movement correction, and outlier replacement in FSL “eddy_cuda” (https://git.fmrib.ox.ac.uk/fsl/conda/fsl-eddy_cuda) on a custom-built Linux workstation using 3 NVIDIA Quadro P5000 GPUs. Susceptibility-induced distortions were corrected with FSL “topup” (<https://fsl.fmrib.ox.ac.uk/fslwiki/topup>) using the repeat acquisitions in opposing phase-encoding directions.²⁶ FSL “BEDPOSTX_GPU” (<https://users.fmrib.ox.ac>

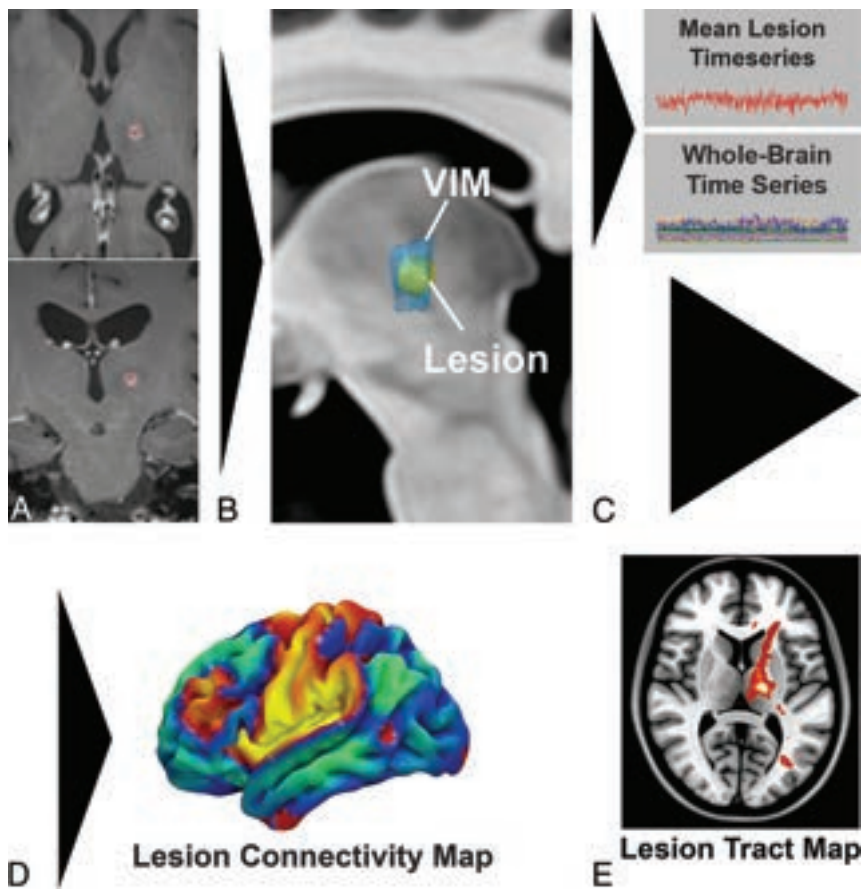


FIG 1. Pipeline for generation of a single-subject lesion connectivity map and lesion tract map (A and B). The lesion is segmented from the posttreatment MR imaging (C). The mean BOLD timeseries for the lesion is extracted and correlated to all other brain voxels. D, The resulting *t*-score map is a patient-specific lesion connectivity map. E, The lesion is used as a seed region to generate a patient-specific lesion tract map representing the probability of all streamlines connected to the lesion.

uk/~moisesf/Bedpostx_GPU/) was used to estimate the orientation distribution functions with 3 fiber orientations modeled per voxel. The diffusion data were coregistered to the T1 MPRAGE using a boundary-based registration implemented in FreeSurfer (<http://surfer.nmr.mgh.harvard.edu>). An exclusion mask was generated to include the ventricles and contralateral hemisphere white matter.

The multiecho BOLD data were initially preprocessed in AFNI, Version 22.0.06 (<https://afni.nimh.nih.gov/>). Preprocessing steps included realignment, spatial smoothing of 4-mm full width at half maximum, and coregistration to the T1 MPRAGE. Denoising of the data was performed with multiecho independent component analysis using TE-dependent analysis implemented in AFNI. Last, motion censoring (framewise displacement of >0.3 mm) and outlier detection were performed using default values in AFNI. Global mean signal regression and regression of motion parameters were also performed.

Connectome Generation

Probabilistic tractography was performed using “probtrackx2_gpu” (https://users.fmrib.ox.ac.uk/~moisesf/Probtrackx_GPU/index.html) from the FMRIB Software Library, Version 6.0.3 ([\[fsl.fmrib.ox.ac.uk\]\(http://fsl.fmrib.ox.ac.uk\)\) in each of the subjects, with 250,000 samples, a curvature threshold of 0.2, modified Euler streamlining \(<https://mycareerwise.com/programming/category/numerical-analysis/modified-euler-method/>\), and a step length of 0.5 mm. A region-of-avoidance was added to exclude the internal capsule and deep white matter of the contralateral hemisphere. Because no plausible fibers or existing evidence implicates tracts connecting the thalamus with the contralateral hemisphere via the capsular fibers, such connections are most likely spurious fibers and their inclusion leads to an artificial increase in directions of freedom with resulting inflation of *P* values. Probabilistic tractography was performed using the segmented lesion as the seed region to generate “lesion tract maps” of all tracts passing through the lesion \(Fig 1\).](http://</p>
</div>
<div data-bbox=)

The preprocessed BOLD resting-state fMRI data underwent a seed-based correlation analysis across the entire brain for each subject using the segmented lesion as the seed point to generate a whole-brain “lesion connectivity map” (Fig 1). The resulting *t*-maps were used for subsequent analysis.

The structural images, lesion connectivity maps, and lesion tract maps were then normalized into Montreal Neurological Institute template space, as described in the Online Supplemental

Data. The right hemisphere lesion connectivity maps and lesion tract maps were nonlinearly flipped to the left hemisphere for comparison across the cohort.

Connectome Analysis

To determine the relationship between structural connectivity and contralateral tremor improvement, we generated an ideal tract fingerprint for the cohort. First, the individual lesion tract maps for each subject were correlated with percentage improvement in the contralateral tremor to generate a Spearman rank-correlation coefficient on a voxel-by-voxel basis. The resultant group R-map, or tract fingerprint, represents an optimal voxel-by-voxel tract map for contralateral tremor improvement.

To assess the significance of the tract fingerprint in predicting outcomes, we performed a leave-one-out cross-validation. An R-map was created by correlating tracts traversing the lesion with the contralateral TRS improvement using all patients except one, withheld for validation. The probabilistic tract map from the left-out patient was then used to calculate spatial similarity (measured via the Fisher *z*-transformed spatial correlation coefficient) with the tract fingerprint generated from the remainder of the cohort. The similarity index for each left-out subject was then correlated

Demographic and clinical outcome data

Criteria	
Age at treatment (yr)	72.3 (SD, 13.1)
Male sex (No.) (%)	17 (63.0%)
Essential tremor (No.) (%)	22 (81.5%)
Parkinson disease (No.) (%)	4 (14.8%)
ET + PD (No.) (%)	1 (3.7%)
Baseline contralateral TRS score (mean)	6.8 (SD, 4.3)
Baseline ipsilateral TRS score (mean)	4.9 (SD, 4.3)
Baseline midline TRS score (mean)	2.5 (SD, 2.8)
Follow-up duration (mean) (mo)	10.0 (SD, 5.0)
Postoperative contralateral TRS improvement (mean)	55.1% (SD, 38.9%)
Postoperative ipsilateral TRS improvement (mean)	9.9% (SD, 61.8%)
Postoperative midline TRS improvement (mean)	27.2% (SD, 90.0%)

Note:—ET indicates essential tremor; PD, Parkinson disease.

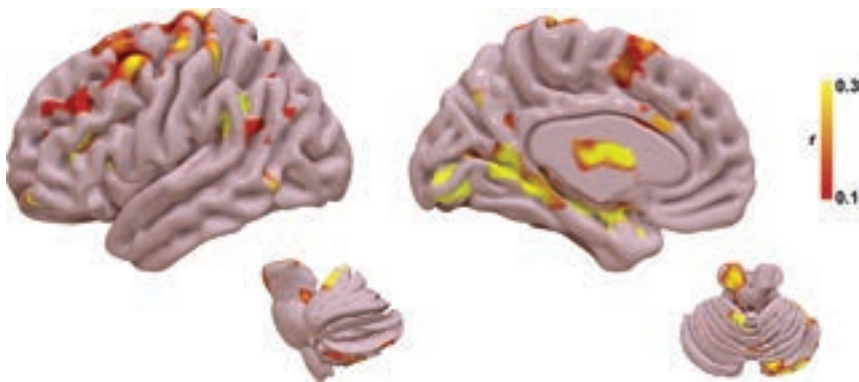


FIG 2. Tract fingerprint representing the ideal tract connectivity pattern for tremor improvement. Commonly implicated areas of abnormality in tremor are identified, including the cerebello-thalamo-cortical motor network, as well as striate and extrastriate cortical regions.

versus the measured tremor improvement using the Spearman correlation.

Next, the process was repeated using the lesion connectivity map generated from the resting-state fMRI for each individual subject to create a functional fingerprint.

Statistics

Demographic data were expressed as mean, range, and SD, as appropriate. The primary outcome measure was the percentage change in the contralateral TRS. Correlation of lesion volume and contralateral TRS improvement was assessed with a non-parametric Spearman correlation. Statistical significance was considered as $P < .05$.

RESULTS

Demographic and Clinical Results

Forty total patients were enrolled in the clinical trial. Three died of unrelated causes before follow-up, 1 declined treatment, 3 patients were not eligible for 3T MR imaging, and 6 patients were lost to follow-up for their imaging and/or clinical assessment, leaving 27 patients for analysis. Demographic and group outcome data are listed in the Table. Twenty-three (85.2%) patients underwent left thalamotomy, while 4 (14.8%) had right thalamotomy. Twenty patients (74.0%) had a $\geq 50\%$ reduction in contralateral

tremor, while 7 patients (26.0%) had $< 50\%$ reduction in contralateral tremor. The mean improvement in the contralateral tremor score was 55.1% (SD, 38.9%). All patients had at least 6 months of clinical follow-up with the mean duration of follow-up being 10.0 (SD, 5.0) months. Adverse events determined to be related to radiosurgery included 1 subject with grade I sensory deficits consisting of numbness in the left first and second digits and left-sided mouth and buccal mucosa dysesthesia occurring 10 months after radiosurgery. Two subjects experienced grade II radiation necrosis consistent with hyper-response. One of these subjects experienced right-foot drag, right-hand grip weakness, right-arm proprioceptive loss, mild expressive aphasia, bilateral lip paresthesia, and left-sided headache occurring 7 months after radiosurgery. One subject experienced falls, dysarthria, right-arm and right-leg weakness, and incoordination occurring 11 months after radiosurgery. Both subjects with grade II radionecrosis reported near-resolution of tremor at 4 months after radiosurgery. All 3 subjects with radiosurgery-related adverse events were treated with tapered corticosteroids and

bevacizumab infusions. There were no grade III–V adverse events related to radiosurgery.

Structural Connectome Analysis

The tract R-map, or tract fingerprint, is shown in Fig 2. The cerebello-thalamo-cortical somatosensory network is a primary component of the affected network, including the primary somatosensory cortex, supplementary motor area, premotor cortex, ventral thalamic nuclei, and cerebellum—primarily cerebellar lobules IV, V, VI, and VIII B, all areas implicated in the cerebellar somatosensory network.²⁷ Additional connectivity to temporal, occipital, and prefrontal areas is also present. The tract pathways correlated to tremor improvement (Fig 3) show primary involvement of the dentato-rubro-thalamic tract (DRTT); thalamocortical tracts to the primary sensorimotor, supplementary motor area, and prefrontal cortex; as well as the pallidothalamic tracts.

Results of the leave-one-out cross-validation of the tractography are shown in Fig 4A. The structural connectivity correlated with measured improvement in contralateral TRS ($r = 0.52$; $P = .006$) and could explain 27.0% of the variance in outcome.

Functional Connectome Analysis

The functional R-map, or functional fingerprint, is shown in Fig 5. The functional connectivity data further corroborate the structural connectivity, showing a correlation with cerebello-thalamo-cortical

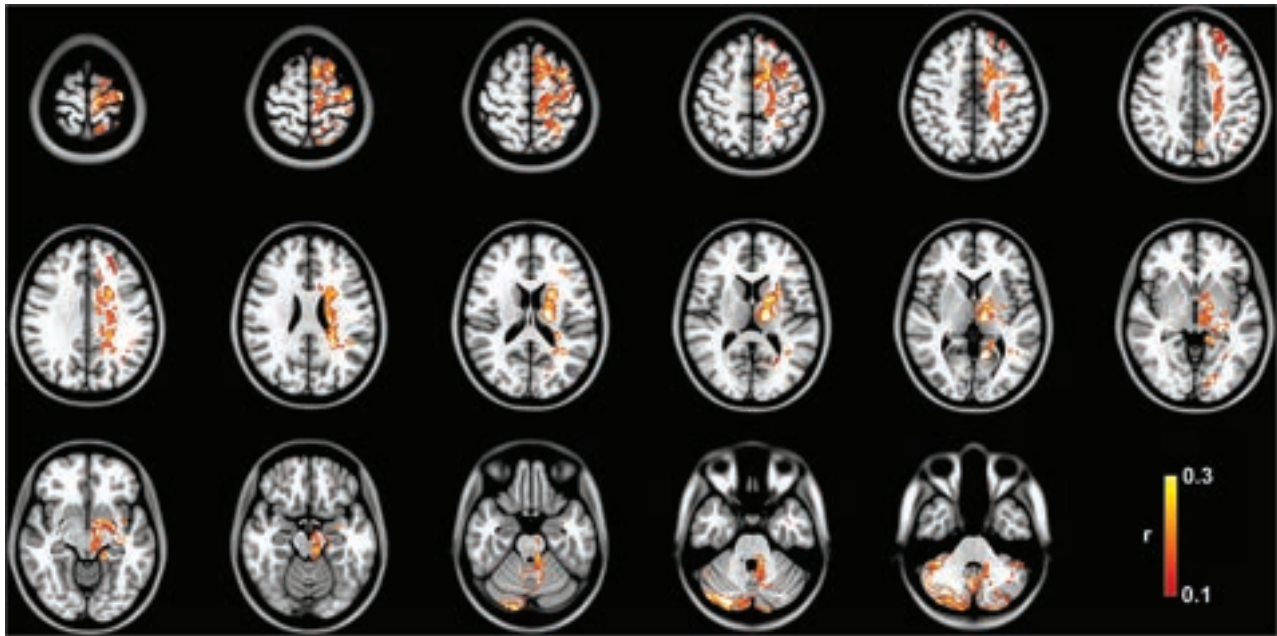


FIG 3. Group tract R-map of pathways most correlated with tremor improvement.

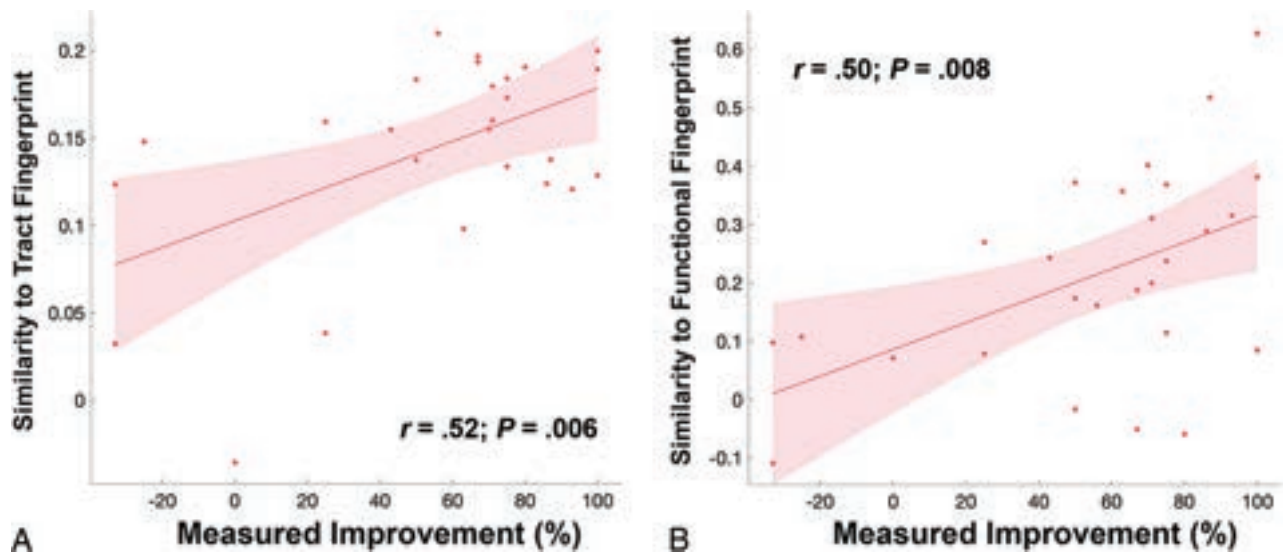


FIG 4. A, Leave-one-out cross-validation of the tract fingerprint shows greater similarity of the individual's lesion tract map to the fingerprint map predicted measured improvement in tremor ($r = 0.52$; $P = .006$). B, Leave-one-out cross-validation of the functional fingerprint also shows that greater similarity of the individual's lesion functional map to the fingerprint map predicted measured improvement in tremor ($r = 0.50$; $P = .008$).

somatosensory network, in particular the primary somatosensory cortex, ventral thalamic nuclei, and cerebellar lobules IV, V, VI, and VIII B. Additional connectivity to temporal, occipital, and prefrontal areas is also present. Results for the leave-one-out cross-validation of the functional connectivity are shown in Fig 4B. The functional connectivity correlated with measured improvement in contralateral TRS ($r = 0.50$; $P = .008$) and could explain 25.0% of the variance in outcome.

DISCUSSION

In this study, we show that improvement in tremor after SRS thalamotomy is significantly correlated with a distinct pattern of

structural and functional connectivity, primarily via the cerebello-thalamo-cortical pathway. This network has been previously demonstrated to be an important driver in tremor pathophysiology and a target for other forms of neuromodulation, such as DBS. Our findings indicate that a significant amount of variance in tremor outcomes after SRS are driven by an identifiable network topology, which may serve as a new therapeutic biomarker for SRS targeting. As opposed to other forms of neuromodulation, such as DBS, there are no intraoperative biomarkers to validate target selection in SRS. By application of the concept of connectomic surgery,¹² we have shown the potential of a lesion connectome fingerprint to predict tremor improvement from a given SRS target using both MR tractography and resting-state fMRI.

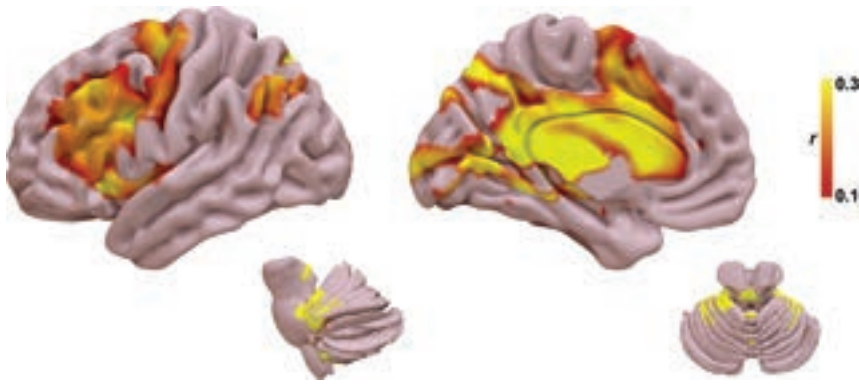


FIG 5. Functional fingerprint representing the ideal tract connectivity pattern for tremor improvement. Similar to the tract fingerprint, commonly implicated areas of abnormality in tremor are identified, including the cerebello-thalamo-cortical motor network as well as the striate and extrastriate cortical regions.

Our approach may enhance network-specific targeting in SRS and provide patient-specific biomarkers.

The optimal target for neuromodulation of tremor has been debated for decades. Most commonly proposed targets have been the ventral intermediate nucleus (VIM) and the posterior subthalamic area, including the caudal zona incerta, prelemniscal radiations, and subthalamic nucleus.¹¹ More recently, connectivity studies in DBS have suggested that these targets are unified by a common network and all targets overlap with the DRTT.^{7,14} The role of the DRTT in tremor improvement has been well-demonstrated in DBS,^{5-14,28-34} but limited data exist on the use of tractography in surgical planning for SRS.^{35,36} Historically, the DRTT is defined by efferent cerebellar fibers originating in the dentate nucleus of the cerebellum that traverse superiorly through the ipsilateral superior cerebellar peduncle, decussate in the midbrain, pass the red nucleus (but without synapsing in the red nucleus), en route to the contralateral VIM and posterior ventral oralis nucleus.^{37,38} Tracts ultimately reach the contralateral primary motor cortex and premotor/supplementary motor cortex from the VIM and ventral oralis nucleus, respectively. More recently, a small number of DRTT fibers have been shown to follow a similar path but without decussation in the midbrain and extend to the ipsilateral thalamus; however, these tracts likely have less of a role in motor function.^{37,38} Our study adds further evidence to the role of the DRTT in the surgical treatment of tremor, particularly implicating a similar therapeutic target in SRS as seen in DBS.

From an anatomic perspective, nodes within the fingerprint maps correspond to areas known to exhibit network abnormalities in tremor. First, the fingerprint network distribution agrees with established network abnormalities attributed to the development of tremor via tremor-specific frequency synchronization within multiple nodes in the cerebello-thalamo-cortical pathway, including the cerebellum, thalamus, primary sensorimotor cortex, supplementary motor cortex, and premotor cortex.^{39,40} Similar to prior work in DBS for essential tremor, we found that a lesion network fingerprint that includes the motor and supplementary motor networks also correlates with tremor improvement in SRS.^{7,14} Additionally, there was correlation with cerebellar lobules

IV, V, and VI, which are regions previously shown to be abnormal in essential tremor and part of the sensorimotor network.⁴¹ Taken together, our results suggest that the therapeutic network involved in SRS thalamotomy provides evidence for targeting biomarkers similar to those in the existing DBS literature.

Most interesting, we also found structural and functional connectivity to the primary and extrastriate visual cortex as part of the tremor connectome fingerprint. While not historically considered a major part of tremor pathogenesis, the primary and associative visual cortices have been the subject of more recent investigation of the role of the visuospatial network in tremor augmen-

tion. Archer et al⁴² showed that visual feedback exacerbates tremor severity in essential tremor and functional changes in extrastriate areas correlate with the worsening of tremor. Likewise, postsurgical alterations in brain connectivity have been observed in the visual cortex that correlated with tremor improvement in MR imaging-guided focused ultrasound⁴³ and SRS;⁴⁴ however, direct activation of this region was not observed with active DBS.⁴⁵ Pretreatment functional connectivity between the ventrolateral thalamus and visual association areas has also been shown as a predictor of tremor improvement after SRS.⁴⁶ Further studies are needed to understand the true causal effect of visual network connectivity versus a coincident change in addition to the cerebello-thalamo-cortical motor network.

Several limitations to our study are noteworthy. Although tremor outcomes were gathered prospectively, the connectomics analyses were applied in retrospect. Thus, future studies would benefit from examining the effects of prospective targeting based on the proposed biomarkers. SRS thalamotomy was effective for tremor and well-tolerated overall. Larger cohorts, however, are needed to expand on these results and better assess the frequency of potential adverse effects. Additionally, intersubject variations in the temporal evolution of the lesion may result in fluctuation of the clinical response and are relatively unpredictable pre-SRS. We chose to use the 3-month post-SRS examination because this was thought to most accurately represent the intended target location with less variability among patients. Last, there are inherent limitations to MR tractography and resting-state fMRI that have been well-described.^{6,31,47} We used a robust probabilistic tracking approach and a lengthy fMRI acquisition to increase the robustness of our connectome modeling; however, these protocols may be challenging to implement in routine clinical care, and further studies will be needed to explore reproducibility with less robust data sets.

CONCLUSIONS

Using a connectomic approach, we have shown that SRS targets with a distinct connectivity profile predict posttreatment tremor improvement. Among these are networks implicated in tremor pathogenesis, including the cerebello-thalamo-cortical network

and visual networks. The use of such connectomic fingerprints may provide a patient-specific biomarker for SRS thalamotomy; however, validation of this approach for use in targeting will require further studies to prospectively validate these results.

Disclosure forms provided by the authors are available with the full text and PDF of this article at www.ajnr.org.

REFERENCES

1. Louis ED, Ferreira JJ. **How common is the most common adult movement disorder? Update on the worldwide prevalence of essential tremor.** *Mov Disord* 2010;25:534–41 CrossRef Medline
2. Sporns O, Tononi G, Kötter R. **The human connectome: a structural description of the human brain.** *PLoS Comput Biol* 2005;1:e42 CrossRef Medline
3. Lozano AM, Lipsman N. **Probing and regulating dysfunctional circuits using deep brain stimulation.** *Neuron* 2013;77:406–24 CrossRef Medline
4. Henderson JM. **“Connectomic surgery”: diffusion tensor imaging (DTI) tractography as a targeting modality for surgical modulation of neural networks.** *Front Integr Neurosci* 2012;6:15 CrossRef Medline
5. Middlebrooks EH, Domingo RA, Vivas-Buitrago T, et al. **Neuroimaging advances in deep brain stimulation: review of indications, anatomy, and brain connectomics.** *AJNR Am J Neuroradiol* 2020;41:1558–68 CrossRef Medline
6. Middlebrooks EH, Okromelidze L, Carter RE, et al. **Directed stimulation of the dentato-rubro-thalamic tract for deep brain stimulation in essential tremor: a blinded clinical trial.** *Neuroradiol J* 2022;35:203–12 CrossRef Medline
7. Middlebrooks EH, Okromelidze L, Wong JK, et al. **Connectivity correlates to predict essential tremor deep brain stimulation outcome: evidence for a common treatment pathway.** *Neuroimage Clin* 2021;32:102846 CrossRef Medline
8. Middlebrooks EH, Tuna IS, Almeida L, et al. **Structural connectivity-based segmentation of the thalamus and prediction of tremor improvement following thalamic deep brain stimulation of the ventral intermediate nucleus.** *Neuroimage Clin* 2018;20:1266–73 CrossRef Medline
9. Neudorfer C, Kroneberg D, Al-Fatly B, et al. **Personalizing deep brain stimulation using advanced imaging sequences.** *Ann Neurol* 2022;91:613–28 CrossRef Medline
10. Tsuboi T, Wong JK, Eisinger RS, et al. **Comparative connectivity correlates of dystonic and essential tremor deep brain stimulation.** *Brain* 2021;144:1774–86 CrossRef Medline
11. Wong JK, Hess CW, Almeida L, et al. **Deep brain stimulation in essential tremor: targets, technology, and a comprehensive review of clinical outcomes.** *Expert Rev Neurother* 2020;20:319–31 CrossRef Medline
12. Wong JK, Middlebrooks EH, Grewal SS, et al. **A comprehensive review of brain connectomics and imaging to improve deep brain stimulation outcomes.** *Mov Disord* 2020;35:741–51 CrossRef Medline
13. Wong JK, Patel B, Middlebrooks EH, et al. **Connectomic analysis of unilateral dual-lead thalamic deep brain stimulation for treatment of multiple sclerosis tremor.** *Brain Commun* 2022;4:fcac063 CrossRef Medline
14. Al-Fatly B, Ewert S, Kubler D, et al. **Connectivity profile of thalamic deep brain stimulation to effectively treat essential tremor.** *Brain* 2019;142:3086–98 CrossRef Medline
15. Middlebrooks EH, Grewal SS, Stead M, et al. **Differences in functional connectivity profiles as a predictor of response to anterior thalamic nucleus deep brain stimulation for epilepsy: a hypothesis for the mechanism of action and a potential biomarker for outcomes.** *Neurosurg Focus* 2018;45:E7 CrossRef Medline
16. Middlebrooks EH, He X, Grewal SS, et al. **Neuroimaging and thalamic connectomics in epilepsy neuromodulation.** *Epilepsy Res* 2022;182:106916 CrossRef Medline
17. Middlebrooks EH, Jain A, Okromelidze L, et al. **Acute brain activation patterns of high- versus low-frequency stimulation of the anterior nucleus of the thalamus during deep brain stimulation for epilepsy.** *Neurosurgery* 2021;89:901–08 CrossRef Medline
18. Middlebrooks EH, Lin C, Okromelidze L, et al. **Functional activation patterns of deep brain stimulation of the anterior nucleus of the thalamus.** *World Neurosurg* 2020;136:357–63.e2 CrossRef Medline
19. Tsuboi T, Charbel M, Peterside DT, et al. **Pallidal connectivity profiling of stimulation-induced dyskinesia in Parkinson’s disease.** *Mov Disord* 2021;36:380–88 CrossRef Medline
20. Horn A, Reich M, Vorwerk J, et al. **Connectivity predicts deep brain stimulation outcome in Parkinson disease.** *Ann Neurol* 2017;82:67–78 CrossRef Medline
21. Li N, Baldermann JC, Kibleur A, et al. **A unified connectomic target for deep brain stimulation in obsessive-compulsive disorder.** *Nat Commun* 2020;11:3364 CrossRef Medline
22. Reich MM, Horn A, Lange F, et al. **Probabilistic mapping of the anti-dystonic effect of pallidal neurostimulation: a multicentre imaging study.** *Brain* 2019;142:1386–98 CrossRef Medline
23. Kundu P, Inati SJ, Evans JW, et al. **Differentiating BOLD and non-BOLD signals in fMRI time series using multi-echo EPI.** *Neuroimage* 2012;60:1759–70 CrossRef Medline
24. Popple RA, Wu X, Brezovich IA, et al. **The virtual cone: a novel technique to generate spherical dose distributions using a multi-leaf collimator and standardized control-point sequence for small target radiation surgery.** *Adv Radiat Oncol* 2018;3:421–30 CrossRef Medline
25. Li G, Ballangrud A, Kuo LC, et al. **Motion monitoring for cranial frameless stereotactic radiosurgery using video-based three-dimensional optical surface imaging.** *Med Phys* 2011;38:3981–94 CrossRef Medline
26. Graham MS, Drobnjak I, Jenkinson M, et al. **Quantitative assessment of the susceptibility artefact and its interaction with motion in diffusion MRI.** *PLoS One* 2017;12:e0185647 CrossRef Medline
27. Buckner RL, Krienen FM, Castellanos A, et al. **The organization of the human cerebellum estimated by intrinsic functional connectivity.** *J Neurophysiol* 2011;106:2322–45 CrossRef Medline
28. Middlebrooks EH, Grewal SS, Holanda VM. **Complexities of connectivity-based DBS targeting: rebirth of the debate on thalamic and subthalamic treatment of tremor.** *Neuroimage Clin* 2019;22:101761 CrossRef Medline
29. Middlebrooks EH, Tipton P, Okromelidze L, et al. **Deep brain stimulation for tremor: direct targeting of a novel imaging biomarker.** *Ann Neurol* 2022;92:341–42 CrossRef Medline
30. Neudorfer C, Kroneberg D, Al-Fatly B, et al. **Reply to “Deep Brain Stimulation for Tremor: Direct Targeting of a Novel Imaging Biomarker.”** *Ann Neurol* 2022;92:343–44 CrossRef Medline
31. Akram H, Dayal V, Mähknecht P, et al. **Connectivity derived thalamic segmentation in deep brain stimulation for tremor.** *Neuroimage Clin* 2018;18:130–42 CrossRef Medline
32. Coenen VA, Allert N, Paus S, et al. **Modulation of the cerebello-thalamo-cortical network in thalamic deep brain stimulation for tremor: a diffusion tensor imaging study.** *Neurosurgery* 2014;75:657–69; discussion 6697–70 CrossRef Medline
33. Coenen VA, Sajonz B, Prokop T, et al. **The dentato-rubro-thalamic tract as the potential common deep brain stimulation target for tremor of various origin: an observational case series.** *Acta Neurochir (Wien)* 2020;162:1053–66 CrossRef Medline
34. Coenen VA, Varkuti B, Parpaley Y, et al. **Postoperative neuroimaging analysis of DRT deep brain stimulation revision surgery for complicated essential tremor.** *Acta Neurochir (Wien)* 2017;159:779–87 CrossRef Medline
35. Kim W, Chivukula S, Hauptman J, et al. **Diffusion tensor imaging-based thalamic segmentation in deep brain stimulation for chronic pain conditions.** *Stereotact Funct Neurosurg* 2016;94:225–34 CrossRef Medline
36. Kim W, Sharim J, Tenn S, et al. **Diffusion tractography imaging-guided frameless linear accelerator stereotactic radiosurgical**

- thalamotomy for tremor: case report.** *J Neurosurg* 2018;128:215–21 CrossRef Medline
37. Gallay MN, Jeanmonod D, Liu J, et al. **Human pallidothalamic and cerebellothalamic tracts: anatomical basis for functional stereotactic neurosurgery.** *Brain Struct Funct* 2008;212:443–63 CrossRef Medline
38. Petersen KJ, Reid JA, Chakravorti S, et al. **Structural and functional connectivity of the nondecussating dentato-rubro-thalamic tract.** *Neuroimage* 2018;176:364–71 CrossRef Medline
39. Hellwig B, Haussler S, Schelter B, et al. **Tremor-correlated cortical activity in essential tremor.** *Lancet* 2001;357:519–23 CrossRef Medline
40. McAuley JH, Marsden CD. **Physiological and pathological tremors and rhythmic central motor control.** *Brain* 2000;123:1545–67 CrossRef Medline
41. Nicoletti V, Cecchi P, Pesaresi I, et al. **Cerebello-thalamo-cortical network is intrinsically altered in essential tremor: evidence from a resting state functional MRI study.** *Sci Rep* 2020;10:16661 CrossRef Medline
42. Archer DB, Coombes SA, Chu WT, et al. **A widespread visually-sensitive functional network relates to symptoms in essential tremor.** *Brain* 2018;141:472–85 CrossRef Medline
43. Xiong Y, Han D, He J, et al. **Correlation of visual area with tremor improvement after MRgFUS thalamotomy in Parkinson's disease.** *J Neurosurg* 2022;136:681–88 CrossRef Medline
44. Tuleasca C, Najdenovska E, Regis J, et al. **Clinical response to VIM's thalamic stereotactic radiosurgery for essential tremor is associated with distinctive functional connectivity patterns.** *Acta Neurochir (Wien)* 2018;160:611–24 CrossRef Medline
45. Gibson WS, Jo HJ, Testini P, et al. **Functional correlates of the therapeutic and adverse effects evoked by thalamic stimulation for essential tremor.** *Brain* 2016;139:2198–210 CrossRef Medline
46. Tuleasca C, Najdenovska E, Régis J, et al. **Pretherapeutic motor thalamus resting-state functional connectivity with visual areas predicts tremor arrest after thalamotomy for essential tremor: tracing the cerebello-thalamo-visuo-motor network.** *World Neurosurg* 2018;117:e438–49 CrossRef Medline
47. Schlaier JR, Beer AL, Faltermeier R, et al. **Probabilistic vs. deterministic fiber tracking and the influence of different seed regions to delineate cerebellar-thalamic fibers in deep brain stimulation.** *Eur J Neurosci* 2017;45:1623–33 CrossRef Medline

Use of the Woven EndoBridge Device for Sidewall Aneurysms: Systematic Review and Meta-analysis

A. Rodriguez-Calienes,¹ J. Vivanco-Suarez,² M. Galecio-Castillo,³ C.B. Zevallos,⁴ M. Farooqui,⁵ M. Malaga,⁶ C. Moran-Mariños,⁷ N.F. Fanning,⁸ O. Algin,⁹ E.A. Samaniego,¹⁰ B. Pabon,¹¹ N. Mouchtouris,¹² D.J. Altschul,¹³ P. Jabbour,¹⁴ and S. Ortega-Gutierrez¹⁵



ABSTRACT

BACKGROUND: The Woven EndoBridge device was originally approved to treat intracranial wide-neck saccular bifurcation aneurysms. Recent studies have suggested its use for the treatment of sidewall intracranial aneurysms with variable success.

PURPOSE: Our aim was to evaluate the safety and efficacy of the Woven EndoBridge device for sidewall aneurysms using a meta-analysis of the literature.

DATA SOURCES: We performed a systematic review of all studies including patients treated with the Woven EndoBridge device for sidewall aneurysms from inception until May 2022 on Scopus, EMBASE, MEDLINE, the Web of Science, and the Cochrane Central Register of Controlled Trials.

STUDY SELECTION: Ten studies were selected, and 285 patients with 288 sidewall aneurysms were included.

DATA ANALYSIS: A random-effects meta-analysis of proportions using a generalized linear mixed model was performed as appropriate. Statistical heterogeneity across studies was assessed with I^2 statistics.

DATA SYNTHESIS: The adequate occlusion rate at last follow-up was 89% (95% CI, 81%–94%; $I^2 = 0\%$), the composite safety outcome was 8% (95% CI, 3%–17%; $I^2 = 34\%$), and the mortality rate was 2% (95% CI, 1%–7%; $I^2 = 0\%$). Aneurysm width (OR = 0.5; $P = .03$) was the only significant predictor of complete occlusion.

LIMITATIONS: Given the level of evidence, our results should be interpreted cautiously until confirmation from larger prospective studies is obtained.

CONCLUSIONS: The initial evidence evaluating the use of the Woven EndoBridge device for the treatment of wide-neck sidewall intracranial aneurysms has demonstrated high rates of adequate occlusion with low procedural complications. Our findings favor the consideration of the Woven EndoBridge device as an option for the treatment of sidewall aneurysms.

ABBREVIATIONS: GCP = good clinical practice; NOS = Newcastle-Ottawa Quality Assessment Scale; WEB = Woven EndoBridge

The endovascular treatment of wide-neck bifurcation aneurysms has prompted the development of new techniques and devices.^{1–3} As a result, intrasaccular flow disruption with the Woven EndoBridge (WEB; MicroVention) device has emerged

as a safe and effective alternative without the requirement of long-term antiplatelet therapy. Good clinical practice (GCP) studies developed in Europe and the United States led to the approval of the WEB device by the US Food and Drug Administration for the treatment of adults with intracranial wide-neck bifurcation aneurysms.^{4–8} Subsequently, several post-marketing prospective studies with long-term follow-up have confirmed the good long-term efficacy, stability, and safety of the WEB for the treatment of bifurcation aneurysms.⁹

Received November 9, 2022; accepted after revision December 18.

From the Departments of Neurology (A.R.-C., J.V.-S., M.G.-C., C.B.Z., M.F., M.M.) and Neurology, Neurosurgery and Radiology (E.A.S., S.O.-G.), University of Iowa Hospitals and Clinics, Iowa City, Iowa; Neuroscience, Clinical Effectiveness and Public Health Research Group (A.R.-C.), Universidad Científica del Sur, Lima, Peru; Unidad de Investigación en Bibliometría (C.M.-M.), Universidad San Ignacio de Loyola, Lima, Peru; Department of Neuroradiology (N.F.F.), Cork University Hospital, Cork, Ireland; Department of Radiology (O.A.), Bilkent City Hospital, Ankara, Turkey; National MR Research Center (O.A.), Bilkent University, Ankara, Turkey; Radiology Department (O.A.), Medical Faculty, Yıldırım Beyazıt University, Ankara, Turkey; Department of Neurosurgery (B.P.), AngioTeam, Medellin, Colombia; Department of Neurological Surgery (N.M., P.J.), Thomas Jefferson University Hospital, Philadelphia, Pennsylvania; and Department of Neurological Surgery (D.J.A.), Montefiore Medical Center, Bronx, New York.

Please address correspondence to Santiago Ortega-Gutierrez, MD, Department of Neurology, Neurosurgery, and Radiology, University of Iowa Hospitals and Clinics, Carver Pavilion, 2150, 200 Hawkins Dr, Iowa City, IA 52242; e-mail: santy-ortega@uiowa.edu; @AaronCalienes

Indicates article with online supplemental data.

<http://dx.doi.org/10.3174/ajnr.A7766>

Following the initial release and experience with the WEB device, several adjustments and innovations to its design and delivery system have been made.^{10,11} Of note, the device is currently available in smaller sizes with improved visibility. In addition, the delivery system has decreased its profile to 0.017-inch microcatheters for WEB sizes 3–7 mm.¹² With these adjustments, the use of the WEB has gradually evolved to include smaller and distally located aneurysms. Furthermore, several published reports have suggested that expanding initial indications might be feasible while maintaining a safe profile.^{10,13–16}

Hence, we sought to evaluate the safety and efficacy of the WEB device for sidewall aneurysms stratified by size and location using our institutional experience and an aggregate meta-analysis of proportions. In addition, we evaluated the predictors of complete occlusion at follow-up using patient-level data.

MATERIALS AND METHODS

Protocol and Guidance

This systematic review used the Preferred Reporting Items for Systematic Reviews and Meta-Analyses (PRISMA) statement to report the search results.¹⁷

Search Strategy and Eligibility Criteria

We performed a comprehensive literature search in Scopus, EMBASE, MEDLINE, the Web of Science, and the Cochrane Central Register of Controlled Trials from inception until May 2022. The complete search strategy is provided in the Online Supplemental Data. Articles were included in the analysis if they met the following criteria: 1) randomized clinical trials, non-randomized trials, and cohort observational studies and case series (≥ 5 cases) of adult (18 years of age or older) patients with sidewall intracranial aneurysms (outside the traditional indications from the GCP studies^{4–7}) and treated with any of the WEB devices, 2) publication language in English or Spanish, and 3) at least 1 of our prioritized outcomes reported. Case reports, abstracts, commentaries, and reviews were excluded.

Study Selection

The search strategy was applied individually to each database. Two reviewers independently screened all studies by titles and abstracts to identify potentially relevant articles. Finally, the same reviewers accessed the full-text versions and determined their eligibility. Any disagreements were resolved through an initial discussion between the 2 reviewers. A third reviewer was considered an arbitrator if no consensus was reached.

Data Collection Process and Outcomes

Two reviewers independently extracted data from the included studies using a standardized electronic form. We extracted baseline, angioarchitectural, and procedural characteristics. An Excel (Microsoft) datasheet was uniformly sent by e-mail to the first and corresponding authors of the selected studies with aggregated data to extract patient-level data. Finally, the received data sets were merged into a summary database for the patient-level analysis.

The primary efficacy outcome was the proportion of adequate angiographic occlusions at the last follow-up, defined as a Raymond-Roy scale of I–II or a Bicêtre Occlusion Scale of 0, 0',

or 1. Secondary efficacy outcomes included complete occlusion at the last follow-up (defined as a Raymond-Roy of I or a Bicêtre Occlusion Scale of 0 or 0'), immediate complete occlusion, mRS at the last follow-up (a favorable outcome was defined as mRS 0–2), aneurysm retreatment, and the technical success rate. The primary safety outcome was a composite including intraprocedural and postprocedural complications. Intraprocedural complications included thromboembolic events, hemorrhagic events, device-deployment issues, and air embolisms. Postprocedural complications included ischemic and hemorrhagic events. Our secondary safety outcomes were the rate of intraprocedural complications, postprocedural complications, and all-cause mortality.

Risk of Bias and Certainty of the Evidence

Two reviewers used the Newcastle-Ottawa Quality Assessment Scale (NOS) for cohort studies to assess the methodologic quality of the included studies. According to the Cochrane recommendations, we assessed the certainty of the body of evidence from eligible studies in the quantitative synthesis.¹⁸ We used the Grading of Recommendation, Assessment, Development, and Evaluation approach.

Data Synthesis

A random-effects meta-analysis of proportions was performed using a generalized linear mixed model to estimate pooled rates and 95% CIs for each prioritized outcome. Statistical heterogeneity across studies was assessed with the I^2 test ($>50\%$ suggests substantial heterogeneity), while heterogeneity between subgroups was assessed with the Cochran Q test for heterogeneity. We planned further prespecified subgroup analyses by using the available patient-level data for the anatomic territory of the aneurysm (anterior circulation subgroup versus posterior circulation subgroup), the maximal diameter of the aneurysm (<7 versus ≥ 7 mm), and the rupture status (ruptured versus unruptured). A mixed-effects logistic regression to study the predictors of complete and adequate occlusion with variables selected via backward stepwise regression was performed using the patient-level data.

Institutional Experience

We performed a retrospective review of all patients with sidewall aneurysms who underwent endovascular treatment with the WEB device at our institution between September 2020 and November 2021. Institutional review board (University of Iowa Hospitals & Clinics) approval was obtained. Data on the demographic, clinical, and radiologic characteristics of the patients were collected. The morphologic features of the aneurysm and treatment outcomes were determined.

The indication for endovascular treatment was determined by a multidisciplinary team of neurovascular surgeons and neurointerventionalists. The selection of the WEB in these patients was determined according to the characteristics of the patient and aneurysm when other management options such as primary coiling, stent-assisted coiling, balloon-assisted coiling, flow diversion, and remodeling were deemed not the best treatment option. The procedure and WEB-size selection were performed in the same fashion as previously described and suggested by the manufacturer.^{14,19} Only when there was a concern for WEB protrusion into the

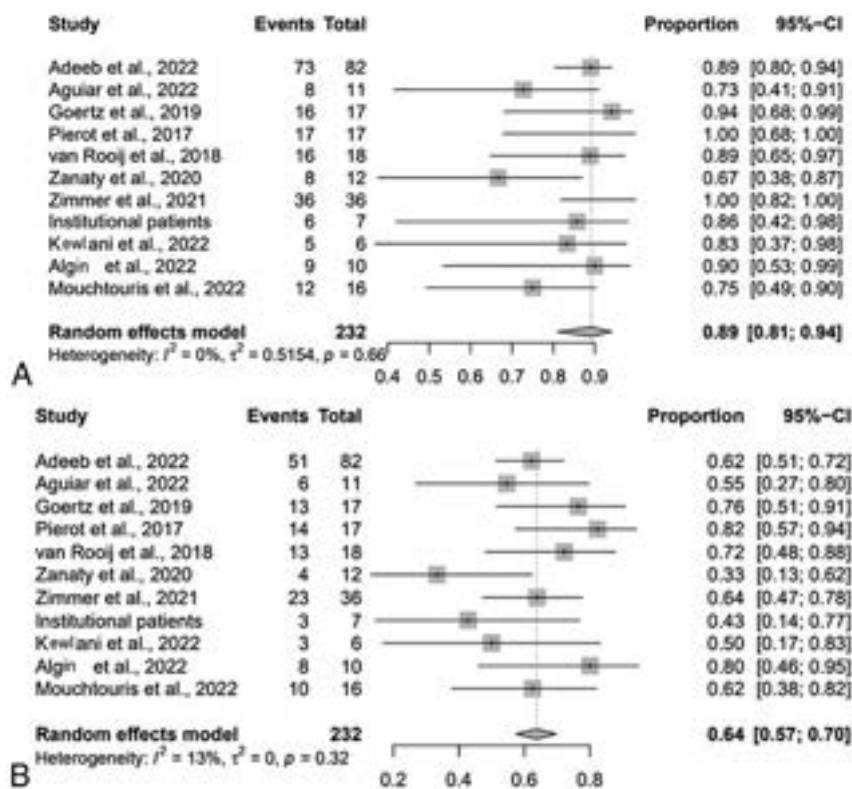


FIG 1. Forest plot for adequate (A) and complete (B) occlusion at last follow-up by study.

parent vessel aspirin was prescribed for 6 weeks following the procedure. In general, the clinical and imaging follow-ups were performed at 3, 6, and 12 months.

RESULTS

Study Selection and Characteristics

A total of 1025 documents were identified, and 626 duplicates were removed (Online Supplemental Data). As a result of the initial screening by title and abstract, there were 50 potentially eligible documents. Next, in the full-text evaluation, 40 documents were excluded due to the type of included population, the absence of data of interest, or the study design (Online Supplemental Data). Finally, 10 studies were included from the final systematic search. Patient-level data from 104 patients, including 9 patients from our institution (Online Supplemental Data) were available and included.

Seven studies were conducted in Europe,^{10,12,14,15,20-22} and 3, in the United States.^{13,16,23} A total of 285 patients (79% female; mean age, 58 years) with 288 sidewall aneurysms (35% ruptured) were included in our aggregate meta-analysis. Most aneurysms were wide-neck (92%). Most were located in the anterior circulation (80%). Of them, the posterior communicating artery (20%), the communicating segment of the internal carotid artery (14%), and the paraophthalmic segment (12%) were the most common locations. From those aneurysms in the posterior circulation (20%), the most common locations were the superior cerebral artery (17%) and the posterior inferior cerebellar artery (17%). Details about the antiplatelet regimens used in each study are summarized

in the Online Supplemental Data. The mean follow-up was 10.4 months and ranged from 3.3 to 29.5 months. The characteristics of all studies are presented in the Online Supplemental Data.

Risk of Bias within Studies and Certainty of the Evidence

Using the NOS, we rated 8 studies as high quality and 2 as moderate quality. All the studies earned one point for representativeness of the exposed cohort. Details are shown in the Online Supplemental Data. The certainty of the evidence was assessed for each outcome individually in the overall population. The assessment for each outcome is presented in the summary of findings table (Online Supplemental Data). Publication bias was detected for immediate complete occlusion, favorable clinical outcome, postprocedural complications, and mortality on the basis of funnel plot visualization (Online Supplemental Data).

Synthesis of Results

At last-follow up, the rate of adequate occlusion was 89% (95% CI, 81%–94%; $I^2 = 0\%$, $P = .66$) (Fig 1A). The technical success rate for implanting the WEB was 99% (95% CI, 79%–100%; $I^2 = 0\%$, $P = 1.00$). The immediate complete occlusion rate was 37% (95% CI, 30%–43%; $I^2 = 0\%$, $P = .5$), and the complete occlusion rate at last follow-up was 64% (95% CI, 57%–70%; $I^2 = 13\%$, $P = .32$) (Fig 1B). The favorable clinical outcome rate (mRS 0–2) was 89% (95% CI, 75%–96%; $I^2 = 48\%$, $P = .07$), and the retreatment rate was 9% (95% CI, 5%–13%; $I^2 = 0\%$, $P = .82$).

The rate of the composite safety outcome was 8% (95% CI, 3%–17%; $I^2 = 34\%$, $P = .13$) (Fig 2A). The intraprocedural complication rate was 6% (95% CI, 4%–10%; $I^2 = 0\%$, $P = .94$) (Fig 2B); 2% (95% CI, 1%–5%; $I^2 = 0\%$, $P = 1.00$) were thromboembolic complications, 1% (95% CI, 0%–14%; $I^2 = 0\%$, $P = .91$) were hemorrhagic, 1% (95% CI, 0%–3%; $I^2 = 0\%$, $P = .99$) were device-deployment issues, and 1% (95% CI, 0%–4%; $I^2 = 0\%$, $P = 1.00$) were vascular dissections. The postprocedural complication rate was 1% (95% CI, 0%–1%; $I^2 = 33\%$, $P = .14$) (Fig 2C). The all-cause mortality rate was 2% (95% CI, 1%–7%; $I^2 = 0\%$, $P = .73$).

Subgroup Analysis

Subgroup analysis for rates of adequate occlusion was consistent with the rates of the entire cohort for ruptured (68%) and unruptured (80%) sidewall aneurysms (Online Supplemental Data). Similarly, composite safety outcome rates were similar for ruptured (6%) and unruptured (6%) sidewall aneurysms (Online Supplemental Data).

Subgroup analysis for adequate occlusion and the composite safety outcome was consistent for the anterior and posterior

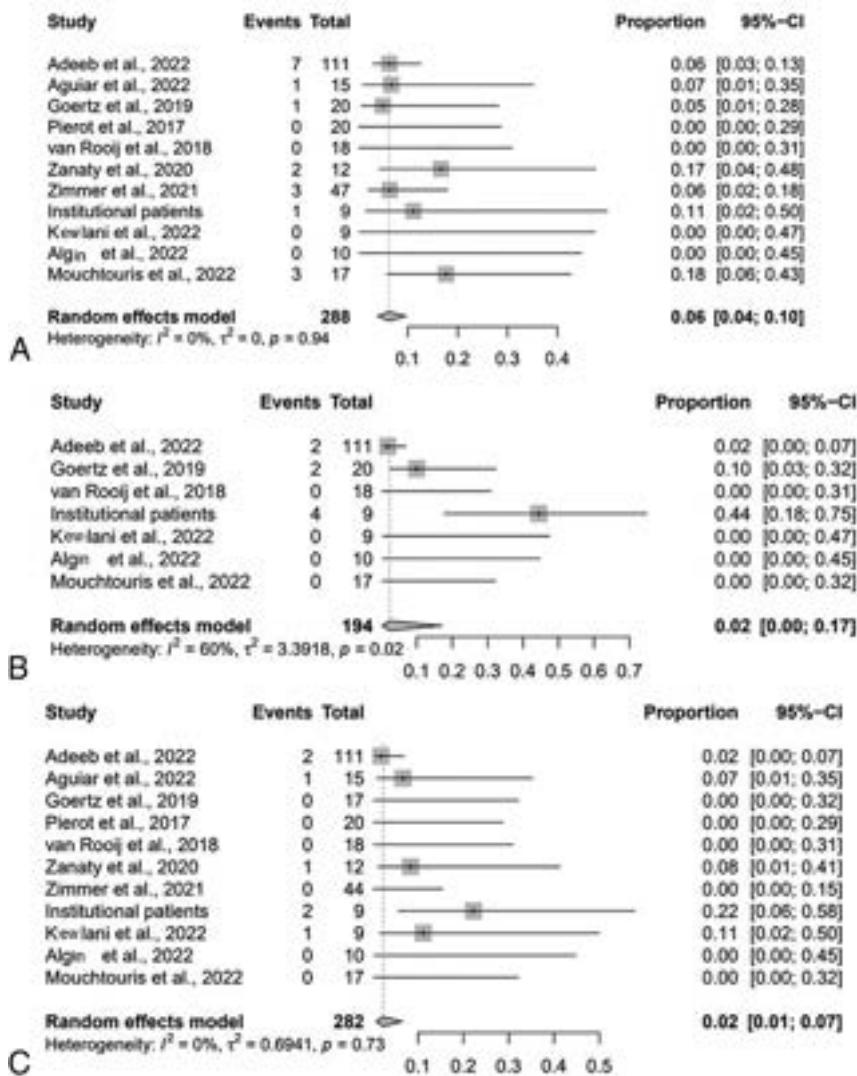


FIG 2. Forest plot for composite safety outcome (A) intraprocedural complications (B), and postprocedural complications (B) by study.

circulation (Online Supplemental Data). On subgroup analysis by aneurysm maximal diameter, adequate occlusion and the composite safety outcome were consistent for aneurysms of <7 and ≥ 7 mm (Online Supplemental Data).

Patient-Level Predictive Analysis

The variables selected using stepwise regression included maximal aneurysm diameter, neck size, height, width, height difference (the difference between the height of the aneurysm and the WEB device [before opening]), and width difference (the difference between the width of the aneurysm and the WEB device [before opening]) (Online Supplemental Data). The aneurysm width (OR = 0.5; 95% CI, 0.26–0.95; $P = .03$) was the only independent predictor of complete occlusion at the last follow-up. None of the variables included predicted adequate occlusion.

DISCUSSION

While multiple prospective and retrospective studies have demonstrated the safety and effectiveness of the WEB device

for intracranial wide-neck bifurcation aneurysms,^{24–27} only a few studies have reported treatment results with the WEB for sidewall aneurysms. In this meta-analysis of patients treated with the WEB for wide-neck sidewall aneurysms, we found the following: 1) The WEB device has an efficient profile with a high rate of adequate occlusion (89%) at follow-up, and 2) it has a safety profile with a low rate of our composite safety outcome (8%). Furthermore, we determined that the aneurysm width was the main predictor of complete occlusion at the last follow-up in wide-neck sidewall aneurysms.

In the cumulative population of the WEB Clinical Assessment of Intracranial Aneurysm Therapy (WEBCAST), French Observatory, and WEBCAST-2 studies (168 patients), complete and adequate occlusion was observed in 52.9% and 79% at 1-year follow-up, respectively.²⁸ Moreover, in the WEB Intracranial Therapy (WEB-IT) study, complete and adequate occlusion rates at 1-year follow-up were 53.8% and 84.6%, respectively.⁴ The rates of complete (64%) and adequate (89%) occlusion at the last follow-up observed in our meta-analysis are comparable with the results from the GCP studies. Furthermore, several meta-analyses have reported similar findings in wide-neck bifurcation aneurysms.^{29–31} On the other hand, recent meta-analyses of flow diversion for the treatment of sidewall aneurysms have shown pooled complete (range, 69.5%–74.9%)^{32,33} and adequate occlusion (range, 84.7%–88.9%) rates,^{33,34} comparable with our findings.

Considering the composite safety outcome of the WEB device for wide-neck sidewall aneurysms, we found an 8% rate of intraprocedural and postprocedural complications. Focusing on the intraprocedural complications, our findings are lower than the 8.4% pooled rate of intraprocedural complications reported by Monteiro et al²⁴ in a recently published meta-analysis evaluating ruptured intracranial aneurysms treated with the WEB device. Furthermore, when we compared our findings with those in a recent meta-analysis that included ruptured and unruptured aneurysms, our hemorrhagic rate was similar to the reported 0.83% rate and our thromboembolic event rate was lower than the 5.6% reported rate.³¹ Of note, meta-analyses of flow diversion for sidewall aneurysms have shown higher pooled complication rates ranging from 7.8% to 27.1%.^{32–34} The definition of complications in the studies we included for meta-analysis was inconsistent, so a direct comparison across studies might be limited. Next, considering the postprocedural complications, our findings were significantly lower than the

14% reported by Tau et al³⁵ on a meta-analysis evaluating the WEB for all types of aneurysms and similar to the 1% rate reported in the previously mentioned meta-analysis of ruptured aneurysms.²⁴

Our patient-level data-predictive analysis found that a smaller aneurysm width increased the probability of complete occlusion at the last follow-up after WEB treatment. Nevertheless, although the rest of the variables included in the model were not statistically significant predictors (Online Supplemental Data), the tendency of the association is according to previous reports.³⁶⁻³⁸ Considering that patient-level data were available for less than half of the patients, a clear limitation was our small number of patients, which was insufficiently powered to detect a modest effect of some of the parameters studied.

Our appraisal of the certainty of the evidence allowed us to assess the quality of the evidence for each of our prioritized outcomes. From this assessment, we have been able to identify limitations of this meta-analysis. First was the methodologic design of the included studies. The retrospective design of all the studies inherently comes with selection bias, and because most did not include direct comparisons with wide-neck bifurcation aneurysms or other treatment strategies, a comparative meta-analysis was not possible. Second, most included studies did not have long-term follow-up periods (>18 months). Third, almost all the evidence from the WEB device is focused on the indications from the GCP studies; therefore, the available literature included in this meta-analysis is limited by studies with small sample sizes, increasing the heterogeneity and lack a standardized assessment of the angiographic parameters. Finally, we did not perform a meta-analysis with adjusted effect sizes for potential covariates due to the limited sample size.

Implications for Clinical Practice

While a detailed characterization of the aneurysm location, angle, size, and morphologic features is fundamental for the best treatment selection, the addition of intrasaccular flow disruption for the treatment of wide-neck sidewall aneurysms expands the neurointerventionalist's toolbox for the treatment of intracranial aneurysms. Furthermore, with the continuous evolution of the WEB device and its delivery system, its use has become less technically challenging, allowing the continual expansion of its use. The flow-disruption technique can potentially become a valuable treatment selection for hard-to-treat aneurysms for which the standard coil-based methods have limited performance.

CONCLUSIONS

The initial evidence evaluating the use of the WEB for the treatment of wide-neck sidewall intracranial aneurysms has demonstrated high rates of adequate occlusion with low procedural complications. Our findings favor the consideration of the WEB device as an option for the treatment of sidewall aneurysms.

Disclosure forms provided by the authors are available with the full text and PDF of this article at www.ajnr.org.

REFERENCES

1. Wang F, Chen X, Wang Y, et al. **Stent-assisted coiling and balloon-assisted coiling in the management of intracranial aneurysms: a systematic review and meta-analysis.** *J Neurol Sci* 2016;364:160–66 CrossRef Medline
2. Zhao B, Yin R, Lanzino G, et al. **Endovascular coiling of wide-neck and wide-neck bifurcation aneurysms: a systematic review and meta-analysis.** *AJNR Am J Neuroradiol* 2016;37:1700–05 CrossRef Medline
3. Pierot L, Biondi A. **Endovascular techniques for the management of wide-neck intracranial bifurcation aneurysms: a critical review of the literature.** *J Neuroradiol* 2016;43:167–75 CrossRef Medline
4. Arthur AS, Molyneux A, Coon AL, et al. **WEB-IT Study Investigators. The safety and effectiveness of the Woven EndoBridge (WEB) system for the treatment of wide-necked bifurcation aneurysms: final 12-month results of the pivotal WEB Intrasaccular Therapy (WEB-IT) study.** *J Neurointerv Surg* 2019;11:924–30 CrossRef Medline
5. Pierot L, Costalat V, Moret J, et al. **Safety and efficacy of aneurysm treatment with WEB: results of the WEBCAST study.** *J Neurosurg* 2016;124:1250–56 CrossRef Medline
6. Pierot L, Gubucz I, Buhk JH, et al. **Safety and efficacy of aneurysm treatment with the WEB: results of the WEBCAST 2 study.** *AJNR Am J Neuroradiol* 2017;38:1151–55 CrossRef Medline
7. Pierot L, Moret J, Turjman F, et al. **WEB treatment of intracranial aneurysms: feasibility, complications, and 1-month safety results with the WEB DL and WEB SL/SLS in the French Observatory.** *AJNR Am J Neuroradiol* 2015;36:922–27 CrossRef Medline
8. US FDA. **Premarket Approval (PMA).** 2019. <https://www.accessdata.fda.gov/scripts/cdrh/cfdocs/cfpma/pma.cfm?id=P190014>. Accessed July 15, 2022
9. Pierot L, Szikora I, Barreau X, et al. **Aneurysm treatment with the Woven EndoBridge (WEB) device in the combined population of two prospective, multicenter series: 5-year follow-up.** *J Neurointerv Surg* 2022 July 8. [Epub ahead of print] CrossRef Medline
10. Zimmer S, Maus V, Maurer C, et al. **Widening the indications for intrasaccular flow disruption: WEB 17 in the treatment of aneurysm locations different from those in the good clinical practice trials.** *AJNR Am J Neuroradiol* 2021;42:524–29 CrossRef Medline
11. Stanca C, Carriero S, Negroni D, et al. **Woven EndoBridge in wide-neck bifurcation aneurysms: digital subtraction angiography at 3-year follow-up.** *J Clin Med* 2022;11:2879 CrossRef Medline
12. van Rooij SB, Peluso JP, Sluzewski M, et al. **The new low-profile WEB 17 system for treatment of intracranial aneurysms: first clinical experiences.** *AJNR Am J Neuroradiol* 2018;39:859–63 CrossRef Medline
13. Adebé N, Dibás M, Diestro JD, et al. **Multicenter study for the treatment of sidewall versus bifurcation intracranial aneurysms with use of Woven EndoBridge (WEB).** *Radiology* 2022;304:372–82 CrossRef Medline
14. Goertz L, Liebig T, Siebert E, et al. **Extending the indication of Woven EndoBridge (WEB) embolization to internal carotid artery aneurysms: a multicenter safety and feasibility study.** *World Neurosurg* 2019;126:e965–74 CrossRef Medline
15. Pierot L, Biondi A, Narata AP, et al. **Should indications for WEB aneurysm treatment be enlarged? Report of a series of 20 patients with aneurysms in “atypical” locations for WEB treatment.** *J Neuroradiol* 2017;44:203–09 CrossRef Medline
16. Zanaty M, Roa JA, Tjoumakaris SI, et al. **Off-label use of the WEB device.** *World Neurosurg* 2020;134:e1047–52 CrossRef Medline
17. Moher D, Liberati A, Tetzlaff J, et al; PRISMA Group. **Preferred reporting items for systematic reviews and meta-analyses: the PRISMA statement.** *PLoS Med* 2009;6:e1000097 CrossRef Medline
18. Higgins JP, Thomas J, Chandler J, et al, eds. *Cochrane Handbook for Systematic Reviews of Interventions.* John Wiley & Sons; 2019
19. Ansari S, Zevallos CB, Farooqui M, et al. **Optimal Woven EndoBridge (WEB) device size selection using automated volumetric software.** *Brain Sci* 2021;11:901 CrossRef Medline
20. Aguiar G, Caroff J, Mihalea C, et al. **WEB device for treatment of posterior communicating artery aneurysms.** *J Neurointerv Surg* 2022;14:362–65 CrossRef Medline

21. Algin O, Corabay S, Ayberk G. **Long-term efficacy and safety of WovenEndoBridge (WEB)-assisted cerebral aneurysm embolization.** *Interv Neuroradiol* 2022;28:695–701 CrossRef Medline
22. Kewlani B, Ryan DJ, Henry J, et al. **A single centre retrospective analysis of short- and medium-term outcomes using the Woven EndoBridge (WEB) device and identification of the device-to-aneurysm volume ratio as a potential predictor of aneurysm occlusion status.** *Interv Neuroradiol* 2022 Apr 22. [Epub ahead of print] CrossRef Medline
23. Mouchtouris N, Hasan D, Samaniego EA, et al. **The Woven EndoBridge (WEB) device: feasibility, techniques, and outcomes after FDA approval.** *J Neurosurg* 2022;136:1266–72 CrossRef Medline
24. Monteiro A, Lazar AL, Waqas M, et al. **Treatment of ruptured intracranial aneurysms with the Woven EndoBridge device: a systematic review.** *J NeuroInterv Surg* 2022;14:366–70 CrossRef Medline
25. Xie Y, Tian H, Xiang B, et al. **Woven EndoBridge device for the treatment of ruptured intracranial aneurysms: a systematic review of clinical and angiographic results.** *Interv Neuroradiol* 2022;28:240–49 CrossRef Medline
26. Harker P, Regenhardt RW, Alotaibi NM, et al. **The Woven EndoBridge device for ruptured intracranial aneurysms: international multicenter experience and updated meta-analysis.** *Neuroradiology* 2021;63:1891–99 CrossRef Medline
27. Essibayi MA, Lanzino G, Brinjikji W. **Safety and efficacy of the Woven EndoBridge device for treatment of ruptured intracranial aneurysms: a systematic review and meta-analysis.** *AJNR Am J Neuroradiol* 2021;42:1627–32 CrossRef Medline
28. Pierot L, Moret J, Barreau X, et al. **Safety and efficacy of aneurysm treatment with WEB in the cumulative population of three prospective, multicenter series.** *J Neurointerv Surg* 2018;10:553–59 CrossRef Medline
29. Zhang SM, Liu LX, Ren PW, et al. **Effectiveness, safety and risk factors of Woven EndoBridge device in the treatment of wide-neck intracranial aneurysms: systematic review and meta-analysis.** *World Neurosurg* 2020;136:e1–23 CrossRef Medline
30. Asnafi S, Rouchaud A, Pierot L, et al. **Efficacy and safety of the Woven EndoBridge (WEB) device for the treatment of intracranial aneurysms: a systematic review and meta-analysis.** *AJNR Am J Neuroradiol* 2016;37:2287–92 CrossRef Medline
31. van Rooij S, Sprengers ME, Peluso JP, et al. **A systematic review and meta-analysis of Woven EndoBridge single layer for treatment of intracranial aneurysms.** *Interv Neuroradiol* 2020;26:455–60 CrossRef Medline
32. Fiorella D, Gache L, Frame D, et al. **How safe and effective are flow diverters for the treatment of unruptured small/medium intracranial aneurysms of the internal carotid artery? Meta-analysis for evidence-based performance goals.** *J Neurointerv Surg* 2020;12:869–73 CrossRef Medline
33. Abbasi M, Savasatano LE, Brinjikji W, et al. **Endoluminal flow diverters in the treatment of sidewall and bifurcation aneurysm: a systematic review and meta-analysis of complications and angiographic outcomes.** *Interv Neuroradiol* 2022;28:229–39 CrossRef Medline
34. Cagnazzo F, di Carlo DT, Cappucci M, et al. **Acutely ruptured intracranial aneurysms treated with flow-diverter stents: a systematic review and meta-analysis.** *AJNR Am J Neuroradiol* 2018;39:1669–75 CrossRef Medline
35. Tau N, Sadeh-Gonik U, Aulagner G, et al. **The Woven EndoBridge (WEB) for endovascular therapy of intracranial aneurysms: update of a systematic review with meta-analysis.** *Clin Neurol Neurosurg* 2018;166:110–15 CrossRef Medline
36. Fujimoto M, Lylyk I, Bleise C, et al. **Long-term outcomes of the WEB device for treatment of wide-neck bifurcation aneurysms.** *AJNR Am J Neuroradiol* 2020;41:1031–36 CrossRef Medline
37. Cortese J, Caroff J, Chalumeau V, et al. **Determinants of cerebral aneurysm occlusion after embolization with the WEB device: a single-institution series of 215 cases with angiographic follow-up.** *J Neurointerv Surg* 2022 Apr 15. [Epub ahead of print] CrossRef Medline
38. Cagnazzo F, Ahmed R, Zannoni R, et al. **Predicting factors of angiographic aneurysm occlusion after treatment with the Woven EndoBridge device: a single-center experience with midterm follow-up.** *AJNR Am J Neuroradiol* 2019;40:1773–78 CrossRef Medline

Evolution of Radiographic Changes of a Vascularized Pedicled Nasoseptal Flap after Endonasal Endoscopic Skull Base Surgery

J.L. Birkenbeuel, A. Abiri, T. Nguyen, B.F. Bitner, E.F. Abello, M. Vasudev, F.P.K. Hsu, E. Kuoy, and E.C. Kuan



ABSTRACT

BACKGROUND AND PURPOSE: There is active research involving the radiographic appearance of the skull base following reconstruction. The purpose of this study was to describe the radiographic appearance of the vascularized pedicle nasoseptal flap after endoscopic skull base surgery across time.

MATERIALS AND METHODS: We performed chart and imaging review of all patients with intraoperative nasoseptal flap placement during endoscopic skull base surgery at a tertiary academic skull base surgery program between July 2018 and March 2021. All patients underwent immediate and delayed (>3 months) postoperative MR imaging. Primary outcome variables included flap and pedicle enhancement, flap thickness, and flap adherence to the skull base.

RESULTS: Sixty-eight patients were included. Flap ($P = .003$) enhancement significantly increased with time. Mean nasoseptal flap thickness on immediate and delayed postoperative scans was 3.8 and 3.9 mm, respectively ($P = .181$). The nasoseptal flap adhered entirely to the skull base in 37 (54.4%) and 67 (98.5%) patients on immediate and delayed imaging, respectively ($P < .001$).

CONCLUSIONS: Our findings demonstrate heterogeneity of the nasoseptal flap appearance after skull base reconstruction. While it is important for surgeons and radiologists to evaluate variations in flap appearance, the absence of enhancement and lack of adherence to the skull base on immediate postoperative imaging do not appear to predict reconstructive success and healing, with many flaps “self-adjusting” with time.

ABBREVIATIONS: EEA = endoscopic endonasal approaches; ESBS = endonasal skull base surgery; NSF = nasoseptal flap

Advancements in surgical techniques and instrumentation have revolutionized endoscopic endonasal skull base surgery (ESBS) from the resection of transsellar masses to a wide spectrum of lesions along the ventral skull base.¹⁻⁵ With endoscopic endonasal approaches (EEAs), intraoperative CSF leaks or large bony defects with dural exposure or both are often encountered.⁶ The mainstay of skull base reconstruction with EEA has become the nasoseptal flap (NSF).^{7,8} The NSF is a vascularized pedicled flap that consists of mucoperiosteum and/or mucoperichondrium supplied by the posterior septal branch of the sphenopalatine artery.⁹ First described in 2006 by Hadad et al,⁸ the NSF has

gained popularity for skull base reconstruction due to its rich blood supply and wide coverage. With its use, the incidence of a postoperative CSF leak after ESBS has significantly decreased.¹⁰

The NSF, unlike other vascularized flaps, cannot undergo traditional monitoring with Doppler or other manual or visual methods. Because frequent endoscopic evaluation is not feasible postoperatively, MR imaging is commonly used to assess the viability of the NSF after surgery.¹¹ Previously, radiologists have looked for flap enhancement as a sign of flap viability. However, a recent study suggested the unreliability of flap enhancement as a proxy for flap viability or as a predictor of postoperative CSF leaks.¹² Reported findings, while limited, have suggested a nonenhancing mucosal gap and displacement of the NSF as possible reasons for postoperative CSF leaks.¹³

Postoperative imaging can also be used to assess flap positioning and changes in appearance with time. Preliminary studies of the radiographic findings of NSFs have reported various changes in thickness and enhancement on follow-up MR imaging, with 1 study by Learned et al¹²⁻¹⁵ reporting stabilization of the imaging features within 2–6 months after surgery. However, there is a general paucity of literature examining the radiographic appearance

Received May 8, 2022; accepted after revision December 6.

From the Departments of Otolaryngology–Head and Neck Surgery (J.L.B., A.A., T.N., B.F.B., E.F.A., M.V., E.C.K.), Neurological Surgery (F.P.K.H., E.C.K.), and Radiology (E.K.), Division of Neuroradiology, University of California, Irvine, Irvine, California.

A. Abiri and T. Nguyen contributed equally to this work.

Please address correspondence to Edward C. Kuan, MD, MBA, Department of Otolaryngology–Head and Neck Surgery, University of California, Irvine, 101 The City Dr South, Orange, CA 92868; e-mail: eckuan@uci.edu

Indicates article with online supplemental data.

<http://dx.doi.org/10.3174/ajnr.A7768>

of the NSF so far. This study therefore aimed to systematically describe the immediate and delayed MR imaging characteristics of the vascularized pedicle NSF and to demonstrate its evolution with time to help clinicians better understand the natural progression of the radiographic appearance of the NSF.

MATERIALS AND METHODS

After the University of California, Irvine, institutional review board approval, we conducted a retrospective review of all patients undergoing endoscopic skull base surgery with intraoperative NSF placement for reconstruction of skull base defects between July 2018 and March 2021. Patients with both sellar and nonsellar pathology were included as long as the NSF was used (eg, transcribriform, transplanum, and transclival approaches were included). Imaging criteria for all postoperative scans were defined by consensus by a rhinologist/skull base surgeon (E.C.K.) and a neuroradiologist (E.K.). Two separate physicians (E.K. and E.C.K.) independently reviewed each case to ensure interobserver agreement, with disagreements resolved after further discussion.

All patients underwent preoperative MR imaging within 48 hours of the operation, immediate postoperative MR imaging within 48 hours of the operation, and delayed postoperative MR



FIG 1. Representative figures of no enhancement (A), weak enhancement (B), and bright enhancement (C).

Table 1: Tumor pathology of all 68 patients

Pathology	No. (%)
Pituitary adenoma	46 (67.6)
Craniopharyngioma	6 (8.8)
Meningioma	6 (8.8)
Pituitary apoplexy	4 (5.9)
Clival chordoma	2 (2.9)
Esthesioneuroblastoma	1 (1.5)
Rathke cleft cyst	2 (2.9)
Vascular malformation	1 (1.5)

Table 2: Changes in outcome variables between immediate and delayed postoperative MR imaging

Variable	Immediate Postop	Delayed Postop	P Value
Flap enhancement, No. (%)			
None	19 (28)	4 (6)	.003 ^a
Weak	14 (20)	20 (29)	
Bright	35 (52)	44 (65)	
Pedicle enhancement, No. (%)			
None	41 (60)	30 (44)	.076
Weak	12 (18)	23 (34)	
Bright	15 (22)	15 (22)	
Mean flap thickness (mm)	3.8 (SD, 1.2)	3.9 (SD, 1.1)	.181
NSF adherence to skull base, No. (%)	37 (54.4)	67 (98.5)	<.001 ^a

Note:—Postop indicates postoperative.

^a P values <.05 are statistically significant.

imaging at least 3 months after the operation. Features evaluated included enhancement of the pedicle and flap (ie, no, weak, or bright enhancement) as evaluated on T1 postgadolinium sequences, flap thickness (in millimeters), flap adherence to the skull base (defined as absence or presence of gaps between the flap and skull base along the length of the flap), and diaphragma sellae descent for both immediate and delayed postoperative MRIs. Flap enhancement was quantified as follows: For each MR imaging, a 200 × 100 pixel window consisting of the flap and pedicle was extracted. Flap enhancement was calculated as the average pixel intensity (range, 0–255 pixels) of the extracted images. The 33rd and 66th percentile intensities were computed from the resulting list of enhancement values, which were used as thresholds to stratify flap and pedicle enhancement into 3 categories: no, weak, or bright enhancement. Representative figures demonstrating no, weak, and strong enhancement based on our objective criteria are shown in Fig 1.

We collected data on overall patient demographics, tumor location, cavernous sinus involvement, suprasellar involvement, American Society of Anesthesiologists (ASA) status, prior transnasal surgery, prior radiation to the lesion, tumor pathology, surgical approach (ie, standard versus extended), intraoperative leak (ie, no leak, low-flow leak, high-flow leak), the presence of a postoperative CSF leak, and lumbar drain use for both groups (Online Supplemental Data).

All statistical analyses were performed using PASW 18.0 (<https://www.malavida.com/en/soft/pasw/>). Paired *t* tests were performed for continuous variables to assess differences in outcomes between immediate and delayed postoperative MR images. McNemar and marginal homogeneity tests were used for 2 and 3 or more categorical variables, respectively, to assess changes between immediate and delayed postoperative images. *P* values ≤ .05 were considered statistically significant.

RESULTS

All 68 patients had observable skull base defects with coverage by the flap, with the C-shaped NSF concave into the operative defects on postoperative coronal and/or sagittal views in all patients. Patient demographics and clinical characteristics are listed in the Online Supplemental Data. There were no postoperative CSF leaks in this cohort. In the 39 patients with a change in NSF enhancement, 27 (69%) flaps increased in enhancement and 12 (31%) flaps decreased in enhancement with time. Fifty-seven percent of flaps

changed in enhancement pattern by 4 months after the operation. There were 27 (40%) NSFs that increased and 41 (60%) that decreased in thickness with time. A list of tumor pathologies is presented in Table 1. Changes in flap and pedicle enhancement, mean flap thickness, and NSF adherence to skull base descent between immediate and delayed MR imaging are reported in Table 2. Examples of changes in NSF enhancement, skull base adherence, and thickness are demonstrated in Figs 2–4, respectively.



FIG 2. A, Immediate postoperative imaging following resection of an endoscopic transsellar pituitary adenoma with an intraoperative CSF leak demonstrates full coverage of sellar defect with the NSF in the shape of a C. There is elevation of the diaphragma sellae and compression of the pituitary gland. The flap pedicle and body are both brightly enhancing, with complete adherence to the skull base. B, Delayed imaging demonstrates continued enhancement of the flap with complete adherence to the skull base, as well as re-expansion of the pituitary gland and collapse of the diaphragma sellae.

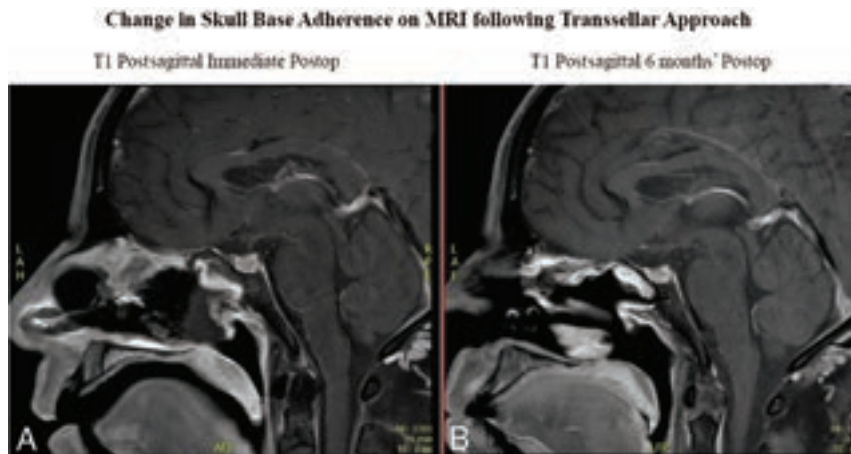


FIG 3. A, Immediate postoperative imaging following resection of an endoscopic transsellar pituitary adenoma with an intraoperative CSF leak shows full coverage of sellar defect, demonstrating that the enhancing nasoseptal flap appears to be nonadherent to the skull base. B, Delayed imaging confirms that the flap is now uniformly opposed to the skull base.

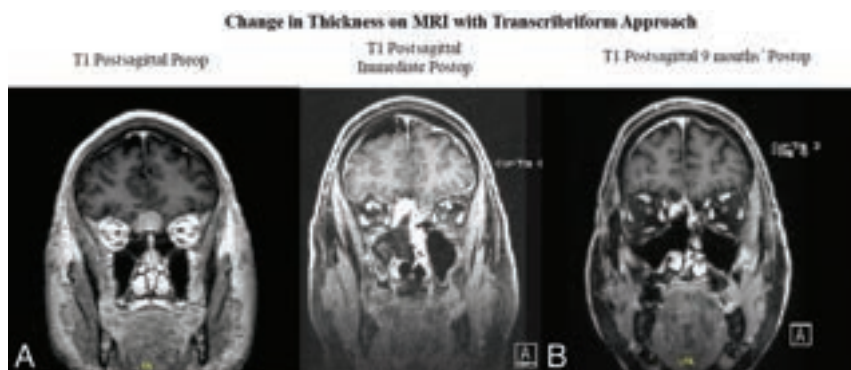


FIG 4. A, Immediate postoperative imaging following an endoscopic unilateral transcribriform approach to an olfactory groove meningioma demonstrates that the flap extends into the defect with bright enhancement. B, Delayed imaging demonstrates mild thinning of the flap with mildly decreased enhancement. Preop indicates preoperative.

DISCUSSION

EEA is a relatively new surgical technique used to resect lesions along the skull base, allowing a wider FOV, improved illumination, and the ability to directly access tumors while avoiding vital structures.¹⁶⁻¹⁸ However, EEA can often create large surgical defects and is associated with the risk of CSF leaks with possible increased morbidity and hospital length of stay.¹² Various attempts have been made to address this dilemma, including the use of fat grafts and extranasal vascularized flaps; however, the risk of a CSF leak with these techniques remained unacceptably high and often added to postoperative morbidity. The NSF is now considered the criterion standard when reconstructing skull base defects after ESBS because it has demonstrated superiority in decreasing postoperative CSF leaks in EEA procedures whenever feasible.^{7,10,15,19,20} The mainstay for radiographic evaluation of the NSF has been MR imaging. While imaging can be used to assess tumor resection and surveillance with time, it can also provide valuable information on NSF enhancement, thickness, positioning, and adherence to the skull base.

In this study, we report heterogeneity in flap appearance on immediate imaging and across time. We found that nearly 60% of NSFs changed in enhancement, with a trend toward increased NSF enhancement on delayed MR imaging (27/39; 69%). Additionally, our study did not find significant changes in flap thickness ($P = .181$). Flap adherence to the skull base significantly increased ($P = .181$), with 98.5% of all NSFs adherent to the skull base on delayed MR imaging. These results provide a better understanding for clinicians on the natural progression of the radiographic appearance of the NSF postoperatively and should assist them in identifying abnormal radiographic findings in future cases.

Variations in flap enhancement on MR imaging have been conventionally used as a predictor of flap failure and the risk of a CSF leak, especially in larger skull base defects when NSFs are used. It has been hypothesized that there is an increased risk of CSF leak in poorly enhancing NSFs due to compromised vasculature. This is thought to be due to injury to or compression of the vascular supply.¹⁵ Our study as well as others have since challenged the notion that enhancement patterns can predict flap failure.¹² As mentioned in previous studies, more likely reasons for a CSF leak include NSF migration or displacement, which would appear as a nonenhancing mucosal gap on imaging.^{12,13}

Although this study did not find enhancement predictive of NSF necrosis, a recent study by Chabot et al²¹ reported a lack of enhancement on MR imaging as a predictor of NSF necrosis. Therefore, if suspicion for flap failure is high (eg, signs of meningitis, clear rhinorrhea), MR imaging may be warranted to better evaluate the NSF.

Most interesting, we also found no relationship between the direct adherence of the NSF to the skull base and subsequent development of postoperative CSF leaks. As reported in this study, only 54% of NSFs were directly adherent to the skull base on immediate postoperative imaging, with an increase to 98.5% on delayed MR imaging. To our knowledge, this feature has not been previously reported and should reassure clinicians that the NSF will improve its direct adherence to the skull base with time. One explanation for this finding is that NSF adherence likely improves as granulation tissue forms and the flap scars down onto the underlying bone. Additionally, the senior author routinely performs multilayer reconstruction using subdural and/or epidural underlay materials, which can also create an artificial space between the flap undersurface and skull base. These materials may break down and may also account for improved flap adherence with time.

Additionally, we found no significant changes in NSF thickness between immediate and delayed postoperative imaging. This finding contrasts with a prior study by Learned et al,¹⁴ which reported a 20%–30% reduction in flap thickness with time. Any increased thickness on delayed postoperative imaging may be due to flap neovascularization that increases flap thickness. However, this feature did not significantly change the thickness across time in our study.

In the current study, we also compared enhancement changes between immediate and delayed postoperative imaging. We found 19 flaps that did not enhance at all on immediate postoperative imaging but ultimately increased in enhancement on delayed imaging, suggesting neovascularization across time as the flap healed over the skull base. Although the NSF may not have been brightly enhancing originally, this characteristic does not appear to affect its long-term integration and healing. We showed 94% flap enhancement (ie, weak or bright) on delayed postoperative imaging. This enhancement pattern on delayed postoperative imaging appears to be similar to that seen with free mucosal graft reconstruction because a prior study by Kim et al²² reported 100% flap enhancement at 3 months after ESBS. This study did not assess free mucosal graft enhancement with time and thus cannot determine whether cases reconstructed with a free mucosal graft have similar enhancement changes from the immediate postoperative imaging to delayed imaging.

Given that CSF leaks were not observed in any patient, it is unlikely that weak-to-no enhancement of the NSF predicts flap failure. Additionally, 9 flaps that originally displayed strong enhancement decreased enhancement with time, suggesting that a decrease in enhancement is also unlikely to predict flap failure. These data, in accordance with prior literature, suggest that using MR imaging to evaluate NSF enhancement serves as a poor proxy for determining flap viability. In these scenarios, a meticulous closure technique, proper flap placement, optimizing wound-healing status, and enforcement of postoperative

precautions likely play a larger role in reconstructive success. There is merit, however, in using MR imaging to determine the risk of CSF leak as it relates to flap position and placement as per the studies by Adappa et al¹² and Learned et al.¹³

An alternative theory for an increase in flap enhancement with time may be due to reactive changes such as granulation tissue or mucosalization of the flap itself.¹⁵ Granulation tissue typically develops within 3–7 days after the operation and would not be evident at the time of the immediate postoperative MR imaging, which was acquired within the first 48 hours.²³ It is, therefore, reasonable to think that granulation tissue would be present on delayed postoperative imaging and may affect flap thickness and enhancement. Although we demonstrate a significant increase in NSF enhancement with time, we did not see a corresponding increase in the thickness of the enhanced tissue. Given these findings, enhancement changes over time are most likely due to changes to the vascularity of the flap rather than secondary to tissue changes of the surrounding tissue. Hypotheses for the increased vascularity of the flap with time are 2-fold. First, the flap is initially compressed and placed on tension as it is rotated back to cover the skull base defect. As the flap matures, there is likely reduced tortuosity on the flap that improves blood flow to the flap. Second, neovascularization near the flap edges that occurs during flap healing likely plays a significant role in the increase in enhancement to the flap.

Limitations

Limitations to the study included its retrospective nature and the limited sample size and the variable interval of the second postoperative imaging. While this study included only 44 patients, this is the largest cohort to date investigating the radiographic appearance of the NSF, to our knowledge. Although several materials were used during the multilayer reconstruction in each case (eg, collagen matrix as underlay, dural sealant, and dissolvable nasal dressings superficial to the flap), this study focused its analysis on the findings of the NSF itself, which is a distinct, readily identifiable, and critical layer for reconstruction. Additionally, we were unable to statistically analyze risk factors for CSF leaks, given that we did not observe any postoperative CSF leaks in our study. Future large-scale, prospective studies are required to better understand radiographic predictors of NSF failure and postoperative CSF leaks.

CONCLUSIONS

Understanding the appearance of the NSF and its changes in postoperative appearance with time is essential for surgeons and radiologists. Our findings demonstrate that the NSF tends to increase in enhancement, with most flaps changing enhancement patterns by 4 months postoperatively. These findings should assist surgeons and radiologists in better appreciating the evolution of the NSF.

Disclosure forms provided by the authors are available with the full text and PDF of this article at www.ajnr.org.

REFERENCES

1. Rolston JD, Han SJ, Aghi MK. **Nationwide shift from microscopic to endoscopic transsphenoidal pituitary surgery.** *Pituitary* 2016;19:248–50 CrossRef Medline

2. Couldwell WT, Weiss MH, Rabb C, et al. **Variations on the standard transsphenoidal approach to the sellar region, with emphasis on the extended approaches and parasellar approaches: surgical experience in 105 cases.** *Neurosurgery* 2004;55:539–50 CrossRef Medline
3. Kaptain GJ, Vincent DA, Sheehan JP, et al. **Transsphenoidal approaches for the extracapsular resection of midline suprasellar and anterior cranial base lesions.** *Neurosurgery* 2008;62:SHC1264–71 CrossRef Medline
4. Dusick JR, Esposito F, Kelly DF, et al. **The extended direct endonasal transsphenoidal approach for nonadenomatous suprasellar tumors.** *J Neurosurg* 2005;102:832–41 CrossRef Medline
5. Gardner PA, Kassam AB, Thomas A, et al. **Endoscopic endonasal resection of anterior cranial base meningiomas.** *Neurosurgery* 2008;63:36–54 CrossRef Medline
6. Dumont A, Kanter A, Jane JA, Jr, et al. **Extended transsphenoidal approach.** *Front Horm Res* 2006;34:29–45 CrossRef Medline
7. Kassam AB, Thomas A, Carrau RL, et al. **Endoscopic reconstruction of the cranial base using a pedicled nasoseptal flap.** *Neurosurgery* 2008;63:ONS44–52; discussion ONS52–53 CrossRef Medline
8. Hadad G, Bassagasteguy L, Carrau RL, et al. **A novel reconstructive technique after endoscopic expanded endonasal approaches: vascular pedicle nasoseptal flap.** *Laryngoscope* 2006;116:1882–86 CrossRef Medline
9. Pinheiro-Neto CD, Snyderman CH. **Nasoseptal flap.** *Adv Otorhinolaryngol* 2013;74:42–55 CrossRef Medline
10. Harvey RJ, Parmar P, Sacks R, et al. **Endoscopic skull base reconstruction of large dural defects: a systematic review of published evidence.** *Laryngoscope* 2012;122:452–59 CrossRef Medline
11. Jyotirmay H, Saxena SK, Ramesh AS, et al. **Assessing the viability of Hadad flap by postoperative contrast-enhanced magnetic resonance imaging.** *J Clin Diagn Res* 2017;11:MC01–03 CrossRef Medline
12. Adappa ND, Learned KO, Palmer JN, et al. **Radiographic enhancement of the nasoseptal flap does not predict postoperative cerebrospinal fluid leaks in endoscopic skull base reconstruction.** *Laryngoscope* 2012;122:1226–34 CrossRef Medline
13. Learned KO, Adappa ND, Loevner LA, et al. **MR imaging evaluation of endoscopic cranial base reconstruction with pedicled nasoseptal flap following endoscopic endonasal skull base surgery.** *Eur J Radiology* 2013;82:544–51 CrossRef Medline
14. Learned KO, Adappa ND, Lee JY, et al. **MR imaging evolution of endoscopic cranial defect reconstructions using nasoseptal flaps and their distinction from neoplasm.** *AJNR Am J Neuroradiol* 2014;35:1182–89 CrossRef Medline
15. Kang MD, Escott E, Thomas AJ, et al. **The MR imaging appearance of the vascular pedicle nasoseptal flap.** *AJNR Am J Neuroradiol* 2009;30:781–86 CrossRef Medline
16. Kassam A, Snyderman CH, Mintz A, et al. **Expanded endonasal approach: the rostrocaudal axis, Part I: crista galli to the sella turcica.** *Neurosurg Focus* 2005;19:1–12 CrossRef Medline
17. Dehdashti AR, Ganna A, Witterick I, et al. **Expanded endoscopic endonasal approach for anterior cranial base and suprasellar lesions: indications and limitations.** *Neurosurgery* 2009;64:677–79 CrossRef Medline
18. Oostra A, van Furth W, Georgalas C. **Extended endoscopic endonasal skull base surgery: from the sella to the anterior and posterior cranial fossa.** *ANZ J Surg* 2012;82:122–30 CrossRef Medline
19. Kassam AB, Prevedello DM, Carrau RL, et al. **Endoscopic endonasal skull base surgery: analysis of complications in the authors' initial 800 patients—a review.** *J Neurosurg* 2011;114:1544–68 CrossRef Medline
20. Cappabianca P, Cavallo LM, Esposito F, et al. **E. Extended endoscopic endonasal approach to the midline skull base: the evolving role of transsphenoidal surgery.** *Adv Tech Stand Neurosurg* 2008;33:151–99 CrossRef Medline
21. Chabot JD, Patel CR, Hughes MA, et al. **Nasoseptal flap necrosis: a rare complication of endoscopic endonasal surgery.** *J Neurosurg* 2018;128:1463–72 CrossRef Medline
22. Kim CS, Patel U, Pastena G, et al. **The magnetic resonance imaging appearance of endoscopic endonasal skull base defect reconstruction using free mucosal graft.** *World Neurosurg* 2019;126:e165–72 CrossRef Medline
23. Lokmic Z, Darby IA, Thompson EW, et al. **Time course analysis of hypoxia, granulation tissue and blood vessel growth, and remodeling in healing rat cutaneous incisional primary intention wounds.** *Wound Repair Regen* 2006;14:277–88 CrossRef Medline

Enhancement in the Round Window Niche: A Potential Pitfall in High-Resolution MR Imaging of the Internal Auditory Canal

T. Brinjikji, C.M. Carr, J.C. Benson, and J.I. Lane

ABSTRACT

BACKGROUND AND PURPOSE: There is limited discussion in current literature about the normal imaging appearance of the round window. The purpose of this study was to assess the prevalence and imaging characteristics of gadolinium enhancement in the round window niche on MR imaging to the internal auditory canal.

MATERIALS AND METHODS: The presence or absence and laterality of enhancement in the round window niche on MR imaging was retrospectively reviewed in 95 patients from 1 institution. All studies included high-resolution (≤ 0.5 -mm section thickness) pre- and postgadolinium 3D FSE T1 with fat-saturation and postgadolinium 3D FLAIR image sequences. T1 and T2 acquisitions were viewed as coregistered overlays to confirm that enhancement was lateral to the round window membrane within the round window niche. CT was reviewed when available to assess the presence and laterality of soft tissue in the round window niche.

RESULTS: Ninety-five patients with internal auditory canal MRIs were included. Enhancement was present in the round window of 15 of 95 patients (15.8%). Of the 27 patients who underwent CT, 4 (14.8%) had concordant soft tissue on CT and MR imaging enhancement in the round window niche. One patient had MR imaging enhancement within the round window niche without a corresponding abnormality on CT. The absence of soft tissue on CT and the corresponding lack of MR imaging enhancement were present in 22 (81.5%) patients.

CONCLUSIONS: Enhancement can be visualized within the round window niche on MR imaging as an incidental finding. This enhancement probably represents postinflammatory granulation tissue and does not require further intervention. However, the potential for this enhancement to be misdiagnosed as a pathologic process can be a pitfall in MR imaging.

ABBREVIATIONS: ENT = ear, nose, and throat; FS = fat-saturation; IAC = internal auditory canal; RW = round window; RWN = round window niche

The round window (RW) is an opening between the middle and inner ear, located along the posterior aspect of the cochlear promontory. It acts as the boundary between the basal turn of the cochlea and the round window niche (RWN) of the mesotympanum. Functionally, the RW vibrates with an opposite phase to vibrations from the oval window, resulting in cochlear fluid movement.^{1,2}

Given the proclivity of middle ear pathologies to affect the ossicular chain and oval window, the RW is often overlooked. Nevertheless, accurate assessment of the RW and RWN is crucial for both diagnostic and preoperative planning purposes.^{3,4} Overall, isolated RWN pathology is rare, though developmental anomalies,

otitis media, otosclerosis, and labyrinthitis ossificans can affect this region.¹ Enhancement isolated to the RWN should not be confused with intralabyrinthine schwannomas^{5,6} or small paragangliomas, which usually arise from the cochlear promontory or extend along Jacobson nerve from the anterior wall of the jugular foramen.⁷

More commonly, nonmalignant, inflammatory abnormalities are found in this region, including fluid, proteinaceous debris and granulation tissue. These benign findings can demonstrate enhancement on MR imaging and may be confused with more sinister entities. For example, the authors of this study have previously encountered several situations in which enhancement on MR imaging was mistakenly noted to be present at the lateral aspect of the basal turn of the cochlea. Precise localization actually revealed that the enhancement was within the RWN, which excluded the possibility of an intracochlear schwannoma. In the current literature, the expected prevalence of enhancement in the RWN region is unknown. Thus, this study set out to assess the frequency of enhancement in the RWN with correlation of opacification on CT imaging.

Received August 29, 2022; accepted after revision December 31.

From the Mayo Clinic Alix School of Medicine (T.B.), Mayo Clinic Ringgold Standard Institution, Rochester, Minnesota; and Department of Radiology (C.M.C., J.C.B., J.I.L.), Mayo Clinic Ringgold Standard Institution, Rochester, Minnesota.

Please address correspondence to Taema Brinjikji, MD, Mayo Clinic Ringgold Standard Institution, Mayo Clinic Alix School of Medicine, 200 First St SW, Rochester, MN 55905; e-mail: Brinjikji.Taema@mayo.edu

<http://dx.doi.org/10.3174/ajnr.A7775>

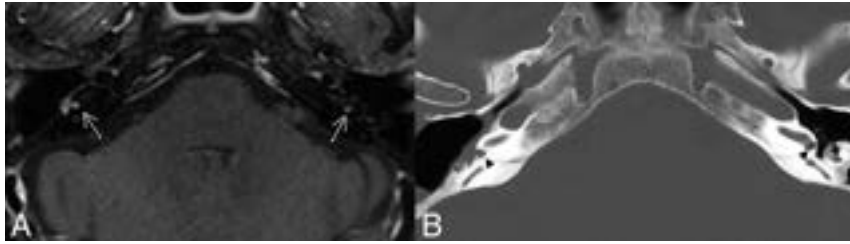


FIG 1. Example of enhancing granulation tissue in the RW. *A*, Axial postcontrast F5 T1WI demonstrates enhancement present bilaterally in the RWs (arrows). *B*, Axial head CT with thin-section bone window reconstructions demonstrates a right-sided canal wall-down mastoidectomy for resection of a cholesteatoma. Opacification of the round windows can be seen bilaterally, correlating to the area of enhancement (arrowheads).

Table 1: Summary of patient demographics, reasons for initial ENT visit, and relevant medical history relating to temporal bone

Patient information	
Demographics	
No. of patients	95
Age at MR imaging (average) (range) (yr)	58 (18–84)
Sex (No.)	
Female	53
Male	42
Reason for ENT visit	
Hearing loss	51
Tinnitus	11
Vertigo/dizziness/ataxia	13
Schwannoma/cholesteatoma/other tumor	13
Headache	2
Other	5
No. of patients with a mastoid effusion ^a	24
No. of patients with prior surgery on temporal bone	
Tympanomastoidectomy	6
Tympanotomy	1
Myringotomy	1

^aNo. of patients with clinical charts indicating the presence of granulation tissue in RW.

Table 2: Summary of MR imaging and CT findings

Findings	
Patients with MR imaging	
Enhancement in RW	15
Right	6
Left	7
Bilateral	2
Patients with both MR imaging and CT	
CT–/MR imaging–	22
CT+/MR imaging+	4
CT–/MR imaging+	1
Patients with CT	
Soft tissue in RW	4
Right	0
Left	3
Bilateral	1

Note:—CT+ indicates soft tissue found, MR imaging+ indicates enhancement found, CT– indicates no soft tissue found, and MR imaging indicates no enhancement found.

MATERIALS AND METHODS

Following institutional review board approval, sequentially obtained internal auditory canal (IAC) protocol MR imaging examinations performed between March 1, 2021, and April 20, 2021, were

compiled. MR imaging examinations were obtained on 3T Magnetom scanners (Skyra, Verio, and Prisma; Siemens) and included high-resolution 3D sampling perfection with application-optimized contrasts by using different flip angle evolution (3D SPACE sequence; Siemens) FSE T2 (TR, 1300 ms; TE, 162 ms; section thickness, 0.6 mm), axial T1 SPACE pregadolinium (TR, 600 ms; TE, 30 ms; section thickness, 0.90 mm), 3D SPACE FLAIR (TR, 5000 ms; TE, 345 ms; section thickness, 1.20 mm), and postgadolinium sagittal T1 fat-saturation (FS) SPACE (TR, 650 ms; TE, 14 ms; section thickness, 0.90 mm), which is a part of our institution's standard IAC protocol. Patients were scanned with a 32- or 64-channel head coil. In total, there were 100 patients who had an IAC MR imaging, with 5 ultimately excluded due to incomplete MR imaging. Of these, 27 (28.4%) patients had a prior temporal bone CT that could be used for evaluation of the presence of soft tissue in the RW.

Imaging and Clinical Review

The IAC MRIs were independently reviewed by 2 fellowship-trained neuroradiologists with Certificates of Added Qualification. The neuroradiologists independently reviewed the postcontrast 3D SPACE FSE T1 coregistered with 3D SPACE FSE T2 to localize the RWN and determine the presence or absence and laterality of enhancing granulation tissue (Fig 1). CT scans of patients ranging from 3 days to 19 years before the MR imaging were also assessed when available for the presence or absence and laterality of soft tissue in the RWN. Discrepancies were resolved via consensus review. Demographic information including age, sex, surgical history, and ear, nose and throat (ENT) diagnosis was obtained from the institution's electronic medical records for the entire cohort.

RESULTS

There were 95 (53 women; 55.8%) patients who made up the cohort, with 190 RWNs evaluated on MR imaging. The average patient age was 58 years (range, 18–84 years) (Table 1). In total, RWN enhancement was noted on the MR imaging of 15/95 patients (15.8%). Twenty-seven patients had a CT scan. There were 4 (14.8%) patients who had RWN enhancement on MR imaging and corresponding abnormal opacification on CT within the RW. A single patient had RWN enhancement on MR imaging without a corresponding abnormality on CT. The remaining 22 (81.5%) patients did not have an abnormality in the RWN on MR imaging or CT (Table 2).

Hearing loss was the most common presentation, comprising 51 patients (53.7%), while tinnitus, dizziness, temporal bone mass, and headache represented the remainder of the presentations (Table 1). Twenty-four patients (25.3%) were found to have a mastoid effusion on MR imaging, 6 of whom also had RW enhancement on MR imaging. Eight patients (8.4%) had an operation on their temporal bones before their MR imaging. Two patients (2.1%) were noted to have granulation tissue in the RW

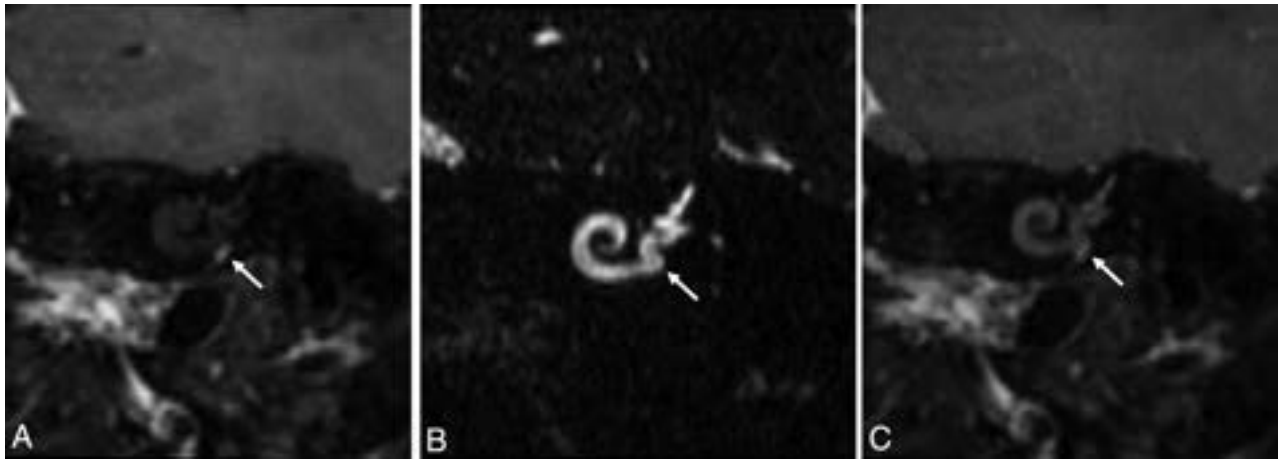


FIG 2. A, Postcontrast FS TIWI reconstructed in the Stenvers view demonstrates focal contrast enhancement. B, Thin-section 3D SPACE T2WI reconstructed in the Stenvers view demonstrates fluid signal throughout the basal turn of the cochlea as well as hyperintense signal lateral to the RW membrane (*white arrow*). Specifically, there is no filling defect within the basal turn of the cochlea. C, Coregistered overlay of the 3D SPACE T2WI and postcontrast FS TIWI illustrate that the enhancement is located lateral to the basal turn and entirely within the RWN (*white arrow*). Without the aid of the T2 SPACE and coregistration, it would be possible to misdiagnose a small intralabyrinthine schwannoma in the basal turn or a glomus tympanicum. The *white arrow* in A is the focal enhancement.

on their chart, one based on imaging and the other on surgical assessment. Both patients were found to have enhancement on MR imaging and soft tissue on CT in the RW.

DISCUSSION

The purpose of this study was to evaluate the prevalence of enhancement in the RWN on high-resolution MR imaging. We found that enhancement in the RW on MR imaging is not uncommon. It is present in 15.8% of cases, even without past surgery. Although CT was not available for all patients in this study, 1 of 5 patients who did have a CT scan and had RWN enhancement on MR imaging did not have a concordant abnormality on CT. To our knowledge, this represents the first description of incidental enhancement in the RWN on MR imaging.

Enhancement of the RWN is a potential pitfall in the imaging evaluation of this region and should not be confused with pathology when observed as an isolated finding. On MR imaging, RWN enhancement will be located lateral to the RW membrane at the level of basal turn of the cochlea. Coregistration with thin-section 3D T2WI or correlation with any concurrent CT imaging will localize the abnormality to the RWN, excluding the possibility of pathology, such as an intralabyrinthine schwannoma or a small glomus tympanicum.

Prior studies describing the anatomic appearance of the RWN on imaging are scarce. Veillon et al⁸ discussed some normal and pathologic RW and RWN findings on CT. They highlighted the importance of imaging in the detection of otosclerotic foci, congenital stenosis, and perilymphatic fistula. Other studies in the literature have described the anatomic landmarks of the RW to guide cochlear implantation procedures.⁹

Roßberg et al,¹⁰ in their retrospective study of conebeam CT examinations in 27 patients before treatment with intratympanic steroids, found granulation tissue obscuring the RWN in 15% (4/27) of patients, similar to our results with a larger cohort. Schachern et al¹¹ found histologic evidence of granulation tissue

in the RWN following experimentally induced otitis media in a cat model. In his postmortem study of 26 temporal bones in patients with a history of chronic otitis media, Djeric¹² found histologic evidence of fibroproliferative or granulation processes in the RWN in all cases. In most of these cases, the inflammatory changes were characterized by cellular debris and cystic spaces containing acidophilic fluid. This finding probably explains the increased T2 signal in the RWN that we observed in several cases of RWN contrast enhancement (Fig 2).

The differential diagnosis of isolated RWN enhancement on MR imaging is quite limited. Several of our cases demonstrated inflammatory changes elsewhere within the middle ear and mastoid air cells, supporting the diagnosis of granulation tissue (Fig 1). Intralabyrinthine schwannomas can extend into the RWN from the basal turn of the cochlea, but no evidence of cochlear enhancement on T1 or filling defects on T2 was observed in any of our cases. Tumor extension into the RWN can be seen with skull base meningiomas or paragangliomas, but again no evidence of adjacent skull base tumor was observed in this cohort.

This study has several limitations. First, it was conducted at a single institution, and the imaging reviewed was retrospective. Next, a small minority of patients had CT images available for comparison reviews. Finally, there was not surgical confirmation in all cases with imaging abnormalities. However, given prior reports of granulation tissue at this location and surgical confirmation of granulation tissue in 1 patient with RWN enhancement on MR imaging, it is likely that the MR imaging and CT findings of this cohort also represent granulation tissue.

CONCLUSIONS

Enhancement in the RWN is well-seen on high-resolution MR imaging and can be a potential pitfall in the interpretation of imaging. In the absence of other findings, the enhancement likely represents granulation tissue and may likely not require further imaging or intervention.

REFERENCES

1. Benson JC, Diehn F, Passe T, et al. **The forgotten second window: a pictorial review of round window pathologies.** *AJNR Am J Neuroradiol* 2020;41:192–99 CrossRef Medline
2. Tóth M, Alpár A, Patonay L, et al. **Development and surgical anatomy of the round window niche.** *Ann Anat* 2006;188:93–101 CrossRef Medline
3. Park E, Amoodi H, Kuthubutheen J, et al. **Predictors of round window accessibility for adult cochlear implantation based on preoperative CT scan: a prospective observational study.** *J Otolaryngol Head Neck Surg* 2015;44:20 CrossRef Medline
4. Hamamoto M, Murakami G, Kataura A. **Topographical relationships among the facial nerve, chorda tympani nerve and round window with special reference to the approach route for cochlear implant surgery.** *Clin Anat* 2000;13:251–56 CrossRef Medline
5. Mafee MF, Lachenauer CS, Kumar A, et al. **CT and MR imaging of intralabyrinthine schwannoma: report of two cases and review of the literature.** *Radiology* 1990;174:395–400 CrossRef Medline
6. Noguchi Y, Takahashi M, Momiyama N, et al. **Intralabyrinthine schwannoma extending into the round window niche and internal auditory canal** [In Japanese]. *Nihon Jibiinkoka Gakkai Kaiho* 2012;115:687–92 CrossRef Medline
7. Larson TC, Reese DF, Baker HL, et al. **Glomus tympanicum chemodectomas: radiographic and clinical characteristics.** *Radiology* 1987;163:801–06 CrossRef Medline
8. Veillon F, Riehm S, Emachescu B, et al. **Imaging of the windows of the temporal bone.** *Semin Ultrasound CT MR* 2001;22:271–80 CrossRef Medline
9. Zou J, Lähelmä J, Koivisto J, et al. **Imaging cochlear implantation with round window insertion in human temporal bones and cochlear morphological variation using high-resolution cone beam CT.** *Acta Otolaryngol* 2015;135:466–72 CrossRef Medline
10. Roßberg W, Goetz F, Timm ME, et al. **Intratympanic application of triamcinolone in sudden hearing loss: radiologic anatomy in cone beam CT and its' correlation to clinical outcome.** *Eur Arch Otorhinolaryngol* 2020;277:1931–37 CrossRef Medline
11. Schachern PA, Paparella MM, Goycoolea MV, et al. **The permeability of the round window membrane during otitis media.** *Arch Otolaryngol Head Neck Surg* 1987;113:625–29 CrossRef Medline
12. Djeriç D. **The round window niche and membrane in chronic suppurative otitis media.** *Med J Islam Repub Iran* 1999;13:111–13

Ultrasound Fusion–Guided Core Needle Biopsy for Deep Head and Neck Space Lesions: Technical Feasibility, Histopathologic Yield, and Safety

X. Li, J. Li, N. Zheng, H. Hu, X. Xie, and G. Huang



ABSTRACT

BACKGROUND AND PURPOSE: Ultrasound is generally considered to have a minor role in guiding biopsies for deep head and neck space lesions. However, the ultrasound fusion technique may have the potential to change this opinion. This study evaluated the feasibility, histopathologic yield, and safety of ultrasound fusion–guided core needle biopsies for deep head and neck space lesions.

MATERIALS AND METHODS: From March 2021 to April 2022, patients with primary deep head and neck space lesions were prospectively included in this study. Ultrasound fusion was performed with contemporaneous CT, MR imaging, or PET/CT studies, and ultrasound fusion–guided core needle biopsy was performed by using a Micro-Convex probe via 4 different needle approaches. Feasibility, histopathologic results, and biopsy-related complications were observed. Descriptive statistics were applied.

RESULTS: Ultrasound-guided biopsy was feasible in all 16 patients (11 women and 5 men; mean age 46 [SD, 16] years; range, 16–76 years). The lesions were located in the parapharyngeal space, infratemporal fossa, and skull base, with a median diameter of 3.8 cm (range, 2.2–6.5 cm). An adequate and definite histopathologic yield was obtained in 15/16 (93.8%) patients; among them, 4/15 lesions (26.7%) were malignant, and 11/15 (73.6%) were benign. No major complications occurred. Minor complications were noted in 2 of the 16 (12.5%) patients (self-limiting inflammation in 1 and bleeding in 1).

CONCLUSIONS: This study demonstrates that ultrasound fusion–guided biopsy of deep head and neck space lesions is feasible and safe, with a high histopathologic yield.

ABBREVIATIONS: H&N = head and neck; US = ultrasound

Lesions arising from deep head and neck (H&N) spaces are uncommon, but clinical management is challenging due to anatomic complexity and histologic diversity.^{1,2} Preoperative biopsy remains standard for better counseling and treatment planning. Open biopsy is used but should be carefully chosen due to risks, while percutaneous imaging-guided biopsy is now increasingly performed. CT guidance is a well-established biopsy method for

H&N lesions,^{3,4} but reports involving deep H&N spaces are few and mostly limited to small samples of patients.^{5–7} In addition, infrared navigation–guided biopsy has been explored in a small number of patients at a few institutes.^{8–10} MR imaging guidance is not widely used because of the longer acquisition times, higher cost, and the need for an open-configuration MR imaging system and MR imaging–compatible needles.^{3,11}

Ultrasound (US) guidance, with its inherent advantages of real-time imaging capability, rapid performance time, vessel depiction without intravenous contrast material, flexibility and portability, lack of radiation exposure, and high cost-effectiveness, is generally the first-line choice for biopsies on many H&N masses. However, to date, almost all researchers consider US unsuitable for the deep H&N region,^{3,5–9,12} for 2 reasons: First, acoustic degradation increases with depth, especially when the depth is >4 cm,¹² increasing the difficulty in delineating a target reliably; and second, osseous or air structures preclude an adequate acoustic window for US scanning.

US fusion has been widely used in biopsy and ablation procedures of the liver, kidney, and prostate.^{13,14} However, it has scarcely been applied in deep H&N spaces, such as the parapharyngeal

Received July 14, 2022; accepted after revision December 31.

From the Department of Medical Ultrasonics (X.L., H.H., X.X., G.H.), Institute of Diagnostic and Interventional Ultrasound, and Department of Otorhinolaryngology (J.L., N.Z.), The First Affiliated Hospital of Sun Yat-Sen University, Guangzhou, China. Xiaoju Li and Jian Li contributed equally to this article.

This work was supported by the National Natural Science Foundation of China (Grant No.92059201).

Please address correspondence to Guangliang Huang, MD, PhD, Department of Medical Ultrasonics, Institute of Diagnostic and Interventional Ultrasound, The First Affiliated Hospital of Sun Yat-Sen University, NO.58, Zhongshan Rd 2, Guangzhou, 510080, People's Republic of China. e-mail: huanggl9@mail.sysu.edu.cn

 Indicates open access to non-subscribers at www.ajnr.org

 Indicates article with online supplemental data.

 Indicates article with supplemental online video.

<http://dx.doi.org/10.3174/ajnr.A7776>

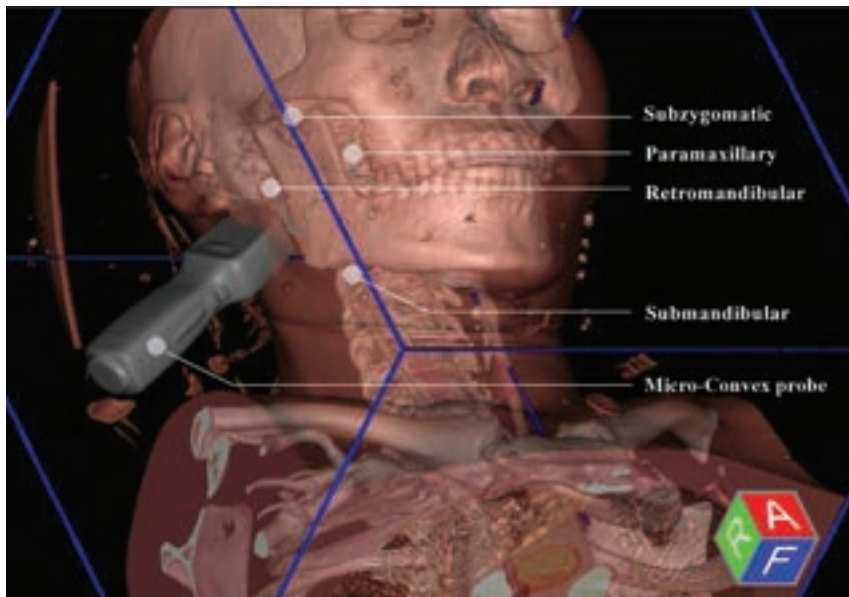


FIG 1. Schematic of US fusion-guided biopsy, with the use of a Micro-Convex probe and 4 available needle approaches.

space, infratemporal fossa, and skull base. To solve the above 2 issues, we have combined 2 advances; first, we have used US fusion imaging with CT, MR imaging, or PET/CT. Second, instead of a traditional Linear Array Probe, we have used a Micro-Convex probe (PVT-382BT; 3.0-5.0 MHz; Canon Medical Systems) for deeper acoustic penetration and better suitability for the narrow space between the bony structures. Thus, our purpose was to evaluate the feasibility, pathologic diagnostic value, and safety of US fusion-guided biopsies for deep H&N space lesions.

MATERIALS AND METHODS

Patients

This study was approved by the institutional review board. Each patient was informed of the risks and consented to the procedure. From March 1, 2021, to April 30, 2022, sixteen patients with primary deep H&N space lesions were prospectively enrolled in this study. The decision regarding biopsies was discussed by a multidisciplinary team, including otolaryngologists, oncologists, and radiologists. The indications for US fusion-guided biopsy were the following: 1) deep H&N space lesions that were difficult to identify on routine B-mode US, and 2) lesions that needed to selectively target the solid, enhancing components or hypermetabolic tissue. The contraindications were as follows: 1) pure cystic lesions; 2) patients who had a pacemaker and could not be in the magnetic field; 3) patients who could not maintain a fixed position during the procedure; and 4) patients with a bleeding disorder. For lesions with contiguous spread into adjacent anatomic spaces, the epicenter of the mass was used to classify the location.

US Fusion Process

The details of CT/MR imaging and whole-body PET/CT techniques are described in the Online Supplemental Data. All data were collected within 1 week before the biopsy, stored in DICOM format, and imported into the fusion platform (Smart-Fusion;

Canon Medical Systems) packaged with the US system (Aplio i900; Canon Medical Systems). An embedded electromagnetic navigation system (3D Guidance; Northern Digital) was used for probe tracking.

One of 2 radiologists with >5 or 10 years of experience performed the procedure. Patients maintained a stable supine position, tilting the head away from the side of the target lesion if necessary. The fusion process was broadly similar to the previous description of abdominal organs, which is based on the same principles of electromagnetic tracking and registration of the cross-sectional images with the live US image.^{13,14} Particularly for the deep H&N space lesions in this study, we used a Micro-Convex probe, which had a smaller volume, deeper penetration, and better suitability to scan via the narrow acoustic window compared

with the traditional Linear Array Probe. The planned US scanning and biopsy approaches included the subzygomatic, retromandibular, paramaxillary, and submandibular approaches (Fig 1). In addition, we used the plane of the globe for initial registration, followed by manual adjustment of the position by point-to-point registration and confirmation by color Doppler flow imaging and the overlay mode. The common anatomic points included optic nerves, carotid bifurcations, nasal tip, hyoid bone, and the thyroid. The registration errors were ≤ 5 mm and validated by > 4 different points in the overlay mode. When registration was successful, the cross-sectional images were coordinated and moved simultaneously with real-time US scanning. The operator could then confidently locate the biopsy target (Online Video). This process took approximately 2–5 minutes for an experienced operator.

US Fusion-Guided Biopsy

We performed all biopsies with the patient under local anesthesia with 1% lidocaine and used an 18-ga semiautomated side-cutting biopsy needle with a slot of 2.2 cm (Magnum; C.R. Bard). Guided by real-time US fusion imaging, the operator inserted the needle through a planned approach to obtain ≥ 2 core specimens, either by the freehand technique or assisted by the needle holder. Meanwhile, the blood vessels and necrotic areas of the lesions were avoided.

Patients were clinically monitored for at least 30 minutes after the biopsy, and they were followed up between 1–3 days and 1 month after the procedure to document any additional short-term or delayed complications.

Statistical Analysis

Statistical analysis was performed using SPSS, Version 22.0 (IBM). Continuous data are described as medians and interquartile ranges or mean (SD), according to the Shapiro-Wilk normality test.

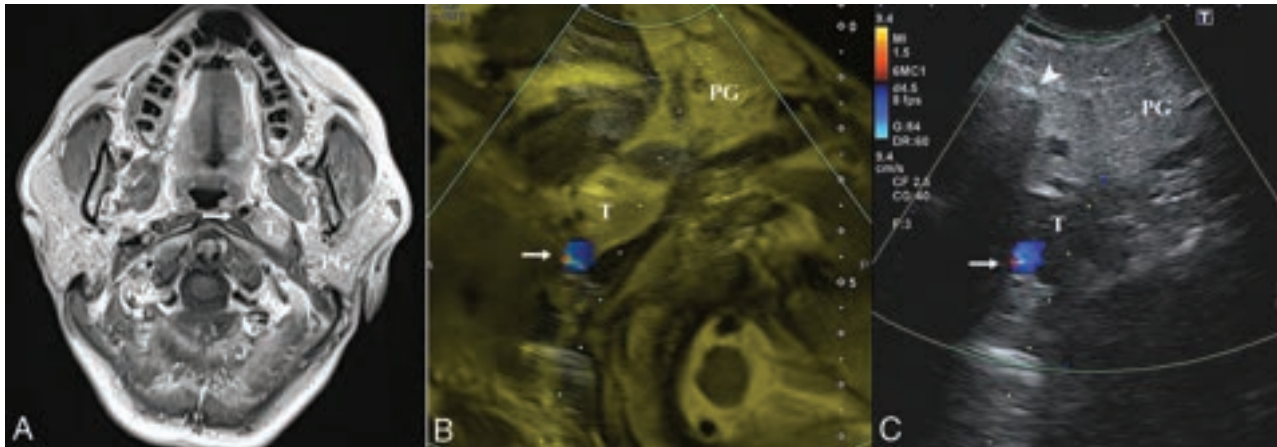


FIG 2. A 58-year-old woman without clinical presentation (patient No. 2). A, Axial T1-weighted post-contrast MR image shows a left parapharyngeal lesion with heterogeneous hyperintensity and a demarcated border. The target lesion is located deep in the parotid gland, and the ICA (arrow) is displaced medially. After a successful fusion of MR imaging (B) and US (C), MR imaging facilitates the accurate localization of the target lesion, which is ill-defined on US, with the ICA (arrow) confirmed on the color Doppler mode and the overlay mode (yellow mask). The dotted line indicates the expected needle path via the retromandibular approach. The histopathologic yield was schwannoma. T indicates target lesion; PG, parotid gland.

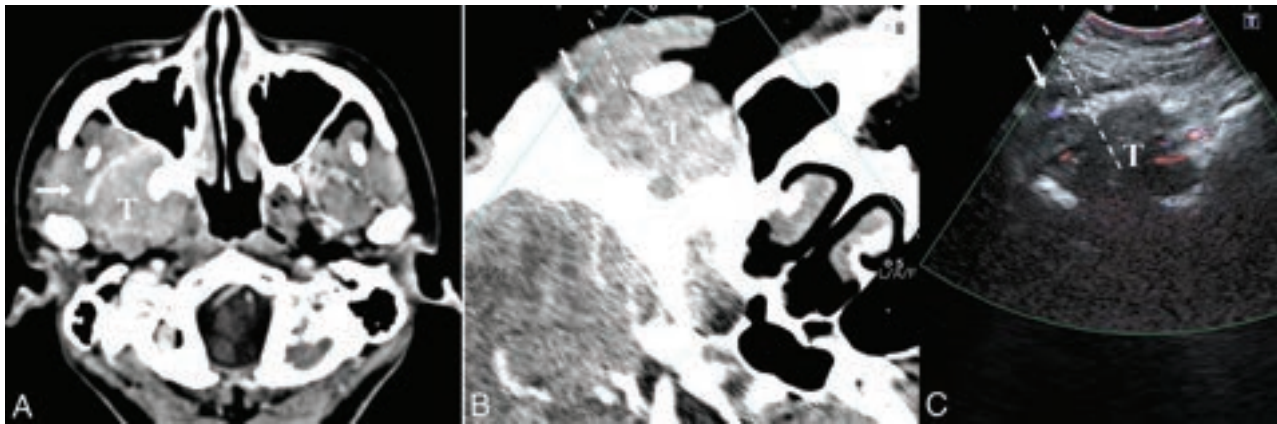


FIG 3. A 30-year-old woman with maxillofacial swelling, pain and dizziness for 2 years (patient No. 3). A, The axial contrast-enhanced CT image shows a homogeneously enhancing lesion involving the infratemporal fossa and pterygopalatine fossa. A branch of the maxillary artery runs superficially around the lesion (arrow). After a successful fusion of CT (B) and US (C), we can locate the target lesion that is occult on US due to the acoustic shadow of the mandible. Color Doppler US helps to avoid the maxillary artery (arrow). The dashed line indicates the expected needle path via the subzygomatic approach. Histopathology demonstrated meningioma (meningothelial subtype, World Health Organization grade I). T indicates target lesion.

RESULTS

Patient Characteristics and Procedural Details

In the 14-month period, 16 patients (11 women and 5 men; mean age, 46 [SD, 16] years; range, 16–76 years) underwent US fusion-guided biopsy of deep H&N space lesions. Presenting symptoms varied, though the 2 most common were swelling (7/16, 43.8%) and tinnitus (4/16, 25.0%). The long-axis diameter of the lesions ranged from 2.2 to 6.5 cm (median, 3.8 cm; interquartile range, 2.7–4.3 cm). The center of the lesion was most frequently the parapharyngeal space (9/16, 56.3%), followed by the infratemporal fossa (4/16, 25%); 3 lesions (3/16, 18.8%) were located in the skull base. CT (11/16, 68.8%) was the most commonly used technique for US fusion, followed by MR imaging (4/16, 25.0%) and PET/CT (1/16, 6.3%). The retromandibular approach (7/16, 43.8%) was the most used needle approach, followed by the

submandibular (4/16, 25.0%), subzygomatic (3/16, 18.8%), and paramaxillary approaches (2/16, 12.5%). The number of needle passes ranged from 2 to 3 (median, 2.5). Detailed information on the patient characteristics and procedural details are provided in the Online Supplemental Data.

Histopathologic Yield

The US fusion-guided biopsies were technically successful in all patients. Adequate samples were obtained for definite pathologic diagnosis in 15 of the 16 biopsies, and the diagnostic rate was 93.8%. Among those, 26.7% (4/15) were malignant, and the remaining 73.6% (11/15) were benign. Schwannoma (Fig 2), meningioma (Fig 3), and lymphatic malformations (Fig 4 and Online Video) were the top 3 benign pathologic types; others included solitary fibrous tumor (1/15, 6.7%), Warthin tumor

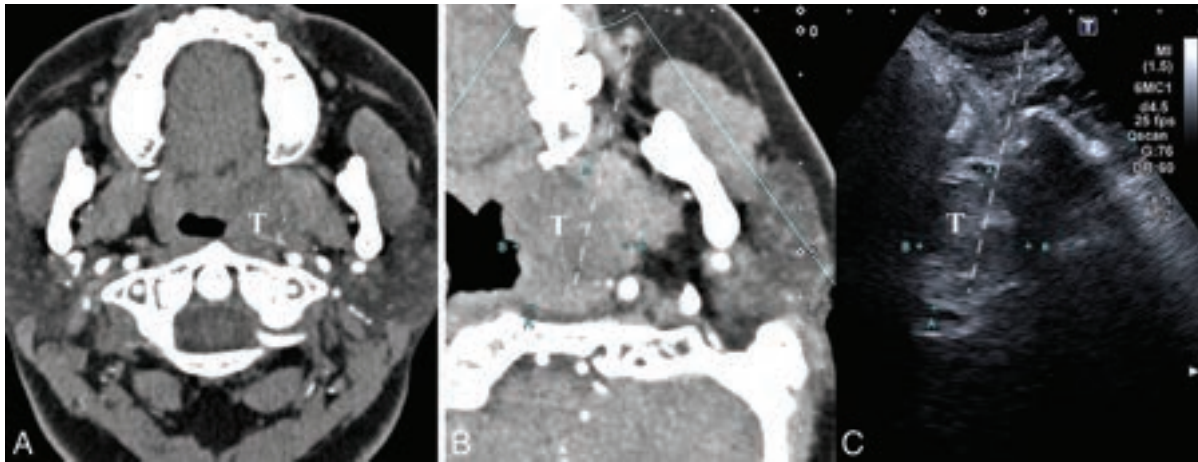


FIG 4. A 32-year-old woman with aural fullness, tinnitus, and hearing loss for 1 year (patient No. 10). *A*, The axial contrast-enhanced CT image shows a parapharyngeal lesion at the level of the alveolar ridge with mild and heterogeneous enhancement, constricting the auditory tube. After successful fusion with CT (*B*), a heterogeneous low-echoic lesion can be identified and located on US. *C*, The paramaxillary approach is chosen (*dashed line*). Histopathology demonstrated lymphatic malformation. T indicates target lesion.

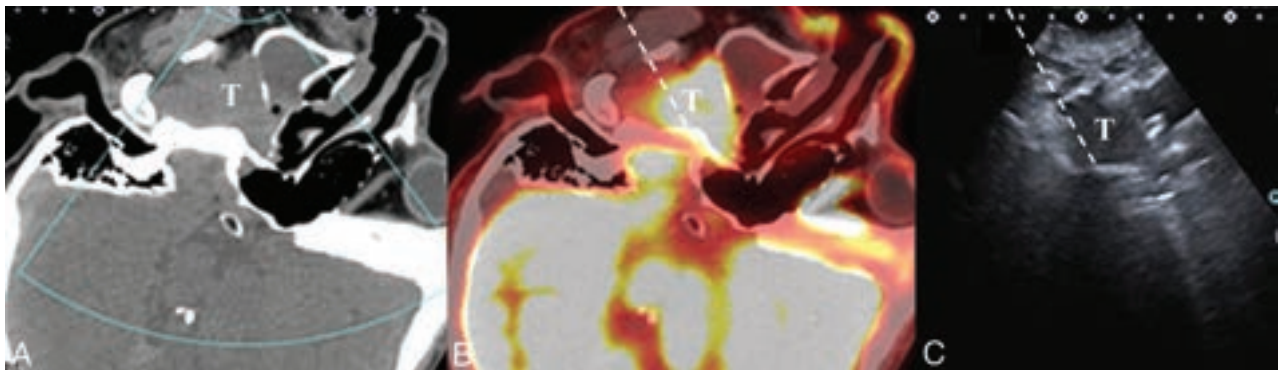


FIG 5. A 39-year-old man with headache for 1 month (patient No. 14). *A*, A multiplanar image of US–PET/CT fusion with the patient’s head tilted to the contralateral side. *A*, The axial plain CT shows an ill-defined lesion centered in the infratemporal fossa with bony destruction. *B*, The axial fused [¹⁸F] FDG–PET/CT reveals a high focal uptake. *C*, The target lesion is occult behind the acoustic shadow of the coronoid process on US, but a selective biopsy can be guided under fusion images. The subzygomatic approach is chosen (*dashed line*). Histopathology revealed nasopharyngeal carcinoma. T indicates target lesion.

(1/15, 6.7%), pleomorphic adenoma (1/15, 6.7%), and paraganglioma (1/15, 6.7%). The malignant diagnoses included invasive meningioma (1/15, 6.7%), acinic cell carcinoma of the parotid gland (1/15, 6.7%), squamous cell carcinoma (1/15, 6.7%), and nasopharyngeal carcinoma (1/15, 6.7%) (Fig 5). One biopsy (1/16, 6.3%) was nondiagnostic due to inadequate tissue sampling.

Biopsy-Related Complications

No major complications occurred after the biopsies. Minor complications were observed 1 day after the biopsy in 2 of 16 (12.5%) patients, both of whom were diagnosed with lymphatic malformation: One had mild inflammation of the puncture site and was treated conservatively in the outpatient clinic, and the other had self-limited bleeding that presented with blood-tinged sputum and required no intervention.

Clinical Management

Four patients (4/16, 25%) with diagnostic biopsies underwent subsequent surgical excision, and a concordant pathologic diagnosis

was obtained in 100% (4/4) of them. One patient (1/16, 6.3%) diagnosed with lymphatic malformation underwent sclerotherapy by tansoral injection of pingyangmycin. One patient (1/16, 6.3%) diagnosed with nasopharyngeal carcinoma was treated by radiation therapy and chemotherapy; the original surgical plan was canceled. One patient (1/16, 6.3%) diagnosed with squamous cell carcinoma refused further treatments. The remainder with benign or less invasive lesions (8/16, 50%) underwent clinical and imaging follow-up, following multidisciplinary discussion and consensus. In our 1 patient with a nondiagnostic specimen, the subsequent surgical pathology revealed low-grade myoepithelial carcinoma ex pleomorphic adenoma.

DISCUSSION

This pilot study showed that US fusion–guided biopsy was feasible, effective, and safe, with a high histopathologic yield for deep H&N space lesions. To our knowledge, this is the first report of the application of US fusion to this challenging area and may

play a role in the work-up of lesions involving the parapharyngeal space, infratemporal fossa, and skull base.

US-guided biopsy is an ideal first-line technique for cervicofacial masses, such as the thyroid, superficial lobe of the parotid gland, and cervical lymph nodes. US has played a minor role in the deep H&N spaces overlaid by bony structures such as the maxilla, mandible, mastoid, and styloid process, as well as the air-containing aerodigestive tract. This role is understandable when operators used only a large Linear Array Probe for scanning these areas, with obstructing anatomy overlying them. As reported in a recent study, preoperative needle biopsies were not feasible in 35% (42/120) of patients with parapharyngeal tumors because ultrasound or transoral palpation could not localize the lesions.¹⁵ However, our study has demonstrated the feasibility of US-guided biopsy for deep H&N spaces when combined with imaging fusion techniques and modification of probe and needle-path selection. In our biopsy procedure, US fusion provided resolution compensation, while the Micro-Convex probe accommodated the acoustic window and reduced the blind zone. All the deep H&N space lesions in this study were technically accessible, even a small skull base lesion measuring approximately 2 cm.

CT guidance has been considered a valuable tool in the biopsy of deep H&N lesions. However, conventional CT guidance lacks real-time feedback during the biopsy procedure, so the operator must confirm the needle path by intermittent scans. Real-time CT-fluoroscopy guidance or conebeam CT guidance is less widely used and can increase the radiation exposure to operators.^{16,17} In comparison, US fusion-guided biopsy is a real-time procedure, crucial for avoiding blood vessels or other structures without radiation exposure. Previous studies have shown a diagnostic rate of CT-guided core needle biopsy of 73%–96.8% in lesions involving the H&N as a whole.⁴⁻⁷ The average size of all target lesions was approximately 2.4–3.3 cm,⁴⁻⁶ including superficial and lower cervical masses. For emerging infrared navigation-guided biopsy, the diagnostic rate was approximately 90%.⁸⁻¹⁰ The target lesion size was reported in only 1 study of 8 patients, ranging from 2.5 to 9.0 cm (median, 3.7 cm).¹⁰ The diagnostic rate in our study was 93.8% (15/16), with a median lesion size of 3.8 cm (range, 2.2–6.5 cm), which is similar to other guidance modalities.

One biopsy sample of a parapharyngeal lesion measuring 3.8 cm was inadequate in this study, yielding a nondiagnostic biopsy rate of 6.3% (1/16). A small lesion size and necrotic components may contribute to nondiagnostic specimens.^{7,11} In retrospectively reviewing this unsuccessful biopsy, we postulated that patient movement during needle insertion may have affected the registration accuracy. The operator should take note of the patient's position and re-perform registration if necessary.

US fusion-guided biopsy was demonstrated to be safe without major complications in this study, in accordance with the results of other studies. Major complications after biopsy of deep H&N masses are rare. The risk of cranial nerve injury remains a theoretic concern but has not been demonstrated in the literature to date. Two cases of severe vascular complications after CT-guided biopsy of a H&N lesion have been reported.^{18,19} According to the authors, avoidance of vascular structures was critical, especially for patients with prior neck surgery and radiation therapy. The minor complication rate was 12.5% (2/16), including mild

inflammation of the puncture site and self-limited blood-tinged sputum. Mild infection and bleeding were the most reported minor complications after image-guided biopsy in the H&N.³⁻¹¹ Other minor complications included vasovagal reaction, transient facial palsy, and CSF leakage, which did not occur in this study.

The major limitation of our study was the small sample size. Because the incidence of deep H&N space lesions is low, US fusion-guided biopsy must be further evaluated in more patients and in multiple centers. In addition, we could not always compare histopathologic concordance between the biopsy and surgical specimens because most of the lesions in this study were benign, and the choice of surgery was avoided or postponed.

CONCLUSIONS

This pilot study demonstrates the feasibility, efficacy, and safety of US-guided percutaneous core needle biopsy for lesions in deep H&N spaces. Our findings may broaden the clinical application of the US fusion technique and contribute to diagnosing deep H&N space lesions accurately and conveniently.

Disclosure forms provided by the authors are available with the full text and PDF of this article at www.ajnr.org.

REFERENCES

1. Amit M, Bell D, Hunt PJ, et al. **Surgical management of carcinomas of the infratemporal fossa and skull base: patterns of failure and predictors of long-term outcomes.** *J Neurosurg* 2020;134:1392–98 CrossRef Medline
2. Lopez F, Suarez C, Vander Poorten V, et al. **Contemporary management of primary parapharyngeal space tumors.** *Head Neck* 2019;41:522–35 CrossRef Medline
3. Gupta S, Henningsen J, Wallace M, et al. **Percutaneous biopsy of head and neck lesions with CT guidance: various approaches and relevant anatomic and technical considerations.** *Radiographics* 2007;27:371–90 CrossRef Medline
4. Jordan RW, Shlapak DP, Benson JC, et al. **Percutaneous CT-guided core needle biopsies of head and neck masses: review of 184 cases at a single academic institution, common and special techniques, diagnostic yield, and safety.** *AJNR Am J Neuroradiol* 2022;43:117–24 CrossRef Medline
5. Wu EH, Chen YL, Wu YM, et al. **CT-guided core needle biopsy of deep suprahyoid head and neck lesions.** *Korean J Radiol* 2013;14:299–306 CrossRef Medline
6. Hillen TJ, Baker JC, Long JR, et al. **Percutaneous CT-guided core needle biopsies of head and neck masses: technique, histopathologic yield, and safety at a single academic institution.** *AJNR Am J Neuroradiol* 2020;41:2117–22 CrossRef Medline
7. Cunningham JD, McCusker MW, Power S, et al. **Accessible or inaccessible? Diagnostic efficacy of CT-guided core biopsies of head and neck masses.** *Cardiovasc Intervent Radiol* 2015;38:422–29 CrossRef Medline
8. Zhu JH, Yang R, Guo YX, et al. **Navigation-guided core needle biopsy for skull base and parapharyngeal lesions: a five-year experience.** *Int J Oral Maxillofac Surg* 2021;50:7–13 CrossRef Medline
9. Gao Y, Wu WJ, Zheng L, et al. **Diagnostic value of navigation-guided core needle biopsy in deep regions of the head and neck with focal FDG uptake on (18)F-FDG PET/CT.** *J Craniomaxillofac Surg* 2020;48:508–13 CrossRef Medline
10. Yang R, Lu H, Wang Y, et al. **CT-MRI image fusion-based computer-assisted navigation management of communicative tumors involved the infratemporal-middle cranial fossa.** *J Neurol Surg B Skull Base* 2021;82:e321–e329 CrossRef Medline

11. Lu Y, Liu M, Li C, et al. **MRI-guided biopsy and aspiration in the head and neck: evaluation of 77 patients.** *Eur Radiol* 2012;22:404–10 CrossRef Medline
12. Lorenzo G, Saindane AM. **Pitfalls in image guided tissue sampling in the head and neck.** *Neuroimaging Clin N Am* 2013;23:167–78 CrossRef Medline
13. Lerchbaumer MH, Fischer T. **Ultrasound fusion biopsy.** *Radiologe* 2021;61:11–18 CrossRef Medline
14. Ahn SJ, Lee JM, Lee DH, et al. **Real-time US-CT/MR fusion imaging for percutaneous radiofrequency ablation of hepatocellular carcinoma.** *J Hepatol* 2017;66:347–54 CrossRef Medline
15. Matsuki T, Miura K, Tada Y, et al. **Classification of tumors by imaging diagnosis and preoperative fine-needle aspiration cytology in 120 patients with tumors in the parapharyngeal space.** *Head Neck* 2019;41:1277–81 CrossRef Medline
16. Grand DJ, Atalay MA, Cronan JJ, et al. **CT-guided percutaneous lung biopsy: comparison of conventional CT fluoroscopy to CT fluoroscopy with electromagnetic navigation system in 60 consecutive patients.** *Eur J Radiol* 2011;79:e133–36 CrossRef Medline
17. Kim H, Park CM, Lee SM, et al. **C-arm cone-beam CT virtual navigation-guided percutaneous mediastinal mass biopsy: diagnostic accuracy and complications.** *Eur Radiol* 2015;25:3508–17 CrossRef Medline
18. Porcellini M, Bernardo B, Perretti B, et al. **Iatrogenic rupture of internal carotid artery aneurysm: a complication of CT-guided needle biopsy of the neck.** *G Chir* 1996;17:531–33 Medline
19. Walker AT, Chaloupka JC, Putman CM, et al. **Sentinel transoral hemorrhage from a pseudoaneurysm of the internal maxillary artery: a complication of CT-guided biopsy of the masticator space.** *AJNR Am J Neuroradiol* 1996;17:377–81 Medline

High-Resolution 7T MR Imaging of the Trochlear Nerve

T. Kumar, G.M. Virador, P. Brahmabhatt, A.A. Bhatt, E.H. Middlebrooks, A. Desai, A. Agarwal, P. Vibhute, and V. Gupta



ABSTRACT

BACKGROUND AND PURPOSE: The trochlear nerve has traditionally been difficult to identify on MR imaging. The advent of 7T MR imaging promises to greatly benefit visualization of small structures due to gains in the signal-to-noise ratio allowing improved spatial resolution. We investigated the utility of a clinically feasible ultra-high-resolution 7T MR imaging protocol for identification of the trochlear nerve, as well as assessment of normal trochlear nerve anatomy.

MATERIALS AND METHODS: Coronal high-resolution 2D T2-weighted TSE images used in a 7T epilepsy protocol of 50 subjects at our institution were reviewed by 2 independent radiologists for visualization of the trochlear nerve at the nerve origin and cisternal, tentorial, and cavernous segments. The frequency of nerve visibility within these segments and their anatomy were documented, and disagreements were resolved by joint review.

RESULTS: Of the 100 nerves reviewed in 50 subjects, at least 2 segments of the trochlear nerve from the brainstem to the cavernous sinus were identified in 100% of cases. The origins from the brainstem and cisternal segment were visible in 65% and 93% of nerves, respectively. The trochlear nerve was identified at the trochlear groove in 100% of cases and in the posterior wall of the cavernous sinus in 74% of cases.

CONCLUSIONS: Coronal high-resolution 2D TSE at 7T reliably identified the trochlear nerve throughout its course and is a promising tool for imaging patients with suspected trochlear nerve pathology.

ABBREVIATIONS: CN = cranial nerve; SAR = specific absorption rate; SCA = superior cerebellar artery

The trochlear nerve, or cranial nerve IV (CN IV), provides motor innervation of the superior oblique muscle and is responsible for inferior abduction of the eye. As a purely motor nerve, trochlear nerve palsy presents as torsional diplopia with a characteristic compensatory head tilt away from the affected side.^{1,2} Numerous disease processes including trauma, microvascular ischemia, or mass effect from a nearby tumor can affect the nerve, in addition to congenital trochlear nerve anomalies.³ Iatrogenic trochlear nerve injury is also an important concern in skull base surgery. It is, therefore, important for the radiologist to be able to visualize the course of the trochlear nerve.

The trochlear nerve has the longest intracranial course of all cranial nerves (60 mm), while also having the smallest diameter of approximately 0.3–1 mm.^{4,5} The course of the nerve has been divided into the brainstem, cisternal, tentorial, cavernous, and

orbital segments.⁶ The brainstem segment refers to the intra-axial course from the nucleus to the exit of the nerve into the quadrigeminal cistern. The longest segment, the cisternal segment, runs in the ambient cistern. The nerve then courses along the tentorium in its tentorial segment before piercing the dura within the trochlear cistern to enter the cavernous sinus. After coursing in the lateral wall of the cavernous sinus, the nerve enters the orbit through the superior orbital fissure, bifurcates, and innervates the superior oblique muscle.

The ability to identify the normal course of the trochlear nerve on imaging may serve as an aid to identify lesions or impingement by nearby structures. However, due to its small caliber and its course along several vascular structures, CN IV has been difficult to identify on imaging.⁵ Delineating its intracranial course has remained challenging even with the state-of-the-art 3T MR imaging sequences, largely due to limits on achievable resolution. An intrinsically higher SNR on 7T offers the potential for ultra-high-resolution imaging and improved visualization of the trochlear nerve.⁷ However, many substantial challenges of ultra-high-field MR imaging, such as B₀ and B₁+ inhomogeneity and an

Received November 8, 2022; accepted after revision December 31.

From the Department of Radiology, Mayo Clinic, Jacksonville, Florida.

Please address correspondence to Vivek Gupta, MD, 4500 San Pablo Rd S, Jacksonville, FL 32224; e-mail: gupta.vivek@mayo.edu

<http://dx.doi.org/10.3174/ajnr.A7774>

increased specific absorption rate (SAR), are barriers to reliable visualization of the trochlear nerve at 7T.⁸ Careful sequence optimization is required to realize the full potential of ultra-high-field MR imaging. The purpose of this study was to investigate the utility of an optimized T2 TSE at 7T in identifying the trochlear nerve from its origin from the brainstem to the cavernous sinus and describe its anatomic relationships and normal variations.

MATERIALS AND METHODS

MR Imaging Technique

Based on the nerve diameter and orientation of its intracranial course, the optimal sequence considerations include coronal section orientation along the vertical axis of the midbrain (orthogonal to the nerve) with the shortest achievable section thickness to reduce volume averaging, in-plane resolution of ≥ 0.4 mm, high nerve-CSF contrast, coverage from posterior midbrain to midorbit, and acquisition time of ≤ 10 minutes for practical clinical utility. Coronal 2D T2-weighted TSE in clinical use for evaluation of the mesial temporal lobe in our recently implemented epilepsy protocol on a clinical 7T Magnetom Terra MR imaging scanner (Siemens) met all the above considerations.

Trochlear nerve segment visualization

	Total Nerve Visualization
Origin at brainstem	65/100 (65%)
Cisternal segment	93/100 (93%)
Tentorial segment	100/100 (100%)
Cavernous segment ^a	74/100 (74%)

^a Only the posterior cavernous segment was visible.

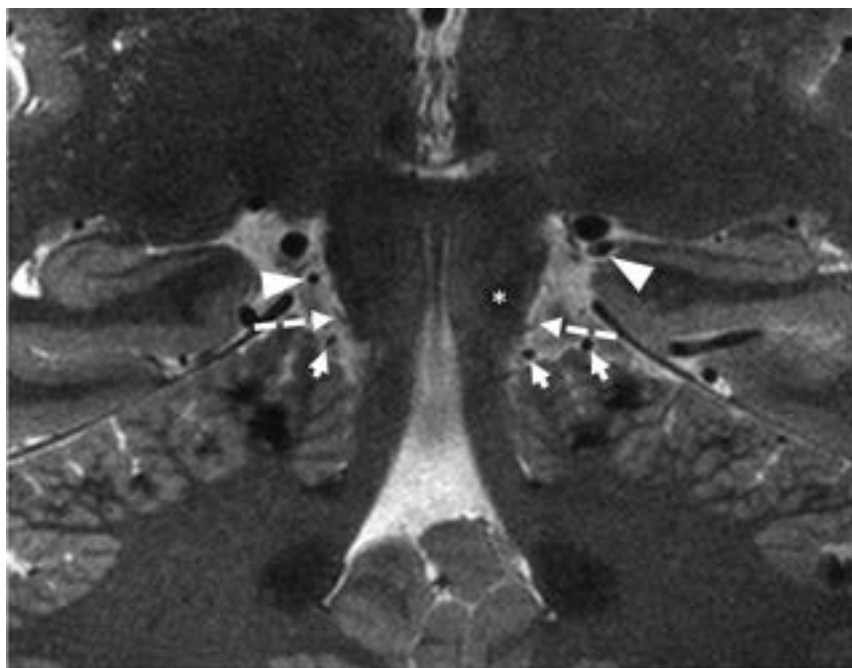


FIG 1. Coronal T2-weighted image showing the origins of trochlear nerve at the pontomesencephalic junction along the posterior aspect of the brainstem (*dashed arrows*), the left inferior colliculus (*asterisk*), rostral branches of the SCA (*arrowheads*), and caudal branches of the SCA (*short arrows*).

Relevant sequence parameters included the following: section thickness = 1.2 mm, TR = 8630 ms, TE = 35 ms, flip angle = 138°, echo-train length = 10, FOV = 150 × 150 mm, in-plane resolution = 0.34 × 0.34 mm (reconstructed at an interpolated voxel size of 0.17 × 0.17 × 1.2 mm), and a total scan time of 8 minutes. This sequence was developed at our institution through extensive volunteer testing with multiple iterations of sequence parameter optimization of contrast and SNR for the desired resolution within a clinically acceptable scan time. Epilepsy is one of the most common clinical indications for 7T MR imaging at our institution, providing a large imaging data set. Furthermore, in this patient cohort, the brainstem and cisternal structures were expected to be normal.

Subjects and Data Acquisition

Scans of 60 consecutive subjects undergoing clinical 7T MR imaging for epilepsy were evaluated, of which 10 scans were excluded from the analysis owing to excessive motion. The age range of the subjects was 16–85 years (mean age, 40.7 years). None of the subjects had any reported history of diplopia or ocular movement disorder.

The coronal T2 TSE images from this data set were evaluated independently by 2 experienced neuroradiologists for identification of each trochlear nerve. Visualization of the nerve was recorded in a binary fashion for each segment: 1) origin from the midbrain, 2) cisternal segment, 3) tentorial segment, and 4) anterior portion of its cavernous segment. Satisfactory identification of the nerve was considered positive in each segment if the nerve was clearly visible in at least ≥ 2 consecutive sections. The course of the trochlear nerve was followed and recorded from its origin from the brainstem, through the ambient cistern, along the tentorium, and into the posterior cavernous sinus. Any disagreements in identification of the nerve between the 2 observers were resolved by joint review. The relationship of the nerve to the major arteries was also recorded, along with the anatomic features of the trochlear groove and the trochlear cistern. The diameter of the nerve in the ambient cistern and measurements of the trochlear groove were also documented.

RESULTS

The incidence of positive identification of the different nerve segments is recorded in the Table. Of the 100 nerves reviewed in 50 subjects, at least some part of each trochlear nerve was identified in 100% of cases. The overall inter-rater agreement in identification of the nerve segments was 93% ($\kappa = 0.76$).

Of the total 100 nerves studied, the origin from the brainstem immediately below the inferior colliculus was confidently identified in 65% and the nerve

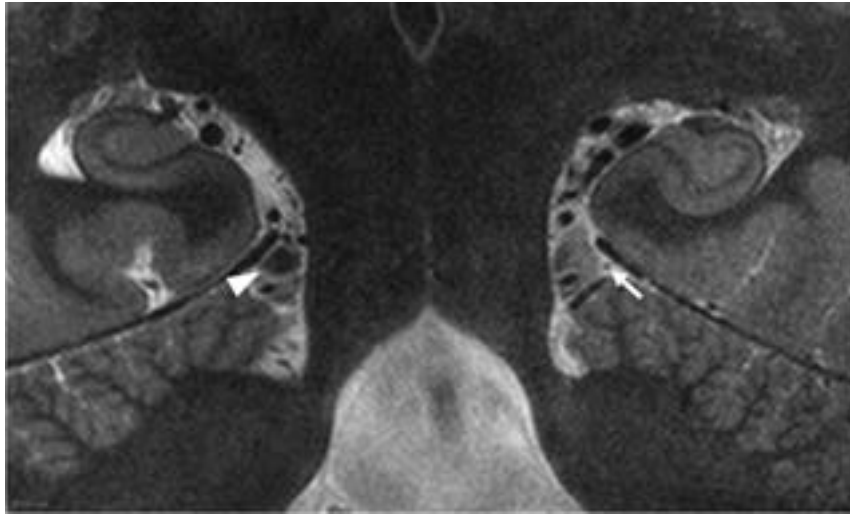


FIG 2. Coronal T2-weighted image showing the left trochlear nerve within the ambient cistern coursing toward the tentorium cerebelli (arrow). Note CSF flow signal obscuring the right trochlear nerve (arrowhead).

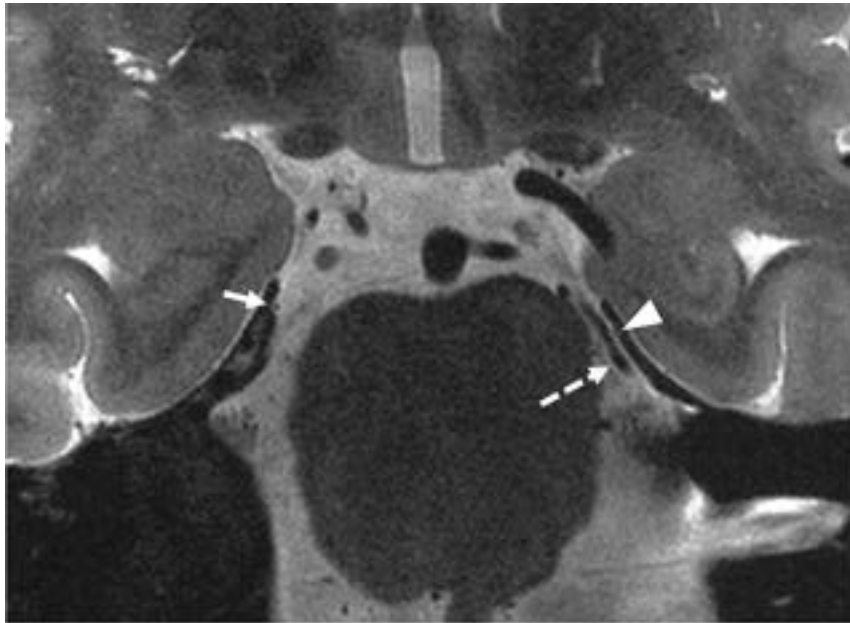


FIG 3. Coronal T2-weighted image showing the left trochlear nerve (arrowhead) crossing the rostral branch of the SCA (dashed arrow) along left tentorium cerebelli, and the right trochlear nerve entering the trochlear groove (arrow).

was visible in the ambient cistern 93% of the time. The nerve was always seen through its course in the trochlear groove, while it was confidently seen in 74% of cases piercing the posterior wall of the cavernous sinus surrounded by varying amounts of CSF in the so-called trochlear cistern. The T2 TSE sequence offered no effective contrast for visualization of the cavernous segment traveling within the fibrous layers of the lateral cavernous dura or the orbital segments, which were, therefore, not evaluated in this study.

The Table shows the visibility of the trochlear nerve segments from its origin to the cavernous sinus.

Trochlear Nerve Anatomy on 7T MRI Sections

Origin from the Brainstem. The origin of the trochlear nerve was seen at the posterior aspect of the pontomesencephalic junction at the inferior margin of inferior colliculus (Fig 1). In all subjects, the rostral branches of the superior cerebellar artery (SCA) were seen coursing above the nerve origin, whereas the caudal SCA branches traversed below it on the superior surface of the cerebellum (Fig 1).

Cisternal Segment. Anterior to its origin, the nerve was seen coursing superiorly and anterolaterally into the ambient cistern to reach the inferior surface of the free edge of the tentorium cerebelli (Fig 2). In 7% of the scans, CSF flow artifacts obscured the entire segment in the ambient cistern (Fig 2). The diameter of the trochlear nerve ranged between 0.4 and 0.5 mm in the ambient cistern.

On reaching the free edge of the tentorium cerebelli, the nerve traveled anterosuperiorly, becoming cranial to the rostral SCA branch before entering the trochlear groove (Fig 3).

Tentorial Segment. The trochlear nerve then passed through a 4- to 6-mm-long depression, ie, the trochlear groove, in the medial surface near the free edge of the tentorium before entering the cavernous sinus (Fig 4). The distance of the groove from the free edge was 1.1–2.0 mm (mean, 1.5 mm), and its depth measured between 0.4 and 0.9 mm (mean, 0.6 mm). After traversing the trochlear groove, the nerve pierced the posterior petroclinoid ligament to enter the lateral wall of the cavernous sinus, posterior and inferior to the oculomotor cistern (Fig 5). At this level, the nerve

was always contained within its own CSF sleeve, the trochlear cistern, and was never seen in the oculomotor cistern (Fig 5). The caliber of the trochlear cistern, seen as a sleeve of CSF surrounding the trochlear nerve, varied considerably among the subjects.

Cavernous Segment. After piercing the posterior petroclinoid ligament, the nerve reached the posterolateral apex of the cavernous sinus within the trochlear cistern, wedged between the anterior petroclinoid ligament laterally and the posterior petroclinoid ligament medially (Fig 6). Thereafter, it continued anteriorly in the lateral wall of the cavernous sinus, immediately below the

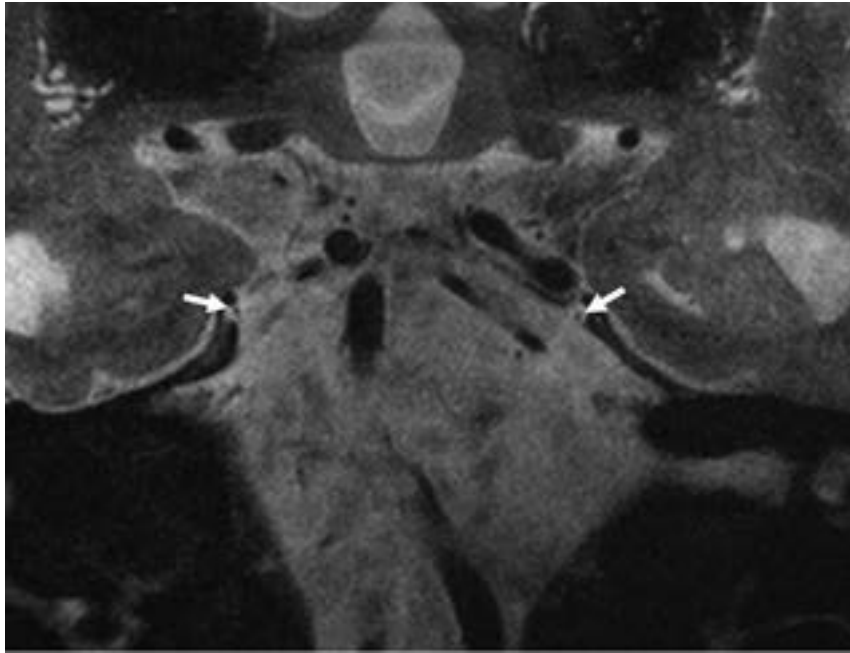


FIG 4. Coronal T2-weighted image showing the trochlear nerves within the trochlear grooves (arrows).

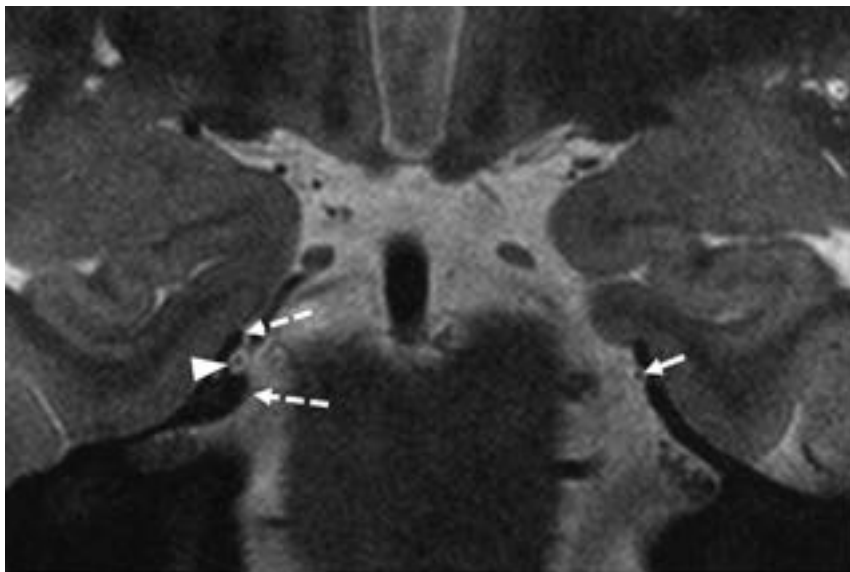


FIG 5. Coronal T2-weighted image showing the right trochlear nerve piercing the dura through the posterior petroclinoid ligament (dashed arrows) encased within the posterior end of the trochlear cistern (arrowhead), and the left trochlear nerve within the trochlear groove before entering the trochlear cistern (arrow).

oculomotor nerve and lateral to the cavernous venous channels and ICA (Fig 7).

Owing to the rather limited contrast between the nerve and adjacent structures on the TSE T2 sequence, the trochlear nerve could not be identified anterior to the midcavernous sinus in our study.

DISCUSSION

The aim of this study was to evaluate the ability of 7T MR imaging to better visualize the trochlear nerve and describe its course from its origin to the cavernous sinus in a large cohort of subjects with

preserved nerve anatomy and normal ocular motor function. We were able to identify the trochlear nerve and its anatomic relationships with a high degree of consistency on our coronal high-resolution 2D T2 TSE sequence. 7T MR imaging is, therefore, a promising tool for the clinical imaging of the trochlear nerve.

Successful identification of the trochlear nerve on conventional MR imaging has remained challenging owing to its size, proximity to adjacent vessels/other structures, and the achievable spatial resolution of MR imaging at standard field strengths.^{5,9} As also noted by Choi et al,⁵ reducing the voxel size below the diameter of the trochlear nerve is critical in detecting the nerve. Previous MR imaging studies at 3T have shown limited success in consistently identifying the nerve throughout its course.^{5,10-12} Consequently, there are incomplete and inconsistent descriptions of the trochlear nerve in the MR imaging literature, particularly in reference to the tentorial segment of the nerve and the trochlear cistern. Moreover, there is little-to-no reference in the imaging literature to the relationship of the nerve to the vessels in the ambient cistern and the dural reflections of the posterior cavernous sinus. Inconsistencies are also encountered in cadaveric, anatomic descriptions. A few postmortem dissections have described the tentorial course of the nerve within the oculomotor cistern, while others note a distinct CSF-containing trochlear cistern, independent of the oculomotor cistern.^{7,13-15}

We were able to address these knowledge gaps and controversies regarding the normal anatomy of the trochlear nerve. No variations of the nerve course were observed apart from the relative distance of the nerve to other cisternal structures. Within the tentorial segment,

the trochlear groove for the nerve was consistently visualized; whenever the cavernous segment was visualized, the nerve always coursed through the posterior cavernous sinus in its own CSF sleeve (ie, the trochlear cistern). These observations are important advancements in our understanding of trochlear nerve anatomy.

Proper identification of the trochlear nerve on MR imaging can be of value both from a presurgical perspective and in cases of suspected trochlear nerve palsy. Imaging has occasionally proved useful in identifying nerve impingement after trauma or nerve absence in some congenital cases of trochlear nerve

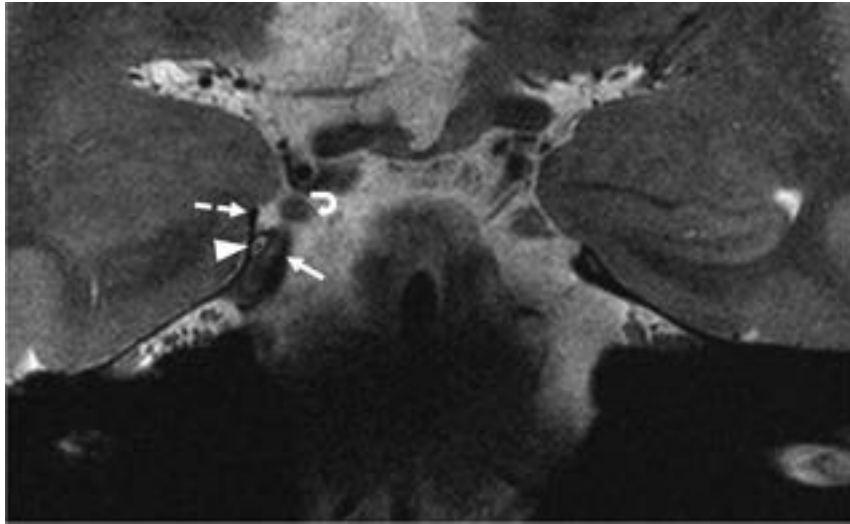


FIG 6. Coronal T2-weighted image showing the right trochlear nerve coursing in the trochlear cistern (*arrowhead*) at the posterolateral apex of cavernous sinus before reaching the lateral wall of the sinus and its relationships to the anterior petroclinoid (*dashed arrow*), the posterior petroclinoid (*arrow*) ligaments, and the right oculomotor nerve (*curved arrow*).

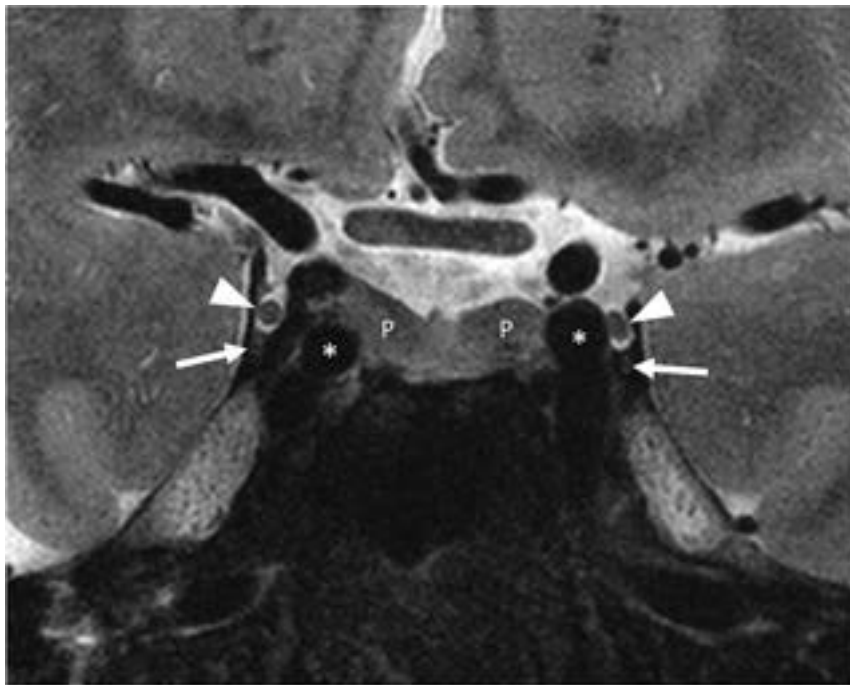


FIG 7. Coronal T2-weighted image showing the trochlear nerves within the lateral wall of middle one-third of the cavernous sinus (*arrows*), the oculomotor nerve and cistern (*arrowheads*), the pituitary gland (P), and the cavernous ICAs (*asterisks*).

palsy.¹⁶⁻¹⁸ Currently, imaging is rarely used in the clinical evaluation of isolated trochlear nerve palsy, largely because of the inability of current techniques to achieve sufficient resolution to identify the nerve. Our observations show that high-resolution 2D TSE MR imaging at 7T permits reliable identification of the trochlear nerve and evaluation of its anatomic relationships.

The 3D techniques commonly used for cranial nerve assessment at lower field strengths, such as CISS, true FISP, and

sampling perfection with application-optimized contrasts by using different flip angle evolution (SPACE sequence; Siemens), have limited data for cranial nerve assessment at 7T. These 3D techniques present unique challenges at ultra-high-field imaging. Due to the sensitivity of CISS and true FISP to phase variations, these techniques have artifacts at ultra-high-field strengths, limiting their use.⁸ While volumetric TSE, such as T2 SPACE, can be advantageous at 7T due to higher SNR and reduced blurring at shorter echo-train lengths, minimal blurring can still limit visualization of small structures, such as CN IV. Additionally, pronounced inhomogeneity in the B_1+ transmit field at 7T limits use of variable flip angle sequences (eg, SPACE). Strategies to improve B_1+ homogeneity, such as parallel transmission, also add to the already high SAR of these sequences limiting achievable resolution in reasonable acquisition times. Given these limitations, we chose an optimized 2D TSE sequence to provide extremely high in-plane resolution to enable visualization of the small nerve while minimizing the section thickness to balance the SAR and scan length. Previous studies using TSE at 7T were unsuccessful in visualizing CN IV, which underscores the value and novelty of our sequence optimization.⁸

Our study has notable limitations. There were no children in our cohort; the application to children is limited by the current weight restrictions of 7T imaging to patients of >30 kg due to the SAR. Furthermore, our study did not include patients with suspected trochlear nerve pathology.

CONCLUSIONS

High-resolution 2D TSE MR imaging at 7T allows reliable visualization of the trochlear nerve in an acceptable acquisition time and appears promising for clinical imaging of the trochlear nerve.

Disclosure forms provided by the authors are available with the full text and PDF of this article at www.ajnr.org.

REFERENCES

1. Keane JR. **Fourth nerve palsy: historical review and study of 215 inpatients.** *Neurology* 1993;43:2439-43 CrossRef Medline

2. Brazis PW. **Isolated palsies of cranial nerves III, IV, and VI.** *Semin Neurol* 2009;29:14–28 CrossRef Medline
3. Altintas AG. **Trochlear nerve palsy: a review of etiology, incidence, diagnostic methods, and treatment alternatives.** *Arch Neurol Neurosci* 2020;7:1–5 CrossRef
4. Villain M, Segnarbieux F, Bonnel F, et al. **The trochlear nerve: anatomy by microdissection.** *Surg Radiol Anat* 1993;15:169–73 CrossRef Medline
5. Choi BS, Kim JH, Jung C, et al. **High-resolution 3D MR imaging of the trochlear nerve.** *AJNR Am J Neuroradiol* 2010;31:1076–79 CrossRef Medline
6. Ammirati M, Musumeci A, Bernardo A, et al. **The microsurgical anatomy of the cisternal segment of the trochlear nerve, as seen through different neurosurgical operative windows.** *Acta Neurochir (Wien)* 2002;144:1323–27 CrossRef Medline
7. Bunch PM, Kelly HR, Zander DA, et al. **Trochlear groove and trochlear cistern: useful anatomic landmarks for identifying the tentorial segment of cranial nerve IV on MRI.** *AJNR Am J Neuroradiol* 2017;38:1026–30 CrossRef Medline
8. Grams AE, Kraff O, Kalkmann J, et al. **Magnetic resonance imaging of cranial nerves at 7 Tesla.** *Clin Neuroradiol* 2013;23:17–23 CrossRef Medline
9. Yousry I, Moriggl B, Dieterich M, et al. **MR anatomy of the proximal cisternal segment of the trochlear nerve: neurovascular relationships and landmarks.** *Radiology* 2002;223:31–38 CrossRef Medline
10. Yousry I, Camelio S, Schmid UD, et al. **Visualization of cranial nerves I–XII: value of 3D CISS and T2-weighted FSE sequences.** *Eur Radiol* 2000;10:1061–67 CrossRef Medline
11. Fischbach F, Müller M, Bruhn H. **High-resolution depiction of the cranial nerves in the posterior fossa (N III–N XII) with 2D fast spin echo and 3D gradient echo sequences at 3.0 T.** *Clin Imaging* 2009;33:169–74 CrossRef Medline
12. Cheng YS, Zhou ZR, Peng WJ, et al. **Three-dimensional-fast imaging employing steady-state acquisition and T2-weighted fast spin-echo magnetic resonance sequences on visualization of cranial nerves III - XII.** *Chin Med J (Engl)* 2008;121:276–79 Medline
13. Iaconetta G, de Notaris M, Benet A, et al. **The trochlear nerve: microanatomic and endoscopic study.** *Neurosurg Rev* 2013;36:227–38 CrossRef Medline
14. Lu D, Chen B, Liang Z, et al. **Comparison of bone marrow mesenchymal stem cells with bone marrow-derived mononuclear cells for treatment of diabetic critical limb ischemia and foot ulcer: a double-blind, randomized, controlled trial.** *Diabetes Res Clin Pract* 2011;92:26–36 CrossRef Medline
15. Everton KL, Rassner UA, Osborn AG, et al. **The oculomotor cistern: anatomy and high-resolution imaging.** *AJNR Am J Neuroradiol* 2008;29:1344–48 CrossRef Medline
16. Ko YS, Yang HJ, Son YJ, et al. **Delayed trochlear nerve palsy following traumatic subarachnoid hemorrhage: usefulness of high-resolution three dimensional magnetic resonance imaging and unusual course of the nerve.** *Korean J Neurotrauma* 2018;14:129–33 CrossRef Medline
17. Kim JH, Hwang JM. **Imaging of cranial nerves III, IV, VI in congenital cranial dysinnervation disorders.** *Korean J Ophthalmol* 2017;31:183–93 CrossRef Medline
18. Yang HK, Lee DS, Kim JH, et al. **Association of superior oblique muscle volumes with the presence or absence of the trochlear nerve on high-resolution MR imaging in congenital superior oblique palsy.** *AJNR Am J Neuroradiol* 2015;36:774–78 CrossRef Medline

The Impact of Interactive MRI-Based Radiologist Review on Radiotherapy Target Volume Delineation in Head and Neck Cancer

D. Adjogatse, I. Petkar, M. Reis Ferreira, A. Kong, M. Lei, C. Thomas, S.F. Barrington, C. Dudau, P. Touska, T. Guerrero Urbano, and S.E.J. Connor



ABSTRACT

BACKGROUND AND PURPOSE: Peer review of head and neck cancer radiation therapy target volumes by radiologists was introduced in our center to optimize target volume delineation. Our aim was to assess the impact of MR imaging-based radiologist peer review of head and neck radiation therapy gross tumor and nodal volumes, through qualitative and quantitative analysis.

MATERIALS AND METHODS: Cases undergoing radical radiation therapy with a coregistered MR imaging, between April 2019 and March 2020, were reviewed. The frequency and nature of volume changes were documented, with major changes classified as per the guidance of The Royal College of Radiologists. Volumetric alignment was assessed using the Dice similarity coefficient, Jaccard index, and Hausdorff distance.

RESULTS: Fifty cases were reviewed between April 2019 and March 2020. The median age was 59 years (range, 29–83 years), and 72% were men. Seventy-six percent of gross tumor volumes and 41.5% of gross nodal volumes were altered, with 54.8% of gross tumor volume and 66.6% of gross nodal volume alterations classified as “major.” Undercontouring of soft-tissue involvement and unidentified lymph nodes were predominant reasons for change. Radiologist review significantly altered the size of both the gross tumor volume ($P = .034$) and clinical target tumor volume ($P = .003$), but not gross nodal volume or clinical target nodal volume. The median conformity and surface distance metrics were the following: gross tumor volume Dice similarity coefficient = 0.93 (range, 0.82–0.96), Jaccard index = 0.87 (range, 0.7–0.94), Hausdorff distance = 7.45 mm (range, 5.6–11.7 mm); and gross nodular tumor volume Dice similarity coefficient = 0.95 (0.91–0.97), Jaccard index = 0.91 (0.83–0.95), and Hausdorff distance = 20.7 mm (range, 12.6–41.6). Conformity improved on gross tumor volume-to-clinical target tumor volume expansion (Dice similarity coefficient = 0.93 versus 0.95, $P = .003$).

CONCLUSIONS: MR imaging-based radiologist review resulted in major changes to most radiotherapy target volumes and significant changes in volume size of both gross tumor volume and clinical target tumor volume, suggesting that this is a fundamental step in the radiotherapy workflow of patients with head and neck cancer.

ABBREVIATIONS: AJCC = American Joint Committee on Cancer; CTV = clinical target volume; CTVN = clinical target nodal volume; CTVT = clinical target tumor volume; DSC = Dice similarity coefficient; GTV = gross target volume; GTVN = gross nodal volume; GTVonc = original oncology GTV; GTVrad = post-radiology review volume; GTVT = gross tumor volume; HD = Hausdorff distance; HN = head and neck; HNC = head and neck cancer; IQR = interquartile range; JI = Jaccard index; PTV = planning target volume; RT = radiotherapy; TRE = target registration error

The efficacy of curative radiotherapy (RT) for head and neck cancers (HNCs) requires the delivery of high doses of radiation to well-defined disease volumes, while sparing normal

tissues as much as possible.¹ HNC target volume delineation relies on accurate interpretation of radiologic imaging with complex locoregional anatomy. While CT provides geometric accuracy and

Received July 14, 2022; accepted after revision December 31.

From the Departments of Oncology (D.A., I.P., M.R.F., A.K., M.L., T.G.U.), Medical Physics (C.T.), and Radiology (C.D., P.T., S.E.J.C.), Guy's and St Thomas' National Health Service Foundation Trust, London, UK; School of Biomedical Engineering and Imaging Sciences (D.A., C.T., S.E.J.C.) and King's College London and Guy's and St Thomas' PET Centre (S.F.B.), School of Biomedical Engineering and Imaging Sciences, King's College London, King's Health Partners, London, UK; Department of Neuroradiology (C.D., S.E.J.C.), King's College Hospital, London, UK; and Faculty of Dentistry, Oral and Craniofacial Sciences (T.G.U.), King's College London, London, UK.

S.F. Barrington acknowledges support from the National Institute for Health Research and Social Care (RP-2-16-07-001), King's College London and the UCL Comprehensive Cancer Imaging Center are funded by the Cancer Research UK and EPSRC in association with the Medical Research Council and Department of Health and Social Care (England). This work was also supported by the Wellcome Trust/Engineering and Physical Sciences Research Council Center for Medical Engineering at King's College London (WT 203148/Z/16/Z).

The views expressed are those of the authors and not necessarily those of the National Health Service, the National Institute for Health Research and Social Care, or the Department of Health and Social Care.

For Dr Steve Connor, this research was funded, in whole or in part, by the Wellcome Trust (203148/Z/16/Z). For the purpose of open access, the author has applied a CC BY public copyright license to any author accepted manuscript version arising from this submission. Authors acknowledge funding support from the Wellcome/Engineering and Physical Sciences Research Council Center for Medical Engineering at King's College London (WT 203148/Z/16/Z); the National Institute for Health Research Biomedical Research Center at Guy's and St Thomas' Hospitals and King's College London; the Cancer Research UK National Cancer Imaging Translational Accelerator (A27066); and the UK Research and Innovation London Medical Imaging and Artificial Intelligence Center.

For Teresa Guerrero Urbano, this work was supported by the Radiation Research Unit at the Cancer Research UK City of London Center [C7893/A28990].

relative electron density–derived dose calculations required for RT planning. MR imaging allows more accurate disease identification, owing to improved soft-tissue contrast resolution.²

Variability of gross target volume (GTV) delineation has been shown to affect dose distribution to tumors and organs at risk.³ The uncertainty of GTV delineation is partially accounted for through the creation of radical clinical and planning target volumes (CTV and PTV). For intensity-modulated RT, it is recommended that radical CTVs be created from geometric expansion of GTVs, rather than larger traditional anatomic boundaries.⁴ Therefore, precise GTV delineation is crucial for improving plan quality and patient outcomes.⁵ MR imaging–based GTV delineation has been shown to reduce interobserver variability.³ Therefore, coregistration of MR imaging with planning CT scans for RT volume delineation is important for optimum disease definition, with acquisition in the RT immobilization mask and position preferred for superior precision of CT-to-MR imaging registration.⁶

Review of oncologist-defined RT target volumes by head and neck (HN) radiologists reportedly changes 52%–55% of volumes when using CT or diagnostic MR imaging.^{7,8} Peer review by fellow oncologists is associated with alteration rates of 14%–39%.^{9,10} The importance of oncology peer review is well-established and is the standard of care in many UK centers, whereas radiologist involvement occurs in only 8% of institutions.¹¹

In 2018, interactive MR imaging–based radiologist review was formally introduced into the RT workflow for patients with HNC at our institution. It was hypothesized that this would result in significant changes to the RT target volumes. This study aimed to describe the frequency, nature, causes, and clinical significance of alterations and to compare the size and conformity indices for target volumes obtained before and after radiologist review.

MATERIALS AND METHODS

The study received local institutional approval as a service evaluation (Guy's and St Thomas' NHS Foundation Trust, No. 9623). All patients prospectively consented to use of anonymized information for audit and quality-improvement purposes at the time of their RT consent.

Participants

From April 2019 to March 2020, consecutive patients undergoing radical volumetric modulated arc therapy for HNC, for which the use of a coregistered MR imaging was indicated for target volume delineation, were prospectively reviewed during weekly interactive oncologist/radiologist sessions.

Imaging and Coregistration Protocols

RT planning CT scans were acquired on a Biograph mCT Flow (Siemens) at 2.5-mm section thickness with contrast enhancement,

unless contraindicated. All planning CT scans were performed using a 5-point thermoplastic immobilization shell.

Patients had a diagnostic MR imaging performed on either 1.5T or 3T MR imaging Magnetom Aera or Skyra scanners (Siemens) using a surface phased-array 20- or 32-channel neck coil. The diagnostic MR imaging protocol included the following: axial T1WI TSE with and without fat suppression, T2WI TSE, and contrast-enhanced T1WI (plus fat suppression); coronal T2WI STIR; and axial DWI. Section thicknesses ranged from 3 mm (STIR) to 4 mm (anatomic and DWI). Wherever possible, patients with paranasal sinus and nasopharyngeal cancer also underwent MR imaging for RT planning in an immobilization mask. The RT planning MR imaging protocol included the following: sagittal T2WI sampling perfection with application-optimized contrasts by using different flip angle evolution (SPACE sequence; Siemens), axial T1WI FLASH, and contrast-enhanced axial T1WI FLASH (+ fat suppression) sequences, all acquired at 1-mm section thickness.

The MRIs were rigidly coregistered with the planning CT within the RT treatment planning system. The institutional protocol in use during the study period mandated the diagnostic or RT planning T2WI sequence for coregistration, because historically this sequence had most frequently been referenced for volume delineation. Additional sequences were coregistered on request or at the discretion of the RT pretreatment team. Coregistration accuracy was retrospectively determined within the RT treatment planning system using the target registration error (TRE) of 1 bony and 2 soft-tissue landmarks. The mean (TREmean) and maximum (TREmax) values for each coregistration were obtained and assessed against the recommended optimum of TREmean of ≤ 2 mm and TREmax of ≤ 5 mm.¹²

Radiologist Review and Definition of Target Volumes

Gross tumor and gross tumor nodal volumes (GTVTs and GTVNs) were generated by 1 of 5 clinical oncologists (with 2, 2, 7, and 12 years of HNC consultant experience) on Eclipse RT Treatment Planning System (Version 15.5; Varian), with concurrent use of Sectra PACS IDS7 (Sectra) and supportive clinical information. Volumes were subsequently reviewed jointly with 1 of 3 HN radiologists (with 2, 6, and 20 years' experience), also using Eclipse and PACS. The review process included interactive discussion with reference to clinical information and other diagnostic imaging (eg, PET/CT) at the discretion of the radiologist. All radiologists and oncologists were aware of the study purpose.

The primary focus was review of the delineation of all gross disease on MR imaging. GTVs were duplicated and saved before radiology review to preserve the original oncology GTV (GTVonc). A second postradiology review volume (GTVrad) was created and amended as necessary. Contours were adjusted by the radiologist or the oncologist under the instruction of the radiologist. All final amended GTVs were also viewed on the CT planning scan to assess discrepancies, which were noted and amended when possible. Patients proceeded to the creation of CTVs and PTVs as per institutional protocol, with no further input from radiologists.

For this evaluation, study CTVs were created by a single observer (the first author of this report who is a clinical oncologist not part of the original delineation or peer review process) to avoid interobserver variability in the CTV delineation process and to

Please address correspondence to Delali Adjogatse, MD, Guy's and St Thomas' Hospitals NHS Foundation Trust, Guy's Hospital, Great Maze Pond, SE1 9RT; e-mail: Delali.adjogatse@gstt.nhs.uk

 Indicates open access to non-subscribers at www.ajnr.org

 Indicates article with online supplemental data.

<http://dx.doi.org/10.3174/ajnr.A7773>

assess the impact of radiology review on CTVs. This process involved geometric expansion of both GTVonc/GTVrad by a 10-mm isotropic margin to create tumor or nodal CTVonc/CTVrad (20 mm for nodes with evidence of extranodal spread) and editing off barriers to tumor spread (ie, air, bone, and muscle if muscle invasion was absent). In postoperative cases, the preoperative disease on MR imaging was used to guide the extent of the CTV, which would ultimately encompass the entire anatomic surgical bed. Therefore, adjustments to preoperative GTVs were included in this study, but not the postoperative CTVs.

Radiation Therapy Planning

All patients underwent volumetric modulated arc therapy, with standard PTV doses and fractionations as follows: 65 Gy in 30 fractions (f) to cover gross disease; 60 Gy/30f to the postoperative tumor bed; and 54 Gy/30f to elective nodal regions, delineated as per consensus guidelines.^{13,14} Isotropic 4-mm margins were added to CTVs to create radical PTVs.

Descriptive Data and Qualitative Analysis

Patient demographics, tumor subsite and staging (American Joint Committee on Cancer [AJCC] and tumor, node and metastasis), delineating oncologist, attending radiologist, and time taken for review were documented prospectively. The nature, anatomic patterns, and contributing factors for volume amendment were noted at the time of review. Anatomic patterns were the following: lymph node (addition/removal), GTVT deep extent (changes to submucosal involvement), GTVT superficial extent (changes primarily along mucosal surface), normal structure exclusion, skull base/bone or perineural spread, intracranial, and sinonasal (intra-sinus) extension. Oncologists also prospectively recorded whether they thought the changes made at peer review were clinically significant. This judgment was qualitative, combining a subjective assessment of clinical significance and a predetermined definition of geographic miss (Online Supplemental Data).

Volumetric and Quantitative Analysis

The absolute and percentage volume differences between the GTVonc and GTVrad (regarded as the expert volume) were recorded. Conformity (degree of spatial overlap) was assessed using the Dice similarity coefficient (DSC) and Jaccard index (JI).¹⁵ The Hausdorff distance (HD) assessed the maximum distance between voxel locations for each tumor volume, to assess the deviation between volumes in 3D.¹⁶ These indices were obtained using MIM Encore (MIM Software). Only amended volumes that were duplicated and saved before peer review were included in volumetric analysis.

Postradiology volume adjustments were retrospectively classified as major or minor on the basis of the guidance of the Royal College of Radiologists (Online Supplemental Data).¹⁷ Alterations to prevent a geographic miss, such as editing a GTVT by ≥ 10 mm or adding suspicious nodes within the radical CTV, were defined as major. Alterations that would otherwise still be clinically acceptable, such as editing of normal tissues, were classified as minor.

Statistical Analysis

Descriptive statistics documented the frequency of GTV change, anatomic patterns of change, and rates of major change. The

Shapiro-Wilk test was used to assess data-distribution normality. The Spearman correlation coefficient assessed an association between years of experience (oncologist/radiologist) and the frequency of any change and major change. The difference in volume size between pre- and postradiology GTVs and CTVs and the differences in the distribution of DSC, JI, and HD between GTVs and CTVs were analyzed using the Wilcoxon signed-rank test. A 2-tailed Fisher exact test was used to determine whether categorical factors were associated with any or major change. Analyzed factors were the following: histology, T stage, N stage, AJCC stage, postoperative status, use of a research trial delineation protocol, and use of DWI for target identification. Registration error (TREMmean and TREmax) and its correlation with frequency of any and major change were assessed using the Mann-Whitney *U* test. Statistical significance was $P < .05$.

RESULTS

Participant Characteristics

We reviewed 50 consecutive patients (Online Supplemental Data): 37 patients with definitive intensity-modulated RT, 11 postoperative patients, and 2 high-dose palliative patients. The median age was 59 years, 72% were men, and 72% had oropharyngeal cancer. There were 50 GTVTs and 42 GTVNs reviewed. One GTVN review was subsequently excluded as new diagnostic information became available (fine-needle aspiration cytology) after GTVNonc delineation. The median radiology time taken per case was 20 minutes (interquartile range [IQR] = 15–30; absolute range = 5–60). Five patients had MR imaging scans for RT planning; all others had diagnostic MRIs. Figure 1 illustrates an example of post-peer review volume adjustments.

Frequency, Nature, and Anatomic Patterns of GTV and CTV Changes following MR Imaging–Based Radiologist Review

Forty-two patients had at least 1 GTV amended (84%). Seventy-six percent of GTVTs (38/50) and 41.5% of GTVNs (17/41) were amended.

Anatomic patterns of change were the following: GTVN, additional nodes identified (82.3%; 14/17); GTVT, deep extent (68.4%; 26/38); GTVT, superficial extent (23.6%, 9/38); normal structure exclusion (GTVT, 5.2%, 2/38; GTVN, 11.8%, 2/17); and GTVT with perineural spread (2.5%, 1/38).

Explanatory documentation for GTV modification was available for all amended volumes and was retrospectively organized into 5 distinct groups (Fig 2). The most common reasons for modifications were imaging misinterpretation (GTVT, 57.8%, 22/38; GTVN, 52.9%, 9/17) and changes made after collaborative discussion (GTVT, 7.9%, 3/38; GTVN, 23.5%, 4/17). Medial extension of oro-/hypopharyngeal tumors ($n = 6$) and superior extension of nasopharyngeal tumors into the nasopharyngeal vault ($n = 4$) were common causes for GTVT alteration. The most frequent reasons for GTVN addition were inclusion of suspicious or pathologic nodes adjacent to correctly delineated nodal disease in cervical levels 1b–3 ($n = 9$) and inclusion of retropharyngeal nodes ($n = 3$: 1 missed despite diagnostic report, 1 pathologic but unreported, 1 highly suspicious and unreported). Of all patients with amended volumes,

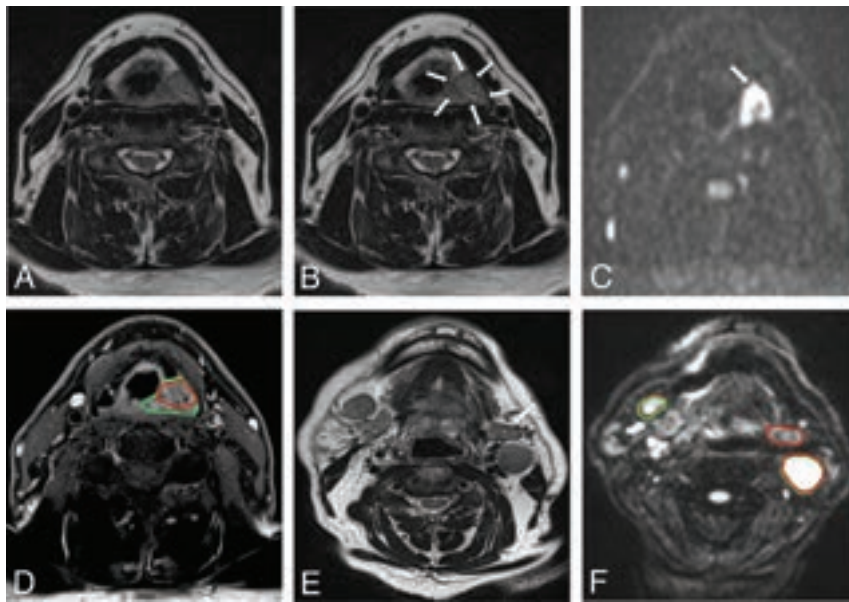


FIG 1. Examples of volume amendments made at peer review. Selected images show the difference in GTVonc and GTVrad delineations. A and B, T2-weighted axial images show an intermediate-signal left piriform fossa tumor (arrows). Following review of the diffusion-weighted imaging ($b = 1000$) (single arrow) (C), the contouring on T1-weighted gadolinium-enhanced axial image is expanded from GTVonc (red) to GTVrad (green) (D). T2-weighted axial image demonstrates multiple bilateral lymph nodes. The left submandibular gland (arrow) was initially included in the GTVonc (red) because it was isointense to other pathologic lymph nodes. F, Diffusion-weighted imaging ($b = 1000$) aided in the identification of the lower signal submandibular gland; hence, it was excluded from GTVrad (green).

Imaging misinterpretation	Clinician Discretion ¹	Use of additional DWI sequences ²	Complex case ³	Use of additional imaging (eg, PET)
Volume added 22	Volume added 7	Volume added 7	Volume added 3	Volume added 3
Volume removed 9	Volume removed 0	Volume removed 0	Volume removed 1	Volume removed 1

FIG 2. Factors contributing to volume amendments: GTVT and GTVN. ¹Changes made following joint discussion between the oncologist and radiologist, eg, inclusion of lymph nodes with borderline pathologic changes. ²Diffusion-weighted MR imaging sequences. ³Tumor volumes described as complex by the oncologist and radiologist at the time of peer review. Includes skull base disease with perineural spread, septate tumor, and postexcisional biopsy changes.

76.2% (32/42) were judged as having clinically significant alterations by the delineating oncologist.

AJCC stage 4 was the only covariate associated with any change to the GTVT ($P = .043$, OR = 5.33; 95% CI, 1.078–26.35). Factors associated with any GTVN amendment were the following: nodal stages 1 ($P = .029$, OR = 0.77; 95% CI, 0.48–0.97) and 3 ($P = .008$, OR = 1.42; 95% CI, 1.04–1.93) and AJCC stages 3 ($P = .028$, OR = 0.10; 95% CI, 0.01–0.92) and 4 ($P = .014$, OR = 11.43; 95% CI, 1.29–100.82).

Volumetric and Quantitative Analysis

Of the 55 amended volumes, 40 were available for volumetric analysis: 31 GTVTs and 9 GTVNs. Seven GTVTs and 8 GTVNs

were excluded because the original GTVonc was not preserved. In addition, 22 study clinical target tumor volumes (CTVTs) and 9 study clinical target nodular volumes (CTVNs) were analyzed. Nine postoperative CTVT were excluded because changes to the GTVT did not affect the CTVT.

Volumetric results of amended volumes are detailed in the Online Supplemental Data. Of these, major changes were seen in 54.8% of GTVTs (17/31) and 66.6% of GTVNs (6/9). Seventy-four percent of GTVTs (23/31) and 77.7% of GTVNs (7/9) were increased. The median percentage volume change was 5.7% and 4.5% for GTVT and GTVN, respectively. An increase in volume was seen across most subsites (Fig 3). Overall volume similarity was very good for GTVT (DSC = 0.93, JI = 0.87, HD = 7.45 mm) and GTVN (DSC = 0.95, JI = 0.91, HD = 20.7 mm). The similarity of tumor volumes increased after GTVT-to-CTVT expansion. Following GTVN-to-CTVN expansion volume similarity varied; surface distance (HD) reduced, however volume overlap (DSC/JI) worsened.

There was a statistically significant difference between the volume sizes of GTVTonc and GTVTrad ($P = .034$) and CTVTonc and CTVTrad ($P = .003$), but not for GTVN or CTVN. Conformity was significantly higher for CTVT versus GTVT with a median DSC of 0.95 versus 0.93 ($P = .003$) and a median JI of 0.90 versus 0.87 ($P = .003$). There were no statistically significant differences in conformity between CTVN and GTVN.

There were no covariates associated with major changes to either GTVT or GTVN. Increasing years of oncologists' experience correlated with increased DSC and JI ($P = .018$) for GTVT. There was no correlation for radiologists' years of experience. Rates of any and major change did not differ depending on the clinician's experience.

Coregistration Error

Fifty-five registration errors were assessed (5 RT planning, 50 diagnostic scans). The median TREmean and TREmax for all coregistrations was 4.5 mm (IQR = 3.15–5.6) and 6.4 mm (IQR = 4.6–8.45), respectively. For RT planning scans, the median TREmean was 2.2 mm (IQR = 1.65–2.75), and the TREmax, 2.8 mm (IQR = 1.9–3.7). Registration error exceeded both optimum TRE values in 52.7% ($n = 29$) of scans.

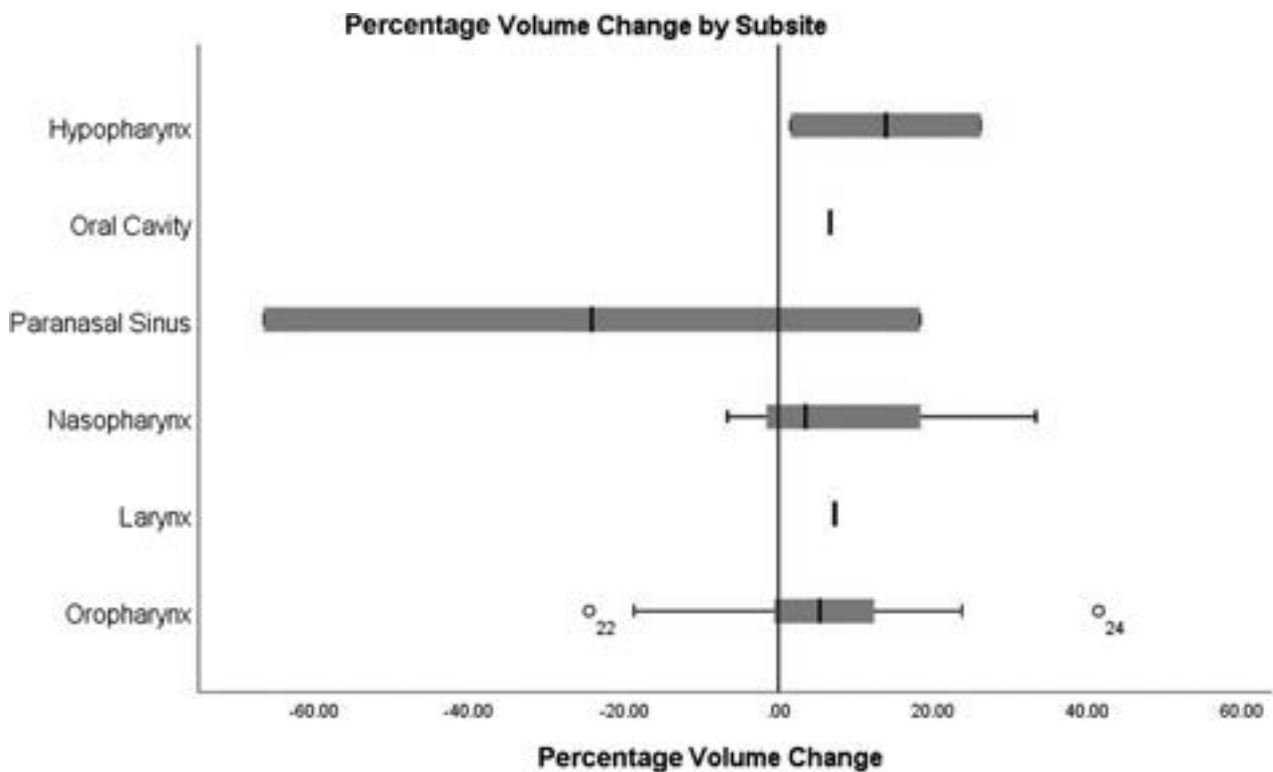


FIG 3. Boxplots of percentage volume change for GTVT by subsite. Case number 22 and 24 (highlighted as superscript numbers on the box plot of oropharyngeal cancer cases) are outliers in terms of percentage volume change. Case 22: the GTVT was reduced by 24.5% on radiologist review due to the removal of normal oral tongue and normal parapharyngeal fat. Case 24; GTVT increased by 41.4% on radiologist review due to imaging misinterpretation of abnormal deep mucosal disease extent.

Registration error did not correlate with the frequency of any change; however, the distribution of TREmean values was higher for cases that underwent major-versus-minor change: median, 4.9 mm (IQR = 3.23–6.53) versus 3.6 mm (IQR = 1.97–5.23), respectively ($P = .048$). No differences were seen in the distribution of TREmax.

DISCUSSION

MR imaging–based radiologist review resulted in amendments to 76% of tumor and 41.4% of nodal volumes, with 54.8% of GTVT and 66.6% of GTVN changes being classified as major. Most GTVT changes were related to the addition of disease in the deep mucosal extent. Some decisions made following collaborative discussion, such as inclusion of borderline nodes, may not have occurred during oncologist-only contouring, and their clinical relevance is uncertain, with a potential for overcontouring resulting in an increased dose to normal tissues. Conformity indices suggested good similarity between the pre- and postradiologist GTVT and GTVN. Because expansion from GTVT was often constrained by adjacent bone and air, there was less impact of the radiologist’s review on representative CTVT volumes, though the small differences in volume size were statistically significant. Conversely, differences among nodal volumes were amplified by expansion to the CTVN. This did not reach statistical significance, possibly due to the small number of nodal volumes available for analysis.

Among radiologists, HN imaging is recognized as a challenging subject requiring specialized training.¹⁸ Oncology training

includes no formal diagnostic radiology education; therefore, radiologist-delineated volumes were presumed to be the criterion standard. In our study, most GTV changes were due to undercontouring. Radiologists routinely analyzed information from multiple sequences and had more familiarity with additional sequences such as DWI, which allows greater confidence in distinguishing pathology from normal tissues and in detecting lymph nodes. Review of the DWI, in particular, was implicated in 7 GTV adjustments on peer review. Oncologists agreed with radiologists’ recommendations to increase volumes to reduce the risk of a geographic miss, as primary tumor recurrence within the irradiated field is rarely salvageable. However, if the radiologic evaluation of superficial tumor extension was thought to be erroneous on the basis of mucosal clinical findings, then this issue was discussed and discounted.

Diagnostic reports were available at contouring; however, most lymph node additions were either misidentified pathologic nodes within the same cervical level as correctly delineated nodes or suspicious nodes that were not formally reported. In our institution, diagnostic reports state the existence of nodal disease per cervical nodal level without listing each individual node, thus increasing the likelihood of imaging misinterpretation by oncologists. In addition to detecting overlooked pathologically appearing (by size and morphological criteria) lymph nodes, there was a tendency for radiologists to suggest the inclusion of borderline enlarged nodes in the lymphatic drainage pathways of the primary tumor that were deemed suspicious, with which the oncologists agreed.

Compared with similar studies, our rate of change to gross volumes was high. However, the proportion of major changes was comparable. Braunstein et al⁷ studied the impact of neuroradiologist peer review on, primarily, CT-based RT planning volumes. They noted a 55% alteration rate, 61% of which was clinically significant. More recently, Chiu et al⁸ evaluated the effects of radiologist input using coregistered MR imaging scans and reported a 52% alteration rate, with major changes seen in 79%. Studies of oncologist-only peer review reported lower rates of any change (14%–39%) and major/clinically significant change (8.8%–13%).^{9,10} The discrepancy between outcomes of radiologist and oncologist peer review may be reflective of the level of expertise in imaging interpretation, possibly exaggerated further when using MR imaging. Moreover, in our institution, radiologists attended interactive review sessions rather than postdelineation peer review meetings. This practice allowed detailed exploration for each case on a one-to-one basis.

Comparison of clinical significance across studies is difficult because definitions for major/clinically significant changes vary. Some articles, such as this one, classified major changes on the basis of volumetric results; therefore, rates were reported only among amended volumes (with prereview volumes saved).⁷ Others reported clinical significance among all reviewed volumes (including unaltered and unsaved volumes).^{8–10} Among all reviewed volumes in this study, 34% of GTVT and 14.6% of GTVN would have undergone major changes. However, the lack of volumetric analysis of 15 unsaved cases of GTVonc likely distorts those results.

Our conformity indices were very good and consistent with quality-assurance studies in clinical trials reporting a median JI of ≥ 0.7 and a DSC of ≥ 0.8 ,^{19,20} and the recent peer-review study of Chiu et al.⁸ Chiu et al reported median GTVT values of DSC = 0.97, JI = 0.94, and HD = 3.6 mm. They also observed a larger HD for GTVN at 37 mm and a reduction in conformity on GTVN-to-CTVN expansion. While a GTVT is usually 1 continuous volume, GTVN often includes multiple separate nodes; therefore, the inclusion of additional nodes will have a greater impact on conformity and distance. In our study, nodes were often added superior and/or inferior to the GTVNonc, expanding the volume within the soft tissues before anatomic barriers were encountered.

Following publication of the study of Braunstein et al,⁷ the use of MR imaging-guided RT volume delineation in HNC has increased, with a projected future move toward delineation based on functional imaging and MR imaging-based synthetic CTs,²¹ hence the focus of our study on MR imaging-based volume delineation. In contrast to earlier, predominantly CT-based studies, we detected a predominance of undercontoured volumes by oncologists when using MR imaging.^{7,22} This may reflect the lack of formal training in MR imaging interpretation for oncologists as well as a conservative approach to include areas/nodes considered suspicious to minimize the risk of a geographic miss. Therefore, involvement of input of specialist radiologists in GTV delineation may be more advantageous, given the increasing complexity of HN MR imaging interpretation, particularly when using functional sequences.

Few MRIs in our study were acquired in the RT treatment position; therefore, registration error exceeded both optimum

TRE values in half of the scans. The effect of suboptimal registration on the degree of volume change is uncertain. Among amended volumes with TREmax > 5mm ($n = 24$), only 1 case corrected the GTVrad, but not GTVonc, on CT. In 3 cases, both GTVonc/rad were contoured on both CT/MR imaging and compared accordingly. In 5 cases, both GTVonc and GTVrad were produced on MR imaging only. In 16 cases, GTVonc and GTVrad were evidently corrected for anatomic mismatch to some degree (ie, both contours edited away from bone/air). In these cases, some soft-tissue discrepancies remained, which may have been due to registration error, but there was no clarifying documentation regarding this aspect. Nevertheless, the accompanying descriptive reasons for volume change for each case suggest that many soft-tissue volume discrepancies would have persisted irrespective of registration error.

There are limitations to this study. It describes a one-to-one comparison for a single oncologist and single radiologist at a given time, without analysis of interobserver agreement within the oncologist and radiologist groups. It is recognized that delineation of GTVs by each of the oncologists and radiologists would have allowed the calculation of agreement parameters for tumor volumes and would have given a better understanding of performance between and across the 2 disciplines. However, the inclusion of multiple different radiologists and oncologists in the review process reflects the range of real-world practice in our institution.

Another limitation includes a lack of longitudinal data to assess the presence of a learning curve, especially important as the more junior oncologists gain experience. The possibility that oncologists may have delayed complex contouring decisions in anticipation of the pending radiologist review, resulting in more volume amendments, cannot be excluded. However, the prospective documentation suggests that when oncologists viewed a case as complex, the radiologist tended to agree. Therefore, the peer review process facilitated decision-making for these difficult cases.

The use of a single observer to create study CTVs may have increased the variation between the GTVs and CTVs. Ideally the oncologist for each case would have produced a CTVonc before peer review; however, this step was impractical because radiologist review and oncology target delineation sessions occurred on the same day. Preoperative GTVTs were included in volumetric analysis because they still provided information on delineation accuracy of the oncologist. However, removing the consequent postoperative CTVTs may have introduced selection bias toward poorer CTVT conformity (no postoperative nodal volumes were amended). Nevertheless, CTVT conformity was still superior to GTVT conformity on both measures.

Additional comparison metrics assessing the extent of undercontouring (geographic miss index) and overcontouring (discordance index) may have provided a more specific assessment of contour similarity, uninfluenced by volume size. However, further metrics would not likely reduce the qualitative benefits of peer review highlighted in this study. Furthermore, as more centers adopt the intensity-modulated RT 5 + 5 consensus,²³ which reduces the margin for the high-risk CTV to 5mm, the need for optimized GTV delineation is increasing.

At our institution, HN oncology and radiology teams agreed on the need for expert radiology review of gross volumes when

MR imaging delineation was introduced in the HNC RT workflow, given the complexity of the tumor site and the lack of specific MR imaging training of oncologists. This study was planned to assess its impact. Since its implementation, we have expanded the use of MRIs in the immobilization mask for patients having definitive intensity-modulated RT, to reduce registration errors. The efficiency and responsiveness of the radiology review process have been enhanced since 2020 by performing remote radiology review using an application equipped with shared screen functions. CTV and PTV volumes are subsequently peer reviewed within the oncology group. In this study, we have shown that the impact of radiology review of tumor and nodal volumes is sufficiently significant to warrant expert review of radiologists in MR imaging-based volume delineation in patients with HNC, something to be considered by institutions and funding bodies.

CONCLUSIONS

Interactive MR imaging-based radiologist review resulted in RT target volume amendments in most patients. Despite high conformity indices, most changes to GTVT and GTVN were considered major. Although volumetric similarities improved on GTVT-to-CTVT expansion, changes to the volume size remained statistically significant for both GTVT and CTVT. The true clinical significance of these changes remains uncertain. However, the quantitative measures and descriptive reasons for volume adjustment illustrate the benefit of the input of radiologists for MR imaging-based volume delineation in HNC.

Disclosure forms provided by the authors are available with the full text and PDF of this article at www.ajnr.org.

REFERENCES

- Jackson A, Marks LB, Bentzen SM, et al. **The lessons of QUANTEC: recommendations for reporting and gathering data on dose-volume dependencies of treatment outcome.** *Int J Radiat Oncol Biol Phys* 2010;76:S155–60 CrossRef Medline
- Chang AE, Matory YL, Dwyer AJ, et al. **Magnetic resonance imaging versus computed tomography in the evaluation of soft tissue tumors of the extremities.** *Ann Surg* 1987;205:340–48 CrossRef Medline
- Bird D, Scarsbrook AF, Sykes J, et al. **Multimodality imaging with CT, MR and FDG-PET for radiotherapy target volume delineation in oropharyngeal squamous cell carcinoma.** *BMC Cancer* 2015;15:844 CrossRef Medline
- Head and Neck Cancer: RCR Consensus Statements.** The Royal College of Radiologists; 2022. <https://www.rcr.ac.uk/publication/head-and-neck-cancer-rcr-consensus-statements>. Accessed November 1, 2022
- Van Herk M. **Errors and margins in radiotherapy.** *Semin Radiat Oncol* 2004;14:52–64 CrossRef Medline
- Prestwich RJ, Sykes J, Carey B, et al. **Improving target definition for head and neck radiotherapy: a place for magnetic resonance imaging and 18-fluoride fluorodeoxyglucose positron emission tomography?** *Clin Oncol (R Coll Radiol)* 2012;24:577–89 CrossRef Medline
- Braunstein S, Glastonbury CM, Chen J, et al. **Impact of neuroradiology-based peer review on head and neck radiotherapy target delineation.** *AJNR Am J Neuroradiol* 2017;38:146–53 CrossRef Medline
- Chiu K, Hoskin P, Gupta A, et al. **The quantitative impact of joint peer review with a specialist radiologist in head and neck cancer radiotherapy planning.** *Br J Radiol* 2022;95:20211219 CrossRef Medline
- Fong C, Sanghera P, Good J, et al. **Implementing head and neck contouring peer review without pathway delay: the on-demand approach.** *Clin Oncol (R Coll Radiol)* 2017;29:841–47 CrossRef Medline
- Ramasamy S, Murray LJ, Cardale K, et al. **Quality assurance peer review of head and neck contours in a large cancer centre via a weekly meeting approach.** *Clin Oncol (R Coll Radiol)* 2019;31:344–51 CrossRef Medline
- Mercieca S, Belderbos J, Gilson D, et al. **Implementing the royal college of radiologists' radiotherapy target volume definition and peer review guidelines: more still to do?** *Clin Oncol (R Coll Radiology)* 2019;31:706–10 CrossRef Medline
- Brock KK, Mutic S, McNutt TR, et al. **Use of image registration and fusion algorithms and techniques in radiotherapy: report of the AAPM Radiation Therapy Committee Task Group No. 132.** *Med Phys* 2017;44:e43–76 CrossRef Medline
- Grégoire V, Eisbruch A, Hamoir M, et al. **Proposal for the delineation of the nodal CTV in the node-positive and the post-operative neck.** *Radiother Oncol* 2006;79:15–20 CrossRef Medline
- Grégoire V, Levendag P, Ang KK, et al. **CT-based delineation of lymph node levels and related CTVs in the node-negative neck: DAHANCA, EORTC, GORTEC, NCIC, RTOG consensus guidelines.** *Radiother Oncol* 2003;69:227–36 CrossRef Medline
- Eelbode T, Bertels J, Berman M, et al. **Optimization for medical image segmentation: theory and practice when evaluating with Dice score or Jaccard index.** *IEEE Trans Med Imaging* 2020;39:3679–90 CrossRef Medline
- Uttenlocher DP, Klanderman GA, Rucklidge WJ. **Comparing images using the Hausdorff distance.** *IEEE Trans Pattern Anal Mach Intell* 1993;15:850–63 CrossRef
- Royal College of Radiologists. Radiotherapy Target Volume Definition and Peer Review—RCR guidance.** <https://www.rcr.ac.uk/publication/radiotherapy-target-volume-definition-and-peer-review-second-edition-rcr-guidance>. Accessed December 2021
- Lysack JT, Hoy M, Hudon ME, et al. **Impact of neuroradiologist second opinion on staging and management of head and neck cancer.** *J Otolaryngol Head Neck Surg* 2013;42:39 CrossRef Medline
- Gwynne S, Spezi E, Wills L, et al. **Toward semi-automated assessment of target volume delineation in radiotherapy trials: the SCOPE 1 pre-trial test case.** *Int J Radiat Oncol Biol Phys* 2012;84:1037–42 CrossRef Medline
- Tsang Y, Hoskin P, Spezi E, et al. **Assessment of contour variability in target volumes and organs at risk in lung cancer radiotherapy.** *Tech Innov Patient Support Radiat Oncol* 2019;10:8–12 CrossRef Medline
- Wong KH, Panek R, Bhide SA, et al. **The emerging potential of magnetic resonance imaging in personalizing radiotherapy for head and neck cancer: an oncologist's perspective.** *Br J Radiol* 2017;90:20160768 CrossRef Medline
- Giraud P, Elles S, Helfre S, et al. **Conformal radiotherapy for lung cancer: different delineation of the gross tumor volume (GTV) by radiologists and radiation oncologists.** *Radiother Oncol* 2002;62:27–36 CrossRef Medline
- Grégoire V, Evans M, Le QT, et al. **Delineation of the primary tumour clinical target volumes (CTV-P) in laryngeal, hypopharyngeal, oropharyngeal and oral cavity squamous cell carcinoma: AIRO, CACA, DAHANCA, EORTC, GEORCC, GORTEC, HKNPCSG, HNCIG, IAG-KHT, LPRHHT, NCIC CTG, NCRI, NRG ONCOLOGY, PHNS, SBRT, SOMERA, SRO, SSHNO, TROG consensus guidelines.** *Radiother Oncol* 2018;126:3–24 CrossRef Medline

Early Fetal Corpus Callosum: Demonstrating Normal Growth and Detecting Pathologies in Early Pregnancy

T. Weissbach, A. Massarwa, E. Hadi, S. Lev, A. Haimov, E. Katorza, A. Brenner-Weissmann, E. Krampl-Bettelheim, G. Kaspran, R. Sharon, R. Achiron, B. Weisz, Z. Kivilevitch, and E. Kassif



ABSTRACT

BACKGROUND AND PURPOSE: A malformed corpus callosum carries a risk for abnormal neurodevelopment. The advent of high-frequency transducers offers the opportunity to assess corpus callosum development in early pregnancy. The aim of the study was to construct a reference chart of the fetal corpus callosum length on ultrasound between 13 and 19 weeks of gestation and to prospectively examine growth patterns in pathologic cases.

MATERIALS AND METHODS: We performed a prospective cross-sectional study between 2020 and 2022 in well-dated, low-risk, singleton pregnancies between 13 and 19 weeks of gestation. A standardized image was obtained in the midsagittal plane. Imaging criteria were used as a confirmation of the early corpus callosum. Measurements were taken by 4 trained sonographers. Intra- and interobserver variability was assessed. Corpus callosum length in centiles were calculated for each gestational week.

RESULTS: One hundred eighty-seven fetuses were included in the study. All cases met inclusion criteria. At 13 weeks of gestation, the margins of the early corpus callosum were sufficiently clear to be measured in 80% (20/25) of fetuses. A cubic polynomial regression model best described the correlation between corpus length and gestational age. The correlation coefficient (r^2) was 0.929 ($P < .001$). Intra- and interobserver variability had high interclass correlation coefficients (>0.99). Presented is the earliest published case of agenesis of corpus callosum and a case of dysgenetic corpus callosum in Rubinstein-Taybi syndrome.

CONCLUSIONS: Provided is a nomogram of the early fetal corpus callosum. Applying imaging criteria helped to identify a case of complete agenesis of the corpus callosum as early as 14 weeks.

ABBREVIATIONS: CC = corpus callosum; GA = gestational age

The corpus callosum (CC) is a commissural structure composed of neuronal fibers crossing the midline, connecting both hemispheres.¹⁻³ Agenesis and dysgenesis of the corpus callosum carry risk for abnormal neurodevelopment.⁴⁻⁶ A short CC may be the first clue of abnormal formation. Normal CC growth charts are available from 16 weeks of gestation.⁷⁻¹⁴ None are provided for earlier weeks. The advent of high-frequency transducers

offers the opportunity to bring forward anomaly screening to the first trimester.¹⁵⁻²⁰ A recent publication depicted the early development of the CC on sonography, between 14 and 17 weeks;²¹ however, whether at 13 weeks of gestation the commissural fibers of the CC have developed and can be demonstrated is still debated.^{3,21,22} The aims of the study were the following: 1) to construct a normal modeled reference chart of the length of the fetal CC on 2D ultrasound between 13 and 19 weeks of gestation, 2) to propose imaging criteria to support identification of the early CC, and 3) to prospectively examine the growth of the CC in suspected or confirmed pathologic cases.

MATERIALS AND METHODS

A prospective cross-sectional study was conducted between 13 and 19 weeks of gestation at a single tertiary care center (Chaim Sheba Medical Center). Inclusion criteria were the following: 1) singleton pregnancies, 2) accurate pregnancy dating using first trimester crown-rump length or a history of regular menses, 3) absence of known major fetal malformations or genetic aberrations, and 4) absence of conditions known to affect fetal growth.

Received September 14, 2022; accepted after revision December 10.

From The Institute of Obstetrical and Gynecological Imaging (T.W., A.M., E.H., E. Katorza, A.B.-W., R.A., B.W., E. Kassif), Department of Obstetrics and Gynecology (S.L., A.H.), and Department of Neurology (R.S.), Sheba Medical Center, Tel Hashomer, Israel; Sackler School of Medicine (T.W., A.M., E.H., S.L., A.H., E. Katorza, A.B.-W., R.S., R.A., B.W., E. Kassif), Tel Aviv University, Tel Aviv, Israel; Department of Obstetrics and Gynecology (E.K.-B.) and Department of Biomedical Imaging and Image-Guided Therapy (G.K.), Medical University of Vienna, Vienna, Austria; and Women's Ultrasound Unit (Z.K.), Maccabi Health Services, Negev Medical Center, Beer-Sheva, Israel.

Please address correspondence to Tal Weissbach, MD, The Institute of Obstetrical and Gynecological Imaging, Department of Obstetrics and Gynecology, Sheba Medical Center, 2 Derech Sheba Rd, Tel-Hashomer, 52621 Ramat Gan, Israel; e-mail: Ferbyt@gmail.com

Indicates article with supplemental online videos.

<http://dx.doi.org/10.3174/ajnr.A7757>

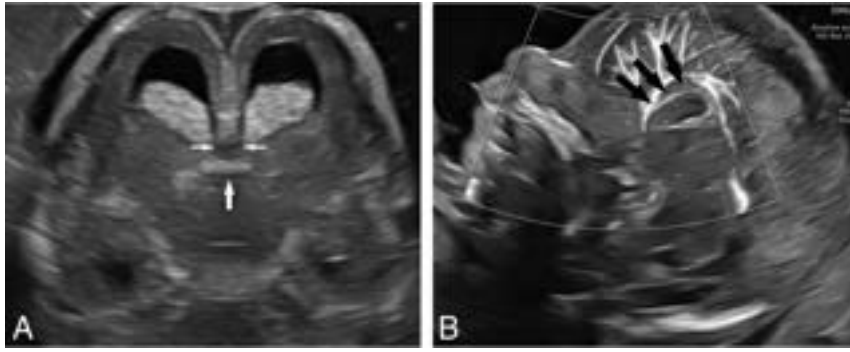


FIG 1. Imaging criteria for early CC identification. A, A hypoechoic structure (*double arrows*) crossing the midline of the brain above the echogenic tela choroidea (*single arrow*), located beneath the pericallosal artery (*black arrows*, B).

Table 1: Maternal characteristics^a

Characteristics	n = 187
Age (yr)	32.3 (SD, 4.6)
IVF	16.5% (31/187)
Prepregnancy weight (mean) (Kg)	63.8 (SD, 12.6)
Height (mean) (cm)	163.15 (SD, 6.6)
BMI (mean)	24 (SD, 4.1)
Gravidity (mean)	2.5 (SD, 1.6)
Parity	1 (SD, 1.1)

Note:—IVF indicates in vitro fertilization; BMI, body mass index.

^aData are presented as mean or percentage (n/N).

Measurements were taken by 4 examiners, Eran Kassif, T.W, A.M., and E.H. using a Voluson E10 ultrasound machine (GE Healthcare) with an abdominal RM6C 2–6 MHz convex probe or a vaginal RIC 6–12 MHz probe (both probes, GE Healthcare) as appropriate. A transvaginal approach was used up to 17 weeks of gestation, and a transabdominal approach, from 18 weeks in a nonvertex presentation.

To acquire a standardized image, we obtained a midsagittal plane of the fetal brain through the anterior fontanelle. The image was magnified so that the fetal head would occupy 70% of the screen. The probe was angled until the CC was horizontal with clear edges. The anterior-posterior length of the CC was measured.

The identification of the early CC was supported by 3 imaging criteria: 1) the appearance of a hypoechoic structure, 2) crossing the midline of the brain, and 3) located beneath the pericallosal artery and above the echogenic tela choroidea (Fig 1 and Online Videos 1 and 2). The pericallosal artery was demonstrated using color Doppler sonography. Slow Flow Doppler was used when the pericallosal artery was not clear or continuous on color Doppler.

We performed an additional pilot study assessing the reproducibility of CC measurements. Fifty-nine fetuses were assessed for intraobserver variability, and 37, for interobserver variability. For intraobserver variability, 2 measurements were taken by the same operator on 2 different images. For interobserver variability, a second operator measured the CC length on a newly acquired image.

Postnatally, we contacted patients in whom the fetal corpus measurement was found to be \leq 5th centile. This was identified

in retrospect after the normal corpus growth chart was constructed. The patients were queried about the details of their pregnancy, delivery, postnatal period, and the development of the children, focusing on the Maternal Child Health Care Clinic visits.

Maternal Child Health Care Clinic Developmental Assessment

The Maternal Child Health Care Clinic is a national health care service in Israel that serves children from birth to 6 years of age, providing vaccines and conducting routine growth and developmental examinations. The Maternal

Child Health Care Clinic assessments are performed regularly during scheduled visits at 1, 2, 4, 6, 9, 12, 18, 24, 36, 48, and 60 months of age. A structured age-based developmental assessment is performed using a standardized protocol addressing 4 developmental domains: gross motor, fine motor, language, and personal-social.²³ This protocol was validated on a large Israeli pediatric population in a recent study.²⁴

The study protocol was approved by Sheba Medical Center ethics committee (5344–18-SMC). All participating patients were informed and consented.

Statistical Analysis

Statistical analyses were performed using SPSS Statistics, Version 20 (IBM), and Excel 2016 software (Microsoft). All tests were 2-tailed, and a *P* value of $<.05$ was considered statistically significant. The intra- and interobserver variability was assessed using the Bland-Altman plot limits of agreement (SD, 1.96).²⁵ The statistical analysis used to calculate the modeled centiles was based on a method previously described.^{26–28}

After assessment of normal distribution using the Shapiro-Wilk test, the fitted mean and SD were calculated using the regression models as a function of gestational age (GA) of the raw data ($y = a + b \times GA + b1 \times GA^2 + b2 \times GA^3$). The r^2 statistic was studied to assess the best quality of fit.

The modeled centiles for a given GA were calculated as follows: centile GA = mean GA + K \times SDGA, where K is the corresponding centile of the Gaussian distribution (for example, determination of the 10th and 90th centiles requires K = ± 1.28 ; determination of the fifth and 95th centiles requires K = ± 1.645 , and so forth). An additional *z* score for assessing model fit was measured by the following formula: $z \text{ score} = (YGA - MGA) / SDGA$. Normal distribution of the *z* scores using the Shapiro-Wilk W test was calculated as well.

RESULTS

One hundred eighty-seven fetuses of low-risk pregnancies were included. All cases met our strict inclusion criteria. Maternal characteristics are summarized in Table 1. The Pearson correlation coefficient showed a positive and significant correlation between CC length and GA (Table 2).

Intra- and Interobserver Variability

A high interclass correlation was achieved for both intra- and interobserver variability: 0.997 (0.995–0.998, 95% CI) and 0.998 (0.996–0.999, 95% CI), respectively, indicating an excellent level of agreement.

The Nomograms

The raw data were best correlated with GA by a cubic polynomial regression formula. The correlation coefficient (r^2) was 0.929 ($P < .001$). After we aggregated the mean and SD for each week, CC length was best fitted according to a cubic polynomial regression formula for the mean CC for GA in weeks.

Table 3 provides the predicted CC length in centiles for each GA. The mean absolute z score between measured and predicted values was 0.127 of 0. The Shapiro-Wilk test indicated a normal distribution with P values of .313.

Corpus Callosum during the 13th Week of Gestation

The appearance of a developing CC was sought in 25 fetuses at 13 weeks of gestation. A biometry concordant for 13 weeks was

Table 2: CC length—correlation with fetal characteristics

	Pearson Correlation Coefficient (r)	P Value
GA	0.948	<.001
Head circumference	0.964	<.001
Abdominal circumference	0.948	<.001
Femur length	0.377	<.001
Estimated fetal weight	0.960	<.001

Table 3: Corpus callosum length (mm)^a

Week	No.	1st	3rd	5th	10th	25th	50th	75th	90th	95th	97th	99th
13	20	1.16	1.33	1.43	1.57	1.81	2.08	2.34	2.58	2.72	2.82	3.00
14	43	1.22	1.49	1.63	1.86	2.23	2.64	3.06	3.43	3.66	3.80	4.08
15	30	1.74	2.14	2.35	2.67	3.21	3.81	4.41	4.96	5.28	5.49	5.90
16	28	2.80	3.35	3.64	4.08	4.83	5.66	6.49	7.24	7.68	7.97	8.54
17	23	4.45	5.18	5.57	6.16	7.16	8.26	9.36	10.35	10.95	11.33	12.09
18	23	6.78	7.72	8.21	8.98	10.26	11.69	13.11	14.39	15.16	15.65	16.63
19	20	9.83	11.02	11.64	12.61	14.23	16.02	17.81	19.43	20.40	21.02	22.25

^a Modeled are the first 99th centiles and reference range from the 13th to 19th week of gestation.

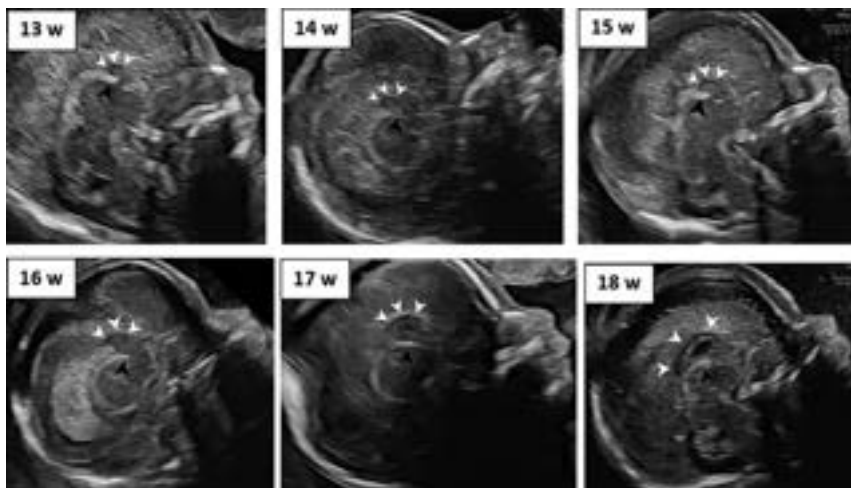


FIG 2. The growing early CC between 13 and 18 weeks. Marked in each image are the tela choroidea (black arrowhead) and CC (white arrowheads). W indicates weeks.

confirmed in all cases. Of these, in 80% (20/25), the early CC was clearly demonstrated and measured. In 5 cases, the margins of the CC were not clear enough for a precise measurement.

Demonstration of CC Growth

Figure 2 shows the gradual growth of the CC between 13 and 18 weeks. In each image, the CC and tela choroidea of the third ventricle are marked.

Short Early CC

We evaluated the outcome of 6 cases that were found to have a short CC (≤ 5 th centile). In 2 of the cases, subsequent measurements of the CC during the second and third trimesters were consistently ≤ 5 th centile as an isolated finding. Both patients refused further investigation due to personal religious beliefs. All patients were contacted postnatally, and they reported having had an uneventful pregnancy and delivery. Currently, these infants are between 7 and 15 months of age. Five infants are developing appropriately, as per the Maternal Child Health Care Clinic developmental assessment. A sixth infant, 7 months of age, was reported as healthy and normally developing by his parents and has never visited the Maternal Child Health Care Clinic, according to the parents' preference. The medical record of this patient was reviewed, confirming normal physical and neurologic development by his pediatrician and also by attending physicians during a hospital admission for a viral infection.

Pathologic Cases. By applying the imaging criteria, we identified 2 pathologic cases. We evaluated the sonographic appearance of the early fetal brains in these cases.

Absent Early CC

The patient was referred for an early anomaly scan at 14.4 weeks. The lateral ventricles appeared prominent, and the choroid plexuses were disproportionately small. On the coronal plane, the midline structure of the tela choroidea was not apparent, resulting in an unroofed third ventricle (Fig 3A). On the midsagittal plane, the hypoechoic structure of the early CC could not be demonstrated (Fig 3B). At 16 weeks, a fetal brain MR imaging confirmed the diagnosis of an absent CC (Fig 3C, -D). Repeat neurosonogram findings at 17 and 21 weeks remained consistent with the diagnosis. Chromosomal microarray and whole exome sequencing results were normal.

Short and Dysgenetic Early CC

The patient was referred for a targeted scan at 19 weeks of gestation due to mild ventriculomegaly and mega cisterna magna. The CC appeared dysgenetic (Fig 4) and measured below the first centile of the new reference chart. On follow-up at 22.4 weeks, the

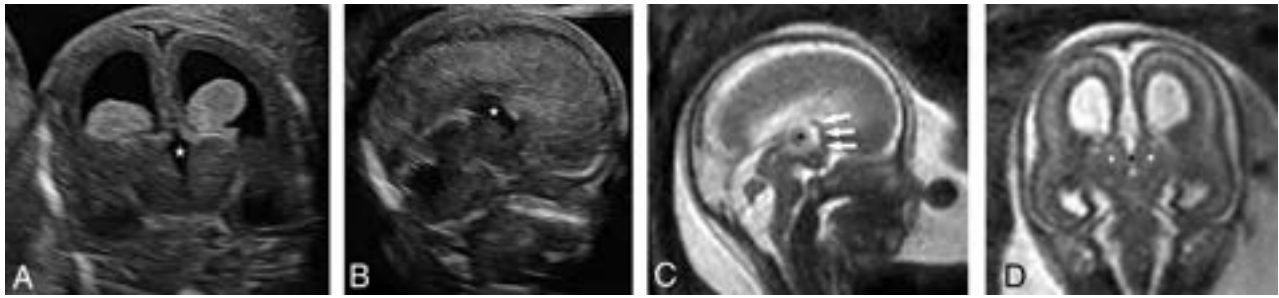


FIG 3. Absent early CC. *A*, In the coronal plane of the third ventricle and thalami, structures crossing the midline are not apparent, resulting in an unroofed third ventricle (*star*). *B*, In the midsagittal plane, a prominent unroofed third ventricle (*star*) is observed in the designated location of the absent CC. *C*, Fetal MR imaging at 16 + 6 gestational weeks in the sagittal plane demonstrating the absence of the CC, resulting in an unroofed third ventricle (*star*) with the partial volume effect of the interthalamic adhesion and the anterior portion of the postcommissural fornix (*white arrows*). *D*, MR imaging in the coronal plane shows the unroofed third ventricle (*black star*) and the adjacent thalami (*white stars*).

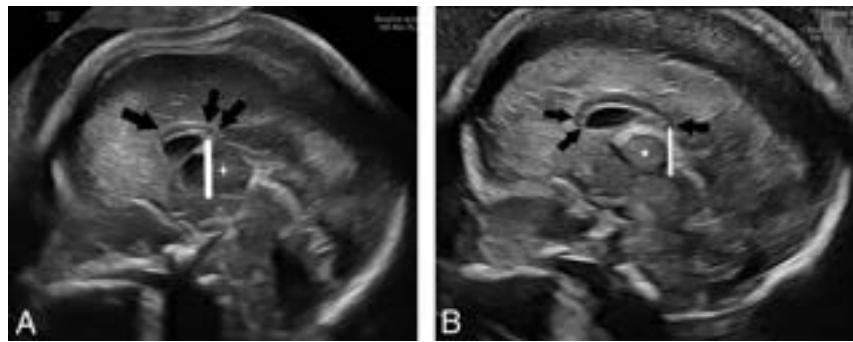


FIG 4. *A*, Short and dysgenetic CC in Rubinstein-Taybi syndrome at 19.3 weeks. The rostrum is absent, the genu is underdeveloped (*single arrow*), and the splenium is short (*double arrow*), terminating prematurely at the anterior aspect (*vertical line*) of the massa intermedia (*star*). *B*, A normal CC at 19 weeks for comparison. The rostrum and genu (*double arrow*) are apparent and splenium (*single arrow*) is observed to extend beyond the posterior border (*vertical line*) of massa intermedia (*star*).

dysgenetic CC again measured below the first centile.¹² Additional findings included delayed sulcation, a falciform sinus, posterior fossa malformation, an enlarged gallbladder, and rotated, low-set ears. Microarray findings were normal; however, whole exome sequencing revealed a mutation in the *CREBBP* gene, corresponding to Rubinstein-Taybi syndrome.

DISCUSSION

Malformation of the CC may result in neurocognitive impairment of various degrees.^{4-6,29} The availability of high-resolution ultrasound machines provides an opportunity for an early diagnosis. The present study provides a nomogram of the early fetal CC between 13 and 19 weeks, displaying linear growth with advancing gestation. The findings of the study support the novel observation that the CC can be demonstrated and measured on prenatal ultrasound as early as 13 weeks. Presented are sonograms and MR images of the earliest prenatally diagnosed case of CC agenesis published so far.

Previous prenatal studies have established nomograms of the fetal CC^{8,12-14,30} but none included the range of 13–15 weeks of gestation and only 2 included 16–17 gestational weeks.^{7,30} One had a small sample size and was performed >20 years ago using sonography machines of lower resolution compared with contemporary machines.⁷ The second study used a transabdominal approach,³⁰ with an inherent limited resolution.

The current study offers imaging criteria to support early CC identification (Fig 1). In the earlier weeks, before the development of the cavum septum pellucidum and callosal sulcus, the small hypoechoic CC may be difficult to discern from its surrounding. The pericallosal artery provides a supportive landmark of the early CC. The use of the pericallosal artery at early gestation as an indirect marker of normal CC development has been previously studied and validated.³¹⁻³³ By 18 weeks of gestation, the cavum septum pellucidum and callosal sulcus have developed, facilitating the visualization of the CC (Fig 2).³⁴

A recent pioneering publication by Birnbaum et al²¹ depicted the development of the early CC from 14 weeks using a 3D multiplanar technique. This study showed the evolution of the developing CC between 14 and 17 weeks of gestation, showing a bidirectional growth of the CC. Similar to the current study, Birnbaum et al recognized the early CC as a small hypoechoic midline structure in the anterior part of the fetal brain, bounded by the pericallosal artery superiorly and the tela choroidea inferoposteriorly.

The current study is the second to address the sonographic demonstration of the developing CC. Furthermore, it extended the lower limit of in vivo sonographic CC demonstration to 13 weeks. This observation is supported by embryologic studies showing the crossing of decussating cingulate, neocortical, and callosal fibers across the midline at 13 weeks.^{2,35} The decussation of callosal fibers is guided by specialized glial cells that form the “glial sling,” a temporary structure serving as a bridge across the midline.³⁴ In the absence of the glial sling, callosal fibers do not cross over, traveling, instead, parallel to the midline.³⁵

Short Early CC

A short early CC under the fifth centile was observed in 3% (6/198) of cases. In 2 cases, the CC was observed to be consistently short yet well-formed throughout pregnancy, supporting the validity of the early CC growth chart.

All patients reported an uneventful pregnancy and delivery of an apparently healthy offspring. Moreover, 5/6 cases were reported to achieve expected milestones at the Maternal Child Health Care Clinic assessment, implying that a short early CC may be a normal variant. This observation is supported by previous studies demonstrating that children with a short but completely formed CC may have normal neurodevelopment.^{5,6}

Early Detection of Pathologic Cases

Our study presents 2 early pathologic cases: complete agenesis (Fig 3) and a short dysgenetic CC (Fig 4). These cases suggest that some callosal pathologies may be apparent in early gestation, contrary to claims in the current literature of a later detection of callosal anomalies.^{4,19,32,36} The availability of informative images of these pathologic cases enhances our understanding of normal-versus-abnormal early brain development. Additional cases are needed to confirm these preliminary observations.

An in-depth review article by Raybaud³⁵ addressing the normal and abnormal development of the forebrain commissures considered commissural agenesis a constellation of features, of which the most prominent is the absence of an apparent interhemispheric connection, as seen in the current agenesis of the CC case. In his review, Raybaud suggested that the term “CC agenesis” was inaccurate because histologic evidence shows that the CC fibers have, in fact, developed but are heterotopic. Unable to cross the midline, the CC fibers reroute parasagittally in a bundle commonly known as Probst bundles, named after Moriz Probst, an Austrian neuroanatomist who first described them in 1901.³⁵ Previous neuropathologic studies of CC agenesis included cases from the midtrimester, reporting late-appearing signs such as Probst bundles, widely spaced lateral ventricles, and the absence of the cavum septum pellucidum.^{33,35,36} Although the current study details only a single case of CC agenesis at 14 weeks, the early signs described herein may aid in raising clinicians’ awareness of signs on the early anomaly scan in future cases.

Strengths and Limitations

There are several limitations to address. First, as an in vivo study of viable fetuses, it lacks histologic correlation to support our observation of an early CC. This is partially overcome by the sequential demonstration of the growing CC, week by week, from a minute curved structure to the characteristic shape of the CC bridging the cavum septum pellucidum, confirming its identity. A second limitation of the study is the absence of follow-up measurements later in pregnancy in all short early CC cases. This was discovered in hindsight after the construction of the reference chart.

The strengths of the study are its novelty in measuring the growth of the CC during early gestation and studying its gradual appearance from the earliest week assessed so far. Moreover, presented is the earliest prenatally diagnosed case of agenesis of the CC, providing an in vivo demonstration of the appearance of the fetal brain in this condition both on ultrasound and MR imaging (Fig 3). Additional strengths of the growth chart include prospective recruitment, strict inclusion criteria, reproducibility, and a well-sized cohort of weekly measurements.

CONCLUSIONS

The developing CC can be demonstrated and measured as early as 13 weeks of gestation using high-resolution sonography. Some major callosal pathologies can be identified at this stage. In an era striving for early detection of fetal anomalies, it is imperative to maximize the potential of early screening and to challenge the limits of existing diagnostic tools. The nomogram of the early fetal corpus callosum and the pathologic cases presented in this study may enhance our understanding of normal and abnormal patterns of callosal development.

ACKNOWLEDGMENTS

The authors are grateful to Professor Shali Mazaki Tovi for providing insight and guidance, supporting the study. We would also like to thank Mr Andrey Greenfield for skillfully editing and illustrating Videos 1 and 2.

Disclosure forms provided by the authors are available with the full text and PDF of this article at www.ajnr.org.

REFERENCES

1. Blaauw J, Meiners LC. **The splenium of the corpus callosum: embryology, anatomy, function and imaging with pathophysiological hypothesis.** *Neuroradiology* 2020;62:563–85 CrossRef Medline
2. Kier EL, Truwit CL. **The normal and abnormal genu of the corpus callosum: an evolutionary, embryologic, anatomic, and MR analysis.** *AJNR Am J Neuroradiol* 1996;17:1631–41 Medline
3. Hewitt W. **The development of the human corpus callosum.** *J Anat* 1962;96(Pt 3):355–58 Medline
4. Bernardes da Cunha S, Carneiro MC, Miguel Sa M, et al. **Neurodevelopmental outcomes following prenatal diagnosis of isolated corpus callosum agenesis: a systematic review.** *Fetal Diagn Ther* 2021;48:88–95 CrossRef Medline
5. Bartholmot C, Cabet S, Massoud M, et al. **Prenatal imaging features and postnatal outcome of short corpus callosum: a series of 42 cases.** *Fetal Diagn Ther* 2021;48:217–26 CrossRef Medline
6. Meidan R, Bar-Yosef O, Ashkenazi I, et al. **Neurodevelopmental outcome following prenatal diagnosis of a short corpus callosum.** *Prenat Diagn* 2019;39:477–83 CrossRef Medline
7. Achiron R, Achiron A. **Development of the human fetal corpus callosum: a high-resolution, cross-sectional sonographic study.** *Ultrasound Obstet Gynecol* 2001;18:343–47 CrossRef Medline
8. Rosenbloom JL, Yaeger LH, Porat S. **Reference ranges for corpus callosum and cavum septi pellucidi biometry on prenatal ultrasound: systematic review and meta-analysis.** *J Ultrasound Med* 2022;41:2135–48 CrossRef Medline
9. Miguelote RF, Vides B, Santos RF, et al. **The role of three-dimensional imaging reconstruction to measure the corpus callosum: comparison with direct mid-sagittal views.** *Prenat Diagn* 2011;31:875–80 CrossRef Medline
10. Plasencia W, Dagklis T, Borenstein M, et al. **Assessment of the corpus callosum at 20–24 weeks’ gestation by three-dimensional ultrasound examination.** *Ultrasound Obstet Gynecol* 2007;30:169–72 CrossRef Medline
11. Rizzo G, Pietrolucci ME, Capponi A, et al. **Assessment of corpus callosum biometric measurements at 18 to 32 weeks’ gestation by 3-dimensional sonography.** *J Ultrasound Med* 2011;30:47–53 CrossRef Medline
12. Pashaj S, Merz E, Wellek S. **Biometry of the fetal corpus callosum by three-dimensional ultrasound.** *Ultrasound Obstet Gynecol* 2013;42:691–98 CrossRef Medline

13. Cignini P, Padula F, Giorlandino M, et al. **Reference charts for fetal corpus callosum length: a prospective cross-sectional study of 2950 fetuses.** *J Ultrasound Med* 2014;33:1065–78 CrossRef Medline
14. Tsur A, Weisz B, Rosenblat O, et al. **Personalized charts for the fetal corpus callosum length.** *J Matern Fetal Neonatal Med* 2019;32:3931–38 CrossRef Medline
15. Kenkhuis MJ, Bakker M, Bardi F, et al. **Effectiveness of 12-13-week scan for early diagnosis of fetal congenital anomalies in the cell-free DNA era.** *Ultrasound Obstet Gynecol* 2018;51:463–69 CrossRef Medline
16. Kassif E, Weissbach T, Raviv O, et al. **Fetal esophageal imaging: Early pregnancy as a window of opportunity.** *Prenat Diagn* 2021;41:861–67 CrossRef Medline
17. Achiron R, Adamo L, Kassif E. **From screening chromosomal anomalies to early diagnosis of fetal malformations.** *Curr Opin Obstet Gynecol* 2020;32:128–33 CrossRef Medline
18. Karim JN, Roberts NW, Salomon LJ, et al. **Systematic review of first-trimester ultrasound screening for detection of fetal structural anomalies and factors that affect screening performance.** *Ultrasound Obstet Gynecol* 2017;50:429–41 CrossRef Medline
19. Edwards L, Hui L. **First and second trimester screening for fetal structural anomalies.** *Semin Fetal Neonatal Med* 2018;23:102–11 CrossRef Medline
20. Syngelaki A, Hammami A, Bower S, et al. **Diagnosis of fetal non-chromosomal abnormalities on routine ultrasound examination at 11-13 weeks' gestation.** *Ultrasound Obstet Gynecol* 2019;54:468–76 CrossRef Medline
21. Birnbaum R, Barzilay R, Brusilov M, et al. **The early pattern of human corpus callosum development: a transvaginal 3D neurosonographic study.** *Prenat Diagn* 2020;40:1239–45 CrossRef Medline
22. Ren T, Anderson A, Shen W-B, et al. **Imaging, anatomical, and molecular analysis of callosal formation in the developing human fetal brain.** *Anat Rec A Discov Mol Cell Evol Biol* 2006;288:191–204 CrossRef Medline
23. Israeli Ministry of Health. **Protocol for developmental assessment of infants and toddlers up to the age of six years** [in Hebrew]. December 2016. https://www.health.gov.il/hozer/bz12_2016.pdf.
24. Sudry T, Zimmerman DR, Yardeni H, et al. **Standardization of a developmental milestone scale using data from children in Israel.** *JAMA Netw Open* 2022;5:e222184 CrossRef Medline
25. Bland JM, Altman DG. **Statistical methods for assessing agreement between two methods of clinical measurement.** *Lancet* 1986;327:307–10 CrossRef Medline
26. Royston P, Wright EM. **How to construct “normal ranges” for fetal variables.** *Ultrasound Obstet Gynecol* 1998;11:30–38 CrossRef Medline
27. Altman DG, Chitty LS. **Charts of fetal size: 1, methodology.** *Br J Obstet Gynaecol* 1994;101:29–34 CrossRef Medline
28. Silverwood RJ, Cole TJ. **Statistical methods for constructing gestational age-related reference intervals and centile charts for fetal size.** *Ultrasound Obstet Gynecol* 2007;29:6–13 CrossRef Medline
29. Santo S, D'Antonio F, Homfray T, et al. **Counseling in fetal medicine: agenesis of the corpus callosum.** *Ultrasound Obstet Gynecol* 2012;40:513–21 CrossRef Medline
30. Zhang H, Yang J, Chen Z, et al. **Sonographic study of the development of fetal corpus callosum in a Chinese population.** *J Clin Ultrasound* 2009;37:75–77 CrossRef Medline
31. Conturso R, Contro E, Bellussi F, et al. **Demonstration of the pericallosal artery at 11-13 weeks of gestation using 3D ultrasound.** *Fetal Diagn Ther* 2015;37:305–09 CrossRef Medline
32. Díaz-Guerrero L, Giugni-Chalraud G, Sosa-Olavarría A. **Assessment of pericallosal arteries by color Doppler ultrasonography at 11-14 weeks: an early marker of fetal corpus callosum development in normal fetuses and agenesis in cases with chromosomal anomalies.** *Fetal Diagn Ther* 2013;34:85–89 CrossRef Medline
33. Pati M, Cani C, Bertucci E, et al. **Early visualization and measurement of the pericallosal artery: an indirect sign of corpus callosum development.** *J Ultrasound Med* 2012;31:231–37 CrossRef Medline
34. Falco P, Gabrielli S, Visentin A, et al. **Transabdominal sonography of the cavum septum pellucidum in normal fetuses in the second and third trimesters of pregnancy.** *Ultrasound Obstet Gynecol* 2000;16:549–53 CrossRef Medline
35. Raybaud C. **The corpus callosum, the other great forebrain commissures, and the septum pellucidum: anatomy, development, and malformation.** *Neuroradiology* 2010;52:447–77 CrossRef Medline
36. Folliot-Le Doussal L, Chadie A, Brasseur-Daudruy M, et al; Perinatal Network of Haute-Normandie. **Neurodevelopmental outcome in prenatally diagnosed isolated agenesis of the corpus callosum.** *Early Hum Dev* 2018;116:9–16 CrossRef Medline

Longitudinal MRI Evaluation of Brain Development in Fetuses with Congenital Diaphragmatic Hernia around the Time of Fetal Endotracheal Occlusion

D. Emam, M. Aertsen, L. Van der Veecken, L. Fidon, P. Patkee, V. Kyriakopoulou, L. De Catte, F. Russo, P. Demaerel, T. Vercauteren, M. Rutherford, and J. Deprest



ABSTRACT

BACKGROUND AND PURPOSE: Congenital diaphragmatic hernia is associated with high mortality and morbidity, including evidence suggesting neurodevelopmental comorbidities after birth. The aim of this study was to document longitudinal changes in brain biometry and the cortical folding pattern in fetuses with congenital diaphragmatic hernia compared with healthy fetuses.

MATERIALS AND METHODS: This is a retrospective cohort study including fetuses with isolated congenital diaphragmatic hernia between January 2007 and May 2019, with at least 2 MR imaging examinations. For controls, we used images from fetuses who underwent MR imaging for an unrelated condition that did not compromise fetal brain development and fetuses from healthy pregnant women. Biometric measurements and 3D segmentations of brain structures were used as well as qualitative and quantitative grading of the supratentorial brain. Brain development was correlated with disease-severity markers.

RESULTS: Forty-two fetuses were included, with a mean gestational age at first MR imaging of 28.0 (SD, 2.1) weeks and 33.2 (SD, 1.3) weeks at the second imaging. The mean gestational age in controls was 30.7 (SD, 4.2) weeks. At 28 weeks, fetuses with congenital diaphragmatic hernia had abnormal qualitative and quantitative maturation, more extra-axial fluid, and larger total skull volume. By 33 weeks, qualitative grading scores were still abnormal, but quantitative scoring was in the normal range. In contrast, the extra-axial fluid volume remained abnormal with increased ventricular volume. Normal brain parenchymal volumes were found.

CONCLUSIONS: Brain development in fetuses with congenital diaphragmatic hernia around 28 weeks appears to be delayed. This feature is less prominent at 33 weeks. At this stage, there was also an increase in ventricular and extra-axial space volume.

ABBREVIATIONS: CDH = congenital diaphragmatic hernia; FETO = fetal endotracheal occlusion; GA = gestational age; SRR = super-resolution reconstruction; TFLV = total fetal lung volume

Congenital diaphragmatic hernia (CDH) is a severe birth defect, occurring in approximately 1 in 3000 live-born neonates.¹ Despite neonatal treatment, the disease is associated with

high mortality, and survivors often have short- and long-term morbidities.¹ These include respiratory, gastrointestinal, and neurologic impairments.² Neurodevelopmental delays as well as behavioral difficulties have been linked to CDH in the past, and certain risk factors have been suggested, including gestational age at birth, disease severity, associated anomalies, the requirement for extracorporeal membrane oxygenation, and long stays in the neonatal intensive care unit.²⁻⁷

In infants with CDH, imaging studies have demonstrated several abnormalities, including increased extra-axial space, delayed sulcation, and white matter injury, but the exact mechanisms

Received April 28, 2022; accepted after revision December 10.

From the Department of Development and Regeneration (D.E., L.V.d.V., L.D.C., F.R., J.D.), Cluster Woman and Child, Group Biomedical Sciences, KU Leuven University of Leuven, Leuven, Belgium; Department Obstetrics and Gynaecology (D.E., L.F.), Faculty of Medicine, Tanta University, Tanta, Egypt; Department of Imaging and Pathology (M.A., P.D.), Clinical Department of Radiology, University Hospitals, KU Leuven, Leuven, Belgium; Clinical Department Obstetrics and Gynaecology (L.V.d.V., L.D.C., F.R., J.D.), University Hospitals Leuven, Leuven, Belgium; Centre for the Developing Brain (P.P., V.K., M.R., J.D.), Division of Imaging Sciences and Biomedical Engineering, Perinatal Imaging and Health and School of Biomedical Engineering and Imaging Sciences (L.F., T.V., J.D.), King's College London, King's Health Partners, St. Thomas' Hospital, London, UK; and Institute for Women's Health (J.D.), University College London, London, UK.

D. Emam and M. Aertsen contributed equally to this work.

D.E. is funded by the Egyptian Educational Scholarship from the Ministry of Higher Education and Scientific Research, Egypt. L.V.d.V. is funded by the Erasmus+ Program of the European Union (framework agreement no. 2013-0040). J.D. and T.V. receive support from the Wellcome Trust (WT101957) and the Engineering and Physical Sciences Research Council (NS/A000027/1). J.D. receives support from the Great Ormond Street Hospital Charity Fund. To support L.F. and T.V., this project has received funding from the European Union's Horizon 2020 research and innovation program under the Marie Skłodowska-Curie grant agreement No 765148.

This publication reflects the views only of the authors, and the Commission cannot be held responsible for any use that may be made of the information contained therein.

Please address correspondence to Michael Aertsen, MD, Department of Radiology, University Hospitals Leuven, Herestraat 49, 3000 Leuven, Belgium; e-mail: Michael.aertsen@uzleuven.be

Indicates open access to non-subscribers at www.ajnr.org

Indicates article with online supplemental data.

<http://dx.doi.org/10.3174/ajnr.A7760>

remain unclear.⁸ As for other congenital malformations with an increased risk for neurodevelopmental abnormalities, parents may ask whether these are already present at the time of prenatal diagnosis or are more likely to be postnatally acquired. This issue will become even more important with the advent of effective fetal therapy,^{9–11} which treats fetuses with the more severe forms of CDH. Those parents and physicians likewise will want to understand whether brain development in CDH is already altered prenatally and, when present, if this would be severity-dependent.¹² Currently, there are limited data on in utero brain development in fetuses with CDH.^{8,12,13} Radhakrishnan et al¹² described enlargement of the extra-axial space and congestion of the venous sinuses in the third trimester. A further study reported a correlation between cerebellar and vermian dimensions and the severity of lung hypoplasia (evidenced by lower fetal lung volume). Recently, we reported, on the basis of sonography, changes in cerebellar growth, in particular after 32 weeks' gestation. We also correlated these to disease severity.¹⁴ The objective in the present study was to use MR imaging data to document cortical folding as well as the dimensions and volume of given brain structures in comparison with findings in healthy fetuses, again, in particular, late in gestation.

MATERIALS AND METHODS

This retrospective cohort study included all consecutive fetuses diagnosed with isolated CDH at the University Hospitals Leuven, Belgium, between January 2007 and May 2019 ($n = 283$) and for whom at least 2 MR imaging examinations were available ($n = 48$ fetuses). Isolated CDH was defined as the presence of normal findings on prenatal genetic testing (conventional karyotyping or comparative genome-wide hybridization array analysis¹⁵) and the absence of a major structural anomaly. Fetuses with poor-quality brain images due to motion artifacts were excluded ($n = 6$). For controls, we used images from fetuses that underwent MR imaging for an unrelated condition, which was presumed not to involve brain development, assessed between 20 and 37 weeks' gestational age (GA) ($n = 26$). The precise indications for MR imaging assessment are provided in the Online Supplemental Data. All brain examinations were reported as showing normal appearances for GA, and no abnormal neurodevelopmental outcome was reported after birth. We added to this control cohort additional fetal images ($n = 30$) obtained by our collaborators from King's College London (Robert Steiner MR Imaging Unit in Hammersmith Hospital, London, UK) between November 2007 and May 2013 in healthy pregnant women who had normal neurodevelopmental follow-up. These data were included in a previous study.¹⁶ Selected patients were chosen to be equally distributed across the same GA period.

MR Imaging Examination

At the University Hospitals Leuven, MR imaging was performed as part of standard clinical care using a 1.5T system (Aera; Siemens). Two small body coils were placed adjacent to each other over the mother. The mother was positioned in the supine or left lateral decubitus position. Before September 2015, maternal sedation (flunitrazepam, 0.5 mg taken orally 20–30 minutes before the examination) was used when the GA was <30 weeks,

a practice that was abandoned.^{17,18} The protocol includes T2-weighted HASTE sequences, obtained in 3 orthogonal planes relative to the fetal head (coronal, axial, and sagittal). Scanning parameters are reported elsewhere.¹⁹ In addition, T2-weighted HASTE sequences, obtained in 3 orthogonal planes relative to the fetal body (coronal, axial, and sagittal) were performed. Scanning parameters were TE = 90 ms; TR = 1000 ms; section thickness = 3.0–4.0 mm; absence of an intersection gap; FOV = 300 × 300–380 × 380 mm. During the study period, the scanner received several software updates that had no influence on the image quality of T2-weighted sequences. However, additional sequences were added to the routine protocol (eg, T2*-weighted sequences and diffusion-weighted imaging), but these are not relevant to this study. Parameters from the MR imaging examination in controls scanned at the Robert Steiner MR Imaging Unit in Hammersmith Hospital, London, UK, were similar and can be found in Kyriakopoulou et al.¹⁶ These examinations were performed using a 1.5T MR imaging system (Achieva; Philips Healthcare) with a 32-channel cardiac array coil. The mother was positioned in a left lateral tilt, and no sedation was used. The images used for this study included T2-weighted images in transverse, sagittal, and coronal planes.

Assessment of Brain Development and Severity of Pulmonary Hypoplasia

Biometric measurements were obtained on standard T2-weighted images and included brain and skull biparietal diameter and fronto-occipital diameter, atrial width, and transverse cerebellar diameter (Online Supplemental Data).¹⁷ Head circumference and extra-axial space percentiles were calculated according to Kyriakopoulou et al.¹⁶ Fetal cortical development was scored using the grading system described by Pistorius et al²⁰ and measured following Egaña-Ugrinovic et al.²¹ We earlier demonstrated that scoring has a good interobserver reproducibility.²² All measurements were performed by D.E. (with limited experience in fetal MR imaging) under direct supervision of M.A. (with >5 years' experience in fetal MR imaging with >2000 fetal MR imaging examinations) after training in scoring the fetal brain on MR imaging with the qualitative and quantitative grading system in 15 cases. The following brain regions were scored subjectively: frontal, parietal, temporal, mesial, insular, and occipital cortex.²⁰ Selected primary sulci and gyri were graded and/or measured, including the parieto-occipital fissure; the central, calcarine, superior temporal, cingulate sulcus; and, for the opercularization, the Sylvian fissure.^{20,21} In addition to the Sylvian fissure depth, which reflects the distance between the inner part of the skull and the insular cortex, the insular depth was also measured, ie, the distance from the midline to the insular cortex.²² The sum of all the graded fissures provides a total grading score for each hemisphere and the whole brain.²²

3D super-resolution reconstruction (SRR) volumes were created from the standard T2-weighted 2D stacks displaying the fetal brain, using NiftyMIC (<https://github.com/gift-surg/NiftyMIC>), a publicly available and state-of-the-art SRR algorithm.²³ The SRR volumes were automatically segmented for white matter, the ventricular system (lateral ventricles, third ventricle, fourth

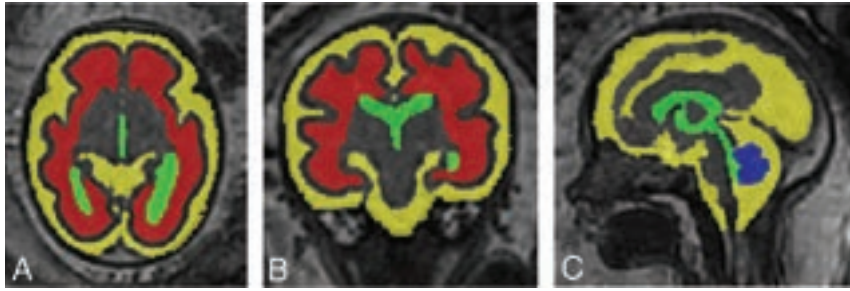


FIG 1. T2-weighted images in the axial (A), coronal (B), and sagittal (C) planes illustrating automated segmentations of the extra-axial space (yellow), white matter (red), ventricular system (green), and cerebellum (blue).

General characteristics of the congenital diaphragmatic hernia group

General Characteristics	
Left/right/bilateral o/e TFLV at first MR imaging	28 (66.7%)/12 (28.6%)/2 (4.8%)
<15%	6 (14.2%)
16%–25%	13 (31%)
26%–45%	22 (52.4%)
>45%	1 (2.4%)
Liver herniation	40 (95.2%)
Liver/thorax ratio	30.13 (9.67)
Fetal position at MR imaging 1 (cephalic/breech/transverse)	28 (67%)/13 (31%)/1 (2%)
Fetal position at MR imaging 2 (cephalic/breech/transverse)	37 (88%)/5 (12%) / 0
GA at MR imaging 1 (mean)	28.0 (SD, 2.1)
GA at MR imaging 2 (mean)	33.2 (SD, 1.3)
Individual interval	4.83 (1.85)
Fetal endoluminal tracheal occlusion	40 (95%)

Note:—o/e indicates observed over expected ratio.

ventricle, and aqueduct), the cavum septi pellucidi and cavum vergae, extra-axial space, and cerebellum with manual correction when necessary (D.E. supervised by M.A.). A deep learning algorithm for the automatic segmentation of white matter, the ventricular system, and cerebellum was used for the first volumes that were processed.²⁴ As the number of volumes segmented for the extra-axial space increased, we trained a new deep learning-based segmentation algorithm²⁵ based on a partially supervised learning method that automatically segments white matter, the ventricular system, the cerebellum, and the extra-axial space. These segmentations were used for volumetric analysis when the quality of the SRR volume allowed further analysis (determined by D.E. and supervised by M.A. and L.F.) (Fig 1).

In all cases in which the fetus underwent fetal endotracheal occlusion (FETO), the date was noted and the time interval between the operation and second MR imaging was documented. The severity of pulmonary hypoplasia in fetuses with CDH was assessed on MR imaging by measuring the right, left, and total fetal lung volume (TFLV), the fetal body volume, liver position, intrathoracic liver volume, and thoracic volume, again measured manually (D.E. supervised by M.A.). From those, we calculated the observed over expected ratio TFLV ratio²⁶ and the liver-to-thoracic volume ratio.²⁷ The latter ratios provide biometric measurements in the index case that are independent of GA and/or fetal weight.

Statistics

Data were analyzed with Analyze-it (Analyze-it for Microsoft Excel 4.81.4; <https://analyze-it.com/>). Data were checked for normality using the Shapiro-Wilk test for normality. All data are expressed as mean (SD) or median (interquartile range), depending on normality; subclassifications were illustrated as number (percentage). Regression analysis of the different variables in healthy fetuses allowed calculation of normal ranges in correlation with GA for each parameter.

This allowed us to calculate an expected value for each observation in the CDH population. Differences between the CDH population at the first and the second time points and the controls were studied with the Wilcoxon-Mann-Whitney test, using the observed/expected ratios based on the reference cohort. To analyze the evolution with time, we performed a Wilcoxon hypothesis test on the difference in the observed/expected ratio between both time points. Correlations were assessed using the Pearson correlation coefficient, and the Bonferroni correction for multiple comparisons was performed.

Ethics Approval

This study was approved by the Ethics Committee of the University Hospitals Leuven (S56786).

RESULTS

Study Population

Twenty-eight fetuses had left, 12 had right, and 2 had bilateral CDH ($n = 42$; Table). The mean GA at the first MR imaging was 28.0 (SD, 2.1) weeks, and at the second, it was 33.2 (SD, 1.3) weeks. The mean difference between the 2 measurements was 4.8 (SD, 1.9) weeks. FETO was performed in 40 fetuses (95%) with a mean GA at FETO of 29.3 (SD, 1.5) weeks. The mean number of days between FETO and the second MR imaging was 26.45 (SD, 11.76). Balloon removal was performed at a mean GA of 33.5 (SD, 1.1) weeks. The mean GA in controls was 30.7 (SD, 4.2) weeks. SRR for volumetric analysis was possible in 25 (60%) fetuses at the first time point and in 23 (55%) at the second time point. Further details of success rates for volumetric measurements at the first and second time points and the number of available measures from paired data are shown in the Online Supplemental Data. In controls, 52 (93%) reconstructions were possible.

Measurement at the First Time Point

The fetal brain and skull biometry were not different between fetuses with CDH and those without. The extra-axial space and atrial width in fetuses with CDH were within the normal range, except for 1 fetus having mild ventriculomegaly (11 mm). The total brain cortical grading for fetuses with CDH was significantly lower than in controls ($P < .003$) (Online Supplemental Data). When we compared the brain grading of each hemisphere, the difference was present on both sides (both $P < .003$). The opercularization was delayed on the left side ($P = .011$), but not on the

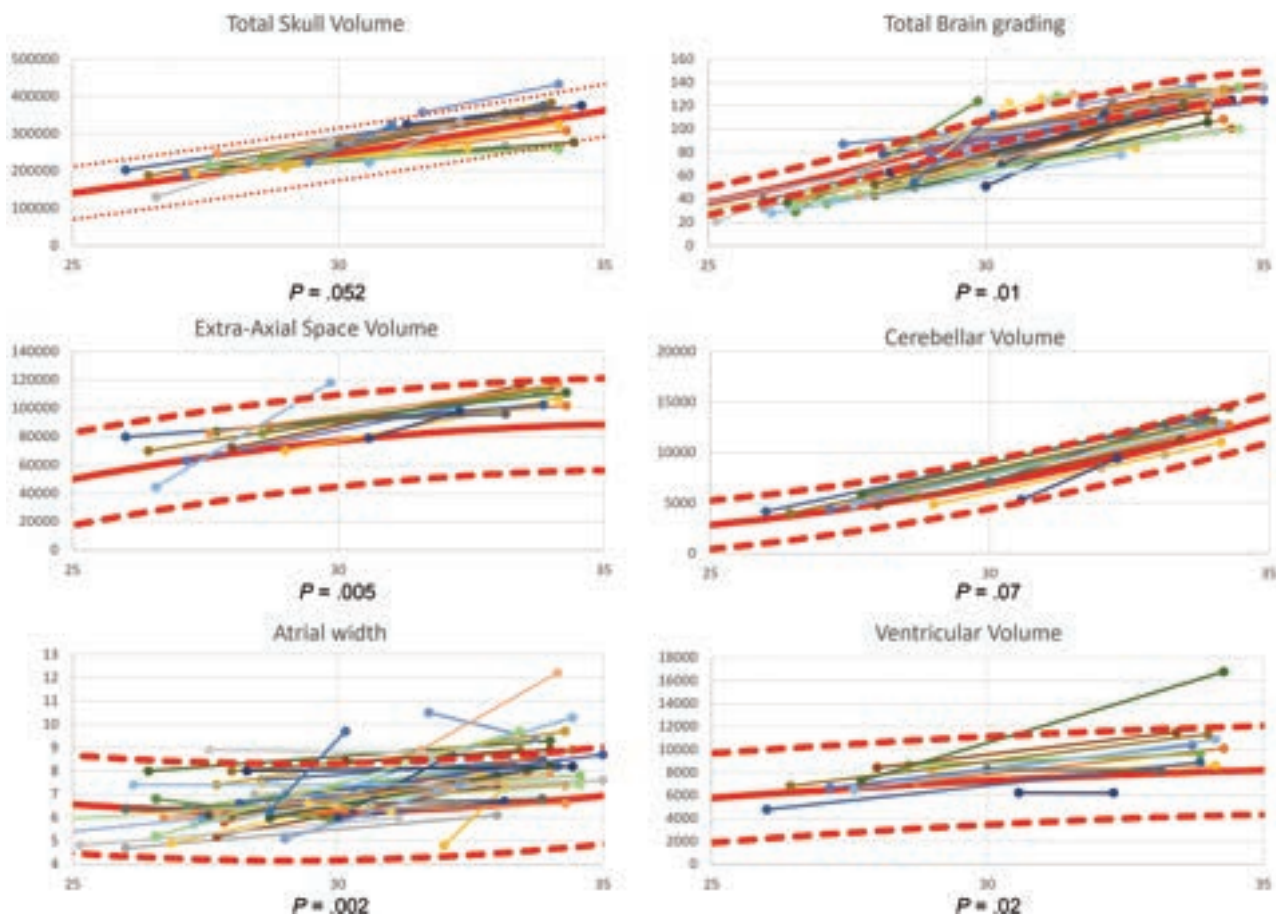


FIG 2. Graphs demonstrating the paired observations of the total skull volume, total brain grading, extra-axial space volume, cerebellar volume, atrial width, and ventricular volume. The provided *P* value is the significance level of the Wilcoxon-Mann-Whitney test comparing the observations at the second time point in fetuses with congenital diaphragmatic hernia with that in healthy controls. The mean values of the control populations (full red line) with the 95% confidence intervals (dashed red line) are also shown.

right ($P = .057$). There was a reduced depth of the parieto-occipital fissure ($P < .003$ on the right and $P = .003$ on the left) and cingulate fissure (left and right, $P < .003$), but the depth of the calcarine fissure was normal on both sides ($P > .05$) compared with controls. The Sylvian fissure was just significantly deeper only on the right ($P = .042$), but not on the left ($P = .055$) in fetuses with CDH. The insular depth in fetuses with CDH was within the normal range ($P > .05$). There was no difference in volume of the total skull, extra-axial space, ventricular system, white matter, or cerebellum between fetuses with CDH and healthy controls (Online Supplemental Data).

Measurement and Change at the Second Time Point

At the second time point, most measurements were within the normal range, except for the atrial width ($P < .003$), the ventricular volume ($P = .024$), and the extra-axial space volume ($P = .005$), which were larger than normal. The total brain cortical grading was lower than normal ($P = .011$) on both sides ($P = .019$ and $P = .035$), and the opercularization was within the normal range ($P > .05$) (Fig 2). The Sylvian fissure depth was deeper (both $P < .003$), but all other fissures were comparable with those in controls. Compared with findings on the initial scans, the atrial width increased further, and the brain fissures that were initially

less deep measured within the normal range. The depth of the Sylvian fissure, which was normal earlier, became abnormally deeper; also, the left-brain hemisphere cortical grading score was abnormal, but significantly less so than at the first time point. Although the difference in brain scoring between the CDH population and the controls was less at the second time point, this was not significantly different from the first time point (Online Supplemental Data).

Correlation with Severity Indicators of Lung Hypoplasia

No correlation was found at either time point between the liver-to-thorax ratio or the observed over expected ratio TFLV on one side or the total brain grading, skull and brain fronto-occipital diameter, atrial width, ventricular volume or extra-axial space volume, cerebellar volume, or total intracranial volume on the other side. No significant difference was found in the variables mentioned above when comparing fetuses with left and right CDH.

DISCUSSION

Danzer et al⁸ reported a lower total maturation score in infants with CDH after birth.⁶ Along the same lines, Lucignani et al²⁸ reported reduced cortical maturation in extended brain areas of

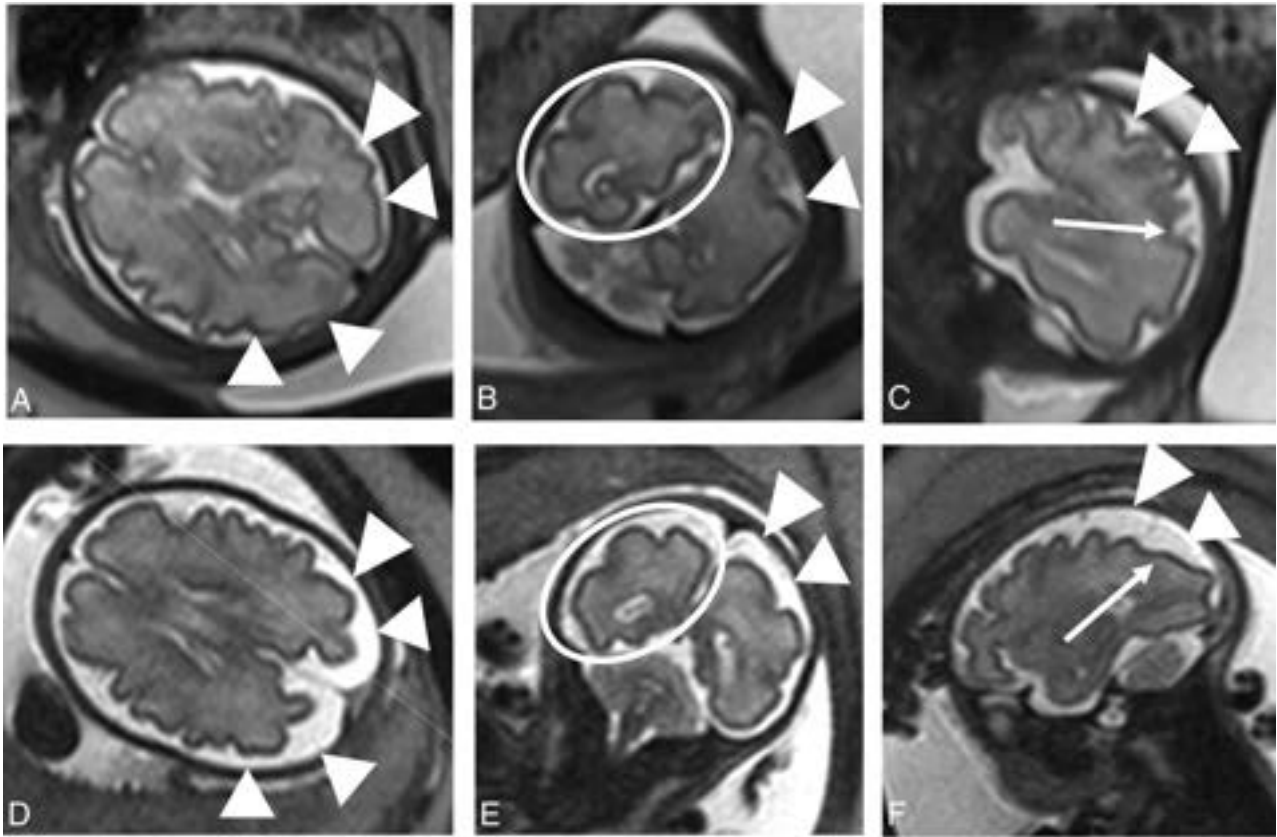


FIG 3. Three orthogonal T2-weighted spin-echo images in a healthy fetus (A–C) and a fetus with a left-sided diaphragmatic hernia (D–F), both at a GA of 30 weeks 4 days. In the axial plane (A and D), the enlarged pericerebral space is evident (*arrowheads*). The difference in gyrification is most evident in the parietal area and best seen in the coronal plane (*circle* in B and E) and to a lesser extent in the sagittal plane (*arrows* in C and F). The enlarged pericerebral space in the coronal and sagittal planes is marked with *arrowheads*.

neonates with CDH compared with healthy controls. In earlier prenatal studies, fetuses with CDH had brain sulcation scores that are indicators of prenatal brain maturation, within the normal range between 20 and 37 weeks.^{12,29} One study on infants who had both pre- and postnatal imaging reported signs of brain injury (eg, hemorrhage, white matter injury. . .) on postnatal but not on prenatal MR imaging. In that study, the injury score correlated with the degree of pulmonary hypoplasia without an indication of delayed sulcation in those fetuses.²⁹

Conversely, our study demonstrates that fetuses with CDH have indications of atypical brain development, ie, with a significant delay at 28 and 33 weeks of gestation (Fig 3). By 33 weeks, the quantitative scores were in the normal range. However, quantitative scoring was performed on primary and not on secondary sulci, limiting the detection of subtle folding abnormalities.³⁰ The qualitative scoring system we used allows a thorough scoring of brain sulcation throughout a wide GA range, because it evaluates the primary formation as well as the presence of secondary and tertiary sulcation.²⁰ We were not able to compare our morphologic findings with the postnatal clinical neurobehavioral assessment. In infants with CDH, 9% (4%–14%) have abnormal opercularization, which translates later into language and speech abnormalities.⁷ In our study, grading of the operculum was significantly lower at the first time point and at the second time point, though only left-sided. It remains unclear whether the

abnormalities we found are related to any of the reported functional consequences observed in infants with CDH or other abnormalities. In earlier studies, scores using the same system correlated well with the Neonatal Behavioral Assessment Scale,³¹ though this correlation was in fetuses with isolated nonsevere ventriculomegaly or late-onset growth restriction.^{14,22} The functional impact of our observations in fetuses with CDH remains to be elucidated. Moreover, one must take into account that any abnormality observed postnatally may as well have been acquired after birth.

Irrespective of the functional impact, the cause of atypical brain folding that we observed in fetuses remains unclear. One factor may be a degree of hemodynamic dysfunction. We have previously reported a decline in the systolic velocity of the MCA peak, hence in brain perfusion in fetuses with CDH.^{14,32} One may recognize similarities to circulatory disturbances in fetuses with congenital heart defects, which coincide with signs of abnormal brain development. In hypoplastic left heart syndrome, a lower blood flow velocity has been associated with lower brain volume.^{33,34} Furthermore, fetuses with this and other congenital heart defects had delayed brain maturation in the late second and early third trimesters, and again, this has been linked to abnormal hemodynamics and oxygen delivery.³⁵ Lucignani et al²⁸ also used this theory to explain their recent findings of altered cortical maturation in neonates with CDH.

The significant increase in the volume of all fluid compartments at 33 weeks' gestation in CDH that we observed (Fig 3) is in line with work of Radhakrishnan et al.¹² Because fetuses had normal biometry of the cerebral hemispheres and lacked major parenchymal abnormalities, the authors questioned the clinical relevance of these findings. Recently, the importance was shown of a diagnostic algorithm that helps to discriminate fetuses with enlargement of the extra-axial space with self-limiting delays from those at risk of a persistent delay.³⁶ Abnormal intracranial fluid volumes have been previously explained by a change in cardiac output in CDH caused by herniation of abdominal structures in turn leading to mild or moderate cardiac hypoplasia in left-sided CDH or cardiac compression, compromising venous return.^{29,37} This may, in turn, cause venous congestion and lead to decreased CSF resorption³⁸ and an overall increase of intracranial fluid. It may be useful to assess cardiac function and hemodynamics in more detail in fetuses with CDH to study whether there is a link with brain development.

We are the first to document in utero brain development in fetuses with CDH using a structured brain evaluation. For this evaluation, we used fetal brain MR imaging because this allows a standardized and reproducible in-depth analysis, as illustrated by other studies.^{21,22} Our analysis was not limited to a qualitative, ie subjective, analysis of the brain maturation but also included a quantitative scoring method.^{20,21} Furthermore, we used a sophisticated segmentation technique²⁵ based on high-resolution motion-corrected 3D volumes.²³ Because all examinations were performed around the time the fetus was assessed for FETO, the GA range in our population is also relatively narrow and at a point at which cortical maturation has already progressed far enough to illustrate subtle differences. Additionally, this range means that the information from our study is from a relevant time point in pregnancy with respect to fetal therapy.

Nevertheless, we acknowledge several limitations. First, its retrospective design may result in selection bias because we included only fetuses with >1 good-quality MR imaging examination and in whom we were able to create a good-quality 3D SRR reconstruction. Second, because we are a fetal surgery center, the group of fetuses with severe hypoplasia is over-represented, and most fetuses (40/42, 95%) underwent FETO between MR imaging examinations. Hence, there may have been an effect of fetal surgery on the second MR imaging because FETO changes the natural history.^{9-11,39} Third, we have no standardized postnatal follow-up information on these cases because many patients do not deliver at our center.

Our results mandate further investigation into the sulcation pattern beyond 34 weeks in fetuses with CDH, including quantitative methods, eg, analysis of cortical folding patterns,⁴⁰ cortical thickness, and the local gyrification index,²⁸ as well as earlier in fetuses not undergoing fetal therapy.

CONCLUSIONS

We report delayed brain development in fetuses with CDH around 28 weeks, which becomes less prominent at 33 weeks. With the advent of fetal surgery,^{9,10} this might become more relevant because it suggests altered brain development in utero in these fetuses. Of note, there was no correlation between brain

development and the severity of lung hypoplasia in this highly selected group. We also observed an increase in extra-axial space and also in ventricular volume in the third trimester.

Disclosure forms provided by the authors are available with the full text and PDF of this article at www.ajnr.org.

REFERENCES

- Leeuwen L, Fitzgerald DA. **Congenital diaphragmatic hernia.** *J Paediatr Child Health* 2014;50:667–73 CrossRef Medline
- Montalva L, Raffler G, Riccio A, et al. **Neurodevelopmental impairment in children with congenital diaphragmatic hernia: not an uncommon complication for survivors.** *J Pediatr Surg* 2020;55:625–34 CrossRef Medline
- Antiel RM, Lin N, Licht DJ, et al. **Growth trajectory and neurodevelopmental outcome in infants with congenital diaphragmatic hernia.** *J Pediatr Surg* 2017;52:1944–48 CrossRef Medline
- Partridge EA, Bridge C, Donaher JG, et al. **Incidence and factors associated with sensorineural and conductive hearing loss among survivors of congenital diaphragmatic hernia.** *J Pediatr Surg* 2014;49:890–94; discussion 894 CrossRef Medline
- Danzer E, Gerdes M, D'Agostino JA, et al. **Neurodevelopmental outcome at one year of age in congenital diaphragmatic hernia infants not treated with extracorporeal membrane oxygenation.** *J Pediatr Surg* 2015;50:898–903 CrossRef Medline
- Bevilacqua F, Morini F, Zaccara A, et al. **Neurodevelopmental outcome in congenital diaphragmatic hernia survivors: role of ventilatory time.** *J Pediatr Surg* 2015;50:394–98 CrossRef Medline
- Van der Veeken L, Vergote S, Kumpulainen Y, et al. **Neurodevelopmental outcomes in children with isolated congenital diaphragmatic hernia: a systematic review and meta-analysis.** *Prenat Diagn* 2022;42:318–29 CrossRef Medline
- Danzer E, Zarnow D, Gerdes M, et al. **Abnormal brain development and maturation on magnetic resonance imaging in survivors of severe congenital diaphragmatic hernia.** *J Pediatr Surg* 2012;47:453–61 CrossRef Medline
- Deprest JA, Benachi A, Gratacos E, et al; TOTAL Trial for Moderate Hypoplasia Investigators. **Randomized trial of fetal surgery for moderate left diaphragmatic hernia.** *N Engl J Med* 2021;385:119–29 CrossRef Medline
- Deprest JA, Nicolaidis KH, Benachi A, et al; TOTAL Trial for Severe Hypoplasia Investigators. **Randomized trial of fetal surgery for severe left diaphragmatic hernia.** *N Engl J Med* 2021;385:107–18 CrossRef Medline
- Russo FM, Cordier AG, Basurto D, et al. **Fetal endoscopic tracheal occlusion reverses the natural history of right-sided congenital diaphragmatic hernia: European multicenter experience.** *Ultrasound Obstet Gynecol* 2021;57:378–85 CrossRef Medline
- Radhakrishnan R, Merhar SL, Burns P, et al. **Fetal brain morphology on prenatal magnetic resonance imaging in congenital diaphragmatic hernia.** *Pediatr Radiol* 2019;49:217–23 CrossRef Medline
- Tracy S, Estroff J, Valim C, et al. **Abnormal neuroimaging and neurodevelopmental findings in a cohort of antenatally diagnosed congenital diaphragmatic hernia survivors.** *J Pediatr Surg* 2010;45:958–65 CrossRef Medline
- Van der Veeken L, Russo FM, Litwinka E, et al. **Prenatal cerebellar growth is altered in congenital diaphragmatic hernia on ultrasound.** *Prenat Diagn* 2022;42:330–37 CrossRef Medline
- Srisupundit K, Brady PD, Devriendt K, et al. **Targeted array comparative genomic hybridisation (array CGH) identifies genomic imbalances associated with isolated congenital diaphragmatic hernia (CDH).** *Prenat Diagn* 2010;30:1198–206 CrossRef Medline
- Kyriakopoulou V, Vatansever D, Davidson A, et al. **Normative biometry of the fetal brain using magnetic resonance imaging.** *Brain Struct Funct* 2017;222:2295–307 CrossRef Medline
- Garel K. **Fetal cerebral biometry: normal parenchymal findings and ventricular size.** *Eur Radiol* 2005;15:809–13 CrossRef Medline

18. Saleem SN. **Fetal MRI: an approach to practice—a review.** *J Adv Res* 2014;5:507–23 CrossRef Medline
19. Aertsen M, Dymarkowski S, Vander Mijnsbrugge W, et al. **Anatomical and diffusion-weighted imaging abnormalities of third-trimester fetal brain in cytomegalovirus-infected fetuses.** *Ultrasound Obstet Gynecol* 2022;60:68–75 CrossRef Medline
20. Pistorius LR, Stoutenbeek P, Groenendaal F, et al. **Grade and symmetry of normal fetal cortical development: a longitudinal two- and three-dimensional ultrasound study.** *Ultrasound Obstet Gynecol* 2010;36:700–08 CrossRef Medline
21. Egaña-Ugrinovic G, Sanz-Cortes M, Figueras F, et al. **Differences in cortical development assessed by fetal MRI in late-onset intrauterine growth restriction.** *Am J Obstet Gynecol* 2013;209:126e1–8 CrossRef Medline
22. Hahner N, Benkarim OM, Aertsen M, et al. **Global and regional changes in cortical development assessed by MRI in fetuses with isolated nonsevere ventriculomegaly correlate with neonatal neurobehavior.** *AJNR Am J Neuroradiol* 2019;40:1567–74 CrossRef Medline
23. Ebner M, Wang GT, Li WQ, et al. **An automated framework for localization, segmentation and super-resolution reconstruction of fetal brain MRI.** *Neuroimage* 2020;206:116324 CrossRef Medline
24. Fidon L, Aertsen M, Mufti N, et al. **Distributionally robust segmentation of abnormal fetal brain 3D MRI: uncertainty for safe utilization of machine learning in medical imaging, and perinatal imaging, placental and preterm image analysis.** In: *Proceedings of the 3rd International Workshop, UNSURE 2021, and 6th International Workshop, PIPPI 2021, Held in Conjunction with MICCAI 2021, Strasbourg, France. October 1, 2021*
25. Fidon L, Aertsen M, Emam D, et al. **Label-set loss functions for partial supervision: application to fetal brain 3D MRI parcellation.** *arXiv* 2021:2107.03846 <https://arxiv.org/abs/2107.03846>. Accessed August 1, 2021
26. Cannie MM, Jani JC, Van Kerkhove F, et al. **Fetal body volume at MR imaging to quantify total fetal lung volume: normal ranges.** *Radiology* 2008;247:197–203 CrossRef Medline
27. Cannie M, Jani J, Chaffiotte C, et al. **Quantification of intrathoracic liver herniation by magnetic resonance imaging and prediction of postnatal survival in fetuses with congenital diaphragmatic hernia.** *Ultrasound Obstet Gynecol* 2008;32:627–32 CrossRef Medline
28. Lucignani M, Longo D, Fontana E, et al. **Morphometric analysis of brain in newborn with congenital diaphragmatic hernia.** *Brain Sci* 2021;11:455 CrossRef Medline
29. Radhakrishnan R, Merhar SL, Su W, et al. **Prenatal factors associated with postnatal brain injury in infants with congenital diaphragmatic hernia.** *AJNR Am J Neuroradiol* 2018;39:558–62 CrossRef Medline
30. Garel C, Elmaleh M, Chantrel E, et al. **Fetal MRI: normal gestational landmarks for cerebral biometry, gyration and myelination.** *Childs Nerv Syst* 2003;19:422–25 CrossRef Medline
31. Brazelton TB, Nugent JK. *Neonatal Behavioral Assessment Scale.* Cambridge University Press; 1995:200
32. Van Mieghem T, Sandaite I, Michielsen K, et al. **Fetal cerebral blood flow velocities in congenital diaphragmatic hernia.** *Ultrasound Obstet Gynecol* 2010;36:452–57 CrossRef Medline
33. Kaltman JR, Di H, Tian Z, et al. **Impact of congenital heart disease on cerebrovascular blood flow dynamics in the fetus.** *Ultrasound Obstet Gynecol* 2005;25:32–36 CrossRef Medline
34. Pearce W. **Hypoxic regulation of the fetal cerebral circulation.** *J Appl Physiol (1985)* 2006;100:731–38 CrossRef Medline
35. Jaimes C, Rofeberg V, Stopp C, et al. **Association of isolated congenital heart disease with fetal brain maturation.** *AJNR Am J Neuroradiol* 2020;41:1525–31 CrossRef Medline
36. Maruccia F, Gomáriz L, Rosas K, et al. **Neurodevelopmental profile in children with benign external hydrocephalus syndrome: a pilot cohort study.** *Childs Nerv Syst* 2021;37:2799–806 CrossRef Medline
37. Vogel M, McElhinney DB, Marcus E, et al. **Significance and outcome of left heart hypoplasia in fetal congenital diaphragmatic hernia.** *Ultrasound Obstet Gynecol* 2010;35:310–17 CrossRef Medline
38. Miyajima M, Arai H. **Evaluation of the production and absorption of cerebrospinal fluid.** *Neurol Med Chir (Tokyo)* 2015;55:647–56 CrossRef Medline
39. Basurto D, Russo FM, Van der Veecken L, et al. **Prenatal diagnosis and management of congenital diaphragmatic hernia.** *Best Pract Res Clin Obstet Gynaecol* 2019;58:93–106 CrossRef Medline
40. Orasanu E, Melbourne A, Cardoso MJ, et al. **Cortical folding of the preterm brain: a longitudinal analysis of extremely preterm born neonates using spectral matching.** *Brain Behav* 2016;6:e00488 CrossRef Medline

Common Neuroimaging Findings in Bosch-Boonstra-Schaaf Optic Atrophy Syndrome

N.K. Desai, S.F. Kralik, J.C. Edmond, V. Shah, T.A.G.M. Huisman, M. Rech, and C.P. Schaaf

ABSTRACT

SUMMARY: Bosch-Boonstra-Schaaf optic atrophy syndrome (BBSOAS) is a rare autosomal dominant syndrome secondary to mutations in *NR2F1* (COUP-TFI), characterized by visual impairment secondary to optic nerve hypoplasia and/or atrophy, developmental and cognitive delay, and seizures. This study reports common neuroimaging findings in a cohort of 21 individuals with BBSOAS that collectively suggest the diagnosis. These include mesial temporal dysgyria, perisylvian dysgyria, posterior predominant white matter volume loss, callosal abnormalities, lacrimal gland abnormalities, and optic nerve volume loss.

ABBREVIATIONS: BBSOAS = Bosch-Boonstra-Schaaf optic atrophy syndrome; COUP-TFI = chicken ovalbumin upstream promoter transcription factor 1

Bosch-Boonstra-Schaaf optic atrophy syndrome (BBSOAS, Online Mendelian Inheritance in Man 615722) is a rare autosomal dominant disorder primarily characterized by visual impairment from optic hypoplasia and/or atrophy and neurocognitive and developmental delay.¹ A wide variety of additional clinical phenotypes has been reported in the literature in subsets of patients, including hypotonia, oromotor dysfunction, hearing abnormalities, seizures, autism spectrum disorder, and personality disorders such as attention deficit/hyperactivity disorder and obsessive compulsive disorder.²

BBSOAS is caused by mutations, nearly all de novo, in the nuclear receptor subfamily 2 group F member 1 (*NR2F1*) gene responsible for encoding the NR2F1 protein, which is also known as the chicken ovalbumin upstream promoter transcription factor 1 (COUP-TFI). This protein stimulates initiation and regulation of transcription but also serves as a nuclear hormone receptor. *NR2F1* is important for myriad central nervous embryologic developments that include ocular globe and optic nerve development as well as cortical development, axonal guidance, neurogenesis and neuronal arborization, hippocampal volume, and functional organization.³⁻⁹

In this report, we describe readily identifiable, common neuroimaging findings of BBSOAS that strongly suggest this genetic diagnosis.

CASE SERIES

Case Selection

A clinical database of multi-institutional (18 total) patients genetically diagnosed with BBSOAS was queried after institutional review board approval at Baylor College of Medicine. This database included patients seen at a single institution during the historic discovery of this unique genetic entity. A total of 51 individuals with BBSOAS were documented at a single institution, having undergone genetic and clinical evaluation. Neurologic and ophthalmologic information was recorded. Brain MR imaging examinations of patients were centrally collected and were available for 21 patients.

Imaging Evaluation

All imaging was performed on 1.5T or 3T MR imaging units. All studies included standard departmental multiplanar T1-weighted, T2-weighted, FLAIR, and DWI sequences of the brain and orbits with expected variations in the protocols per the multiple institutions. Most of the studies were performed without contrast. In a small number of patients in whom intravenous contrast was administered, the T1-weighted postcontrast imaging was reviewed but was noncontributory in all cases and will not be discussed further. Brain MR imaging examinations of all patients were collectively consensus-reviewed by 2 board-certified pediatric neuroradiologists (N.K.D. and S.F.K.), each with 10 years of experience. Neuroimaging findings of the orbit, optic nerve apparatus, cortical gray and hemispheric white matter of the cerebrum, cerebellum, vermis, central gray matter, and midline structures were categorically reviewed and

Received June 20, 2022; accepted after revision December 6.

From the Department of Radiology (N.K.D., S.F.K., T.A.G.M.H.), Texas Children's Hospital Baylor College of Medicine Houston, Texas; Department of Ophthalmology (J.C.E.), Dell Medical School, The University of Texas at Austin, Austin, Texas; Department of Ophthalmology (V.S.), Cincinnati Children's Hospital, Cincinnati, Ohio; Sleep and Anxiety Center of Houston (M.R.), Department of Psychology, University of Houston, Houston, Texas; and Institute of Human Genetics, Heidelberg University (C.P.S.), Heidelberg, Germany.

Please address correspondence to Nilesh K. Desai, MD, Department of Radiology, Texas Children's Hospital, 6701 Fannin St, Suite 470, Houston, TX 77030; e-mail: nkdesai@texaschildrens.org

<http://dx.doi.org/10.3174/ajnr.A7758>

recorded. For the corpus callosum, qualitative and quantitative evaluations were performed. Quantification included measurement of the overall callosal anterior-posterior dimension (also called callosal length) as well as segmental thickness of the genu, body, isthmus, and splenium. Callosal measurements of \leq 3rd percentile or \geq 97th percentile were deemed abnormal compared with the previously published reference measurements by Garel et al.¹⁰ Pertinent data-based medical history was retrospectively reviewed, including demographics, clinical signs and symptoms, as well as the results of a detailed neuro-ophthalmologic evaluation.

RESULTS

Demographic and Clinical Findings

The mean age of the children at MR imaging was 4.5 years (range, 0.33–16 years) with 12/21 (57%) being female. A variety of de

Table 1: Pathogenic variants in NR2F1

Pathogenic Variant	No.
Missense mutation in DNA binding domain of NR2F1	9/21 (43%)
Deletions (variable including, among others, NR2F1, FAM172AA, KIAA0825)	4/21 (19%)
Translation initiation mutation of NR2F1	3/21 (14%)
Missense in ligand binding domain or exon 3 of NR2F1	3/21 (14%)
Frameshift mutation of NR2F1	1/21 (5%)
Nonsense mutation in exon 3 of NR2F1	1/21 (5%)

Table 2: Ophthalmologic phenotypes

Phenotype	No.
General visual impairment	19/21 (90%)
Cerebral visual impairment ^a	10/20 (50%)
Optic atrophy/optic disc pallor	18/21 (86%)
Optic nerve hypoplasia/small optic nerve ^a	8/20 (40%)
Nystagmus ^a	12/20 (60%)
Alacrima or decreased tear production ^a	15/19 (79%)

^a Incomplete data.

Table 3: Neurocognitive phenotypes

Phenotype ^a	No.
Developmental/intellectual delay	16/19 (84%)
Speech delay	17/19 (89%)
Autism spectrum disorder or features	16/19 (84%)
Unusually strong long-term memory	14/17 (82%)
Motor delay	15/19 (79%)
Oromotor dysfunction	16/19 (84%)
Hypotonia	18/19 (95%)
Seizures, infantile spasms	12/19 (63%)

^a Each row in column 1 has incomplete data.

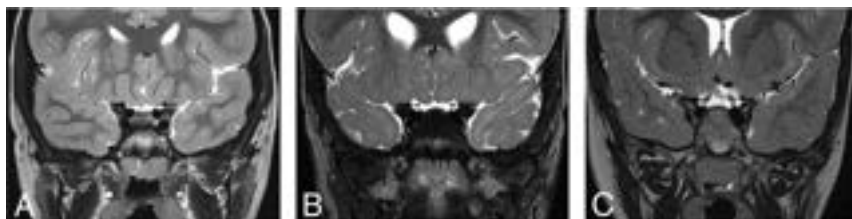


FIG 1. Coronal T2WI in multiple patients with BBSOAS. Bilateral, symmetric, severe optic nerve volume loss in patient 19, a 6-year-old boy (A) (black arrows); mild-to-moderate volume loss in patient 18, a 3-year-old girl (B) (black arrows); and normal optic nerves in patient 11, a 4.7-year-old girl (C) (black arrows).

novo pathogenic variants in NR2F1 were present in this cohort, most commonly missense mutations in NR2F1, present in 9/21 (43%) patients (Table 1).

Ophthalmologic abnormalities are a hallmark of BBSOAS with general visual impairment present in 19/21 (90%) patients of this cohort, of which many (1 patient without specific documentation) were found to have cerebral visual impairment (10/20, 50%). A cerebral visual impairment diagnosis was based on clinical examination by 2 pediatric neuro-ophthalmologists of visual behavior not consistent with anterior visual pathway dysfunction (ie, optic nerve abnormality) alone and clinically observed features (vision inattention, low-light gazing, difficulty with visual complexity) consistent with a cerebral visual impairment diagnosis. Furthermore, a cerebral visual impairment diagnostic screening questionnaire was given to all patients' families. Optic nerve atrophy, optic nerve hypoplasia, or both were noted in 18/21 (86%) and 8/20 (40%) patients, respectively (1 patient did not have specific documentation on the presence or absence of optic nerve hypoplasia). Nystagmus and alacrima (decreased tear production) were seen in 12/20 (60%) (1 patient without specific documentation) and 15/19 (79%) patients (2 patients without specific documentation), respectively (Table 2). Detailed ophthalmologic findings will be discussed in a forthcoming publication.

Developmental data were available for 19/21 (90%) patients. Intellectual, and speech delay were common in the group, seen in 16/19 (84%) and 17/19 (89%) patients. Autistic features were present in 16/19 (84%) patients. Most interesting, despite such delays, 14/17 (82%) patients were clinically reported to have unusually strong long-term memory ability (2 patients without specific documentation). Motor impairment including general motor delay, oromotor dysfunction, and hypotonia were similarly present with high frequency in 15/19 (79%), 16/19 (84%), and 18/19 (95%) patients, respectively. Seizures or infantile spasms were present in 12/19 (63%) patients (Table 3). Detailed genotypic-phenotypic findings have been previously published by this group.¹¹

Ophthalmologic Imaging

Eighteen of 21 patients (86%) demonstrated bilateral symmetric volume loss consistent with optic atrophy and/or hypoplasia of the optic apparatus, including of the optic nerves, chiasm, and optic tracts (Fig 1). Such volume loss was subjectively noted to be of variable severity from mild to moderate to severe. These findings correlated with the presence or absence of optic nerve hypo-

plasia and/or atrophy in all patients. Of the 3/21 (14%) patients with normal optic nerves on imaging, 1/3 patients (67%) had abnormal ophthalmologic examination findings with atrophy. Data on optic nerve hypoplasia were not available in 1/21 (5%) patients.

An interesting clinical hallmark reported in 15/19 (79%) patients in this cohort is alacrima or decreased tear production. Thirteen of 21 (62%) patients had hypoplastic bilateral lacrimal glands

on MR imaging, and 8/21 (38%) patients had normal lacrimal glands. Data on tear production were not available in 2/21 (10%) patients. One of 19 (5%) patients with hypoplastic lacrimal glands did not have abnormal tear production. Three of 19 (16%) patients with normal lacrimal glands on imaging had normal tear production. Five of 19 (26%) patients with normal lacrimal glands on imaging had decreased tear production. Ten of 19 (58%) patients with hypoplastic lacrimal glands had absent or decreased tear production (Fig 2).

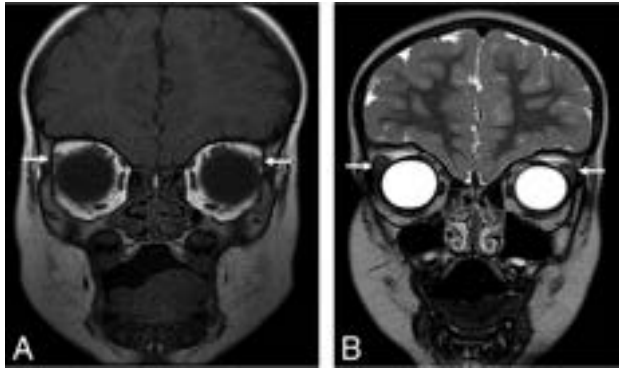


FIG 2. Patient 2, an 0.8-year-old girl. Coronal T1WI of the orbits demonstrates hypoplastic lacrimal glands (arrows) (A). Patient 11, a 4.7-year-old girl. Coronal T2WI image of the orbits demonstrates normal lacrimal glands (arrows) in comparison (B).

Midline Imaging

Fourteen of 21 (67%) patients had an abnormal corpus callosum (Fig 3). We observed several different imaging phenotypes:

- 1) Thickened genu and body, thinned splenium with normal callosal length (1/21) (5%)
- 2) Thickened body and normal callosal length (1/21) (5%)
- 3) Thickened body and splenium with normal callosal length (1/21) (5%)
- 4) Thickened genu and body and normal callosal length (1/21) (5%)
- 5) Thinned splenium with normal callosal length (3/21) (14%)
- 6) Thinned body with normal callosal length (1/21) (5%)
- 7) Thinned splenium with decreased callosal length (2/21) (10%)
- 8) Thinned body, isthmus, and splenium with decreased callosal length (1/21) (5%)
- 9) Normal thickness with isolated decreased callosal length (1/21) (5%)
- 10) Thickened genu and body and thinned splenium with decreased callosal length (1/21) (5%)
- 11) Thickened body and thinned splenium with decreased callosal length (1/21) (5%)
- 12) Normal corpus callosum (7/21) (33%)

All patients had a normal septum pellucidum and hypothalamic-pituitary axis. One of 21 (5%) patients had a hypoplastic left olfactory bulb. One of 21 (5%) patients demonstrated subjective

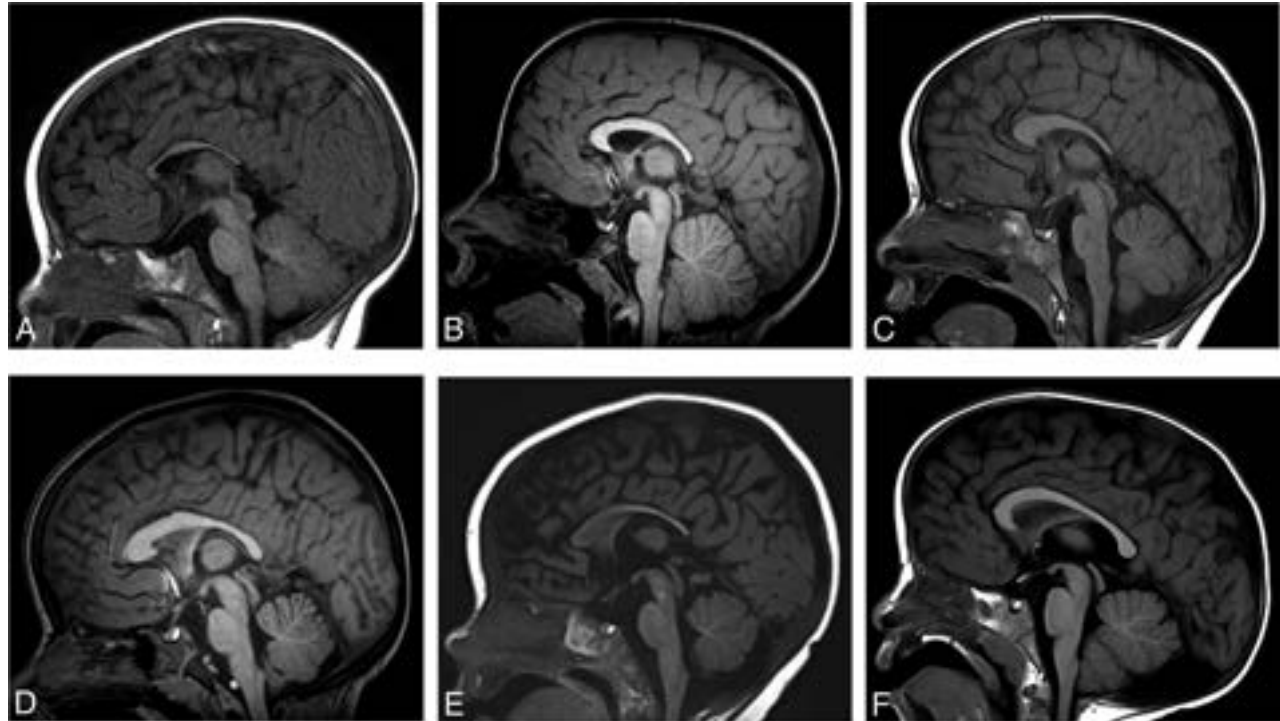


FIG 3. Midline sagittal T1WI in multiple patients with BBSOAS. Patient 5, a 0.5-year-old boy. Decreased callosal length with a thinned body, isthmus, and splenium of the corpus callosum (A). Patient 20, a 5-year-old boy. Decreased callosal length with thinning of the isthmus (B). Patient 8, a 2-year-old boy. Decreased callosal length with a thickened genu and body but a thinned splenium (C). Patient 21, a 6-year-old girl. Normal callosal length, thickened genu and body with a thinned splenium (D). Patient 14, a 0.6-year-old girl. Normal callosal length with a thinned splenium (E). Patient 9, a 6-year-old boy. Normal corpus callosum. Incidental note is made of a retrocerebellar arachnoid cyst (F).

decreased volume of the pons. A separate patient, 1/21 (5%), demonstrated a vermian cleft. One of 21 (5%) patients, an 8-month-old infant (patient 15), demonstrated T2 hyperintensity of the bilateral central tegmental tracts. Otherwise, midline posterior fossa anatomy, including the brainstem and vermis, was normal in all patients.

Lobar Imaging

Twenty-one of 21 (100%) patients had dysgyria, defined as an abnormal gyral pattern with abnormal sulcal depth or orientation but with normal cortical thickness and normal gray-white matter differentiation along the bilateral mesial temporal lobes. Perisylvian dysgyria was present in 15/21 (71%) patients, occurring bilaterally in 14/15 (93%) patients. Perisylvian dysgyria in our cohort group included a variety of different radiologic phenotypes. These principally included ≥ 1 of the following: craniocaudal elongation of the temporal lobes, lateral temporal dysgyria, and posterior perisylvian dysgyria involving the inferior parietal lobule with posterior elongation of the Sylvian fissure or other generally dysmorphic Sylvian fissures including, for example, underpercularization and steep craniocaudal angulation of the Sylvian fissure axis (Figs 4–6). There were no abnormalities of myelination to suggest leukodystrophy. None of the patients had gray matter heterotopia or cortical dysplasia.

Decreased cerebral white matter volume was present posteriorly in 11/21 (52%) patients. Decreased anterior and posterior cerebral white matter volume was present in 3/21 (14%) patients (Fig 7). Twelve of 14 (86%) patients with lobar white matter volume loss had abnormalities of the corpus callosum. Of the 18/21 (86%) patients with optic nerve abnormalities on imaging, 12/18 (67%) demonstrated lobar white matter volume loss.

One of 21 (5%) patients had a cavernous malformation.

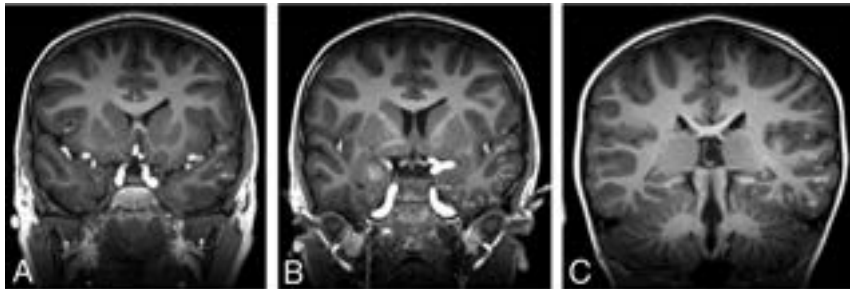


FIG 4. Coronal 3D T1WI (A–C) demonstrating normal anatomy of the temporal lobes as a reference. PHG indicates parahippocampal gyrus; CS, collateral sulcus; OTG, occipitotemporal gyrus; OTS, occipitotemporal sulcus; ITG, inferior temporal gyrus; ITS, inferior temporal sulcus; MTG, middle temporal gyrus; STS, superior temporal sulcus; STG, superior temporal gyrus; SF, Sylvian fissure.

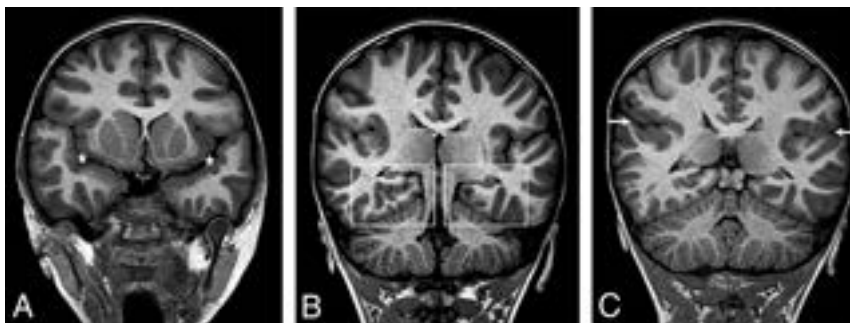


FIG 5. Patient 6, a 16-year-old boy. Coronal 3D T1WI demonstrates dysmorphic Sylvian fissures (stars, A). The anterior temporal lobes appear large with significant dysgyria (A) and craniocaudal elongated morphology. Dysgyria is noted in the bilateral mesial temporal lobes (boxes, B). Dysgyria broadly involves the posterior right lateral temporal lobe, appearing as gross overgyration with small gyri and shallow sulci (C), with right mesial temporal lobe dysgyria still noted. The right Sylvian fissure is significantly asymmetric to the left (arrows), with an exaggerated upslope (C).

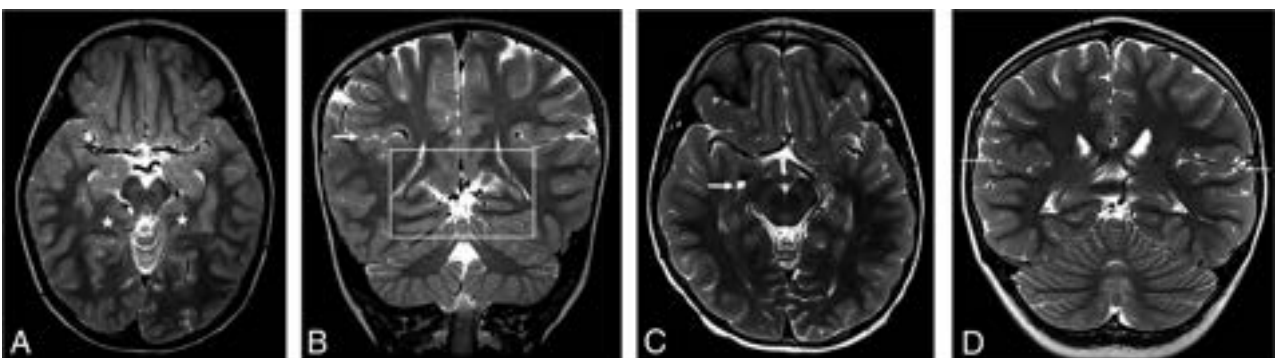


FIG 6. Patient 21, a 6-year-old girl. Axial T2WI demonstrates dysgyria of the mesial temporal lobes (stars, A). Coronal T2WI demonstrates dysgyria of the mesial temporal lobes (box, B). Dysgyria broadly involves the posterior right lateral temporal lobe. Both temporal lobes appear elongated craniocaudally. The right Sylvian fissure is significantly asymmetric to the left (arrows), with an exaggerated upslope (B). Bilateral perisylvian dysgyria is present. Normal findings on axial and coronal T2WI are shown for comparison (C–D). An enlarged perivascular space is incidentally noted on the right (arrow, C). Note the normal, mostly horizontal axis of the Sylvian fissures and the normal anatomy of the temporal lobes and perisylvian parenchyma (arrows) (D).

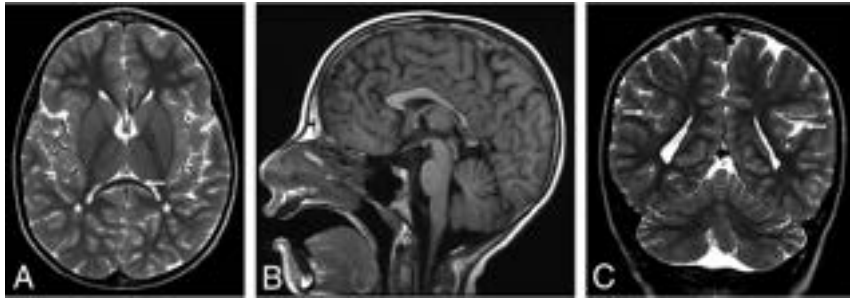


FIG 7. Patient 1, an 8 year-old girl. Axial T2WI demonstrates significant posterior white matter volume loss (stars, A). Note the thinning of the splenium of the corpus callosum (arrow), similarly seen on the sagittal T1 image (B). Coronal T2WI demonstrates dysmorphic Sylvian fissures bilaterally, with an exaggerated upslope of the fissures bilaterally. Bilateral perisylvian dysgyria is present with craniocaudal elongated temporal lobes bilaterally (arrows, C).

DISCUSSION

BBSOAS is a rare autosomal dominant disorder due to loss-of-function mutations in *NR2F1*, also known as COUP-TF1, originally described in 2014 by Bosch et al.¹ Patients are characterized by visual and neurocognitive deficits but may also manifest additional clinical symptoms of hypotonia, seizures, autism spectrum disorders, oromotor dysfunction, and hearing abnormalities.

Neuroimaging findings in BBSOAS have been partially reported in the literature to date. Thinning of the corpus callosum has been reported by multiple authors, including 8/15 patients by Chen et al.^{2,12} We similarly discovered abnormalities in the corpus callosum in 67% patients. However, callosal abnormalities were quite heterogeneous with variable combinations of the following findings: normal or decreased anterior-posterior callosal length and segmental thinning and/or thickening. All patients in this study had a normal septum pellucidum and a normal hypothalamic pituitary axis.

Thinning of the optic apparatus has also been expectedly reported in previous literature, corresponding with ophthalmologic findings common to these patients.^{2,13,14} Nearly all of the patients in our group (86%) demonstrated bilateral optic nerve volume loss of variable severity with all other patients demonstrating normal optic nerves. Additional orbital findings in our patient population included subjectively hypoplastic (13/21) lacrimal glands, which, in a subset of patients, did correlate with alacrima.

As noted, *NR2F1* is important for myriad central nervous embryologic developments that include cortical development, axonal guidance, neurogenesis and neuronal arborization, and hippocampal volume and functional organization.³⁻⁹ Recently, Bertacchi et al¹² reported altered gyration, described as being polymicrogyria-like in the supramarginal and angular gyrus of only the left inferior parietal lobule. These authors also reported elongation of the right superior occipital gyrus and prominent occipital gyration in a separate patient. We, similarly, found abnormal gyration and sulcation of the perisylvian parenchyma in 15/21 (71%) patients, of which 14/15 (93%) were bilateral, but we also report more common similar findings in the mesial temporal lobes bilaterally in 21/21 (100%) patients. These imaging findings are best termed dysgyria, defined as an abnormal gyral pattern with abnormal sulcal depth or orientation but with normal cortical thickness and normal gray-white matter differentiation.

While Bertacchi et al¹² described this anomalous gyration as polymicrogyria-like, the findings are not polymicrogyria (as they note), given the lack of cortical thickening as evidenced by the sample images in their publication. None of the patients in our cohort had findings of cortical dysplasia or gray matter heterotopia, and this has not been reported elsewhere, to our knowledge. As Bertacchi et al noted, much work is needed to better understand the role of *NR2F1* in human cortical folding patterns, gyri and sulci positioning, and the effect of *NR2F1* on progenitor subtypes that ultimately lead to the neuroradiologic phenotypes discussed here and their eventual clinical phenotypic expressions.¹²

Mesial temporal dysgyria is not specific to BBSOAS. In fact, it has been well-reported with other, unrelated entities, including, for example, Apert syndrome due to mutations in *FGFR2*. Similarly, achondroplasia, thanatophoric dysplasia, and hypochondroplasia, all of which are due to mutations in *FGFR3*, are typified by such dysgyria.^{15,16} Furthermore, perisylvian dysgyria, an entity seldom reported in the literature, is not specific to BBSOAS, having recently been described in individuals with the *ACTA2* gene mutation.¹⁷ Dysgyria, in general, has also been described in patients with microtubule mutations.¹⁸ Thematic to dysgyria in these examples, however, is the linkage of mutations in genes important for axonal guidance and neuronal migration.

Many of our patients (14/21) demonstrated subjective posterior or anterior and posterior cerebral white matter volume loss, with 12/14 (86%) patients with lobar white matter volume loss having abnormalities of the corpus callosum. Similarly, of the 18/21 (86%) patients with optic nerve abnormalities on imaging, 12/18 (67%) demonstrated lobar white matter volume loss.

A limitation of our study is the heterogeneous imaging performed in the cohort, because patients and therefore imaging were collected from a variety of institutions. Most imaging performed was, therefore, nonvolumetric conventional 2D imaging, thwarting our ability to perform systematic volumetric analysis of the whole and ultrastructural brain. Given our findings and those already in the literature, volumetric analysis would be of special interest at the level of the temporal lobes and the limbic system.

Most interesting, unusually strong long-term memory was found in 82% of patients, despite most demonstrating intellectual disability, indicating that additional quantification of brain volumetry may provide insights into this disorder. Similarly, advanced imaging including DTI or functional MR imaging was not uniformly available to evaluate the microstructural white matter architecture or connectivity of the brain. Such analyses may prove revealing in the deeper understanding of *NR2F1* gene function as it relates to the human brain. In *Nr2f1*^{+/-} mice, MR imaging has already demonstrated decreased hippocampal volumes and increased volume of the caudate nucleus, putamen, and neocortex, with preserved neuronal cell density foreshadowing the potential of these MR imaging techniques.¹⁹

CONCLUSIONS

Patients with BBSOAS commonly manifest abnormalities of the optic pathway, lacrimal glands, corpus callosum, and dysgyria of the temporal lobes and perisylvian cortex, which, in combination, can suggest this disorder and indicate a need for genetic testing.

Disclosure forms provided by the authors are available with the full text and PDF of this article at www.ajnr.org.

REFERENCES

1. Bosch DM, Boonstra F, Gonzaga-Jauregui C, et al; Baylor-Hopkins Center for Mendelian Genomics. **NR2F1 mutations cause optic atrophy with intellectual disability.** *Am J Hum Genet* 2014;94:303–09 CrossRef Medline
2. Chen CA, Bosch DG, Cho MT, et al. **The expanding clinical phenotype of Bosch-Boonstra-Schaaf optic atrophy syndrome: 20 new cases and possible genotype-phenotype correlations.** *Genet Med* 2016;18:1143–50 CrossRef Medline
3. Faedo A, Tomassy GS, Ruan Y, et al. **COUP-TFI coordinates cortical patterning, neurogenesis, and laminar fate and modulates MAPK/ERK, AKT, and β -catenin signaling.** *Cereb Cortex* 2008;18:2117–31 CrossRef Medline
4. O'Leary DDM, Studer M, Armentano M, et al. **COUP-TFI regulates the balance of cortical patterning between frontal/motor and sensory areas.** *Nat Neurosci* 2007;10:1277–86 CrossRef Medline
5. Zhou C, Tsai SY, Tsai MJ. **COUP-TFI: an intrinsic factor for early regionalization of the neocortex.** *Genes Dev* 2001;15:2054–59 CrossRef Medline
6. Zhou C, Qiu Y, Pereira FA, et al. **The nuclear orphan receptor COUP-TFI is required for differentiation of subplate neurons and guidance of thalamocortical axons.** *Neuron* 1999;24:847–59 CrossRef Medline
7. Qiu Y, Pereira FA, DeMayo FJ, et al. **Null mutation of mCOUP-TFI results in defects in morphogenesis of the glossopharyngeal ganglion, axonal projection, and arborization.** *Genes Dev* 1997;11:1925–37 CrossRef Medline
8. Tang K, Xie X, Park J, et al. **COUP-TFs regulate eye development by controlling factors essential for optic vesicle morphogenesis.** *Development* 2010;137:725–34 CrossRef Medline
9. Flore G, Di Ruberto G, Parisot J, et al. **Gradient COUP-TFI expression is required for functional organization of the hippocampal septo-temporal longitudinal axis.** *Cereb Cortex* 2017;27:1629–43 CrossRef Medline
10. Garel C, Cont I, Alberti C, et al. **Biometry of the corpus callosum in children: MR imaging reference data.** *AJNR Am J Neuroradiol* 2011;32:1436–43 CrossRef Medline
11. Rech ME, McCarthy JM, Chen C, et al. **Phenotypic expansion of Bosch-Boonstra-Schaaf optic atrophy syndrome and further evidence for genotype-phenotype correlations.** *Am J Med Genet A* 2020;182:1426–37 CrossRef Medline
12. Bertacchi M, Romano AL, Loubat A, et al. **NR2F1 regulates regional progenitor dynamics in the mouse neocortex and cortical gyrification in BBSOAS patients.** *EMBO J* 2020;39:e104168 CrossRef Medline
13. Park SE, Lee JS, Lee S, et al. **Targeted panel sequencing identifies a novel NR2F1 mutations in a patient with Bosch-Boonstra-Schaaf optic atrophy syndrome.** *Ophthalmic Genet* 2019;40:359–61 CrossRef Medline
14. Bojanek EK, Mosconi MW, Guter S, et al. **Clinical and neurocognitive issues associated with Bosch-Boonstra-Schaaf optic atrophy syndrome: a case study.** *Am J Med Genet A* 2020;182:213–18 CrossRef Medline
15. Manikkam SA, Chetcuti KK, Howell KB, et al. **Temporal lobe malformations in achondroplasia: expanding the brain imaging phenotype associated with FGFR3-related skeletal dysplasias.** *AJNR Am J Neuroradiol* 2018;39:380–84 CrossRef Medline
16. Tan AP, Mankad K. **Apert syndrome: magnetic resonance imaging (MRI) of associated intracranial anomalies.** *Childs Nerv Syst* 2018;34:205–16 CrossRef Medline
17. Subramanian S, Biswas A, Alves CAPF, et al. **ACTA2-related dysgyria: an under-recognized malformation of cortical development.** *AJNR Am J Neuroradiol* 2022;43:146–50 CrossRef Medline
18. Mutch CA, Poduri A, Sahin M, et al. **Disorders of microtubule function in neurons: imaging correlates.** *AJNR Am J Neuroradiol* 2016;37:528–35 CrossRef Medline
19. Chen C, Wang W, Pedersen SE, et al. **Nr2f1 heterozygous knockout mice recapitulate neurological phenotypes of Bosch-Boonstra-Schaaf optic atrophy syndrome and show impaired hippocampal synaptic plasticity.** *Hum Mol Genet* 2020;29:705–15 CrossRef Medline

Fully Automatic Method for Reliable Spinal Cord Compartment Segmentation in Multiple Sclerosis

C. Tsagkas,¹ A. Horvath-Huck,² T. Haas,³ M. Amann,⁴ A. Todea,⁵ A. Altermatt,⁶ J. Müller,⁷ A. Cagol,⁸ M. Leimbacher,⁹ M. Barakovic,¹⁰ M. Weigel,¹¹ S. Pezold,¹² T. Sprenger,¹³ L. Kappos,¹⁴ O. Bieri,¹⁵ C. Granziera,¹⁶ P. Cattin, and K. Parmar



ABSTRACT

BACKGROUND AND PURPOSE: Fully automatic quantification methods of spinal cord compartments are needed to study pathologic changes of the spinal cord GM and WM in MS in vivo. We propose a novel method for automatic spinal cord compartment segmentation (SCORE) in patients with MS.

MATERIALS AND METHODS: The cervical spinal cords of 24 patients with MS and 24 sex- and age-matched healthy controls were scanned on a 3T MR imaging system, including an averaged magnetization inversion recovery acquisition sequence. Three experienced raters manually segmented the spinal cord GM and WM, anterior and posterior horns, gray commissure, and MS lesions. Subsequently, manual segmentations were used to train neural segmentation networks of spinal cord compartments with multidimensional gated recurrent units in a 3-fold cross-validation fashion. Total intracranial volumes were quantified using FreeSurfer.

RESULTS: The intra- and intersession reproducibility of SCORE was high in all spinal cord compartments (eg, mean relative SD of GM and WM: $\leq 3.50\%$ and $\leq 1.47\%$, respectively) and was better than manual segmentations (all $P < .001$). The accuracy of SCORE compared with manual segmentations was excellent, both in healthy controls and in patients with MS (Dice similarity coefficients of GM and WM: ≥ 0.84 and ≥ 0.92 , respectively). Patients with MS had lower total WM areas ($P < .05$), and total anterior horn areas ($P < .01$ respectively), as measured with SCORE.

CONCLUSIONS: We demonstrate a novel, reliable quantification method for spinal cord tissue segmentation in healthy controls and patients with MS and other neurologic disorders affecting the spinal cord. Patients with MS have reduced areas in specific spinal cord tissue compartments, which may be used as MS biomarkers.

ABBREVIATIONS: AMIRA = averaged magnetization inversion recovery acquisitions; bSSFP = balanced steady-state free precession; DSC = Dice similarity coefficient; EDSS = Expanded Disability Status Scale; HC = healthy control; HD = Hausdorff distance; MDGRU = multidimensional gated recurrent units; RSD = relative SD (also known as coefficient of variation); SC = spinal cord; SCWM = spinal cord WM; SCGM = spinal cord GM; SCORE = automatic spinal cord compartment segmentation; TIV = total intracranial volume

The spinal cord (SC) is an important part of the CNS, and SC involvement is seen in various neurologic disorders of diverse pathophysiology (eg, genetic, inflammatory, demyelinating, degenerative, infectious, and so forth).^{1,2} In MS, focal SC lesions are the result of inflammatory demyelinating events,^{3,4} whereas diffuse

tissue volume loss (also known as atrophy) also occurs and reflects an independent neurodegenerative process.^{5,6} This heterogeneous SC injury is seen to various extent with nonuniform involvement

C. Tsagkas was supported by the Swiss National Science Foundation (grant No. 320030_156860), the Stiftung zur Förderung der Gastroenterologischen und Allgemeinen Klinischen Forschung, as well as the University of Basel (grant No. 3MSI020 and 3MSI049). C. Granziera is funded by the Swiss National Science Foundation (grant No. PP00P3_176984), the Stiftung zur Förderung der Gastroenterologischen und Allgemeinen Klinischen Forschung, and the Eurostar Program of Horizon 2020 (grant No. E113682). M. Weigel was supported by the Swiss National Science Foundation (SNSF, grant number: 320030_156860), the Swiss Multiple Sclerosis Society, and the Stiftung zur Förderung der Gastroenterologischen und Allgemeinen Klinischen Forschung. He is currently funded by the Swiss National Science Foundation (grant No. PP00P3_176984) and Biogen.

Please address correspondence to Charidimos Tsagkas, MD, MD-PhD, Neurologic Clinic and Policlinic, Departments of Medicine, Clinical Research and Biomedical Engineering, University Hospital Basel and University of Basel, Petersgraben 4, CH-4031 Basel, Switzerland; e-mail: charidimos.tsagkas@usb.ch

Indicates open access to non-subscribers at www.ajnr.org

Indicates article with online supplemental data.

<http://dx.doi.org/10.3174/ajnr.A7756>

Received January 5, 2022; accepted after revision December 5.

From the Neurologic Clinic and Policlinic, Departments of Medicine (C.T., M.A., J.M., M.W., T.S., L.K., C.G., K.P.), Clinical Research and Biomedical Engineering; Translational Imaging in Neurology Basel (C.T., A.T., J.M., A.C., M.B., M.W., C.G., K.P.), Department of Medicine and Biomedical Engineering; Division of Radiological Physics (T.H., M.W., O.B.), Department of Radiology; Department of Neuroradiology (A.T.), Clinic for Radiology & Nuclear Medicine; and Research Center for Clinical Neuroimmunology and Neuroscience Basel (RC2NB) (L.K.), Departments of Medicine, Clinical Research, and Biomedical Imaging, University Hospital Basel and University of Basel, Basel, Switzerland; Department of Biomedical Engineering (A.H.-H., M.A., A.C., M.B., M.W., S.P., O.B., C.G., P.C.), University of Basel, Allschwil, Switzerland; Medical Image Analysis Center AG (M.A., A.A.), Basel, Switzerland; Medical Faculty (M.L., P.C.), University of Basel, Basel, Switzerland; Department of Neurology (T.S.), DKD Helios Klinik Wiesbaden, Wiesbaden, Germany; and Reha Rheinfelden (K.P.), Rheinfelden, Switzerland.

C. Tsagkas and A. Horvath-Huck contributed equally to this work.

of the SC GM and WM with regard to both lesions and atrophy.⁷⁻⁹ Therefore, structural measures of the SC compartments can improve our understanding of SC pathology in MS and may contribute substantially to patient management in the future.

MR imaging is the principal tool for the evaluation of SC damage in research settings and clinical routine.¹⁰ However, accurate volumetric measurements of SCGM and SCWM have been challenging using “conventional” SC MR imaging. To that end, the averaged magnetization inversion recovery acquisitions (AMIRA) approach was suggested for morphometry-dedicated MR imaging of the cervical SC, which allows excellent SCGM/WM contrast in clinically feasible acquisition times of 51 seconds/slice.¹¹ Moreover, fully automatic segmentation methods using different approaches were able to reliably segment SCGM and WM in healthy subjects in the past few years.¹²⁻¹⁶ Most recently, multidimensional gated recurrent units (MDGRU) neural segmentation networks¹⁷ of SCGM/WM have demonstrated highly accurate and reproducible results in healthy cervical SC AMIRA images.¹⁸ However, an accurate and reproducible segmentation method in patients with MS is more challenging due to the presence of SC lesions.¹⁶

In this study, we developed a fully automated cervical SC compartment segmentation (SCORE) method for quantification of the SCGM (as well as its subdivisions: anterior/posterior horns and gray commissure), WM, and lesions in patients with MS and healthy controls (HCs). Our approach used MDGRU neural segmentation networks for postprocessing of AMIRA images. We then validated the reproducibility and accuracy of SCORE and did an explorative analysis of SC measurements in patients with MS.

MATERIALS AND METHODS

Subjects and MR Imaging Acquisition

Twenty-four patients with MS from an ongoing prospective multicenter cohort study¹⁹ (14 women; 15 relapsing-remitting, 6 secondary-progressive, and 3 primary-progressive MS cases; mean age, 41.2 [SD, 11.9] years; mean disease duration, 12.0 [SD, 8.6] years); and 24 sex- and age-matched HCs with no history of neurologic, psychiatric, or other medical disorders (15 women; mean age, 40.2 [SD, 10.8] years) were recruited from July 2017 until October 2018. The diagnosis of MS was made in accordance with the established criteria of an international panel,²⁰ and patients underwent a clinical examination including the Expanded Disability Status Scale (EDSS; median score, 2.25 [SD, 1.84]; relapsing-remitting MS, 1.5; progressive MS, 4.0, $P < .01$). Experimental procedures conformed to the Declaration of Helsinki, and the local ethics committee approved the study (EKNZ-BASEC 2016-01461). All participants signed an informed consent.

All participants were scanned in two 3T whole-body MR imaging systems: Cervical SC MR imaging was performed on a Magnetom Prisma (Siemens) system, whereas brain images were acquired on a Magnetom Skyra (Siemens) system (as part of the above-mentioned prospective multicenter cohort study¹⁹). HCs enrolled in this study were scanned 3 times in a test-retest fashion. The first 2 MR images were obtained back-to-back without repositioning to allow intrasession comparisons. The third scan was obtained after subject repositioning to allow intersession comparisons. Patients with MS underwent a single MR imaging scan.

In each scan, we acquired 12 axial AMIRA slices (FOV = 128 × 128 mm², slice thickness = 8 mm, 4-mm slice overlap, in-plane resolution = 0.67 × 0.67 mm², TE bSSFP = 2.14 ms, TR bSSFP = 5.13 ms, no signal averaging, acquisition time = 51 seconds per slice, total acquisition time = 10 minutes 12 seconds) over a 52-mm SC segment, extending approximately from the C2 to C5 vertebral level.^{11,16,18} The most rostrally acquired slice was placed with its lower surface adjacent to the most rostral surface of the C2/C3 intervertebral disc. For precise positioning of each individual slice and its orthogonal angulation to the course of the SC, a strongly T2-weighted TSE sequence with high contrast between CSF and SC was used as a reference. For each slice, the AMIRA approach acquired 8 images of considerably different tissue contrast among SCGM, WM, and CSF with effective TIs = 97.1, 158.7, 220.2, 281.8, 343.3, 404.9, 466.5, and 528.0 ms (Fig 1). Averaging of the first 5 images yielded MR images with an enhanced GM/WM contrast-to-noise ratio, whereas averaging of the last 3 images generated MR images with a high WM/CSF contrast-to-noise ratio.

The cervical SC protocol also included a TSE sequence and a high-resolution 3D MPRAGE sequence. Brain MR imaging protocol also included a high-resolution 3D MPRAGE sequence (Online Supplemental Data).

Postprocessing of MR Images

The SCORE method was developed as follows: Three experienced raters segmented the SC/CSF, SCGM/WM, as well as lesional/nonlesional SC tissue borders in all AMIRA slices of the HCs (only the first of 3 scans) and patients with MS. Interrater reproducibility of manual segmentations is shown in and the Online Supplemental Data. One rater also segmented all HC AMIRA slices to allow intrasession and intersession agreement comparisons between manual and automatic segmentations (Online Supplemental Data). A manual consensus from the 3 raters was reached using majority voting for each segmentation.

Subsequently, as proposed in a previous study,¹⁸ manual segmentations were used to train MDGRU neural segmentation networks for SCGM and WM as well as MS lesions. In short, MDGRU is a generalization of a bidirectional recurrent neural network that can process medical images in multiple dimensions. It achieves this task by treating each direction along each of the spatial dimensions independently as a temporal direction. MDGRU is fed by individual 2D AMIRA slices without stacks of consecutive slices. MDGRU processed each 2D image using 2 convolutional gated recurrent units for each image dimension, 1 in a forward and 1 in a backward direction, and then combined all individual results. The MDGRU framework offers on-the-fly data augmentation. A model diagram regarding network architecture as well as detailed analysis of MDGRU was published previously by Andermatt et al.¹⁷ Furthermore, the manual hyperparameter search for the MDGRU framework was described in detail in a previous conference article reporting a preliminary version of our method.¹⁸ All hyperparameters are used unchanged for all models in this work. Each MDGRU neural network was trained by the manual segmentations of a single rater.

To prevent “inverse crime,” we applied 3-fold cross-validation in the following manner: During training of MDGRU neural

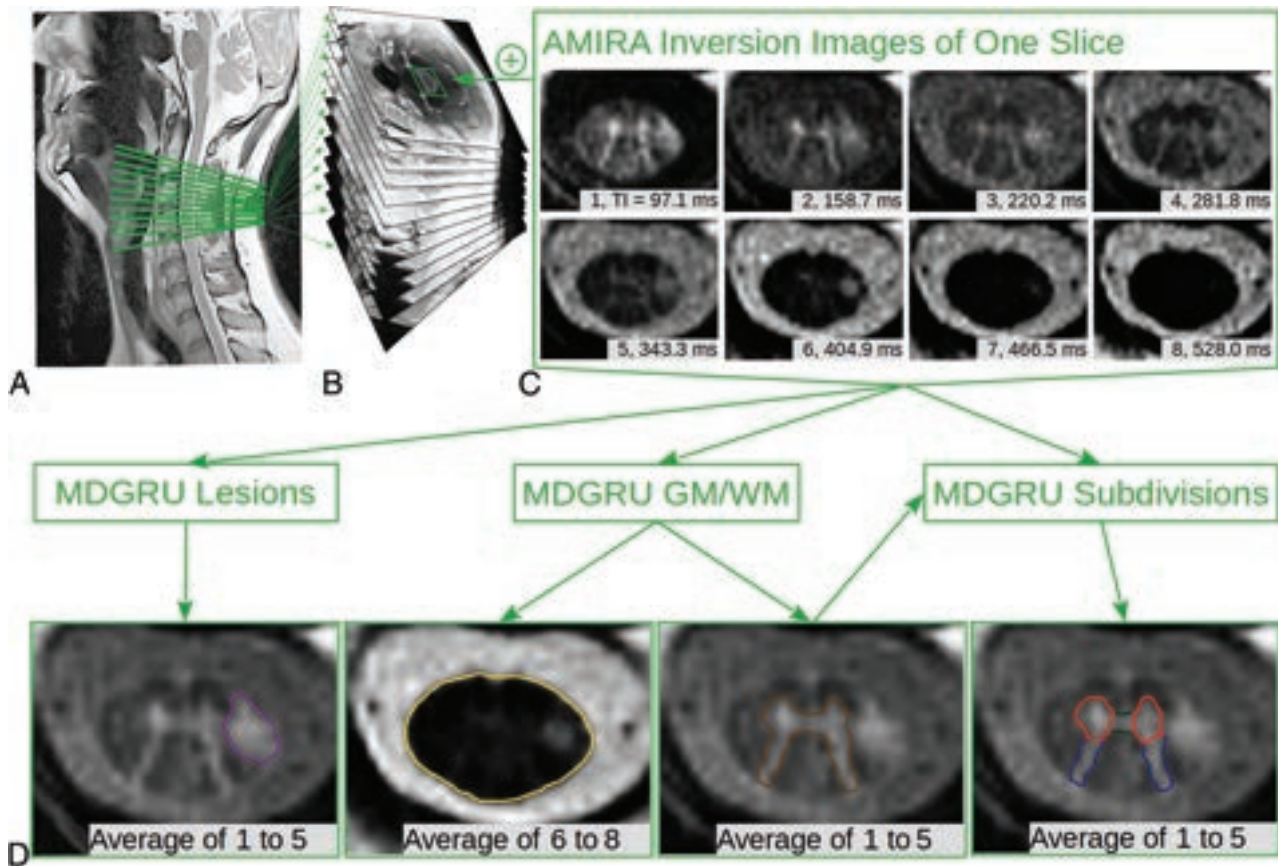


FIG 1. Schematic illustration of the automatic SCORE method using AMIRA images and subsequent segmentation of all SC compartments using MDGRU in HCs and patients with MS. *A*, Median slice of a TSE sequence with indications of the acquired AMIRA slices in green. *B*, Stack of AMIRA slices; each slice constitutes an average of all inversion images. *C*, AMIRA inversion images of 1 representative slice acquired at different inversion times. *D*, Different averages of selected inversion images. Manual segmentations were performed using the 1–5 AMIRA average for the SC GM/WM and MS lesion borders, and the 6–8 AMIRA average for the SC/CSF borders. These manual segmentations were used to train MDGRU neural networks for automatic segmentation of the SC/CSF borders (gold), SC GM/WM (dark brown), SCGM subdivisions (anterior horns, red; posterior horns, dark blue; gray commissure, dark green) and SC MS lesion borders (purple). MDGRU always used all 8 inversion images simultaneously without averaging.

networks for SC GM-WM as well as MS lesions, our manual segmentations were separated into 3 mutually disjoint subsets; then, two-thirds of our manual segmentations were used as training data sets, and the “left-out” one-third, as test data sets. For the networks trained on the HC data, all 3 acquisitions of each subject were used, but all 3 scans of each HC were used within only 1 subset. This process was repeated for each combination of subsets (3 times in total). By means of this method, AMIRA images from all patients with MS and HCs were automatically segmented once as “unseen” or independent test data sets, and no subject or slice of the test data set was ever used for the training of an MDGRU network during the entire development of SCORE. This process was performed separately for segmentations of each SC compartment, as well as separately for HCs and patients with MS. In the end, SC compartments in each AMIRA slice from all patients with MS and HCs were automatically segmented as test data sets 3 times, 1 for each trained neuronal network originating from each of the 3 raters performing manual segmentations. A validation step for tuning parameters was performed as described previously.¹⁸ Finally, a MDGRU consensus of these 3 segmentations was then reached

using majority voting (Fig 1), which was then used as the final SCORE segmentation.

In a second step, using the SCORE SCGM segmentations, one experienced rater delineated the borders of the spinal canal area as well as between the anterior horns (approximately laminae VI–IX), posterior horns (approximately laminae I–V), and gray commissure (approximately lamina X), as proposed before in manual delineations of the SCGM (Fig 1, right image in the lower row).^{21,22} Again, these manual segmentations (in combination with SCORE SCGM segmentations) were used to train neural segmentation networks with MDGRU in a 2-fold cross-validation fashion (Fig 1). The full code of MDGRU is available on <https://github.com/zubata88/mdgru> (Horvath et al¹⁸). No manual corrections of SCORE segmentations were performed. SCORE segmentations were visually inspected for quality, and segmentation failures were excluded from our analysis.

The estimated total intracranial volume (TIV) was extracted from brain MPRAGE image in an automatic fashion using the longitudinal stream in FreeSurfer (Version 6.0.0; <http://surfer.nmr.mgh.harvard.edu>) (Online Supplemental Data)²³ for further use as a normalization factor for SC measurements.

Statistical Analysis

Relative SDs (RSDs) (also known as coefficients of variation), Dice similarity coefficients (DSCs), and Hausdorff distances (HDs) were used for assessment of the intra- and intersession reproducibility in manual and SCORE consensus segmentations as well as accuracy (SCORE versus manual) (Online Supplemental Data). Because of non-normally distributed data, we performed a Tukey ladder of powers transformation in RSD, HD, and DSC values before further statistical analysis.

Comparisons between SCORE and manual reproducibility measures, between intra- and intersession measures, between SC compartments among the axial slice levels (1–12), and between accuracy measurements in HCs and patients with MS were investigated using multivariate analysis of variance with an additional Tukey post hoc analysis of variance, as well as with paired, 2-sided *t* tests corrected for multiple comparisons using the false discovery rate approach. Correlations between areas of SC compartments and TIV as well as spinal canal areas, age, and sex were investigated using linear mixed-effects regression models using 2 random intercepts to allow variance among slice levels and subjects. TIV, spinal canal areas, age, and sex were evaluated as normalization factors for measurements of SC compartments, as proposed in previous studies.^{24,25} The statistical formulas used for normalization are shown in the Online Supplemental Data. The normalization effect of a single or combination of normalization factors was evaluated by comparing the RSD of the raw and normalized values using the Feltz and Miller asymptotic test.²⁶ By means of linear mixed-effects regression models, differences between patients with MS and HCs were evaluated and corrected with multiple comparisons using the false discovery rate approach. Hierarchic multiple linear regression analysis was performed to investigate the associations between mean cross-sectional areas of cervical SC compartments (calculated using linear mixed-effects regression models) and the EDSS, using a backward elimination procedure.

RESULTS

Each scan was performed a total of 3 times for each HC and once for each patient with MS, and 12 slices were acquired per scan. Hence, in total, $3 \times 12 \times 24 = 864$ slices from 24 HCs and $12 \times 24 = 288$ slices from 24 patients with MS were acquired. Nine of 864 and 1/288 axial cervical SC slices acquired in HCs and patients with MS, respectively, were excluded from further analysis because of severe image artifacts. Subsequently, SCORE successfully segmented 96% (817/855) and 94% (271/287) of the remaining slices in HCs and patients with MS, respectively (Fig 2). In HCs, 4% of all SCORE segmentations (34/855) failed because of poor image quality (2/855) or contact of the cervical SC with the posterior vertebral arch (32/855), which reduced the contrast between the SC and the CSF. In patients with MS, 6% of all SCORE segmentations failed because of mild image artifacts (5%, 14/287) and misclassification of SC lesions (1%, 3/287) either as CSF or as SCGM (Online Supplemental Data.). These failed SCORE segmentations involved images of 5/24 (21%) HCs and 4/24 patients with MS (17%) included in our study. Failed SCORE segmentations were excluded from further statistical analysis. Reproducibility and accuracy

measurements including SCORE segmentation failures are shown in the Online Supplemental Data.

Reproducibility

Individual intra- and intersession reproducibility measurements of SCORE and manual segmentations as well as comparisons between the 2 approaches and also between intra- and intersession reproducibility in HCs are displayed in Fig 3 and the Online Supplemental Data.

In HCs, both intra- and intersession reproducibility of SCORE segmentations was high in all SC compartments except for the gray commissure (all mean RSD $\leq 5.54\%$, DSC ≥ 0.87 , HD ≤ 0.60 mm). Reproducibility of SCORE segmentations was higher compared with manual segmentations (all, $P < .001$). Both intra- and intersession reproducibility generally increased in the following order: gray commissure < posterior horns < anterior horns \sim GM < WM < total SC, as measured by RSD and DSC (all, $P < .001$). Intra- and intersession reproducibility also slightly decreased in more caudally acquired SC slices (all, $P < .001$).

In SCORE segmentations, intersession reproducibility was slightly lower compared with intrasession reproducibility in all SC compartments except for the anterior horns (total SC and GM, $P < .001$; gray commissure, $P < .01$; WM and posterior horns, $P < .05$).

Accuracy

Individual accuracy measurements of SCORE compared with manual segmentations in HCs and patients with MS, comparisons between patients with MS and HCs, and comparisons between normal-appearing and total SC compartments are shown in the Online Supplemental Data and Fig 4. Most analyzed AMIRA slices in patients with MS (198 of 271; 73%) demonstrated SC lesions. No lesions were found in any analyzed AMIRA slices in a total of 3/24 patients with MS (13%). Examples of MS lesion SCORE segmentations are shown in the Online Supplemental Data.

In HCs and patients with MS, the accuracy of SCORE compared with manual segmentations was high in all SC compartments except for the gray commissure and lesions (HCs/patients with MS: all, mean DSC $\geq 0.89/0.85$, HD $\leq 0.56/1.12$ mm, RSD $\leq 6.29\%/11.09\%$, respectively). Accuracy was slightly lower in patients with MS compared with HCs in all homologous SC compartments except for the total SC and the normal-appearing posterior horns (total posterior horns, $P < .01$; all other comparisons, $P < .001$). In addition, the accuracy of SCORE compared with manual segmentations varied between SC compartments. In HCs, accuracy generally increased in the following order: GM < WM < total SC (all, $P < .001$). In patients with MS, accuracy generally increased in the following order: lesions < GM < WM \sim total SC (all, $P < .001$). Because the borders between SCGM subdivisions were delineated on SCORE SCGM segmentations, comparisons between these SC compartments were evaluated separately. Accuracy in the SCGM subdivisions of HCs generally increased in the following order: gray commissure < posterior horns \sim anterior horns (all, $P < .001$), and in MS in the following order: gray commissure < posterior horns < anterior horns (all, $P < .001$, except for posterior-versus anterior horns, $P < .01$). Moreover, in

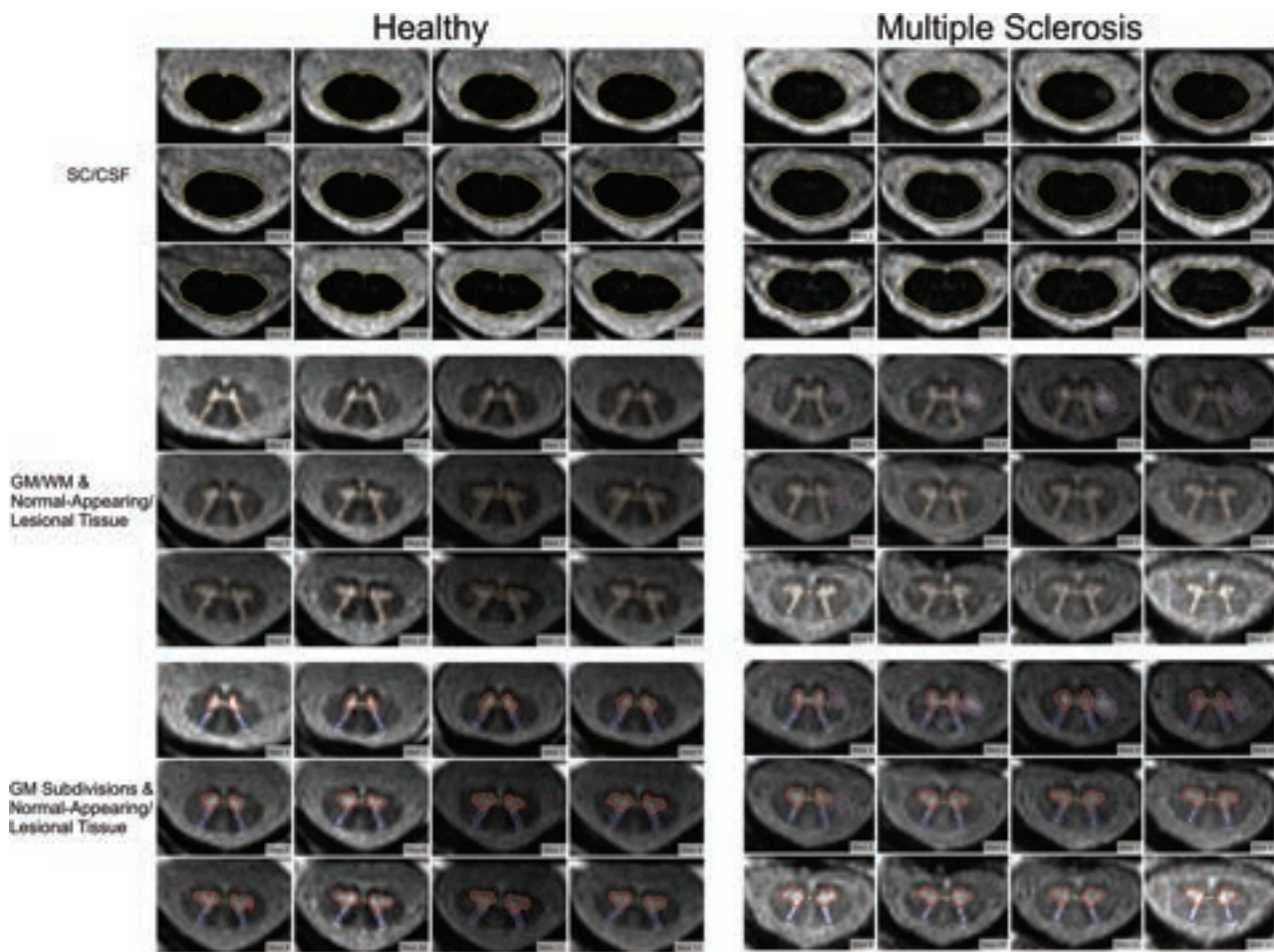


FIG 2. Cross-sectional areas of all SC compartments in HCs and patients with MS. Representative SCORE segmentations of all AMIRA slices acquired in one HC and one patient with MS. The SC/CSF borders are depicted in gold; the SC GM/WM borders, in dark brown; the anterior horn borders, in red; the posterior horn borders, in dark blue; the gray commissure borders, in dark green; and the lesion borders, in purple.

both HCs and patients with MS, accuracy also slightly decreased in more caudally acquired SC slices (both, $P < .001$).

Furthermore, in patients with MS, accuracy was similar for normal-appearing and total areas of all SC compartments, except for lower accuracy in the normal-appearing WM compared with total WM ($P < .01$). Accuracy also decreased in patients with MS, with higher EDSS scores ($P < .001$, Online Supplemental Data). Finally, accuracy was similar in patients with relapsing-remitting and progressive MS, except for the total GM (higher in relapsing-remitting) and normal-appearing posterior horns (higher in progressive MS, $P < .001$) (Online Supplemental Data).

Areas of SC Compartments and Normalization Strategies

SCORE versus Manual Segmentations. Areas of SC compartments as measured by SCORE and manual segmentations as well as comparisons between the 2 approaches in HCs and patients with MS are shown in the Online Supplemental Data. Compared with manual segmentations, SCORE slightly overestimated normal-appearing SCGM areas as well as normal-appearing and total anterior horn areas and underestimated normal-appearing as well as total posterior horn areas, normal-appearing gray commissure areas, and lesion areas in patients with MS (all, $P < .001$).

No other significant differences between manual and SCORE segmentations were found in HCs and patients with MS.

Patients with MS versus HCs. In view of the results of the normalization analysis (Online Supplemental Data), total SC and WM areas were normalized using TIV. After multiple-comparison correction, patients with MS had measures lower than controls in total SC ($P < .05$), total WM ($P < .001$ and $P < .05$), and the total anterior horn ($P < .01$) (Online Supplemental Data). Total GM areas and total gray commissure areas were similar between groups. Patients with progressive MS had lower total GM and anterior horn areas compared with those with relapsing-remitting MS ($P < .05$), but areas of all other SC compartments were similar between these groups (Online Supplemental Data).

Correlation with Clinical Outcomes

Lower total WM and larger lesion areas were the most significant independent predictors of higher EDSS scores in a multivariate analysis ($\beta_{wm} = -0.38$, $\beta_{lesion} = 0.40$). Together with disease duration and disease type as covariates, the final model accounted for 81% of the EDSS variance.

Intra- and Intersession Reproducibility

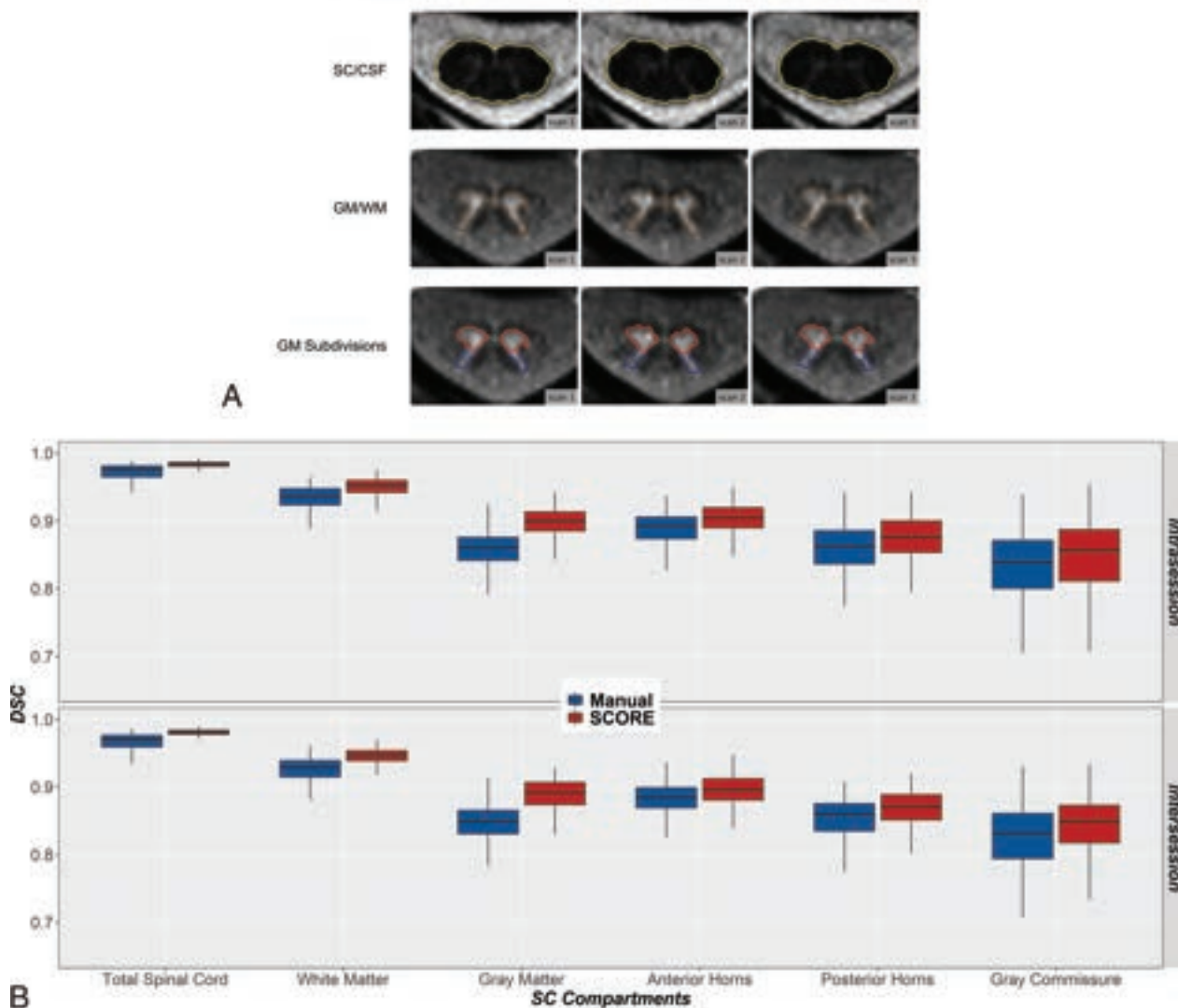


FIG 3. Reproducibility of SCORE and manual segmentations in all SC compartments of HCs. **A**, Representative SCORE segmentations of respective AMIRA slices acquired in a scan-rescan fashion on a single HC. The SC/CSF borders (gold) are shown on the average of the last 3 TI AMIRA images of each slice, whereas the SC GM/WM (dark brown) and SC GM subdivision borders (anterior horns, red; posterior horns, dark blue; gray commissure, dark green) are shown on the average of the first 5 TI AMIRA images. The first 2 MR images were obtained back-to-back without repositioning to allow intrasession comparisons. The third scan was obtained after patient repositioning to allow intersession comparisons. Note the high agreement of SCORE segmentations between scans. Intra- and intersession reproducibility of manual (blue) and SCORE (red) was measured by DSC (**B**).

DISCUSSION

In this work, we propose a novel method, called SCORE, for fully automatic quantification of cervical SC compartments in HCs and patients with MS, combining the exquisite properties of the AMIRA sequence to image the spinal cord and MDGRU neural networks to segment GM/WM and MS lesions. We show that this method is capable of accurate quantification of both the normal-appearing and lesional SCWM and GM as well of the different regions of the SCGM in MS. Moreover, we evaluated demographic and skull- and spine-derived metrics that could be used in normalization strategies to reduce intersubject variability in cervical SC cross-sectional measures and then applied the best normalization strategy to compare cervical SC compartments between patients with MS and HCs.

The 2D AMIRA sequence provides a unique contrast as well as low motion and flow sensitivity in 51 seconds/slice.^{11,16} In fact, only <1% of the slices in this study were discarded due to motion artifacts, and generally, the scans were well-tolerated, even by patients with MS with serious disability. Previously, we had also shown that it was possible to provide reliable and reproducible segmentations of the SC GM and WM using MDGRU in healthy subjects.¹⁸

Our method demonstrated high reproducibility and accuracy in HC data (Online Supplemental Data). Intra- and intersession reproducibility in HC data was markedly higher in SCORE compared with a reference of 3 expert manual segmentations. Moreover, the new framework increased the quantification reproducibility by approximately 50% in HCs compared with a previous approach using a different segmentation method.¹⁶ SCORE

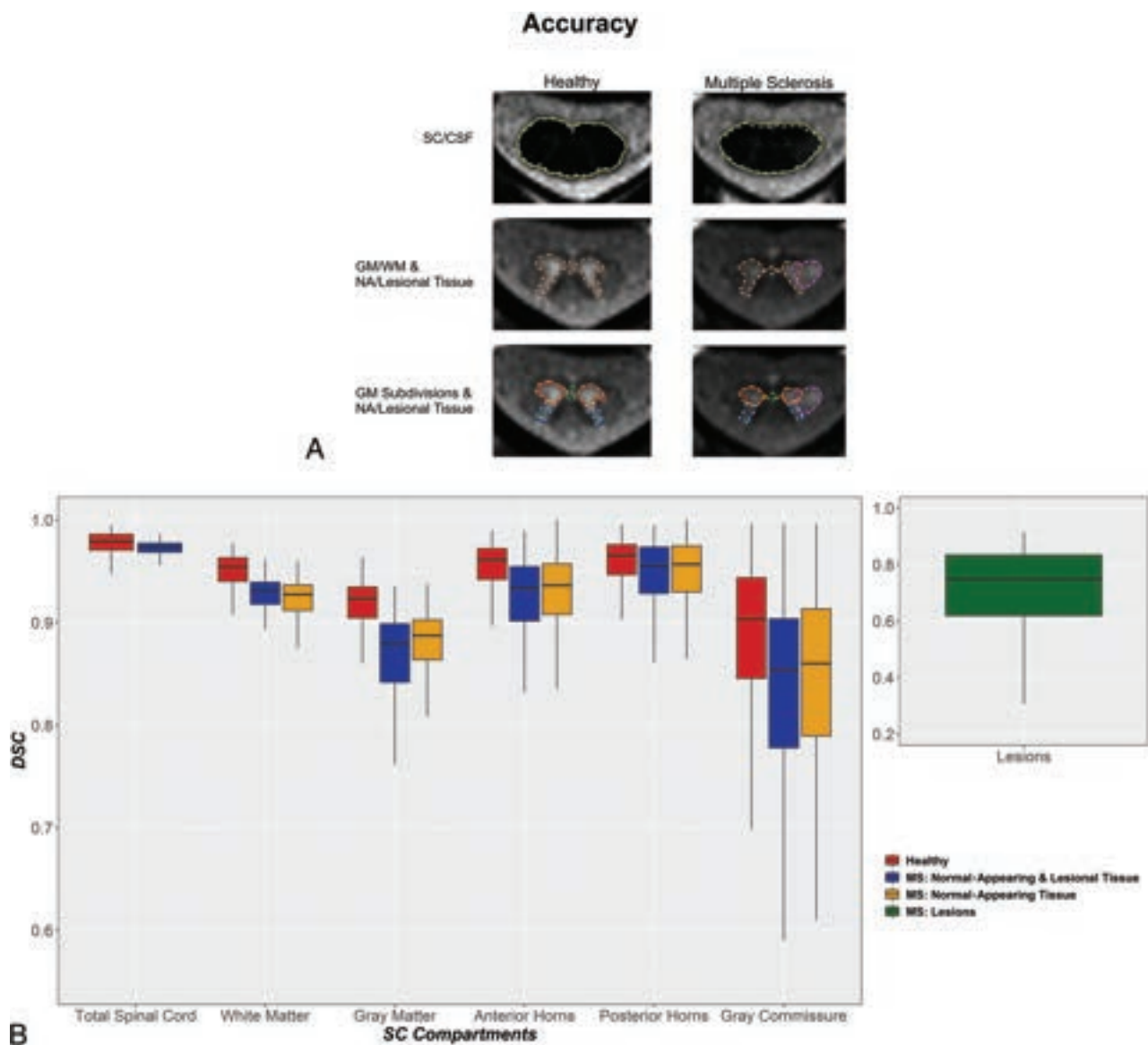


FIG 4. Accuracy of SCORE versus manual segmentations in all SC compartments of HCs and patients with MS. **A**, Representative SCORE and manual segmentations of AMIRA slices acquired in 1 HC and 1 patient with MS. The SC/CSF borders of manual and SCORE segmentations are shown in aqua (*dashed line*) and gold, respectively. The SC GM/WM borders of manual and SCORE segmentations are shown in coral (*dashed line*) and dark brown, respectively. The SC anterior horns, posterior horns, and gray commissure of manual and SCORE segmentations are shown in orange, turquoise, lime (*dashed lines*), red, navy blue, and dark green, respectively. Finally, the lesion borders of manual and SCORE segmentations are shown in violet (*dashed line*) and dark purple, respectively. Note the high agreement between manual and SCORE segmentations. The accuracy of SCORE versus manual segmentations was measured by DSC (**B**) and was generally high. Healthy, normal-appearing and lesional tissue and normal-appearing tissue are shown separately for each SC compartment in red, blue, and yellow, respectively. SC MS lesions are shown separately in green. Note the high accuracy of SCORE compared with manual segmentations in all SC compartments except for the gray commissure and lesions in both HCs and patients with MS.

segmentations showed slightly better intra- than intersession reproducibility for most spinal cord compartments. This finding points to a marginal effect of patient repositioning in the MR imaging scanner on our measurements, also possibly related to our 2D imaging approach. However, because both intra- and intersession reproducibility was high in all SC compartments, our pipeline for quantification of SC compartments is promising for longitudinal measurements in both research settings and clinical routine. Pitfalls such as misclassification of lesions as CSF did not occur, as was the case in the past.¹⁶ Furthermore, the current

algorithm demonstrated slightly higher intra- and intersession reproducibility as well as accuracy in HC data (eg, mean DSC in total SC: 0.98 versus 0.95; WM: 0.95 versus 0.90; GM: 0.92 versus 0.86) compared with a preliminary algorithm version applied in the same HC MR imaging data,¹⁸ possibly due to the addition of further raters for training of MDGRU neural networks.

A head-to-head comparison of previously published methods with ours using the same data set is currently not possible due to technical limitations. However, considering the raw numbers, our method showed higher intersession reproducibility in HCs

(eg, RSD for SCGM in Prados et al¹² = 7.4% [SD, 4.9%], currently proposed = 3.50% [SD, 2.61%]; intraclass correlation coefficient in Datta et al¹³ = 0.88, currently proposed = 0.89, not shown in the analysis). In addition, accuracy was quite high when SCORE segmentations were compared with the manual agreement by 3 experienced raters. Indeed, our method showed higher accuracy compared with the established iterative nonlocal simultaneous truth and performance level estimation (STAPLE) algorithm by Asman et al,²⁷ even with additional “tuning” of this algorithm to our HC AMIRA data, as shown previously.²⁸ Furthermore, preliminary work using MDGRU¹⁸ already showed remarkable accuracy in HCs when tested on a different cohort (40 training data sets and 40 test data sets acquired at 4 different sites) and compared with 8 methods for in vivo quantification of SCGM including the 6 methods used in a recent SCGM segmentation challenge.^{18,29-31} In addition, the current version of our automatic segmentation method shows higher accuracy in HCs, though tested in a different data set and with a different imaging approach (eg, Perone et al,²⁹ currently integrated in the Spinal Cord Toolbox (<https://spinalcordtoolbox.com/>), for SCGM in HCs: mean DSC = 0.85 [SD, 0.04], mean HD = 2.61 [SD, 2.15] mm; currently proposed: mean DSC = 0.92 [SD, 0.03], mean 0.53 [SD, 0.32] mm. Finally, our current method also demonstrated accuracy results comparable with those of a recent study evaluating the accuracy of SCGM segmentations using the deep, dilated convolutions approach of Perone et al on an ex vivo acquired image data set.²⁹ However, these comparisons should be considered with caution due to differences in the data sets, the number of participants, MR imaging sequences, MR imaging scanners, and study design included in these studies.

Regarding the performance of SCORE in cervical SC images of patients with MS, accuracy was high in all SC compartments despite the fact that the presence of lesions, the atrophic involution of GM and WM tissues, as well as difficulties to sustain prolonged scans could be challenging aspects for SC segmentation in patients with MS (Online Supplemental Data). In addition, SCORE demonstrated higher accuracy than a previously proposed fully automatic segmentation algorithm applied in patients with MS, though in a different patient cohort with a different imaging approach (Prados et al¹² for SCGM in patients with clinically definite MS: mean DSC = 0.74–0.79, mean HD = 1.61–1.44 mm; currently proposed mean DSC = 0.84, mean HD = 0.89 mm). However, agreement with manual segmentations was lower compared with that of HCs. The reason for this finding probably lies, at least in part, in the presence of SC lesions affecting both the SCGM and WM, diminishing the contrast between the 2 SC compartments and posing additional challenges for exact delineation of SCGM and WM. Moreover, the GM/WM contrast reduction in lesions led to lower precision and higher variability of the manual segmentations, which were then used for subsequent algorithm training; this issue also possibly contributed to a worse SCORE performance in lesions. Another explanation for this reduction of accuracy in patients with MS compared with HCs is the smaller slice number used to train MDGRU neural segmentation networks in patients with MS because data from 3 MR imaging scans (acquired back-to-back for reproducibility measurements) were available in HCs, whereas a single scan was

used in patients with MS. This notion is also supported by the fact that the accuracy of spinal canal area SCORE segmentations was also lower in patients with MS compared with HCs.

SCORE segmentations of cervical SC lesions demonstrate significantly lower accuracy compared with other SC compartments with a mean DSC of 0.69, and they underestimated SC lesion areas compared with manual segmentations. However, these results show higher accuracy compared with a recently developed automated SC lesion-segmentation approach based on a sequence of 2 convolutional neural networks using T2-weighted and T2*-weighted SC images of patients with MS, which reached a median DSC of 0.60, albeit on another patient cohort.³² These findings should also be seen in the light of the big interrater variability in manual segmentations of SC lesions, as previously reported.³²

In previous MR imaging and histopathologic studies, controversial results were shown with regard to whether GM and/or WM atrophy drives SC volume loss in MS.^{7-9,33} Our patients with MS showed a similar reduction in SCWM and GM (10% and 8%, respectively) compared with HCs. Besides, both normal-appearing as well as total SCWM and anterior horn areas were found to be reduced in patients with MS. This finding indicates neuronal injury that is, at least partially, not related to focal SC lesions and possibly reflects the aftermath of a distinct neurodegenerative pathomechanism. Most surprising, patients with MS had lower anterior horn (14% reduction) but similar posterior horn areas compared with HCs, especially at the cervical SC enlargement (Fig 2 and Online Supplemental Data), a result that is in line with a previous pathologic study demonstrating loss of interneurons and lower motor neurons in the normal-appearing and lesional anterior horns.³⁴ Future studies should further investigate the origin of this finding. However, in our small MS cohort, smaller SCWM areas and larger SC lesions were the most important independent predictors of more neurologic deficits. Although SC lesions are a well-established correlate of physical disability in MS,^{7,35,36} the greater importance of SCWM, and not GM, contradicts findings of previous studies in this field.^{7,9,33} However, this contradiction may be caused by the small sample size of the present MS cohort. Nevertheless, from the neuroanatomic standpoint, the correlation between SCWM atrophy and clinical disability is most probably related to demyelination and axonal loss occurring in WM tracts related to sensorimotor functions.

Some limitations of our study should be mentioned. Reproducibility was assessed only in HCs and not in patients with MS because of the burden of repetitive spinal cord MR imaging on our patients. Moreover, SCORE was trained in a relatively small number of participants. However, in total, 1088 slices were analyzed for algorithm development, whereas the 3-fold cross-validation during the development of SCORE should have increased the robustness of the method. In addition, SCORE is currently capable of reliably segmenting only AMIRA images of the cervical SC. Due to the distinct shape of the SCGM in different regions of the SC (eg, cervical versus thoracic), SCORE might not perform with the same reproducibility and accuracy demonstrated in the current work. Hence, for segmentation of other SC regions, separate MDGRU neural networks should be trained and validated. Moreover, our results concerning differences between patients with MS and HCs in areas of SC compartments

should be considered with caution because of our small sample size. To that end, further larger cross-sectional and longitudinal analyses are required to confirm the presented findings. The current study did not include a direct comparison between our segmentation method and other established segmentation algorithms (eg, the Spinal Cord Toolbox¹⁵) because this would require training of separate neural networks of other algorithms in our AMIRA data set. However, the comparison of a previous version of our SC segmentation algorithm with multiple other approaches on an independent imaging data set of HCs (including images originating from different imaging protocols with different FOVs, size, and resolution) indicated a remarkable performance of MDGRU neural networks.¹⁸ In addition, our patients were recruited at a single institution and imaged on a single scanner, which may limit the generalizability of our results. Thus, a comparison of different segmentation algorithms on a common multi-centric MR imaging data set of patients with MS including different imaging techniques should be considered in the future. Finally, AMIRA is currently not fully available in clinical routine, limiting the use of the proposed quantification method to research settings for now.

CONCLUSIONS

In this work, we demonstrate a novel, reliable quantification method in patients with MS and HCs for SC GM and WM, as well as for subdivisions of the SCGM and MS lesions. This method will allow future investigation of SC compartments in a number of neurologic disorders, including MS, in both research and clinical settings. As motivation for future scientific effort on this matter, our patients with MS were found to have reduced areas in specific SC compartments, which may be used as imaging biomarkers in this disease.

ACKNOWLEDGMENTS

We would like to thank all participants of our study as well as all medical and nonmedical staff of the Neurology Department at the University Hospital Basel for assistance during subject recruitment.

Disclosure forms provided by the authors are available with the full text and PDF of this article at www.ajnr.org.

REFERENCES

- Ginsberg L. Disorders of the spinal cord and roots. *Pract Neurol* 2011;11:259–67 CrossRef Medline
- Amukotuwa SA, Cook MJ. Spinal disease: neoplastic, degenerative, and infective spinal cord diseases and spinal cord compression. In: Schapira AHV, Byrne E, DiMauro S, et al, eds. *Neurology and Clinical Neuroscience*. Mosby; 2007:511–38
- Bot JC, Barkhof F, Polman CH, et al. Spinal cord abnormalities in recently diagnosed patients with MS: added value of spinal MRI examination. *Neurology* 2004;62:226–33 CrossRef Medline
- Weier K, Beck A, Magon S, et al. Evaluation of a new approach for semi-automatic segmentation of the cerebellum in patients with multiple sclerosis. *J Neurol* 2012;259:2673–80 CrossRef Medline
- Tsagkas C, Magon S, Gaetano L, et al. Spinal cord volume loss: a marker of disease progression in multiple sclerosis. *Neurology* 2018;91:e349–58 CrossRef Medline
- Tsagkas C, Magon S, Gaetano L, et al. Preferential spinal cord volume loss in primary progressive multiple sclerosis. *Mult Scler* 2019;25:947–57 CrossRef Medline
- Bonacchi R, Pagani E, Meani A, et al. Clinical relevance of multi-parametric MRI assessment of cervical cord damage in multiple sclerosis. *Radiology* 2020;296:605–15 CrossRef Medline
- Petrova N, Carassiti D, Altmann DR, et al. Axonal loss in the multiple sclerosis spinal cord revisited. *Brain Pathol* 2018;28:334–48 CrossRef Medline
- Schlaeger R, Papinutto N, Panara V, et al. Spinal cord gray matter atrophy correlates with multiple sclerosis disability. *Ann Neurol* 2014;76:568–80 CrossRef Medline
- Wheeler-Kingshott CA, Stroman PW, Schwab JM, et al. The current state-of-the-art of spinal cord imaging: applications. *Neuroimage* 2014;84:1082–93 CrossRef Medline
- Weigel M, Bieri O. Spinal cord imaging using averaged magnetization inversion recovery acquisitions. *Magn Reson Med* 2018;79:1870–81 CrossRef Medline
- Prados F, Cardoso MJ, Yiannakas MC, et al. Fully automated grey and white matter spinal cord segmentation. *Sci Rep* 2016;6:36151 CrossRef Medline
- Datta E, Papinutto N, Schlaeger R, et al. Gray matter segmentation of the spinal cord with active contours in MR images. *Neuroimage* 2017;147:788–99 CrossRef Medline
- Dupont SM, De Leener B, Taso M, et al. Fully-integrated framework for the segmentation and registration of the spinal cord white and gray matter. *Neuroimage* 2017;150:358–72 CrossRef Medline
- De Leener B, Lévy S, Dupont SM, et al. SCT: Spinal Cord Toolbox, an open-source software for processing spinal cord MRI data. *Neuroimage* 2017;145:24–43 CrossRef Medline
- Tsagkas C, Horvath A, Altermatt A, et al. Automatic spinal cord gray matter quantification: a novel approach. *AJNR Am J Neuroradiol* 2019;40:1592–600 CrossRef Medline
- Andermatt S, Pezold S, Cattin P, et al. Multi-dimensional gated recurrent units for the segmentation of biomedical 3D-data. In: Carneiro G, Mateus D, Peter L, eds. *Deep Learning and Data Labeling for Medical Applications. Lecture Notes in Computer Science*. Springer-Verlag International Publishing; 2016:142–51
- Horvath A, Tsagkas C, Andermatt S, et al. *Spinal Cord Gray Matter-White Matter Segmentation on Magnetic Resonance AMIRA Images with MD-GRU*. Vol 11397. Springer-Verlag; 2019
- Disanto G, Benkert P, Lorscheider J; et al; SMSC Scientific Board. The Swiss Multiple Sclerosis Cohort-Study (SMSC): a prospective Swiss wide investigation of key phases in disease evolution and new treatment options. *PLoS One* 2016;11:e0152347 CrossRef Medline
- Thompson AJ, Banwell BL, Barkhof F, et al. Diagnosis of multiple sclerosis: 2017 revisions of the McDonald criteria. *Lancet Neurol* 2018;17:162–73 CrossRef Medline
- Grabher P, Mohammadi S, David G, et al. Neurodegeneration in the spinal ventral horn prior to motor impairment in cervical spondylotic myelopathy. *J Neurotrauma* 2017;34:2329–34 CrossRef Medline
- Huber E, David G, Thompson AJ, et al. Dorsal and ventral horn atrophy is associated with clinical outcome after spinal cord injury. *Neurology* 2018;90:e1510–22 CrossRef Medline
- Reuter M, Schmansky NJ, Rosas HD, et al. Within-subject template estimation for unbiased longitudinal image analysis. *Neuroimage* 2012;61:1402–18 CrossRef Medline
- Papinutto N, Asteggiano C, Bischof A, et al. Intersubject variability and normalization strategies for spinal cord total cross-sectional and gray matter areas. *J Neuroimaging* 2020;30:110–18 CrossRef Medline
- Papinutto N, Schlaeger R, Panara V, et al. Age, gender and normalization covariates for spinal cord gray matter and total cross-sectional areas at cervical and thoracic levels: a 2D phase sensitive inversion recovery imaging study. *PLoS One* 2015;10:e0118576 CrossRef Medline

26. Feltz CJ, Miller GE. **An asymptotic test for the equality of coefficients of variation from k populations.** *Stat Med* 1996;15:647–58 CrossRef Medline
27. Asman AJ, Smith SA, Reich DS, et al. **Robust GM/WM segmentation of the spinal cord with iterative non-local statistical fusion.** *Med Image Comput Comput Assist Interv* 2013;16(Pt 1):759–67 CrossRef Medline
28. Tsagkas C, Horvath A, Altermatt A, et al. **Automatic spinal cord gray matter quantification: a novel approach.** *AJNR Am J Neuroradiol* 2019;40:1592–1600 CrossRef Medline
29. Perone CS, Calabrese E, Cohen-Adad J. **Spinal cord gray matter segmentation using deep dilated convolutions.** *Sci Rep* 2018;8:5966 CrossRef Medline
30. Prados F, Ashburner J, Blaiotta C, et al. **Spinal cord gray matter segmentation challenge.** *Neuroimage* 2017;152:312–29 CrossRef Medline
31. Porisky A, Brosch T, Ljungberg E, et al; **Gray matter segmentation in spinal cord MRIs via 3D convolutional encoder networks with shortcut connections.** In: Cardoso MJ, Arbel T, Carneiro G, et al. eds. *Deep Learning in Medical Image Analysis and Multimodal Learning for Clinical Decision Support.* Springer-Verlag International Publishing; 2017:330–337
32. Gros C, De Leener B, Badji A, et al. **Automatic segmentation of the spinal cord and intramedullary multiple sclerosis lesions with convolutional neural networks.** *Neuroimage* 2019;184:901–15 CrossRef Medline
33. Schlaeger R, Papinutto N, Zhu AH, et al. **Association between thoracic spinal cord gray matter atrophy and disability in multiple sclerosis.** *JAMA Neurol* 2015;72:897–904 CrossRef Medline
34. Gilmore CP, DeLuca GC, Bö L, et al. **Spinal cord neuronal pathology in multiple sclerosis.** *Brain Pathol* 2009;19:642–49 CrossRef Medline
35. Lukas C, Sombekke MH, Bellenberg B, et al. **Relevance of spinal cord abnormalities to clinical disability in multiple sclerosis: MR imaging findings in a large cohort of patients.** *Radiology* 2013;269:542–52 CrossRef Medline
36. Brownlee WJ, Altmann DR, Mota PAD, et al. **Association of asymptomatic spinal cord lesions and atrophy with disability 5 years after a clinically isolated syndrome.** *Mult Scler* 2017;23:665–74 CrossRef Medline

Patterns of Intrathecal Ossification in Arachnoiditis Ossificans: A Retrospective Case Series

B. Thejeel, C.S. Geannette, M. Roytman, D.J. Pisapia, J.L. Chazen, and S.T. Jawetz



ABSTRACT

SUMMARY: Arachnoiditis ossificans is an uncommon end-stage appearance of chronic adhesive arachnoiditis. Imaging features of arachnoiditis ossificans are characteristic and should be diagnosed to avoid unnecessary intervention and guide prognosis and management. In this case series, we retrospectively analyzed CT and MR imaging of 41 patients to identify common patterns of intrathecal ossification and present the common etiologies. Thirty-two patients had a confirmed history of spinal instrumentation, 7 were discovered on imaging without prior surgical history, 1 had a history of ankylosing spondylitis, and 1 had trauma. The most frequent site of ossification was at the conus and cauda equina. Four patterns of ossification were identified, including central, nerve root encasing, weblike, and peripheral. Arachnoiditis ossificans is an important, likely under-recognized consideration in patients who present with back pain. Diagnosis can be made readily on CT; MR imaging diagnosis is also possible but may be challenging.

ABBREVIATION: AO = arachnoiditis ossificans

Chronic adhesive arachnoiditis is a spectrum of entities of varying severity and assorted imaging appearances. This pathologic entity involves the arachnoid mater layer of the meninges, which is often inconspicuous on cross-sectional imaging and becomes apparent in diseased states.¹ Chronic adhesive arachnoiditis predominates as thickening and scarring of the arachnoid and pial surfaces and can also involve the nerve roots. The typical features of chronic adhesive arachnoiditis include nerve root thickening, nerve root clumping, nerve root peripheralization (empty thecal sac), intradural soft-tissue masses, and thecal sac deformity, all of which can be visualized on MR imaging.^{2,3} Chronic adhesive arachnoiditis is not associated with a specific etiology but rather can be seen following surgery, infection, inflammation, and/or trauma.^{2,4} Some case reports have even demonstrated findings after intrathecal administration of medications such as contrast or chemotherapy.^{5,6}

Arachnoiditis ossificans (AO) is an infrequent pathologic entity that appears on the spectrum of chronic adhesive arachnoiditis, often as the end-stage disease process.^{2,7} In 1982, Barthelemy⁸

published the first case of AO diagnosed on CT. Before this, AO was often suspected radiologically; however, it was only diagnosed surgically or at postmortem examination. Since that time, CT of the spine has allowed greater diagnosis of AO, with the largest case series documenting 5 patients.³ The underlying histopathology in AO is thought to be osseous metaplasia in the setting of chronic arachnoid inflammation leading to intrathecal ossification.^{9,10} However, despite chronic adhesive arachnoiditis being easily seen on MR imaging, arachnoid ossification can be inconspicuous and may, therefore, be overlooked or misdiagnosed. Although AO is a rare entity, it is likely more widespread than previously thought. CT is considered a more accurate imaging technique for AO because it can more accurately distinguish intrathecal AO from the overarching diagnosis of chronic adhesive arachnoiditis.^{3,11}

The aim of this work was to identify patterns of ossification on CT that are characteristic of AO and can assist radiologists in making the correct diagnosis.

CASE SERIES

Institutional ethics review board at the Hospital for Special Surgery and Weill Cornell University-New York Presbyterian Hospital approval was obtained for this retrospective case series from an orthopedic surgical hospital as well as a tertiary trauma center for imaging studies performed between January 1, 2000, and July 1, 2021. Cases were acquired through a search of an institutional PACS, identifying patients with the diagnosis of AO on either CT or MR imaging with histopathologic confirmation.

Received October 27, 2022; accepted after revision December 19.

From the Department of Radiology and Diagnostic Imaging (B.T.), University of Alberta, Edmonton, Alberta, Canada; Department of Radiology and Imaging (C.S.G., J.L.C., S.T.J.), Hospital for Special Surgery, New York, New York; Department of Radiology (M.R.), New York-Presbyterian Hospital, Weill Cornell Medicine, New York, New York; and Department of Pathology and Laboratory Medicine (D.J.P.), Weill Cornell Medicine, New York, New York.

Please address correspondence to Shari T. Jawetz, MD, Department of Radiology and Imaging, Hospital for Special Surgery, 535E 70th St, New York, New York; e-mail: jawetzsh@hss.edu

<http://dx.doi.org/10.3174/ajnr.A7764>

Table 1: CT protocol used in spine imaging of the 41 patients included in the case series

CT Protocol	
kV(peak)	120
mAs	AutomA and SmartmAs with maximum dose 400 mA
Section thickness	0.625-mm section thickness, Bone Plus Algorithm
Reformations	Multiplanar reformations, 2-mm reformats in sagittal and coronal planes and to disc levels and in soft-tissue windows

Table 2: MR imaging protocol used in spine imaging of the 41 patients included in the case series

	2D Sagittal T2	2D Coronal T2	2D Axial T2	2D Sagittal T1	2D Sagittal T2 FLEX
TR (ms)	3500	4000	3500	620	5500
TE (ms)	110	104	110	10	110
Flip angle	180°	90°	180°	90°	142°
FOV (mm ²)	260	280	280	280	260
Matrix	512 × 256	512 × 256	416 × 224	512 × 256	416 × 224
NEX	1.5	1	1.5	1	1
Receiver bandwidth (MHz)	±83.33	±195.31	±83.33	±195.31	±244.14
Section thickness (mm)	3.5	3.5	3.5	3.5	3.5
Echo-train length	14	12	12	3	16
Acquisition time (min)	3–4	3–4	4–5	3–4	3–4

Note:— FLEX indicates 2-point Dixon fat-suppression.

Table 3: Demographics and characteristics of 41 patients with confirmed diagnosis of AO

Demographics and Characteristics	
Total patients	41
Age (yr)	63 (SD, 18.8); range, 16–92
Etiology	
Postsurgical	32
Idiopathic	7
Inflammatory	1
Posttraumatic	1
Sex	
Male	18
Female	23
Location	
Lumbar spine	36
Thoracic spine	5
Follow-up duration	3.9 (SD 3.7) years; range, 8 months to 14 years
No follow-up	18 patients
Patients with MR imaging correlation	25

The search yielded the following unique cases: 50 of AO, 383 of chronic arachnoiditis, 7 of intrathecal ossification, and 3 of intrathecal calcification. Cases without CT or pathologic confirmation were excluded. The electronic medical record was reviewed to collect data on patient demographics. Prior relevant surgical and medical history was acquired, including history of trauma, central nervous system infection, and inflammatory disease.

MR imaging was performed on a 1.5T unit (Optima MR450w, Discovery MR450, Signa HDxt; GE Healthcare) and on a 3T unit (Signa Premier; GE Healthcare). CT was performed using a 64-section scanner (Discovery 750 HD; GE Healthcare). Imaging protocols can be reviewed in Tables 1 and 2.

The patients' imaging studies were reviewed in consensus by 3 radiologists (a fellowship-trained musculoskeletal radiologist with 10 years' experience, a neuroradiologist with 2 years' experience, and a musculoskeletal radiology fellow). Imaging was evaluated for the presence of meningeal ossification, location of the

ossification, associated spinal cord or nerve root distortion, and a pattern of ossification. Common patterns of ossification were described and categorized. When available, MR imaging was reviewed to evaluate corresponding lesions as well as associated signal abnormalities within the nerve roots and cord. The data sets were collected and collated in de-aggregate form. A series of 41 cases of AO was identified. A summary of patient demographics and characteristics is included in Table 3.

Four major etiologic categories were identified with the following frequency: 1 inflammatory, 1 posttraumatic, 7 idiopathic, and 32 postsurgical. A 38-year-old male patient with a remote history of gunshot wound to the thoracic and lumbar spine with follow-up imaging demonstrating lumbar spine AO (Fig 1) was included; this patient did not undergo any spinal surgery because he was hemiparetic at the time of injury. One patient with a history of ankylosing spondylitis was included, and, in addition to findings of AO, imaging demonstrated classic features of diffuse syndesmophyte ankylosis with a "bamboo spine" appearance, interspinous ligament ossification, and intradiscal calcification (Fig 2).

In 7 patients, AO was found without a history of symptoms, inciting events, or risk factors. One of these patients was a 24-year-old female gymnast presenting with low back pain without a history of known trauma, infection, or inflammatory disorder. Another case was a 20-year-old man who presented for whole-spine CT following a suicide attempt, and AO was discovered at the distal-most aspect of the thecal sac. AO was also found within the thoracic spine on a CT scan of the chest in 2 patients imaged for screening for lung nodules. In another patient, AO was found in the lumbar spine on a CT scan of the pelvis performed for evaluation of the hip joints. Pre-existing AO was found on 2 lumbar spine CT scans in 1 patient presenting for imaging in the setting of acute trauma and in another patient being evaluated for multiple myeloma.

The largest subset of patients consisted of 32 cases with a history of spinal surgery. Two patients underwent tethered cord release, 8 patients underwent laminectomy only, and 22 patients underwent combined laminectomy and instrumented arthrodesis (Fig 3). The diagnosis of AO was made in patients with a history of

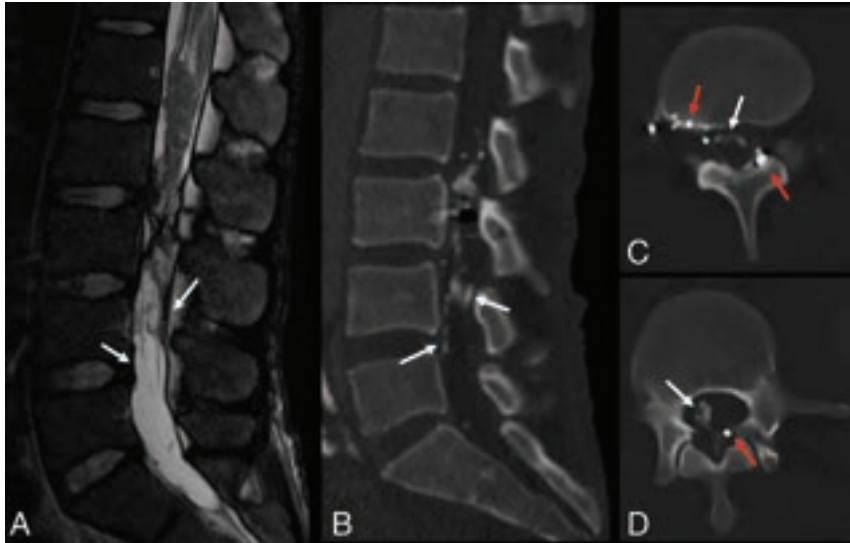


FIG 1. A 38-year-old male patient presenting 7 years following gunshot injury to the lumbar spine. Imaging from the time of the injury was unavailable for review. Sagittal T2-weighted MR imaging (A) demonstrates low signal thickening of the thecal sac as well as contour deformity of the thecal sac and its contents. Intermediate-signal tissue is present at the conus medullaris, relating to a posttraumatic scar. CT image (B) demonstrates peripheral and weblike ossification within the thecal sac (white arrows), which is not definitively identified on MR imaging (white arrows). The weblike ossification is better demonstrated on axial CT images (C and D), which also show multiple foci of metallic debris related to the prior gunshot injury (red arrows).

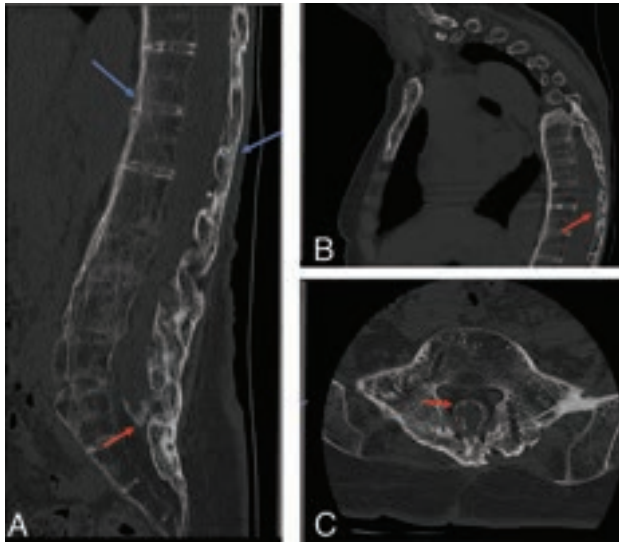


FIG 2. CT images from a 66-year-old female patient with back pain and stiffness. Sagittal (A and B) and axial (C) CT demonstrate features of spinal ankylosis relating to inflammatory spondyloarthropathy (blue arrows). AO is evident by thick peripheral ossification of the meninges most prominent at the tip of the thecal sac; however, it can also be seen in the thoracic spine (red arrows).

surgery, on average, 13.4 (SD 14.7) years following the operation, with a range of 1–47 years. Of these patients, 1 underwent spinal fusion in the setting of a gunshot injury. All patients presenting following surgery had back pain. In 5 patients with history of spinal fusion, consecutive CT demonstrated progression of ossification in the setting of worsening of the patient’s symptoms (Fig 4).

One patient with a history of tethered cord release developed lumbar spine AO and subsequently underwent surgical resection of the ossification. Histopathologic analysis was performed following staining with H&E. The resection specimen demonstrated peripheral areas of osseous formation along the margins of resected tissue, consisting of meningotheelial cells within leptomeninges with scattered foci of calcification (Fig 5).

Review of all imaging demonstrated 4 typical patterns of ossification seen in our case series (Fig 6). Patients either presented with a dominant pattern or demonstrated a mixed presentation. The first observed pattern was peripheral ossification along the border of the thecal sac, which can be completely or partially circumferential; this pattern was observed in 8 patients. The second observed pattern was central longitudinal ossification within the thecal sac with a filamentous morphology on sagittal imaging, which was seen in 5

patients; depending on the location and appearance, this may represent ossification surrounding the filum terminale. The third pattern was weblike ossification that fills the CSF space and insinuates throughout the thecal sac; 7 patients presented with this pattern. Finally, a pattern in which the ossification encased ≥ 1 nerve root was seen in 3 patients. In 18 patients, a mixed pattern of ossification was observed, which predominated as a combination of central and peripheral as well as peripheral and weblike. In these patients, the 2 patterns contributed equally to the overall appearance of AO (Fig 7). In the 4 patients presenting with neurologic symptoms of unilateral lower extremity weakness, numbness, and neurogenic claudication, peripheral and nerve-encasing patterns of ossification were seen.

Twenty-five patients had both MR imaging and CT of the spine. MR imaging of the spine included sagittal and axial T1 and T2, coronal T2, and sagittal STIR sequences; gradient-echo sequences were not used and are not part of our routine non-supervised MR imaging of the thoracic and lumbar spine. Regions of ossification demonstrated on CT corresponded to findings on MR imaging predominating as areas of low-signal-intensity thickening of the thecal sac and surrounding the nerve roots as well as clumping up the nerve roots and contour distortion of the thecal sac and nerve roots. Ossification was not reliably demonstrated on MR imaging. The findings demonstrated on MR imaging are not specific to AO and can be seen in the spectrum of chronic adhesive arachnoiditis. Of 25 patients, 23 had a history of spinal surgery, 1 had a gunshot injury, and 1 was in the incidental group. In all except 1 patient, MR imaging was performed before the CT scan. The only person who had a CT scan before MR imaging had sustained a gunshot wound to the thoracic spine. In the patients with a history of spinal instrumentation, all

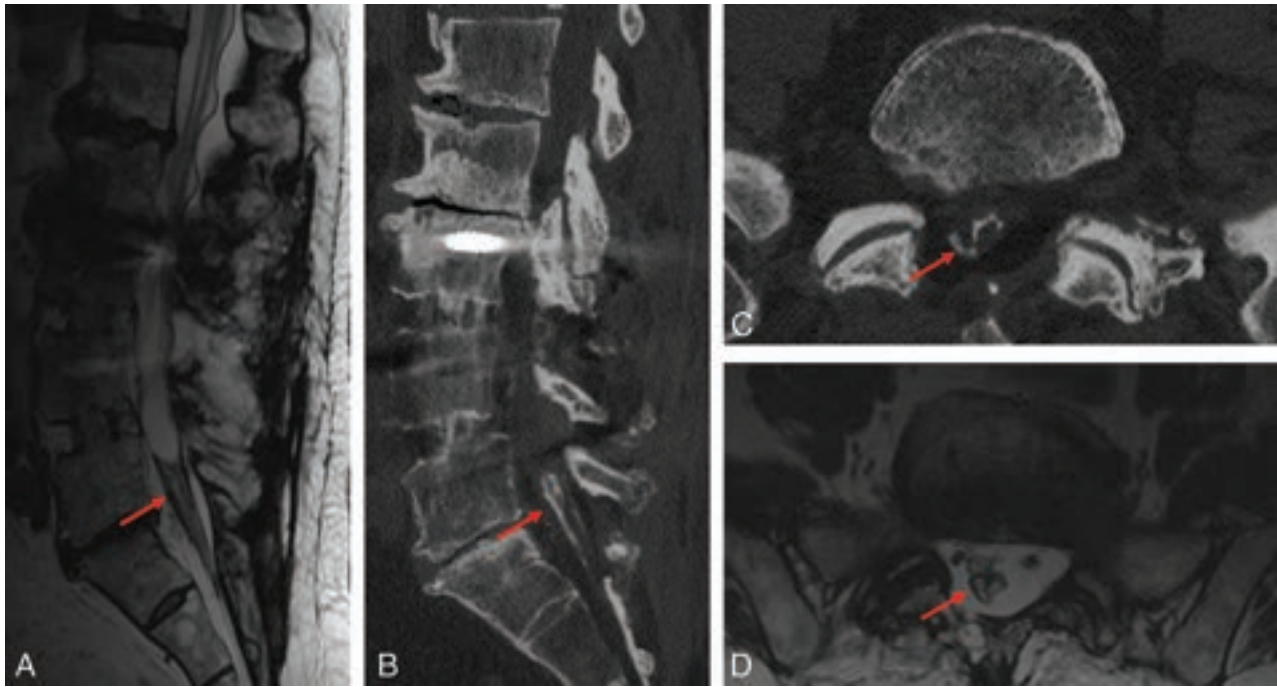


FIG 3. A 78-year-old man status post multiple lumbar surgeries. T2-weighted MR imaging of the lumbar spine including sagittal (A) and axial (D) reformats demonstrates low signal thickening of the thecal sac and surrounding the nerve roots (red arrows), which manifests as weblike ossification on sagittal (B) and axial (C) CT images (red arrows). MR images (A and D) depict the associated thecal sac distortion.



FIG 4. Comparison of CT scans of the lumbar spine of the same patient performed in 2008 with follow-up in 2018 demonstrates progression of ossification (red arrows), which potentially contributes to progression of pain and neurologic dysfunction.

underwent MR imaging followed by CT. CT was acquired to better evaluate fusion hardware and the cause of back pain.

DISCUSSION

Chronic adhesive arachnoiditis is a pathologic entity seen in the spine that includes a spectrum of severity. The most severe type, AO, is rare, and recognition is important in patients presenting with back pain and neurologic deficits.^{2,12}

This is the largest published series of patients diagnosed with AO secondary to various etiologies. Within the published literature, case reports and series of AO confirmed on imaging can be found dating back to 1982.⁸ Most of the published literature is limited to

single case reports, with the largest case series including 5 patients.³ The most common etiology for AO in the literature was spinal instrumented arthrodesis. Other etiologies included trauma, infection, spondyloarthropathy, intrathecal drug administration, and remote intrathecal contrast administration. The lumbar spine was the most common location for AO within the published case reports, with the second most common location reported in the thoracic spine;^{6-9,13-21} no cases of cervical spine AO were reported. The most common clinical presentations were lower extremity weakness and back pain. Given this distribution, we believe that there is a link between location and etiology.

This series of patients was largely consistent with the demographics and characteristics of patients in the literature. In this series, 78% of patients had undergone spinal surgery, most whom underwent spinal decompression or fusion, which speaks to the prevalence of AO in this patient population. Thus, recognition is important given the increasing volume of spinal surgery.^{22,23} While there are proposed treatment options primarily designed to restore CSF flow dynamics, such as attempts to lyse adhesions, these attempts have demonstrated limited success; therefore, AO should be considered a “do-not touch lesion”^{3,24} because intervention does not lead to symptom improvement or prevent progression of the pathologic process. Like many pathologic processes without robust treatment, we believe that correct diagnosis of AO

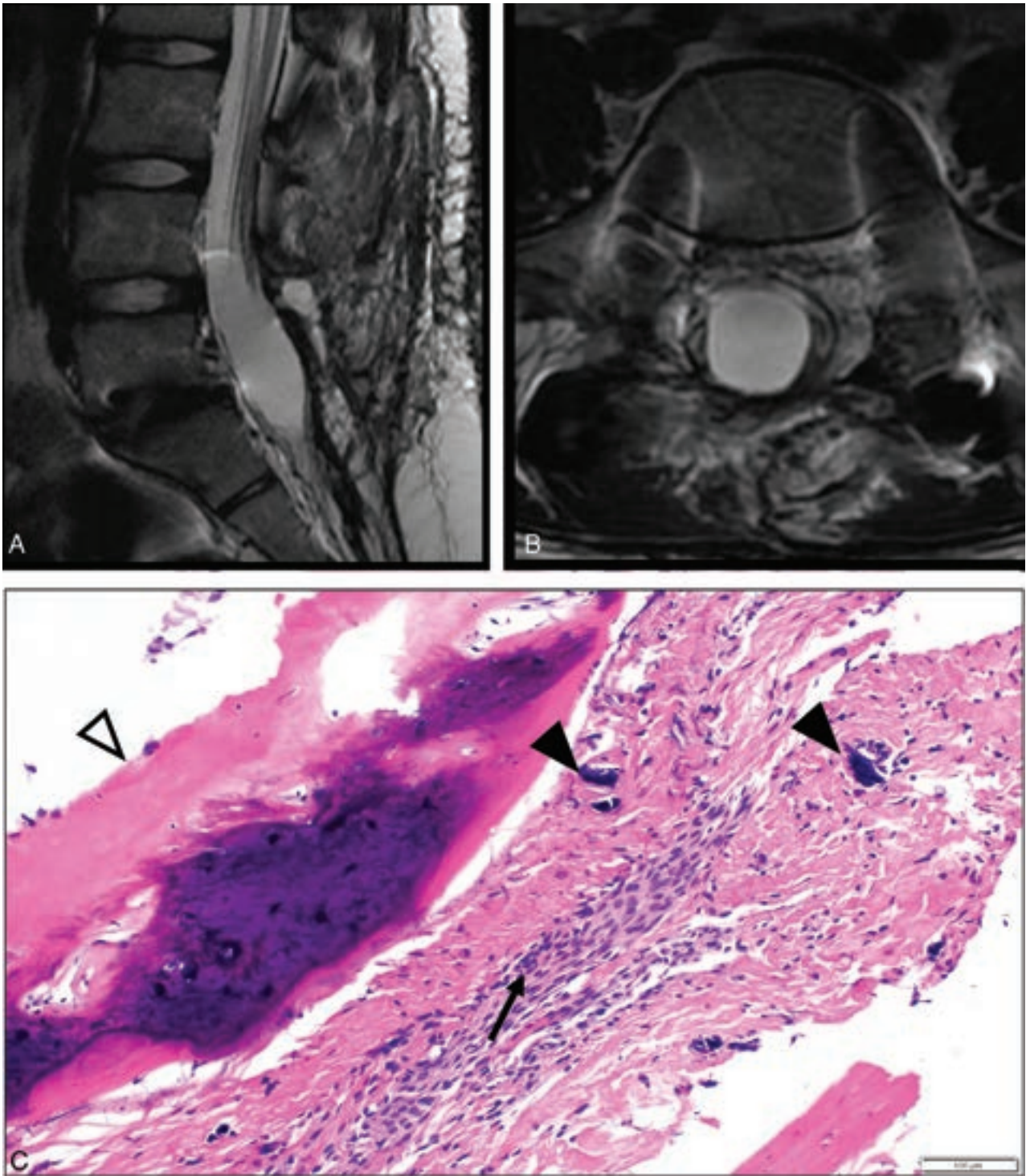


FIG 5. A 16-year-old female patient with a history of remote tethered cord release and posterolateral fusion. MR imaging T2-weighted images in the sagittal (A) and axial (B) planes demonstrate low signal thickening of the thecal sac with peripheralization and clumping of the nerve roots. C, H&E stains of the resection specimen from the thecal sac at the lumbar spine demonstrate meningeal cells within the resected leptomeninges (black arrow), with ossification along the margin of the specimen (white arrowhead) as well as scattered foci of calcification (black arrowheads), consistent with AO.

is important, even in the absence of definitive treatment, because it may prevent unnecessary testing such as CSF sampling, biopsy, and even surgery, thus stressing the importance of acknowledging the various imaging appearances and patterns of AO to prevent misdiagnosis.

Most interesting, this series had 7 cases of idiopathic AO in patients who were reportedly asymptomatic. Given the retrospective nature of this study, clinical information in this group of patients was limited; thus, data were not always available to confirm the presence or absence of symptoms. This finding can be

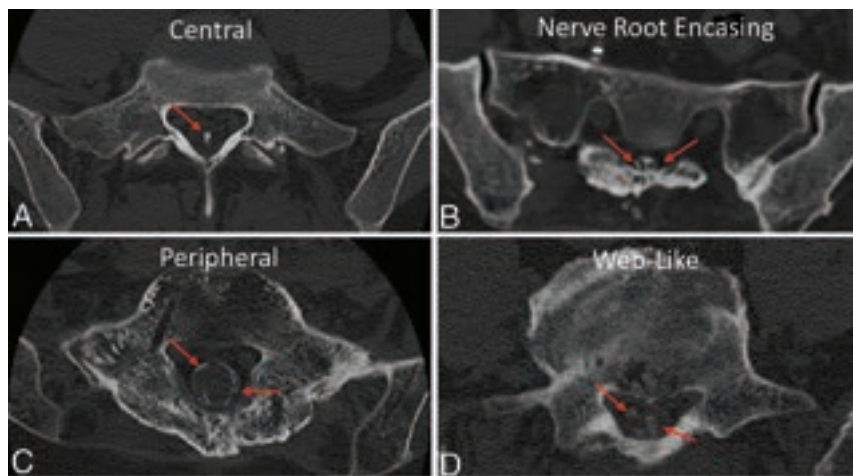


FIG 6. In this series of 41 patients, 4 patterns of ossification that can be seen in AO were identified. Ossification can occur as a combination of patterns, which was the most common in this series. CT images demonstrate the 4 patterns. A, The central pattern demonstrates central ossification within the thecal sac and can have the appearance of a dagger on the sagittal plane. B, Nerve root encasement appears as circumferential ossification surrounding single or multiple roots of the cauda equina. C, The peripheral pattern involves the walls of the thecal sac and can be circumferential or discontinuous. D, The weblike pattern appears as ossification filling the thecal sac and insinuating between the nerve roots. In all panels the *red arrows* point out the areas of ossification.

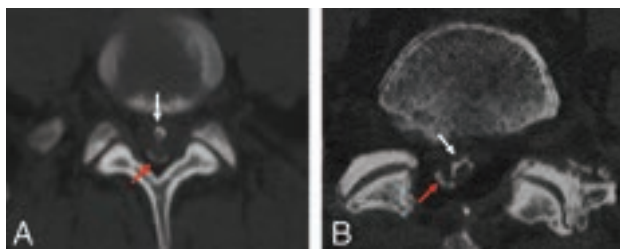


FIG 7. In some patients, a combined pattern of ossification was observed. Axial CT images in 2 unique patients demonstrate 2 patterns coexisting. A, The *red arrow* demonstrates the peripheral pattern of ossification coupled with a central pattern as shown by the *white arrow*. B, In this patient, the *red arrow* also indicates a region of peripheral ossification, coupled with weblike ossification as indicated by the *white arrow*.

interpreted in 2 major ways: One hypothesis is that not all patients experience symptoms from these ossifications; alternatively, the ossification may simply represent a “red herring” in the work-up of patients who have a multitude of reasons for back pain including failed back surgery. These findings further support the importance of recognizing AO as a do not touch lesion. Future prospective and longitudinal studies will be required to answer this question.

The patterns of ossification seen in AO can be variable as demonstrated in our series and within the literature. This variability may result in interpreters under-recognizing AO or mistaking it for another entity. In the literature, attempts have been made to characterize and classify the patterns of ossification. In a study by Domenicucci et al,²⁵ the authors proposed a classification system based on their review of 3 of their own case reports; however, the analysis is limited due to the small sample size. The large size of this series lends itself well to pattern analysis, and the

most common ossification patterns were classified. The 4 main patterns of ossification identified, including peripheral, central, weblike, and nerve encasing, can serve as a guide for the physician interpreting CT of the spine when faced with meningeal ossification. Given the retrospective nature of this case series, it is difficult to associate the different patterns with the severity of symptoms or the presence of neurologic deficits. Most of these patients presented with symptoms of pain, with only 10% presenting with neurologic deficits including weakness and paresthesia. In patients with neurologic deficits, peripheral and nerve-encasing patterns of ossification were seen. This observation suggests that these patterns of ossification may correlate with patient symptoms. However, larger prospective studies are needed to determine this effect.

In 25 patients, MR imaging was available for review. However, the diagnosis of AO was not possible prospectively from the MR imaging nor were there specific MR imaging features to suggest AO. Theoretically, given the underlying osseous metaplasia driving AO, a centrally T1-hyperintense and peripherally hypointense lesion may be considered to represent AO; however, in our experience, the MR imaging finding predominates as T1/T2 low signal indicative of cortical bone. Allowing for the small size of the ossific lesion, the lower spatial resolution and higher section thickness of MR imaging can conceal the T1-hyperintense fatty medullary component of AO, which can be readily seen on CT as hypodensity. In these cases, MR imaging demonstrated low signal thickening of the thecal sac and nerve roots as well as nerve root clumping and contour distortion of thecal sac, all of which are nonspecific for AO and can be seen in the spectrum of chronic adhesive arachnoiditis.

CT remains the technique of choice for the diagnosis of AO. However, in many patients with back pain and neurologic symptoms, MR imaging may be indicated for diagnosis; thus, in these patients who undergo only MR imaging, AO may be underdiagnosed. Radiologists supervising these examinations may elect to add sequences such as fat-suppressed 3D-FLASH sequences²⁶ or a T2-weighted gradient recalled-echo sequence²⁷ for better imaging of cortical bone. These sequences have been reliably used for many years to image osseous morphology and are readily available at most imaging suites. Emerging techniques in MR imaging may, in the future, allow better identification of AO. One such technique is zero-TE, which allows better characterization of ossification and bone structures by acquiring signal immediately after applying the radiofrequency pulse, resulting in near-zero TEs, which allow imaging of structures with very short transverse relaxation times (T2) such as bones.²⁸ This technique is not currently widely used clinically and remains in the research phase; however, many studies evaluating musculoskeletal structures, specifically the spine,^{29,30} have shown promise.

CONCLUSIONS

AO is an important consideration, likely underdiagnosed, in patients who present with back pain following spine surgery. CT is considered diagnostic for AO, and MR imaging is less reliable for definitive diagnosis though it is complementary in evaluating chronic adhesive arachnoiditis. Ossification can progress with time, and it is important to consider with worsening pain/weakness postoperatively. We present the largest series of patients with AO during a 20-year period and demonstrate patterns of ossification: peripheral, central, encasing nerve roots, and weblike.

Disclosure forms provided by the authors are available with the full text and PDF of this article at www.ajnr.org.

REFERENCES

1. Romano N, Castaldi A. **What's around the spinal cord? Imaging features of extramedullary diseases.** *Clin Imaging* 2020;60:109–22 CrossRef Medline
2. Peng H, Conermann T. **Arachnoiditis.** In: *StatPearls*. StatPearls 2021. <http://www.ncbi.nlm.nih.gov/books/NBK555973/>. Accessed January 10, 2022
3. Frizzell B, Kaplan P, Dussault R, et al. **Arachnoiditis ossificans: MR imaging features in five patients.** *AJR Am J Roentgenol* 2001;177:461–64 CrossRef Medline
4. Wright MH, Denney LC. **A comprehensive review of spinal arachnoiditis.** *Orthop Nurs* 2003;22:215–19; quiz 220–21 CrossRef Medline
5. Ward M, Mammis A, Barry MT, et al. **Novel association between intrathecal drug administration and arachnoiditis ossificans.** *World Neurosurg* 2018;115:400–06 CrossRef Medline
6. Wang S, Ahuja CS, Das S. **Arachnoiditis ossificans: a rare etiology of oil-based spinal myelography and review of the literature.** *World Neurosurg* 2019;126:189–93 CrossRef Medline
7. Whittle IR, Segelov JN. **Spinal arachnoiditis ossificans.** *Neurosurgery* 1983;13:737 CrossRef Medline
8. Barthelemy CR. **Arachnoiditis ossificans.** *J Comput Assist Tomogr* 1982;6:809–11 CrossRef Medline
9. Wijdicks CA, Williams JM. **Spinal arachnoid calcifications.** *Clin Anat* 2007;20:521–23 CrossRef Medline
10. Singh H, Meyer SA, Jannapureddy MR, et al. **Arachnoiditis ossificans.** *World Neurosurg* 2011;76:478.e12–14 CrossRef Medline
11. Bakhsh WR, Mesfin A, Bridwell KH. **Arachnoiditis ossificans after revision adolescent idiopathic scoliosis surgery: a 22-year follow-up and review.** *Spine (Phila Pa 1976)* 2013;38:E1166–70 CrossRef Medline
12. Anderson TL, Morris JM, Wald JT, et al. **Imaging appearance of advanced chronic adhesive arachnoiditis: a retrospective review.** *AJR Am J Roentgenol* 2017;209:648–55 CrossRef Medline
13. Abrams J, Li G, Mindea SA, et al. **Arachnoid ossificans containing metaplastic hematopoietic marrow resulting in diffuse thoracic intrathecal cysts and severe myelopathy.** *Eur Spine J* 2012;21(Suppl 4):S436–40 CrossRef Medline
14. Bagley JH, Owens TR, Grunch BH, et al. **Arachnoiditis ossificans of the thoracic spine.** *J Clin Neurosci* 2014;21:386–89 CrossRef Medline
15. Bailey D, Mau C, Rizk E, et al. **Arachnoiditis ossificans in the thoracic spine with associated cyst and syringomyelia: a rare, intraoperative finding complicating dural opening.** *Cureus* 2021;13:e16910 CrossRef Medline
16. Cosan TE, Kabukcuoglu S, Arslantas A, et al. **Spinal toxoplasmic arachnoiditis associated with osteoid formation: a rare presentation of toxoplasmosis.** *Spine (Phila Pa 1976)* 2001;26:1726–28 CrossRef Medline
17. Kahler RJ, Knuckey NW, Davis S. **Arachnoiditis ossificans and syringomyelia: a unique case report.** *J Clin Neurosci* 2000;7:66–68 CrossRef Medline
18. Papavaslopoulos F, Stranjalis G, Kouyialis AT, et al. **Arachnoiditis ossificans with progressive syringomyelia and spinal arachnoid cyst.** *J Clin Neurosci* 2007;14:572–76 CrossRef Medline
19. Slavin KV, Nixon RR, Nesbit GM, et al. **Extensive arachnoid ossification with associated syringomyelia presenting as thoracic myelopathy: case report and review of the literature.** *J Neurosurg* 1999;91:223–29 CrossRef Medline
20. Toribatake Y, Baba H, Maezawa Y, et al. **Symptomatic arachnoiditis ossificans of the thoracic spine: case report.** *Paraplegia* 1995;33:224–27 CrossRef Medline
21. Joković M, Grujićević D, Baščević V, et al. **Thoracic arachnoiditis ossificans associated with multifocal motor neuropathy: a case report.** *Br J Neurosurg* 2019 June 19 [Epub ahead of print] CrossRef Medline
22. Beschloss A, Ishmael T, Dicindio C, et al. **The expanding frontier of outpatient spine surgery.** *Int J Spine Surg* 2021;15:266–73 CrossRef Medline
23. Meara JG, Leather AJM, Hagander L, et al. **Global Surgery 2030: evidence and solutions for achieving health, welfare, and economic development.** *Lancet* 2015;386:569–24 CrossRef Medline
24. Scalia G, Certo F, Maione M, et al. **Spinal arachnoiditis ossificans: report of quadruple-triggered case.** *World Neurosurg* 2019;123:1–6 CrossRef Medline
25. Domenicucci M, Ramieri A, Passacantilli E, et al. **Spinal arachnoiditis ossificans: report of three cases.** *Neurosurgery* 2004;55:985 CrossRef Medline
26. Algin O, Gokalp G, Ocakoglu G. **Evaluation of bone cortex and cartilage of spondyloarthropathic sacroiliac joint: efficiency of different fat-saturated MRI sequences (T1-weighted, 3D-FLASH, and 3D-DESS).** *Acad Radiol* 2010;17:1292–98 CrossRef Medline
27. Tang MY, Chen TW, Zhang XM, et al. **GRE T2*-weighted MRI: principles and clinical applications.** *Biomed Res Int* 2014;2014:312142 CrossRef Medline
28. Weiger M, Brunner DO, Dietrich BE, et al. **ZTE imaging in humans.** *Magn Reson Med* 2013;70:328–32 CrossRef Medline
29. Argentieri EC, Koff MF, Breighner RE, et al. **Diagnostic accuracy of zero-echo time MRI for the evaluation of cervical neural foraminal stenosis.** *Spine (Phila Pa 1976)* 2018;43:928–33 CrossRef Medline
30. Hou B, Liu C, Li Y, et al. **Evaluation of the degenerative lumbar osseous morphology using zero echo time magnetic resonance imaging (ZTE-MRI).** *Eur Spine J* 2022;31:792–800 CrossRef Medline

Regarding “Rates of Epidural Blood Patch following Lumbar Puncture Comparing Atraumatic versus Bevel-Tip Needles Stratified for Body Mass Index”

We read with interest the article by Philip et al¹ on postprocedural complications after fluoroscopically-guided dural puncture (fLP) because their results were dissimilar to those in our own research.² In our study of 2141 patients who underwent fLP with Quincke needles, 0.8% (18/2141) required an epidural blood patch (EBP) for postprocedural headache. In contrast, of the 2258 patients who underwent fLP with Quincke needles in the study by Philip et al, 4.3% (97/2258) required EBP. Of the patients who underwent fLP with Whitacre spinal needles in their study, 1.4% (30/2177) required EBP. We have several questions for Philip et al that might help us to understand the higher rates of EBP in their patients and may call into question their conclusion that atraumatic needles result in lower rates of EBP from fLP in overweight and obese patients.

Young age and female sex are predisposing factors for positional headaches following lumbar puncture, as confirmed in our study.² No data were provided in the article by Philip et al¹ regarding the age and sex of patients. There might be a higher percentage of young women among the patients treated with Quincke needles or among their patient population overall compared with our cohort.

We note in Table 3 of the article by Philip et al¹ that the *P* value for needle caliber was <.001 in patients with a body mass index of >30, yet the 95% confidence interval of the odds ratio encompasses unity. These statistics appear to be internally discrepant. We note this particularly because in our study, we did not find the needle caliber to be a predictive variable.

All procedures in our study were performed by a single experienced operator. Philip et al¹ indicated that procedures in their study were performed by radiologists, but they provided no information about years in practice or number of cases performed by each practitioner in a typical year. It is unclear whether trainees were the primary operators in these procedures. Given that Quincke needles are more steerable, might radiology residents

prefer them while the more experienced attending radiologists prefer Whitacre needles? Needles were chosen by the operators in this retrospective study, so operator preference, experience, and expertise are important confounding variables that were not included.

The advantages of atraumatic needles in unguided (blind) dural punctures have been established in the neurology literature. It remains controversial, however, whether these advantages are present when image guidance is used. The rate of EBP in fLP is markedly lower than that for unguided punctures, which may obviate any advantage of needle choice.

It is unclear to us why our rate of postprocedural EBP is substantially lower than that recorded by Philip et al.¹ This rate may reflect differences in technique, patient population, or operator expertise. The work by Philip et al is interesting, but firm conclusions regarding the relative advantages of needle type in fLP should be based on literature that controls for patient characteristics such as age and sex as well as operator characteristics such as experience.

Disclosure forms provided by the authors are available with the full text and PDF of this article at www.ajnr.org.

REFERENCES

1. Philip JT, Flores MA, Beegle RD, et al. Rates of epidural blood patch following lumbar puncture comparing atraumatic versus bevel-tip needles stratified for body mass index. *AJNR Am J Neuroradiol* 2022;43:315–18 CrossRef Medline
2. Rodriguez D, Branstetter BF, Agarwal V, et al. JOURNAL CLUB: incidence of complications following fluoroscopically guided lumbar punctures and myelograms. *AJR Am J Roentgenol* 2016;206:20–25 CrossRef Medline

● B. Branstetter
● V. Agarwal
● M. Hughes

Department of Radiology
University of Pittsburgh Medical Center
Pittsburgh, Pennsylvania

<http://dx.doi.org/10.3174/ajnr.A7562>

REPLY:

We appreciate the feedback from Branstetter et al. As with any retrospective study, our study has limitations. One of the main limitations of our study is that the lumbar punctures (LPs) were performed by a variety of radiologists with variable levels of experience, including trainees.¹ While this feature introduces potential confounding variables, we believe it is more indicative of how LPs are performed in most radiology departments; thus, it is a more accurate estimation of post-dural puncture headaches (PDPHs) necessitating an epidural blood patch (EBP). The number of LPs performed in radiology has been increasing.² They are performed by a variety of practitioners with a variety of experience levels, including increasingly by nonphysician providers such as in the study of Rodriguez et al.³ We believe our study is a “real-world” estimation of EBP rates in a heterogeneous patient population with a heterogeneous group of operators. Our study was designed to examine whether there were differences in EBP rates when comparing traumatic with atraumatic needles stratified to the body mass index, not to determine whether there were different EBP rates based on sex or age.

We do not know why our rates of EBP in the Quincke group were higher than those found in the study of Rodriguez et al.³ A different patient cohort certainly could be contributory. At the institution where the data were collected, there was a relatively low threshold to perform an EBP in patients with post-LP headaches, and there was a streamlined process for clinicians to refer patients for EBP. Perhaps the threshold for performing an EBP was different at the two institutions. The rate of post-LP “any headache” was higher than the “severe headache” rate at 2.2% in the study of Rodriguez et al.³ Our rate of EBP in the Quincke group was well below that reported in the study from Hatfield et al.⁴ for fluoroscopically guided LPs with a 22-ga Quincke needle, which was 15.2%.

We acknowledge an error in Table 3 of our article. As stated in our results section, we found no statistically significant difference

in rates of EBP when comparing the 22-ga Quincke with the 20-ga Quincke needle. The confidence interval in Table 3 is correct. The corrected *P* value is .411.

We believe that our study and other studies involving both fluoroscopically guided and non-fluoroscopically guided LPs are compelling in demonstrating an increased rate of PDPHs necessitating an EBP when comparing traumatic-versus-atraumatic spinal needles. However, these studies suffer from the inherent limitations of retrospective studies. We believe a well-designed prospective randomized study would likely end any remaining debate.

REFERENCES

1. Philip JT, Flores MA, Beegle RD, et al. **Rates of epidural blood patch following lumbar puncture comparing atraumatic versus bevel-tip needles stratified for body mass index.** *AJNR Am J Neuroradiol* 2022;43:315–18 CrossRef Medline
2. Johnson DR, Waid MD, Rula EY, et al. **Comparison of radiologists and other specialists in the performance of lumbar puncture procedures over time.** *AJNR Am J Neuroradiol* 2021;42:1174–81 CrossRef Medline
3. Rodriguez D, Branstetter BF, Agarwal V, et al. **JOURNAL CLUB: incidence of complications following fluoroscopically guided lumbar punctures and myelograms.** *AJR Am J Roentgenol* 2016;206:20–25 CrossRef Medline
4. Hatfield MK, Handrich SJ, Willis JA, et al. **Blood patch rates after lumbar puncture with Whitacre versus Quincke 22- and 20-gauge spinal needles.** *AJR Am J Roentgenol* 2008;190:1686–89 Medline

● J.T. Philip

University of Texas Southwestern Medical Center
Dallas, Texas

● M.A. Flores

● R.D. Beegle

● S.C. Dodson

AdventHealth Medical Group Radiology at Central Florida
Orlando, Florida

● S.A. Messina

Mayo Clinic Rochester
Rochester, Minnesota

● J.V. Murray, Jr.

Mayo Clinic
Jacksonville, Florida

<http://dx.doi.org/10.3174/ajnr.A7770>

CAA-ri and ARIA: Two Faces of the Same Coin?

In their article, Cogswell et al¹ offered a valuable critical reflection on the past, present, and future challenges in the application of detection and reporting recommendations for amyloid-related imaging abnormalities (ARIAs) associated with amyloid β ($A\beta$)-lowering immunotherapy for Alzheimer disease (AD) in real-world clinical settings. Increased evidence suggests that drug-induced ARIAs are the iatrogenic manifestation of cerebral amyloid angiopathy-related inflammation (CAA-ri), a rare autoimmune encephalopathy associated with elevated CSF concentrations of spontaneous anti- $A\beta$ autoantibodies (autoAbs) and transient focal areas of swelling (also known as ARIA-E in clinical trials) and CAA-related microhemorrhage (also known as ARIA-H in clinical trials).^{2,3}

In this framework, research and experience in the comparison of ARIAs and CAA-ri in the past decade indicate 3 main critical considerations: First, evidence from trials is limited to an extremely well-selected and neuroradiologically monitored subpopulation of patients with AD. Therefore, current results may have limited generalizability to the broadened community of AD in real clinical settings. In fact, to minimize the occurrence of ARIA, common exclusion criteria are ≥ 5 cerebral microbleeds (CMBs), irrespective of their location, any cortical superficial siderosis (cSS), and a history of intracerebral hemorrhage (ICH) at baseline MR imaging. However, CMBs, ICH, and cSS do not completely account for the neuroradiologic semiology of small vessel diseases. Given the well-known comorbidity of CAA in AD, further research evaluating the combination of microhemorrhage and no hemorrhagic presentations to increase the sensitivity and specificity in the diagnosis and prediction of ARIA may reveal a strategic issue, as recently reported in the improved Boston criteria 2.0 for the diagnosis of CAA.⁴

Second, the acronym ARIAs was intended to strictly define the occurrence of neuroimaging abnormalities, not to provide information concerning the associated clinical manifestations. Indeed, current rating systems for ARIA have demonstrated no correspondence between the severity of ARIAs and clinical status and a poor capacity in advising about continuing treatment in patients presenting with mild and asymptomatic ARIA-E. The recent natural history study of CAA-ri in a large, multicenter, prospective longitudinal cohort from a real clinical practice highlighted the transient and potentially remitting nature of ARIA-E, with 84% of clinical and neuroimaging recovery within, respectively, 3 and 6 months and 38% of recurrences within 2 years, which were more common when intravenous corticosteroid therapy was suddenly discontinued without a slow oral tapering.^{2,3}

Third, given the lack of samples and data in trials for independent research, the pathophysiologic mechanisms of ARIAs remain largely unknown. According to the ARIA paradox pathophysiologic model, ARIA-E is a complex and multifactorial phenomenon resulting from the imbalance between the autoantibodies-mediated removal of $A\beta$ from plaques and the downstream effects that an excessive mobilization of the protein can cause on intramural periarterial drainage pathways and neuroinflammation. This hypothesis has been recently investigated in a longitudinal case series of CAA-ri showing a regional and temporal association between ARIA-E and microglial activation and the CSF levels of autoAbs.² Most interesting, this study also showed that current ARIA-E rating systems alone might not fully capture the complex underlying biology of the phenomenon, suggesting that the combination of MR imaging markers and fluid-based biomarkers can increase the capacity to perform a correct diagnosis. To this end, high levels of autoAbs at baseline may constitute a risk factor, and the CSF testing for autoAbs may meet the specific requirement of companion diagnostic biomarkers for drug tailoring based on the individual risk for iatrogenic CAA-ri. Taken together, this evidence suggests that iatrogenic ARIA-E can be part of the increasingly recognized inflammatory spectrum in $A\beta$ -driven pathologies of aging and that the current diagnosis of spontaneous and iatrogenic CAA-ri can be missed if not properly investigated.⁴

Increased understanding of the biology of ARIA should reveal a strategic area of research because it could advance the design of second generations of therapeutics and the discovery of the safety and response-to-treatment biomarkers to improve how we currently report, treat, and manage spontaneous and iatrogenic CAA-ri.

Then, a multidisciplinary and interdisciplinary joint effort among neuroradiology, clinical, and translational researchers has never been so important. A common research strategy for ARIA and CAA-ri could reveal strategic information to advance current knowledge gaps and issues in the field, including providing convincing plans for the treatment and management of ARIA when these drugs enter real clinical practice. Only by working together will we really make progress.

Disclosure forms provided by the authors are available with the full text and PDF of this article at www.ajnr.org.

REFERENCES

1. Cogswell PM, Barakos JA, Barkhof F, et al. Amyloid-related imaging abnormalities with emerging Alzheimer disease therapeutics: detection

- and reporting recommendations for clinical practice. *AJNR Am J Neuroradiol* 2022;43:E19–35 CrossRef Medline
2. Piazza F, Caminiti SP, Zedde M, et al. **Association of microglial activation with spontaneous ARIA-E and CSF levels of anti-A β autoantibodies.** *Neurology* 2022;99:e1265–77 CrossRef Medline
 3. Antolini L, DiFrancesco JC, Zedde M, et al. **Spontaneous ARIA-like events in cerebral amyloid angiopathy-related inflammation: a multicenter prospective longitudinal cohort study.** *Neurology* 2021;97:e1809–22 CrossRef Medline
 4. Charidimou A, Boulouis G, Frosch MP, et al. **The Boston criteria version 2.0 for cerebral amyloid angiopathy: a multicentre, retrospective, MRI-neuropathology diagnostic accuracy study.** *Lancet Neurol* 2022;21:714–25 CrossRef Medline

● **M. Zedde**

Neurology Unit, Stroke Unit
Azienda Unità Sanitaria Locale-IRCCS di Reggio Emilia
Reggio Emilia, Italy

● **R. Pascarella**

Neuroradiology Unit, iCA β International Network
Azienda Unità Sanitaria Locale-IRCCS di Reggio Emilia
Reggio Emilia, Italy

● **F. Piazza**

CAA and AD Translational Research and Biomarkers Lab, School of Medicine
University of Milano-Bicocca
Monza, Italy